Studying Galaxy-Galaxy Lensing and Higher-Order Galaxy-Mass Correlations Using the Halo Model

DISSERTATION

zur

Erlangung des Doktorgrades (Dr. rer. nat.)

der

Mathematisch-Naturwissenschaftlichen Fakultät

der

Rheinischen Friedrich-Wilhelms-Universität Bonn

vorgelegt von

JENS RÖDIGER

aus

Dortmund

Bonn 2009

Contents

Introduction and Overview

In recent years, our understanding of the evolution of the Universe has made a great leap forward. A decisive factor for this achievement is that we have collected an enormous amount of high-quality cosmological data, e.g., the positions and shapes of millions of galaxies. The improvements in data collection are founded in the design of modern observational instruments and the ability to store and process large amounts of data on computers. Along with the progress of the experimental techniques, we have developed a consistent theoretical framework which accurately reproduces the data. This (ongoing) progress makes cosmology a precision science where important cosmological parameters can be constrained with percentage accuracy. However, our improved understanding also raises new fundamental questions of the physical processes involved. Most importantly, the nature of dark matter and dark energy, which together comprise 96 per cent of the energy composition of the Universe, is still unknown. Dark matter is postulated to explain, among other observations, the flat rotation curves in spiral galaxies. Up to now, attempts to directly detect dark matter particles or to reproduce them in high-energy accelerators have failed. Dark energy is a hypothetical form of energy which is introduced to explain the current accelerated phase in the expansion history of the Universe. At the moment and in the near future several complementary experiments are underway and being planned to get an insight into these unsolved issues, making this a particular exciting time for cosmologists.

A successful cosmological model needs to explain measurements of the early Universe, such as the abundance of primordial elements and the temperature fluctuations in the cosmic microwave background (CMB) radiation, as well as measurements of the local Universe such as the distribution of galaxies. The connection between the two regimes is that the large-scale structure we observe today is believed to have formed by gravitational collapse of small density fluctuations that were present in the early Universe. With the knowledge of the initial distribution of these density perturbations, which can be accurately measured by observations of the CMB temperature fluctuations, we can predict the statistical properties of the large-scale structure observed today. To describe this evolution, we need the physics of gravitational clustering as described by general relativity or for scales much smaller than the Hubble radius even by a Newtonian approach. Up to now, theoretical predictions have been essentially limited to dark matter fluctuations, whereas observations measure the light or galaxy distribution of the Universe. The difficulty is that, in general, the statistics of galaxy clustering is not the same as the statistics of dark matter clustering and the scale-dependent difference between both is known as the galaxy bias. To find a connection between theoretical predictions and observations, the modeling of the bias is one of the crucial challenges in

modern cosmology.

A promising cosmological probe to infer the bias is galaxy-galaxy lensing which describes the deflection of light from background galaxies caused by the gravitational field of foreground galaxies. The gravitational field around the foreground galaxies is dominated by the dark matter halos in which the galaxies are embedded. The advantage of galaxy-galaxy lensing compared to other cosmological probes is that it does not rely on luminous tracers of the underlying mass distribution. Moreover, it can probe the potential of the dark matter halo out to much larger distances from the halo center than it is possible with measurements of rotation curves in spiral galaxies. Recently, the concept of galaxy-galaxy lensing has been generalized to a method which is sensitive to the distortion pattern around pairs of foreground galaxies rather than the distortion around a single galaxy. This new method is termed galaxy-galaxy-galaxy lensing (GGGL). A potentially beneficial application of GGGL is to study the environment of bound systems which are composed of a small number of galaxies, like galaxy groups.

Theoretical predictions of measurements of galaxy-galaxy lensing need to provide an accurate model of gravitational clustering. These models necessarily have to include a treatment of nonlinearities in the matter density field in order to describe the small-scale regime of the measurements. There are three main approaches to deal with these nonlinearities: on large to intermediate scales, the dynamical equations can be solved analytically with a perturbative ansatz which, however, breaks down on small scales. Alternatively, one can simulate the evolution of the density and velocity fields in dark matter N-body simulations. The drawback of using simulations is that they are limited to a specific volume size and are very time-consuming to conduct. Finally, there are analytic models which combine the results from simulations and theoretical results. These models allow for a physical interpretation and may help to find a solution of the gravitational clustering equations valid for the whole range of scales. The drawback is that they need to be well tested against numerical simulations.

We apply the third approach and consider an analytic model where all the dark matter of the Universe is bound in spherically symmetric halos. The standard paradigm for the formation of galaxies is then that baryonic gas can only cool and form stars in potential wells which are provided by dark matter halos. On large scales, galaxy clustering is then dominated by the well-known clustering of halos, and on small scales it is dominated by the clustering of galaxies in their host halo. The latter can be predicted by modeling the halo occupation distribution which is the mean number of galaxies contained in a halo of a specific mass. In addition, one needs to specify the radial distribution of galaxies in their host halo. This analytic approach is known as the *halo model* for galaxy clustering. If one considers only dark matter clustering one speaks of the dark matter halo model.

To extract cosmological information from the observed large-scale structure, the best we can do is to adopt a statistical approach where our observable Universe is a stochastic realization of a random field. The key observables are the moments of this random field which are the n-point correlation functions in real space. Only for the special case of Gaussian random fields does the two-point correlation function, or its

Fourier counterpart the power spectrum, encode the full statistical information of the field. However, the process of structure formation inevitably leads to nonlinearities in the fields which also give rise to higher-order correlation functions. It is interesting to study the three-point correlation function, or its Fourier counterpart the bispectrum, since it is the lowest-order non-vanishing moment which describes non-Gaussian effects. Furthermore, it is beneficial to study the fourth-order moment, which is the so-called trispectrum in Fourier space, since it determines the expected statistical errors for a given power spectrum estimator. In addition to these aspects, the determination of higher-order spectra allows one to lift cosmological parameter degeneracies and to enhance the signal-to-noise ratio of observations of galaxy clustering. The halo model provides a simple framework for analytic calculations of higher-order spectra.

Overview

In this thesis we focus on the modeling and cosmological interpretation of higher-order spectra. In particular, we aim to develop a quantitative model for the GGGL signal, combining the dark matter halo model and the halo model for galaxy clustering. In addition, we want to predict the statistical error matrix for a given unbiased estimator for the projected matter-galaxy power spectrum which is applicable for the whole range of scales probed by observations. The results can be used to perform a likelihood analysis of the galaxy-galaxy lensing signal which shows how well potential future experiments can constrain cosmological parameters.

The outline of the thesis is as follows:

- In Chapter 1, we derive the important relations of the homogeneous background Universe and discuss how different cosmological probes can determine the important cosmological parameters. In addition, we present the observational evidence which in recent years has led to the cosmological standard model. As an important example for a mechanism beyond the standard model, we discuss the inflationary phase of the early Universe.

- Chapter 2 deals with the physical description of cold dark matter structure formation via the nonrelativistic fluid equations. We show that these can be solved with a perturbative approach, first presenting the well-known linear solution, and then giving a valid general perturbative solution. In addition, we introduce n-point correlation functions which are used to infer statistical information on the matter or galaxy clustering.

- In Chapter 3, we first present the ingredients of the dark matter halo model such as the halo mass function, the halo density profile and the halo bias. Then we show that we can construct general n-point correlation functions in terms of these ingredients which are valid on large and on small scales. We give explicit results for the two-, three- and four-point correlation functions and their corresponding

Fourier space counterparts, i.e., the power spectrum, the bispectrum and the trispectrum, which are needed for the subsequent chapters.

- The results of the dark matter halo model are extended to the halo model of galaxy clustering which is shown in Chapter 4. The main new ingredients are the halo occupation distribution $P(N|m)$ which is the conditional probability that a halo of mass m contains N galaxies, and the radial distribution of galaxies in their host halo. We focus on the development of cross-spectra which are probed by galaxy-galaxy lensing, and give the explicit relations for the power spectra, bispectra and trispectra.

- In Chapter 5, we review the basic concepts of gravitational lensing. Then we focus on cosmic shear as a cosmological probe whose signal is a filtered version of the angular spectra. The angular and spatial spectra are related by Limber's approximation. We use our implementation of the dark matter halo model developed in Chapter 3 to produce theoretical predictions.

- In Chapter 6, we first discuss galaxy-galaxy lensing and the estimation of its signal with the halo model. The main emphasis is on the recently introduced GGGL method for which we show halo model predictions of the signal. For these predictions we need the results of the halo model for galaxy clustering as given in Chapter 4.

- Chapter 7 deals with the theoretical modeling of the covariance of the galaxy-galaxy lensing power spectrum. In particular, we include the non-Gaussian part which was neglected in previous studies. Moreover, we analyze the influence of shot and shape noise on the correlations of different scales.

The main new results of this thesis are summarized at the end of Chapter 6 and Chapter 7. The thesis concludes with a general summary and gives an outlook on future related work.

Chapter 1

The Cosmological Standard Model

At first sight it seems impossible to describe the evolution of the Universe. Fortunately, observational data indicate that on the largest scales we live in a highly symmetric Universe which makes a theoretical description feasible. Going to smaller scales, however, we see many structures like galaxies that are not distributed isotropically. The standard paradigm is that these structures originated from small perturbations that were present in the early Universe and which subsequently grew due to gravitational instability. Here we focus first on the cosmological model of the homogeneous background Universe neglecting all perturbations. In the next chapters we will discuss in detail the process of structure formation leading to the observed inhomogeneous structures on small scales in the environment of the mean background model. Understanding the properties of the mean background Universe and the dynamical formation of structure are the key theoretical concepts that are needed for the interpretation of experimental results of cosmological probes.

The great improvement of observational techniques, theoretical models and numerical simulations in recent years helped us to develop a consistent picture of the origin and evolution of the Universe, the so-called *standard model*. It is based on the following observations: the expansion of the Universe first observed by Hubble, the observation of primordial elements from nucleosynthesis formed in the early Universe and the isotropic temperature distribution of the photons of the cosmic microwave background (CMB) radiation. However, there are still many open questions, for example the origin of the accelerated expansion in the recent history of the Universe, the (particle) nature of dark matter and the physical process that led to inflation in the early Universe. The advent of precision cosmology, which allows us to determine cosmological parameters at percentage-level accuracy, will constrain the concordance model even better with upcoming surveys. Maybe, taking advantage of the present rapid theoretical and observational progress, we will then be able to probe the processes that are not (yet) part of the standard model.

This chapter is organized as follows: In Sect. 1.1 we introduce the concept of a homogeneous background Universe and derive the most important relations which describe the kinematical and dynamical properties of this background Universe. We review then the determination of the cosmological density parameters in Sect. 1.2 that quantify the energy budget of the Universe. This is followed by Sect. 1.3, where we

give a concise presentation of the physical phenomena that are part of the cosmological standard model and review the history of the Universe from the Big Bang to the current large-scale structure. Furthermore, we discuss the inflationary phase of the very early Universe which is a necessary extension of the standard model.

1.1 Homogeneous Background Universe

In this section we derive the most important relations of the homogeneous background Universe which are used for the rest of the thesis, namely the Friedmann equations, the cosmological redshift and the distance-redshift relations.

1.1.1 Robertson-Walker Metric

The *Copernican principle*[1] states that the Earth has no special position in the Universe. A generalization of this concept leads to the assumption that there is no favored position in space at all. In addition, observations indicate that the Universe looks isotropic around the Earth. Combining both points, we deduce isotropy around every point in space. One can show mathematically that global isotropy implies homogeneity of space. In summary, this leads to the famous statements

1. the Universe is homogeneous,

2. the Universe is isotropic,

which is the so-called *cosmological principle.* Of course, the homogeneity and isotropy of the Universe does not apply on small scales because we see a large variety of galactic and extragalactic structures. It is rather understood as an averaging process over sufficiently large cells with spatial extent of $> 100\,\mathrm{Mpc}$.

When applying the cosmological principle, Robertson and Walker independently showed that the general metric of space-time $\mathrm{d}s^2 \equiv g_{\mu\nu}\mathrm{d}x^\mu\mathrm{d}x^\nu$ can be reduced due to the underlying symmetry to the simple form of[2]

$$\mathrm{d}s^2 = c^2\mathrm{d}t^2 - a^2(t)\left[\mathrm{d}w^2 + f_K^2(w)\mathrm{d}\Omega^2\right]\,, \qquad (1.1)$$

with

$$\mathrm{d}\Omega^2 = \mathrm{d}\theta^2 + \sin^2\theta\,\mathrm{d}\phi^2\,. \qquad (1.2)$$

These are the coordinates of *fundamental observers* which move on geodesics with the cosmic fluid. The spatial coordinates of these fundamental observers are thus called *comoving coordinates* here denoted by (w, θ, ϕ) and t is the *cosmic time* as measured in

---

[1]This goes back to the work of Nicolaus Copernicus who showed that the Earth is not the center of the solar system but is instead moving around the Sun.

[2]We assume the Einstein summation convention, namely that we sum over identical upper and lower indices. Greek indices run over the four relativistic coordinates, e.g., $\mu = 0\dots 3$.

the rest frame of a comoving clock. We see that the evolution of the Universe is governed by the time-dependent scale factor $a(t)$. The form of the metric shows that space-time can be decomposed into spatial hypersurfaces of constant time and curvature, where isotropy requires these three-dimensional surfaces to be spherically symmetric. The *comoving angular diameter distance* $f_K(w)$ is either a trigonometric, linear or hyperbolic function of w corresponding to the curvature K of the hypersurfaces:

$$
f_K(w) = \begin{cases} K^{-1/2} \sin(K^{1/2}w) & \text{for } K > 0\,, \\ w & \text{for } K = 0\,, \\ (-K)^{-1/2} \sinh[(-K)^{1/2}w] & \text{for } K < 0\,. \end{cases} \tag{1.3}
$$

Note that in this convention of the Robertson-Walker metric the curvature K has the units of length^{-2} and the scale factor is dimensionless.

1.1.2 Cosmological Redshift

Edwin Hubble discovered in 1929 that almost all galaxies are receding from us with a radial velocity that is on average proportional to their distance from us. As a result of the expansion of the Universe, the light of distant sources arriving at the Earth appears redshifted in its wavelength. Let us consider a light ray that is emitted from a comoving source at time t_e ("e" for emitter) and reaches a comoving observer at time t_o ("o" for observer). Since light rays travel on null geodesics we have $ds^2 = 0$. In addition, we assume that we have radial light rays which are characterized by a constant value of θ and ϕ. If we apply these conditions to the metric (1.1) we find

$$
c|\mathrm{d}t| = a(t)\mathrm{d}w\,. \tag{1.4}
$$

The coordinate distance for both comoving observers remains constant by definition:

$$
w_{\mathrm{eo}} = \int_{t_e}^{t_o} \mathrm{d}w = \int_{t_e}^{t_o} \mathrm{d}t\, \frac{c}{a(t)} = \text{const.} \tag{1.5}
$$

This equation can be written equivalently as

$$
\frac{\mathrm{d}t_o}{\mathrm{d}t_e} = \frac{a(t_o)}{a(t_e)}\,. \tag{1.6}
$$

Describing the infinitesimal change in time by $\mathrm{d}t \equiv \nu^{-1}$, where ν is the frequency of the light wave, Eq. (1.6) becomes

$$
\frac{\nu_e}{\nu_o} = \frac{\lambda_o}{\lambda_e} = 1 + \frac{\lambda_o - \lambda_e}{\lambda_e} = 1 + z = \frac{a(t_o)}{a(t_e)}\,, \tag{1.7}
$$

where the introduced redshift factor z describes the relative change in the wavelength λ.

For the rest of this work we deal with the situation where the observer is situated on Earth or in space and the time of the observer is today. The scale factor is normalized to unity today, i.e., $a(t_0) = 1$. Then the relation between the redshift z and the scale factor a is

$$a(z) = \frac{1}{1+z} \,. \tag{1.8}$$

1.1.3 Einstein Field Equations

In the previous sections we applied the cosmological principle to achieve a geometrical description of the Universe. In the following, we want to predict the time dependence of the scale factor and therefore the dynamics of the Universe. The fundamental equations used to describe the dynamics of the Universe are the Einstein field equations. In an enormous intellectual work, Einstein developed an extension of his theory of special relativity which incorporates also gravity. This theory, known as *general relativity*, describes space-time as a four-dimensional manifold with a metric tensor $g_{\mu\nu}$. The Einstein equations couple the metric with the matter-energy content of the Universe that is described by the energy-momentum tensor $T_{\mu\nu}$:

$$G_{\mu\nu} = -\frac{8\pi G_N}{c^4} T_{\mu\nu} \,, \tag{1.9}$$

with the Einstein tensor given by

$$G_{\mu\nu} = R_{\mu\nu} - \frac{1}{2} R g_{\mu\nu} + \Lambda g_{\mu\nu} \,, \tag{1.10}$$

where $R_{\mu\nu}$ is the Ricci tensor and its contraction R is called the Ricci scalar. Both depend on first- and second-order derivatives of the metric. The Einstein tensor and the energy momentum tensor satisfy the Bianchi identity $\nabla^\nu G_{\mu\nu} = 0$ and energy conservation $\nabla^\nu T_{\mu\nu} = 0$, respectively. Here ∇^ν denotes the covariant derivative. Since the metric is constant with respect to covariant derivatives ($\nabla^\alpha g_{\mu\nu} = 0$), the stated conservation laws allow to add a term that is proportional to the metric on either side of the Einstein equation. This was introduced as the Λ-term by Einstein in 1917 on the left-hand side of Eq. (1.9) because he wanted to achieve a static Universe, i.e., a Universe which is not expanding at all. Alternatively, one can also put the Λ-term on the right-hand side of Einstein's equation. Then it acts as a source of energy as Heisenberg already pointed out. In this case theoretical particle physics tells us that the constant term could be the vacuum energy of the Universe. We will come back to this point later in this section. Note that we already included the Λ-term in the Einstein tensor in Eq. (1.10). Taking the weak-field limit of the Einstein equation including the Λ-term leads to a modification of the Poisson equation of Newtonian gravity which is discussed in detail in Sect. 2.1.1.

The energy-momentum tensor of the Universe is assumed to be that of a perfect relativistic fluid

$$T_{\mu\nu} = (\rho + p/c^2) U_\mu U_\nu - p g_{\mu\nu} \,, \tag{1.11}$$

where ρ is the density and p is the pressure of the perfect fluid and U_μ is the relativistic four-velocity. For comoving coordinates the four-velocity takes the particular simple form of $U^\mu = (1, 0, 0, 0)$.

1.1.4 Friedmann Equations

The Einstein equations (1.9) can be solved for a given metric. Choosing the Robertson-Walker metric (1.1), we obtain the two famous Friedmann equations for a homogeneous and isotropic Universe:

$$H^2(t) \equiv \left(\frac{\dot{a}}{a}\right)^2 = \frac{8\pi G_N}{3}\rho - \frac{Kc^2}{a^2} + \frac{\Lambda}{3}\,, \tag{1.12}$$

$$\frac{\ddot{a}}{a} = -\frac{4\pi G_N}{3}\left(\rho + \frac{3p}{c^2}\right) + \frac{\Lambda}{3}\,, \tag{1.13}$$

where we have also introduced the Hubble rate $H(t)$. The value of the Hubble rate today is the so-called *Hubble constant*

$$H_0 = 100\, h\, \mathrm{km\, s^{-1}\, Mpc^{-1}}\,, \tag{1.14}$$

where the Hubble parameter h quantifies the uncertainties in the measurements. The origin of this parameter is founded in the large uncertainties in the measurements of the Hubble constant several years ago. Today the Hubble key project provides a much more accurate determination of the Hubble constant (Freedman et al. 2001), where they find $h = 0.72 \pm 0.08$. We note that we can define a critical point from the first Friedmann equation (1.12): the curvature of the Universe is flat, implying $K = 0$, if the density is equal to the *critical density*

$$\rho_{\mathrm{crit}}(t) = \frac{3H^2(t)}{8\pi G_N}\,, \tag{1.15}$$

where we neglected the Λ-term in the first Friedmann equation. It is possible to combine both Friedmann equations to the *adiabatic equation*

$$\frac{\mathrm{d}}{\mathrm{d}t}(a^3\rho c^2) + p\frac{\mathrm{d}}{\mathrm{d}t}a^3 = 0\,, \tag{1.16}$$

which is analog to the first law of thermodynamics. In other words, the change in energy in a comoving volume element is equal to minus the pressure times the change in volume. Note that it is possible to find this equation, without solving the Einstein equations, from the energy-momentum conservation of general relativity, i.e., $\nabla_\mu T^{\mu\nu} = 0$.

We now derive the time dependence or alternatively the dependence on the scale factor of the density ρ by solving the adiabatic equation (1.16). However, we need a relation between the pressure and the density. This is obtained by an equation of state (EOS) similar to the ideal gas in thermodynamics. We parametrize the EOS by

$p = p(\rho) = c^2 w \rho$, where w is the equation of state parameter. The most general case we consider is a time-dependent w, in which case the solution of the adiabatic equation is

$$\rho(a) = \rho_0 \exp \left\{ -3 \int_1^a \frac{\mathrm{d}a'}{a'} \left[1 + w(a') \right] \right\} , \qquad (1.17)$$

where ρ_0 is the density of the considered matter species today, i.e., $\rho_0 \equiv \rho(a = 1)$. If w is constant then the integration in the exponential can be performed and yields

$$\rho(a) = \rho_0 a^{-3(1+w)} . \qquad (1.18)$$

This implies that to find the parameter w, we must specify the equation of state for certain forms of matter. The matter content in the Universe can be divided into relativistic and non-relativistic matter which are often called radiation and pressureless dust, respectively. For radiation the EOS is derived from special relativity as

$$p_\mathrm{r} = \frac{\rho_\mathrm{r} c^2}{3} , \qquad w_\mathrm{r} = \frac{1}{3} . \qquad (1.19)$$

Non-relativistic matter can be approximated by

$$p_\mathrm{m} = 0 , \qquad w_\mathrm{m} = 0 . \qquad (1.20)$$

Using these relations, we find from Eq. (1.18)

$$\rho_\mathrm{m}(t) = \rho_{\mathrm{m},0} a(t)^{-3} , \qquad \rho_\mathrm{r}(t) = \rho_{\mathrm{r},0} a(t)^{-4} , \qquad (1.21)$$

for matter and radiation density, respectively. These results provide an intuitive interpretation: The first equation describes the dilution of the number density of particles with the expanding Universe. Radiation has an additional reductional factor of a^{-1} due to the energy dependence on redshift.

In 1998, the accelerated expansion of the present Universe was independently detected by two groups observing supernova type Ia (SNIa) (Riess et al. 1998; Perlmutter et al. 1999). This came as a surprise because the physical origin of the accelerated expansion is still unknown and one of the biggest theoretical and observational challenges in modern physics. The mysterious form of energy that is responsible for the acceleration is called *dark energy*. From the second Friedmann equation (1.13) an accelerated expansion ($\ddot{a}(t) > 0$) occurs when the equation of state parameter fulfills $w_\mathrm{de} < -1/3$. In particular, a constant energy density can be achieved when $w_\mathrm{de} = -1$ (see Eq. 1.18). This is the simplest dark energy model and is called *cosmological constant*. When the EOS parameter is time dependent, one needs to use the general equation (1.17) and we speak of *quintessence models* of dark energy.

Introducing the density parameters $\Omega_i \equiv \rho_{i,0}/\rho_{\mathrm{crit},0}$ for the i-th species and replacing $\rho \rightarrow \rho_\mathrm{r} + \rho_\mathrm{m} = \rho_{\mathrm{m},0} a^{-3} + \rho_{\mathrm{r},0} a^{-4}$, we can rewrite the first Friedmann equation (1.12) as

$$H^2(a) = H_0^2 \left[a^{-4} \Omega_\mathrm{r} + a^{-3} \Omega_\mathrm{m} - a^{-2} \frac{K c^2}{H_0^2} + \Omega_\Lambda \right] , \qquad (1.22)$$

where the density parameter for the cosmological constant is defined by

$$\Omega_\Lambda \equiv \frac{\Lambda}{3H_0^2} \,. \tag{1.23}$$

Setting $t = t_0$ in Eq. (1.22) the parameters today are related by

$$K = \left(\frac{H_0}{c}\right)^2 (\Omega_\mathrm{m} + \Omega_\mathrm{r} + \Omega_\Lambda - 1) \equiv \left(\frac{H_0}{c}\right)^2 (\Omega_\mathrm{tot} - 1) \,, \tag{1.24}$$

where we defined Ω_tot in the second step, which is the total density parameter today. This equation tells us that the total energy density and the geometry of the Universe are closely related: for $\Omega_\mathrm{tot} = 1$ we obtain a flat Universe ($K = 0$), $\Omega_\mathrm{tot} < 1$ corresponds to an open Universe ($K < 0$) and $\Omega_\mathrm{tot} > 1$ characterizes a closed Universe ($K > 0$).

Replacing the curvature in Eq. (1.22) with this relation, the first Friedmann equation finally reads for the matter-dominated era, i.e., for $\Omega_\mathrm{r} \ll 1$:

$$H^2(a) = H_0^2 \left[a^{-3}\Omega_\mathrm{m} + a^{-2}(1 - \Omega_\mathrm{m} - \Omega_\Lambda) + \Omega_\Lambda \right] \,. \tag{1.25}$$

Scale-factor dependent density parameters $\Omega_i(a)$ can also be defined. Their evolution can be written explicitly by using Eq. (1.25):

$$\Omega_\mathrm{m}(a) \equiv \frac{\rho_\mathrm{m}(a)}{\rho_\mathrm{crit}(a)} = \frac{8\pi G_N}{3H^2(a)}\rho_{\mathrm{m},0}a^{-3} = \frac{\Omega_\mathrm{m}}{a + \Omega_\mathrm{m}(1 - a) + \Omega_\Lambda(a^3 - a)} \,, \tag{1.26}$$

$$\Omega_\Lambda(a) = \frac{\Lambda}{3H^2(a)} = \frac{\Omega_\Lambda a^3}{a + \Omega_\mathrm{m}(1 - a) + \Omega_\Lambda(a^3 - a)} \,, \tag{1.27}$$

where we also neglected the contribution from Ω_r. These equations have the asymptotic behavior $\Omega_\mathrm{m}(a) \to 1$ and $\Omega_\Lambda(a) \to 0$ as $a \to 0$ independent of the values of Ω_m and Ω_Λ today.

1.1.5 Cosmological Distance Measures

Here we introduce the main distance measures used in cosmology and derive their distance-redshift relations.

The comoving distance D_com is the distance between two observers comoving with the cosmic flow, thus $D_\mathrm{com} \equiv w$. We found in Sect. 1.1.2 that radial light rays fulfill $c\,\mathrm{d}t = -a\,\mathrm{d}w$. We rewrite this relation in terms of the scale factor

$$\mathrm{d}w = -\frac{c}{a}\mathrm{d}t = -\frac{c}{a}\left(\frac{\mathrm{d}a}{\mathrm{d}t}\right)^{-1}\mathrm{d}a = -\frac{c}{a^2 H(a)}\mathrm{d}a \,, \tag{1.28}$$

where we used the definition of the Hubble rate in Eq. (1.12) in the last step. Thus, the comoving distance for an observer at $a = 1$ to a source located at the scale factor a is

$$w(a) = \frac{c}{H_0} \int_a^1 \mathrm{d}a' \, [a'\Omega_\mathrm{m} + a'^2(1 - \Omega_\mathrm{m} - \Omega_\Lambda) + a'^4\Omega_\Lambda]^{-1/2} \,. \tag{1.29}$$

Since in cosmology one often uses the redshift dependence instead, we rewrite the comoving distance as

$$w(z) = \frac{c}{H_0} \int_0^z dz' \left[(1+z')^3 \Omega_{\mathrm{m}} + (1+z')^2 (1 - \Omega_{\mathrm{m}} - \Omega_{\Lambda}) + \Omega_{\Lambda}\right]^{-1/2}. \tag{1.30}$$

The pre-factor is the so-called *Hubble distance* and has a value of $c/H_0 = 2998\, h^{-1}\, \mathrm{Mpc}$. However, the comoving distance is not directly accessible to observations. Instead, observations measure the angular extent or the luminosity of an object which lead to the definition of the *angular diameter distance* and *luminosity distance*, respectively. Both quantities depend on the comoving distance. Thus, the comoving distance is the most basic distance quantity.

In Euclidean space, the angular extent $\Delta\theta$ of a source of size l that is located at distance D from the observer is given by

$$\Delta\theta = \frac{l}{D}, \tag{1.31}$$

where we used the small-angle approximation. We can use this relation to define the *angular diameter distance*

$$D_{\mathrm{A}} = \frac{l}{\Delta\theta} \tag{1.32}$$

for an arbitrary metric. Suppose the observer is located at a redshift z_1, and the source is lying at a redshift z_2 with $z_1 < z_2$. From the angular part of the Robertson-Walker metric (see Eq. 1.1) we find then $l = a(z_2) f_K[w(z_1, z_2)]\Delta\theta$. Therefore, the angular diameter distance is given by

$$D_{\mathrm{A}}(z_1, z_2) = a(z_2) f_K[w(z_1, z_2)]. \tag{1.33}$$

The luminosity distance is especially important for the evidence of dark energy from supernova observations. If we have a source with absolute luminosity L_{e} at a distance D then an observer at $t = t_0$ receives a flux $\mathcal{F}$ given by

$$\mathcal{F} = \frac{L_{\mathrm{e}}}{4\pi D^2} \tag{1.34}$$

in Euclidean space. Therefore, we define the luminosity distance as

$$D_{\mathrm{L}} = \left(\frac{L_{\mathrm{e}}}{4\pi\mathcal{F}}\right)^{1/2}. \tag{1.35}$$

Now we want to calculate the flux for a Robertson-Walker metric. We find that the area of the sphere of the emitted light which reaches the observer at $t = t_0$ is given by $A = 4\pi a^2(t_0)[f_K(w)]^2$. Hence, the observed flux is given by

$$\mathcal{F} = \frac{L_0}{4\pi[a_0 f_K(w)]^2} \tag{1.36}$$

Due to the redshift of photons, the connection between emitted and received luminosity is

$$L_{\mathrm{e}} = (1 + z)^2 L_0 \,. \tag{1.37}$$

Finally, combining Eqs. (1.35), (1.36) and (1.37) the expression for the luminosity distance is (setting $a_0 = 1$)

$$D_{\mathrm{L}}(z) = \frac{1}{a(z)} f_K[w(z)] \,. \tag{1.38}$$

These different distance measures lead in general to different results because the concept of distance is ambiguous in curved space-time in contrast to Euclidean or Minkowski space. For small redshifts ($z \ll 1$) all distance measures can be described by the local Hubble law

$$d(z) = \frac{v}{H_0} = \frac{c}{H_0} z \tag{1.39}$$

because the curvature of the Universe is negligible in this case. The relation between the redshift and the velocity v is due to the linear non-relativistic Doppler effect. The linear behavior between distance and receding velocity was first discovered by Edwin Hubble in 1929 after a long period of measurements of nearby cepheids. It was one of the first hints that the Universe is expanding.

1.2 Energy Composition of the Universe

We review the status of the determination of today's energy composition of the Universe quantified by the dimensionless density parameters. Ideally, we have many different and/or complementary measurement methods to reduce systematic effects and break parameter degeneracies. This is indeed the case for most parameters and the agreement between different methods strengthens our evidence that we live in a flat Universe dominated by non-baryonic dark matter and dark energy. Finally, we discuss different time evolutions of the expansion of the Universe, so-called world models. With the measurements of today's cosmological parameters we can infer that the Universe started from a Big Bang singularity. In some parts we follow the discussion in Dodelson (2003).

1.2.1 Radiation Density

The term radiation density refers to the energy density of relativistic particles. Today, the temperature of the Universe dropped significantly compared to the hot plasma after the Big Bang. Hence, the relativistic density today is dominated by massless particles where the most abundant are CMB photons and relic neutrinos. Therefore we define

$$\Omega_{\mathrm{r}} = \Omega_{\gamma} + \Omega_{\nu} \,. \tag{1.40}$$

In the following we determine the amount of both components today.

Photons

The CMB radiation measured by the COBE[3] satellite mission has a perfect Planck spectrum with a temperature $T_\gamma = 2.725 \pm 0.002\,\mathrm{K}$ (Mather et al. 1999). We can then infer the energy density of photons:

$$\rho_\gamma = 2 \int \frac{\mathrm{d}^3 p}{(2\pi)^3} \frac{p}{\exp(p/T_\gamma) - 1} = \frac{\pi^2}{15} T_\gamma^4 \,, \tag{1.41}$$

where we used the fact that photons have two degrees of freedom corresponding to the two polarization states and that the rest mass of the photons is zero, i.e., $E = \sqrt{m^2 + p^2} = p$. Note that we used natural units in Eq. (1.41) where $\hbar = c = k_B = 1$. Inserting the observed CMB temperature, we can deduce the value of the photon density parameter:

$$\Omega_\gamma = \frac{\rho_\gamma}{\rho_{\mathrm{crit}}} = 2.47 \times 10^{-5}\, h^{-2} \,. \tag{1.42}$$

Note that in addition to the isotropic CMB temperature, the COBE satellite found tiny fluctuations in the angular distribution of the CMB temperature of the order $\Delta T/T \propto 10^{-5}$. We will discuss this observation in Sect. 1.3.3 where we talk about the origin of the CMB radiation.

Neutrinos

In contrast to the CMB radiation, the relic neutrino radiation has not been directly observed because of the small interaction cross sections of these low energy neutrinos. However, using relatively simple theoretical arguments, we can derive the temperature of the neutrinos from the temperature of the CMB photons.

   In the early Universe neutrinos were kept in equilibrium with electrons by weak interactions. Hence, they are part of a thermal bath where the particles share the same temperature. At an energy slightly above $1\,\mathrm{MeV}$ the neutrino interaction rates become so small that they decouple from the thermal bath. Shortly thereafter, at the energy of $E = 2m_e \simeq 1\,\mathrm{MeV}$, the pair production of electrons and positrons $\gamma\gamma \to e^+ e^-$ stops and because neutrinos are absent from the thermal bath the annihilation energy of the electron-positron pairs is only transferred to the photons. As a consequence, photons are hotter than the neutrinos. Using the conservation of the entropy density we find

$$\frac{T_\nu}{T_\gamma} = \left(\frac{4}{11}\right)^{1/3} \,, \tag{1.43}$$

where T_ν and T_γ denote the neutrino and photon temperature, respectively. Plugging this result into Eq. (1.41) leads to

$$\rho_\nu = 3\frac{7}{8} \left(\frac{4}{11}\right)^{4/3} \rho_\gamma \,, \tag{1.44}$$

---

[3]Cosmic Background Explorer.

where the factor 7/8 is due to the fact that neutrinos obey Fermi-Dirac statistics in contrast to the photons which obey Bose-Einstein statistics. In addition, considering that there are 3 generations of neutrinos and anti-neutrinos, they have 6 degrees of freedom[4] compared to the 2 degrees of freedom of photons. This results in the factor of 3 for the density of neutrinos. Finally, we find for the density parameter of neutrinos

$$\Omega_\nu = 1.68 \times 10^{-5} \, h^{-2} \, . \tag{1.45}$$

Combining the results from photons (1.42) and neutrinos (1.45), we get $\Omega_{\mathrm{r}} = 4.15 \times 10^{-5} \, h^{-2}$.

We have to keep in mind that the derivation of this result is only valid for massless neutrinos. Recently, however, there is strong evidence for massive neutrinos from atmospheric (Fukuda et al. 1998) and solar neutrino oscillation experiments (Ahmad et al. 2001). The result of the experiments is that at least one of the neutrinos has a rest mass above $m_\nu = 0.05 \, \mathrm{eV}$. The effect of massive neutrinos is that at high temperatures they behave relativistically, whereas at low temperatures there is a turnover in the density evolution, where neutrinos act as non-relativistic matter with a scaling $\rho_\nu \propto a^{-3}$. This behavior makes massive neutrinos a natural candidate for non-baryonic dark matter (see also next section below). However, intensive studies on structure formation using numerical simulations show that relativistic neutrinos (so-called *hot dark matter*) cannot reproduce the statistical properties of the large-scale structure we observe today. Neutrinos would "wash out" perturbations of the background cosmology and significantly reduce the formation of bound objects like galaxies and galaxy clusters. Hence, at least partly, dark matter must be composed of an unknown type of matter which is able to reproduce the statistical properties of the observed large-scale structure.

1.2.2 Matter Density

The matter density is composed of non-relativistic particles. Today, this includes ordinary baryonic matter and non-baryonic dark matter (plus a small contribution from massive neutrinos), and thus the density parameter is $\Omega_{\mathrm{m}} = \Omega_{\mathrm{b}} + \Omega_{\mathrm{dm}}$.

Baryon Density

There are many established ways to infer the baryon density of the Universe. The simplest method is to determine the amount of gas in groups and clusters of galaxies. Note that the contribution from the intergalactic medium is larger than the contribution from individual stars. Another method are measurements of spectra of distant quasars, where the amount of absorbed gas is a measure of the intervening hydrogen, and thus an estimate of the baryon density. However, the two most precise predictions come from measurements of the CMB temperature fluctuations and of the abundance of primordial elements. Changing the baryon density of the Universe leaves characteristic

---

[4]Each neutrino has one spin degree of freedom ($g_\nu = 1$).

imprints in the temperature fluctuations of the CMB radiation making it one of the easiest parameters to extract.

The amount of primordial deuterium predicted from nucleosynthesis is very sensitive to the assumed baryon-to-photon ratio. Thus, measurements of primordial deuterium can be compared to model predictions to infer the photon-to-baryon ratio. Since we know the photon density very well from the CMB radiation, we obtain an estimate for the baryon density. We can measure the deuterium abundance by determining the absorption of light from distant QSOs by intervening neutral hydrogen systems (Burles & Tytler 1998). The main absorption feature is the Lyα-transition, which is slightly different for hydrogen and deuterium due to the different masses of the nuclei. Hence, in the absorption spectrum, deuterium leaves a clear feature which is shifted relative to the hydrogen spectrum and is less damped because of the small amount of deuterium.

Remarkably, the result from the presented methods agree and yield $\Omega_{\rm b}h^2 \approx 0.02$. For a fiducial value of $h = 0.7$, we obtain $\Omega_{\rm b} \approx 0.04$.

Dark Matter Density

The presented methods to obtain the baryon density all involve the interactions between matter and radiation. In contrast, measurements that are sensitive to the gravitational field of bound systems only depend on the total mass of the system. Surprisingly, there is very strong evidence that both mass estimates disagree leading to the proposal of an unknown form of matter that does not interact with electromagnetic radiation. In the following we present different probes that measure the total mass.

One of the first probes to infer an estimate was the measurement of the mass-to-light ratio of bound systems (e.g., Tinker et al. 2005). For small to intermediate size systems, the mass-to-light ratio is an increasing function of the length scale. However, on the largest scales corresponding to galaxy clusters and superclusters the mass-to-light ratio approaches a constant value. Hence, if we assume that the matter content in superclusters is representative of the matter content of the Universe, we can infer the total mass density $\Omega_{\rm m}$.

More recent methods involve observations of the distribution of galaxies which depends on the matter density of the Universe (Cole et al. 2005). A very similar method is the determination of the peculiar velocity field which can be simply related to the density field by using the continuity equation (Hawkins et al. 2003). Finally, the distribution of the temperature fluctuations of the CMB radiation is sensitive to the combination $\Omega_{\rm m}h^2$.

Another approach is to use methods that depend on the ratio $\Omega_{\rm b}/\Omega_{\rm m}$. Then using the result of the baryon density of the previous section, we can deduce the total matter density. An example are galaxy clusters, where most of the baryonic mass is situated in the intercluster medium in the form of hot gas. Measurements of the X-ray emission of the hot gas or the scattering of CMB photons of the electrons in the plasma (Sunyaev-Zel'dovich effect) are sensitive to the amount of gas relative to the total mass (LaRoque et al. 2006). Clusters collapse from a large volume of the order of 1000 Mpc

and thus their composition should reflect the baryon-dark matter ratio of the Universe. Furthermore, baryonic acoustic oscillations in the baryon-photon plasma in the early Universe leave characteristic imprints in the galaxy distribution that can be used to infer the density ratio (Eisenstein et al. 2005).

This is only an excerpt of the various number of cosmological probes. Most notably, we left out the discussion of the cosmic shear power spectrum which is introduced in Sect. 5.2. All different probes obtain $\Omega_{\mathrm{m}} \simeq 0.3$ for the total matter density of the Universe. Hence, this result requires in addition to the baryonic matter another form of matter that interacts only gravitationally, dubbed as *dark matter*. Furthermore, compared to the result of the baryon density in the previous section, this unknown form of matter clearly dominates the total matter density.

1.2.3 Dark Energy

The recent Universe undergoes a phase of accelerated expansion rather than a slowdown which can be explained by a recent domination of a new energy component, termed dark energy. We show the evidence for dark energy and give results to its contribution to the energy budget of the Universe.

Measurements of the CMB temperature fluctuations determine at high accuracy that the density of the Universe is very close to critical implying that the Universe is flat. However, the total matter density only contributes roughly a third to the critical density and the amount of the radiation density is negligible today. Hence, to achieve the observed flatness, where $\Omega_{\mathrm{tot}} = 1$ (see Eq. 1.24), we need to propose another dominating energy form that fulfills $\Omega_{\Lambda} = 1 - \Omega_{\mathrm{m}}$.

The other evidence comes from cosmological probes that are sensitive to distance-redshift relations (see Eqs. 1.33 and 1.38) and/or the Hubble rate $H(z)$ (see Eq. 1.25) because they directly depend on the amount of Ω_{Λ}. An example is the observation of SNIa as standard candles to obtain the distance-redshift relation of the luminosity distance. In particular, the results suggest that the luminosity distance is best fitted by a theoretical model with a dominant contribution from a cosmological constant. In contrast an *Einstein-de Sitter* model[5], where $\Omega_{\mathrm{m}} = 1$ and $\Omega_{\Lambda} = 0$, is strongly disfavored by the data. Especially the large amount of dark energy came as a big surprise to most cosmologists. However, there were also still doubts about the evidence because of the partly unknown amount of systematics in the measurements, for example in the understanding of supernova explosions. From then on, we have collected ever growing evidence on dark energy as a result of the availability of larger data sets and improvements in the modeling of systematics. In addition, complementary probes like gravitational lensing caused by the large-scale structure (cosmic shear), the CMB temperature fluctuations, observations of galaxy clustering, baryonic acoustic oscillations, cluster mass function, etc., also need dark energy. Hence, the new evidence put the recent dark energy domination on a firm foundation, and the different probes find $\Omega_{\Lambda} \approx 0.7$.

---

[5]For a long time this was the standard cosmological model of the Universe.

On the theoretical side there are fundamental problems to find a model that predicts the observed amount of dark energy. The first idea is to assume that dark energy corresponds to the energy of the vacuum of the Universe. However, standard quantum field theory predictions are about 10^{121} orders of magnitude larger than the observed value. This is known as the famous cosmological constant problem. These difficulties lead to the proposal of a time-varying dark energy component, which is described by so-called quintessence models. Nevertheless, the problems to produce a theory that solves the cosmological constant problem and is falsifiable remains and a lot of effort is put in new theoretical models and in observations that obtain improved constraints on the amount and the EOS of dark energy. In particular, the main goal is to determine the EOS of dark energy at percentage-level accuracy to be able to distinguish between cosmological constant and dynamical (time-varying) dark energy models.

Basically there are three types of theoretical models to explain dark energy. The first idea is to change the right-hand side of the Einstein equation (1.9), which is equivalent to changing the energy density of the Universe. On the other hand, we can also change the left-hand side side of the Einstein equation which corresponds to a modification of gravity. Both solutions have their own difficulties. For example a modification of gravity still needs to converge to Einstein's theory on small scales because it is very well tested on solar system scales. The third approach to explain dark energy are the so-called *backreaction* models, where inhomogeneities in the large-scale structure lead to a breakdown of the cosmological principle. In this scenario we have to modify the Friedmann equation and need to introduce averaging schemes over the inhomogeneities of the large-scale structure. For comprehensive reviews of the work on theoretical models and future experiments we refer to the report of the dark energy task force (Albrecht et al. 2006) and the reviews by Copeland (2007) and Frieman et al. (2008).

1.2.4 Cosmological World Models

With the knowledge of the energy composition, we can now constrain the past and future global evolution of the Universe and provide evidence for the presence of a Big Bang. This problem involves solving the first Friedmann equation (1.25) for the scale factor a as a function of cosmic time t. In general this can be done only numerically. Today we can neglect the radiation density parameter due to its smallness ($\Omega_r \simeq 10^{-5}$). Qualitatively, we have then an interplay between the attractive gravitational force acting on matter and the repulsive or attracting[6] force of the cosmological constant. There are three types of world models:

- an eternally expanding Universe,

- a Universe that will recollapse in the future, i.e., the expansion of the Universe stops and turns into a contraction,

---

[6]We are also considering negative values for Ω_Λ, in which case dark energy is an attractive force.
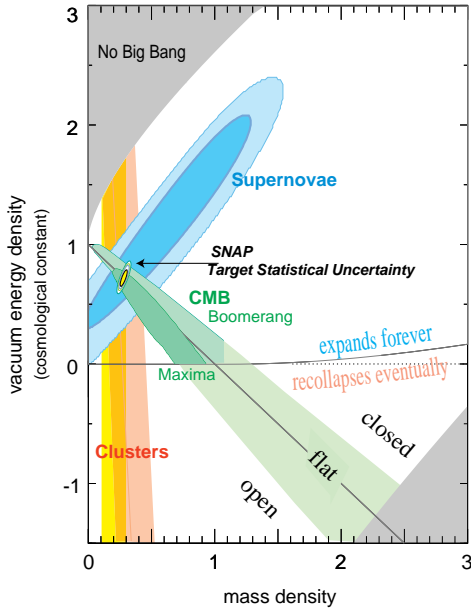
Figure 1.1: Ω_{m}-Ω_{Λ}-plane with confidence regions for three cosmological probes: SNIa, CMB temperature fluctuations and galaxy clustering. Each individual probe show large degeneracies between the two parameters and is thus not capable to give tight constraints on the cosmological model. However, the combination of all three observations clearly favors a flat ΛCDM model with a dominant contribution from a cosmological constant. In addition, the diagram is separated into regions corresponding to different geometries of the Universe. Taken from Aldering et al. (2002).

- a bouncing Universe, i.e., a Universe that started without a Big Bang singularity at the scale factor a then contracted due to matter domination and turned over to expansion at $a < 1$. A subclass of this model is the *loitering* Universe which is the critical case between bouncing and eternally expanding Universe. It lingers for a long time at a constant redshift z_{max} when the influence of the Λ-term takes over and yields an expanding Universe.

To illustrate the dependence of these different world models on cosmological parameters, we show in Fig. 1.1 the Ω_{m}-Ω_{Λ}-plane. One can read off the following results:

- A negative Λ always implies recollapse, which is clear because Λ supports in this case the gravitational attraction of matter.

- For $\Omega_{\Lambda} > 0$ and $\Omega_{\mathrm{m}} < 1$ the Universe always expands to infinity.

- For $\Omega_{\mathrm{m}} \gg \Omega_{\Lambda}$ the recollapse is still possible with a positive $\Omega_{\Lambda} < 1$,

- For $\Omega_{\Lambda} > 1$ it is possible to find a bouncing Universe depending on the matter content of the Universe.

Bouncing models can be ruled out by observations of high-redshift objects. Depending on the matter content Ω_m, one can calculate a maximal redshift that is obtained in this model. For example, a conservative lower limit of $\Omega_\mathrm{m} \geq 0.1$ rules out a bouncing Universe once objects are seen at redshifts beyond $z = 2$. This is indeed the case as observations of high-redshift quasars beyond $z > 6$ show. Hence, we conclude that the Universe started from a Big Bang singularity. In addition, the combination of results from SNIa, galaxy clusters and CMB experiments in Fig. 1.1 show that we are living in a flat, dark energy dominated Universe. Hence, the scenario that the Universe recollapses in the future with a *Big Crunch* is strongly ruled out by the data.

1.3 The Cosmological Standard Model and Extensions

The cosmological standard model is based on three important observations: the expansion of the Universe discovered by Hubble, primordial nucleosynthesis and the cosmic microwave background radiation. After reviewing the important epochs in the history of the Universe, we present the predictions of primordial nucleosynthesis and of the CMB radiation released at recombination. We conclude this section with an important extension of the standard model: the inflationary phase of the very early Universe.

1.3.1 History of the Universe

The history of the Universe begins at the Big Bang singularity. Very shortly thereafter it undergoes an accelerated expansion due to inflation. In addition, inflation amplifies the quantum fluctuations to build the seeds of structure formation. The early Universe is composed of a hot and dense plasma, where particles are maintained in thermal equilibrium by the rapid rate of particle interactions. On the other hand, the expansion of the Universe results in a subsequent cooling which leads to a reduction in the particle interaction rates. As a consequence, particles for which the Hubble expansion is larger than their corresponding interaction rate are not able to maintain equilibrium anymore and freeze out. The next important epoch is the process of nucleosynthesis, where the temperature is low enough that neutrons and protons can form deuterium which leads in the end to the formation of helium nuclei. Going back to the solution of the energy density for matter and radiation in Eq. (1.21), we note that there is a time in the past where both components are of the same size which is known as *matter-radiation equality*. Combining the result of Sect. 1.2.1 with the definition of the matter density, we find

$$a_\mathrm{eq} = 4.15 \times 10^{-5} \, \Omega_\mathrm{m}^{-1} h^{-2} \, . \tag{1.46}$$

Hence, the larger the mass density the earlier the time of matter-radiation equality. At around $300\,000$ years ($z \simeq 1100$) after the Big Bang the Universe cooled enough to allow electrons and protons to combine to build neutral hydrogen[7]. This epoch is called

---

[7]The recombination of helium atoms occurs at higher redshifts.
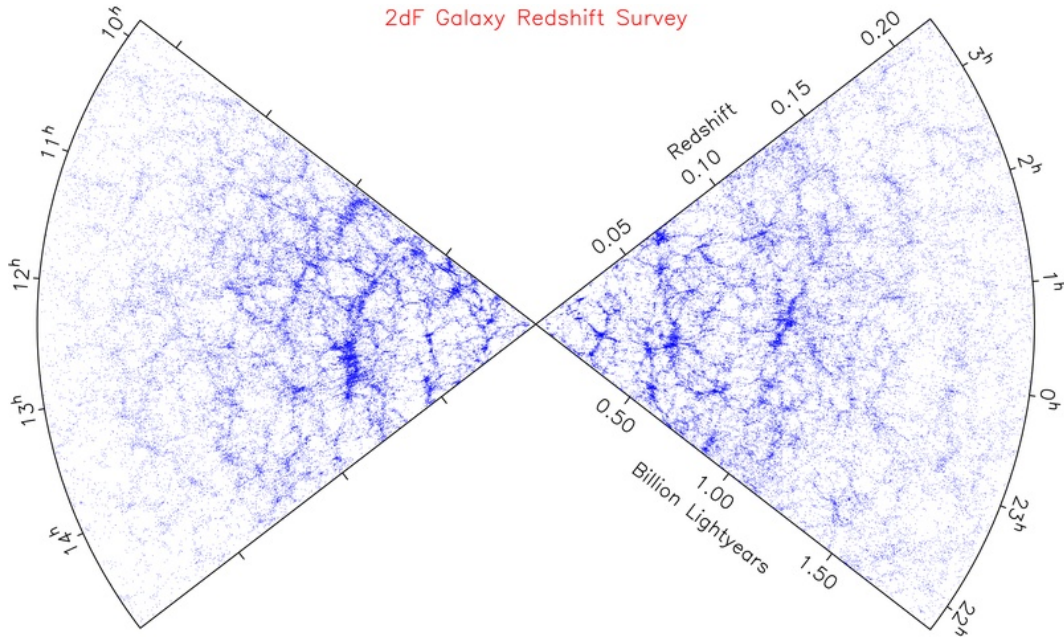
Figure 1.2: Distribution of galaxies observed in the Two Degree Field Galaxy Redshift Survey (2dF) (Colless et al. 2001). As can be seen in the figure, the survey probes in this data release the galaxy distribution up to redshifts of $z \approx 0.2$.

recombination and is the origin of the CMB radiation as the photons can now travel freely through the Universe. From then on until the formation of the first objects we are unable to probe the structure of the Universe and this epoch is therefore called the *dark ages*. The only indirect observable is the light emitted from the 21 centimeter transition of neutral hydrogen[8]. During the dark ages the hierarchical growth of structure due to selfgravity leads to the first giant metal-poor stars, the so-called population III stars, or AGNs. Subsequent explosions of these first giant stars lead then to an ionization of the surrounding gas. These ionized regions begin then to grow and overlap. The metal enrichment of the explosions of population III stars lead to the possibility that population II stars can be formed which also contribute to the ionization of the Universe. Observations of distant quasars and of the CMB radiation show the reionization takes place around $z \simeq 6$–15 in the history of the Universe (see the review Barkana & Loeb 2007). Ongoing structure formation results in the large-scale structure we observe today composed of galaxies, clusters, voids, filaments etc. (see results of the galaxy distribution of the 2dF in Fig. 1.2). Only very recently the Universe changed from a slowdown due to the matter domination to an acceleration of the expansion due to dark energy domination.

---

[8]The 21 centimeter line comes from the transition of the two hyperfine lines in the 1s ground state.

1.3.2 Primordial Nucleosynthesis

The theory of Big Bang nucleosynthesis (BBN) mainly predicts the fraction of helium nuclei produced in the early Universe through the following reaction chain

$$p + n \rightarrow D + \gamma \,, \qquad D + D \rightarrow n + {}^3\text{He} \,, \qquad {}^3\text{He} + D \rightarrow p + {}^4\text{He} \,. \qquad (1.47)$$
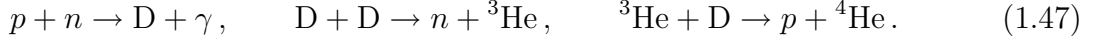
However, the number density of baryons is much smaller than the number density of photons and thus any time a nucleus is formed in a reaction it is destroyed by a high-energy photon. The formed nuclei can only remain stable when the temperature of the Universe drops below a critical temperature. The first reaction of the chain (1.47) indicates that the neutron-to-proton ratio is a key quantity for the formation of helium.

The following weak interactions keep neutrons and protons in equilibrium until $T \approx 1\,\text{MeV}$:

$$p + \bar{\nu} \leftrightarrow n + e^+ \,, \qquad p + e^- \leftrightarrow n + \nu \,, \qquad n \rightarrow p + e^- + \bar{\nu} \,. \qquad (1.48)$$
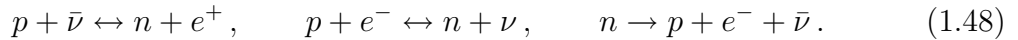
In equilibrium the neutron-to-proton ratio in the nonrelativistic limit is given by

$$\frac{n_n^{(0)}}{n_p^{(0)}} = \mathrm{e}^{-Q/(k_B T)} \,, \qquad (1.49)$$

where $Q = (m_n - m_p)c^2 = 1.293\,\text{MeV}$ is the energy of the mass difference between neutrons and protons. Hence, at high temperatures the number density of neutrons is equal to the number density of protons. On the other hand, as the temperature drops below $1\,\text{MeV}$, the neutron fraction gets reduced. Considering only the equilibrium case, where weak interactions are completely efficient, the neutron fraction would drop to zero. However, at temperatures below $1\,\text{MeV}$ we have to consider out-of-equilibrium processes which involves solving the Boltzmann equation for the reactions in Eq. (1.48) to obtain the neutron-to-proton ratio (see Dodelson 2003). The (integrated) Boltzmann equation describes the fact that the rate of change in the abundance of a given particle is equal to the difference between the production and elimination rates of that particle. At temperatures below $0.1\,\text{MeV}$ the decay of neutrons ($n \rightarrow p + e^- + \bar{\nu}$) and the production of deuterium ($n + p \rightarrow D + \gamma$) become important resulting in a strong reduction of neutrons. To quantify this reduction, we define the ratio

$$X_n \equiv \frac{n_n}{n_n + n_p} \,. \qquad (1.50)$$

Numerical solutions of the Boltzmann equation show that at a temperature around $T_{\text{nuc}} = 0.07\,\text{MeV}$ the formation of deuterium and very shortly thereafter of helium begins, and the fraction is reduced to $X_n(T_{\text{nuc}}) = 0.11$. All neutrons present combine to the stable nucleus of ${}^4\text{He}$ which has the highest binding energy of light nuclei. Since each helium nuclei is composed of two neutrons, we have $n_{{}^4\text{He}} = n_n/2$. The ratio of ${}^4\text{He}$ to the total baryon density is given by (Cyburt et al. 2005)

$$Y = \frac{4n_{{}^4\text{He}}}{4n_{{}^4\text{He}} + n_{\text{H}}} = \frac{2n_n}{n_n + n_p} = 2X_n = 0.22 \,. \qquad (1.51)$$

where $n_H = n_p - n_n$ is the number density of protons after the formation of helium because helium is composed of the same number of neutrons and protons. Thus, the central prediction of BBN is that about 1/4 of the elements in the Universe should be in the form of helium. This is in excellent agreement with observational results of unprocessed systems usually identified by low metallicities.

However, not all of the deuterium combines to form helium nuclei. A tiny fraction of 10^{-5}–10^{-4} is still left at the end of the helium production. The resulting primordial deuterium abundance is very sensitive to the baryon fraction of the Universe. This is due to the fact that the reactions become rarer if we reduce the baryon density in the early Universe. Hence, the depletion of deuterium is reduced which results in an enhancement of the deuterium abundance.

As there are no stable nuclei with mass number 5 or 8, nucleosynthesis basically stops at ^{4}He, with the exception of a tiny amount of ^{7}Li. In stars heavier elements are produced by triple alpha processes, where ^{4}He $+ ^4$He $+ ^4$He $\rightarrow ^{12}$C. But for collisions between three nuclei the baryon density in the early Universe is far too low.

1.3.3 Origin of the CMB Radiation

The combination of free electrons with nuclei produced during BBN leads to the formation of neutral atoms. Naively, we would expect that if the temperature drops slightly below the binding energy of neutral hydrogen, the Rydberg energy of $E_{\text{Ryd}} = 13.6\,\text{eV}$, the formation takes place. However, as was the case for the formation of nuclei, the abundance of high-energy photons directly ionizes each neutral atom and thus the temperature needs to be significantly below the Rydberg energy.

The onset of recombination can be estimated from considering that the reaction

$$e^- + p \leftrightarrow H + \gamma \tag{1.52}$$

remains in equilibrium. We define the ionization fraction as

$$X_e \equiv \frac{n_e}{n_e + n_H} = \frac{n_p}{n_p + n_H}, \tag{1.53}$$

where n_H is the number density of neutral hydrogen and in the second step we assumed that the Universe is charge neutral resulting in $n_e = n_p$. If no neutral hydrogen is produced the ratio goes to $X_e = 1$. From the equilibrium condition we can derive Saha's equation (e.g., Dodelson 2003):

$$\frac{X_e^2}{1 - X_e} \approx \frac{1}{\eta_b n_\gamma} \left[\left(\frac{m_e T}{2\pi} \right)^{3/2} e^{-E_{\text{Ryd}}/T} \right], \tag{1.54}$$

where $\eta_b \equiv n_b/n_\gamma$ is the photon-to-baryon ratio. Numerical solutions of Saha's equation for X_e show that at $T \approx 1/4\,\text{eV}$ or at redshift $z \approx 1000$ the number density of free electrons begins to drop which marks the beginning of recombination. This reduction of

free electrons hampers the maintenance of equilibrium and thus results in a breakdown of Saha's equation. Then, at lower redshifts, we need to consider out-of-equilibrium processes and solve the Boltzmann equation. Note that recombination to the ground state leads to the emission of a photon that immediately ionizes another neutral atom. Hence, this process does not provide a net result of neutral atoms. Instead, recombination takes place through the extremely rare 2γ-transition. In this case, the energy of each of the two emitted photons is too low to ionize another atom.

Another time that is closely related to recombination is the *decoupling* or *last scattering* of photons from matter (electrons). We can roughly estimate the redshift of decoupling as the time when the Compton scattering rate becomes smaller than the expansion of the Universe. Clearly, this depends crucially on the ionization ratio X_e, i.e., the number density of free electrons. The result is that photons decouple from matter when X_e drops below 10^{-2}. From the Boltzmann equation of recombination we know that the ratio drops quickly from unity to 10^{-3} and thus decoupling takes place during recombination. The photons released at recombination can travel freely from $z \approx 1000$ to us without interactions. Hence, the photons of this early phase of the Universe should be still observable today. This cosmic background radiation was already predicted in 1948 by Alpher and Hermann as a direct consequence of the hot, dense Universe and was 16 years later serendipitously detected (Penzias & Wilson 1965).

Theoretical models predict that the CMB radiation before decoupling follows a Planck spectrum. One can show that the expansion of the Universe results in CMB photons with a reduced temperature that are still described by a Planck function with the corresponding temperature. The COBE mission showed for the first time that the CMB temperature indeed is almost perfectly fitted by the predicted Planck function. This remarkable result led to the general acceptance of the hot Big Bang scenario. Furthermore, the COBE satellite measured the first full-sky map of the CMB temperature distribution and showed that the temperature of the CMB radiation is isotropic to a high precision. However, by removing the radiation from the galactic plane, COBE found in 1992 small deviations from isotropy in the temperature distribution. In particular, they measured small temperature fluctuations at a level of $\Delta T/T \approx 10^{-5}$. These temperature fluctuations provide a snapshot of the fluctuations in the baryon-photon plasma at recombination. The evolution of these fluctuations results in the end in the large-scale structure we observe today. Both discoveries, the blackbody radiation and the anisotropy of the CMB, led in 2006 to the Nobel prize jointly awarded to John C. Mather and George F. Smoot as they provided an important step for cosmology to become a precision science.

The successor satellite mission of COBE is the Wilkinson Microwave Anisotropy Probe (WMAP) which yields much improved measurements of the temperature fluctuations. As the distribution of the observed temperature fluctuations depend on cosmological parameters, like Ω_{m} and Ω_{Λ}, we can use the improved measurements to constrain cosmological models of the Universe (Spergel et al. 2003). Established theoretical models for predictions of the CMB fluctuations and a good understanding of observational systematics makes the measurements of the CMB one of the most important cosmological

probes which gives up to now the most accurate constraints (see the latest WMAP 5 year release in Komatsu et al. 2009).

1.3.4 Inflation

We present two problems of the standard model namely the horizon and flatness problem and show that a very short period of accelerated expansion in the early Universe, a so-called inflationary phase, can solve both problems.

Horizon Problem

The comoving distance of a photon emitted at time t_1 and received at t_2 is

$$r_{\rm h}(t_1, t_2) = \int_{t_1}^{t_2} \frac{c \, {\rm d}t}{a(t)} \,. \tag{1.55}$$

As information cannot be exchanged faster than the speed of light, the comoving distance determines the maximal distance between a region at time t_1 and a region at time t_2 to have been in causal contact. Therefore, if the integral is finite photons can only propagate a finite distance and if the integral diverges everything is in causal contact. We define the *particle horizon* as the limit $t_1 \to 0$ and $t_2 \equiv t$ which is the comoving distance a photon could have traveled since the Big Bang. On the other hand, the *event horizon* is the largest distance a photon can travel starting at time t until infinity, where $t_1 \equiv t$ and $t_2 \to \infty$. For our purposes only the particle horizon is interesting. Rewriting the particle horizon in terms of the scale factor yields

$$r_{\rm h}(a) = \int_0^a \frac{c}{H(a')a'^2} \, {\rm d}a' \,. \tag{1.56}$$

We find a simple solution for this integral considering $a_{\rm eq} \ll a \ll 1$, which is the matter-dominated era well before dark energy and curvature domination:

$$r_{\rm h}(a) = 2\frac{c}{H_0}\sqrt{\frac{a}{\Omega_{\rm m}}} \simeq \frac{6000}{\sqrt{\Omega_{\rm m}z}} \, h^{-1}\,{\rm Mpc} \,. \tag{1.57}$$

We can apply this approximation to calculate the size of the horizon at the time of the origin of the CMB radiation. We find for $z \equiv z_{\rm rec} \simeq 1100$ a comoving distance of the order $100\,{\rm Mpc}$, which corresponds to an angle of $1°$ on the sky. However, today we measure the temperature of the CMB to be nearly completely isotropic although huge parts of the CMB photons were never in causal contact. This is the well known *horizon problem* which is a generic feature of the hot Big Bang model.

Flatness Problem

We can rewrite the Friedmann equation (1.22) in the following form:

$$|\Omega_{\rm tot}(a) - 1| = \frac{Kc^2}{a^2 H^2(a)} \,, \tag{1.58}$$

where $\Omega_{\text{tot}}(a)$ is the total density parameter, i.e., the sum of the individual scale-dependent density parameters. We note that if the Universe is flat at some time, where $\Omega_{\text{tot}} = 1$, it will remain flat for all subsequent time. In the matter-dominated era the time dependence of the scale factor is $a(t) \propto t^{2/3}$ and thus we find

$$|\Omega_{\text{tot}}(t) - 1| \propto t^{2/3}. \tag{1.59}$$

The deviation of Ω_{tot} from unity is a growing function of cosmic time. Today, we measure $\Omega_{\text{tot}} = 1.011(12)$ (Amsler et al. 2008) which is close to spatial flatness. Hence, for example at nucleosynthesis when the Universe was $1\,\text{s}$ old the deviation from flatness is

$$|\Omega_{\text{tot}}(t_{\text{nuc}}) - 1| \lesssim 10^{-16}. \tag{1.60}$$

Going to earlier times, the deviation from flatness is even smaller. This is the *flatness problem*, where the initial conditions set up after the Big Bang need to be extremely fine-tuned to reach the present day flatness.

The Inflationary Mechanism

The inflationary mechanism provides a solution to the horizon and flatness problem as shown in the following. At first, we rewrite the comoving horizon in the form:

$$r_{\text{h}}(a) \propto \int_0^a \frac{\mathrm{d}a'}{a'} \frac{1}{\sqrt{\rho a'^2}}. \tag{1.61}$$

To solve the horizon problem described above, the integral needs to diverge. This is the case when the product ρa^2 is an increasing or constant function of the scale factor at early times. However, the two standard energy density forms of radiation $\rho \propto a^{-4}$ and matter $\rho \propto a^{-3}$ do not fulfill this condition. Hence, we need to propose another unknown form of energy density dominating at early times to solve the horizon problem. Using Eq. (1.18), we see that such an energy density needs to have an equation of state of $w < -1/3$ implying a negative pressure. Then we obtain from the second Friedmann equation (1.13) that $\ddot{a} > 0$, i.e., accelerated expansion. Thus, we say at very early times the Universe underwent a phase of *inflationary expansion*.

Another equivalent way to define inflation is that the comoving Hubble radius is a decreasing function of cosmic time:

$$\frac{\mathrm{d}}{\mathrm{d}t}\left(\frac{c}{H(a)a}\right) < 0. \tag{1.62}$$

This is exactly the condition to solve the flatness problem as the right-hand side of Eq. (1.58) gets smaller with increasing cosmic time.

A scalar field ϕ naturally fulfills the condition of negative pressure needed to start inflation, where the scalar field is sometimes known as the *inflaton*. Because inflation starts at very early times, the energy at that time is well beyond the energy range

accessible to particle physics colliders. Hence, we can only try to match the predictions of inflation with cosmological observations to verify the theory. The Lagrangian of a scalar field ϕ with potential $V(\phi)$ is given by

$$\mathcal{L} = \frac{1}{2}\partial_\mu\phi\partial^\mu\phi - V(\phi)\,, \tag{1.63}$$

where the first term is the kinetic energy and the second term the potential energy. From the Euler-Lagrange equations, we obtain the equation of motion of the scalar field

$$\ddot{\phi} + 3H\dot{\phi} + \frac{\mathrm{d}V}{\mathrm{d}\phi} = 0\,, \tag{1.64}$$

where we assumed a homogeneous field that only depends on time, i.e., $\phi = \phi(t)$. The energy density and pressure are obtained from the energy-momentum tensor

$$T_{\mu\nu} = \partial_\mu\phi\partial_\nu\phi - g_{\mu\nu}\mathcal{L}\,. \tag{1.65}$$

In the end, we find

$$\rho_\phi = \frac{\dot{\phi}^2}{2} + V(\phi)\,, \qquad p_\phi = \frac{\dot{\phi}^2}{2} - V(\phi)\,. \tag{1.66}$$

Hence, we infer the important result that as long as $\dot{\phi}^2/2 \ll V(\phi)$, we find $\rho_\phi = -p_\phi$ leading to the desired accelerated expansion. This condition is for example fulfilled by a scalar field that is trapped in a false vacuum which is the original interpretation of inflation developed by Guth (1981). However, in this model the field never attains the true vacuum necessary for ending the phase of inflation. To avoid this problem, subsequent models proposed that the field is slowly rolling down its potential to the true vacuum. This scenario also fulfills the condition that the kinetic energy of the field is much smaller than the potential energy. In addition, the equation of motion of a time-varying field in Eq. (1.64) has to satisfy the *slow roll conditions*:

$$\epsilon = \frac{m_{\mathrm{pl}}^2}{16\pi}\left(\frac{V'}{V}\right)^2 \ll 1\,, \qquad \eta = \frac{m_{\mathrm{pl}}^2}{8\pi}\left(\frac{V''}{V}\right) \ll 1\,, \tag{1.67}$$

where a prime denotes the derivative of the potential with respect to ϕ and m_{pl} is the Planck mass given by

$$m_{\mathrm{pl}} = \sqrt{\frac{\hbar c}{G_N}} \approx 2.43 \times 10^{18}\,\mathrm{GeV/c^2}\,. \tag{1.68}$$

Besides solving the horizon and flatness problem inflation provides a mechanism to explain the origin of tiny density fluctuations that were present in the early Universe and which built the seeds of structure formation. In fact, quantum fluctuations of the inflaton field are amplified during inflation such that at the end of inflation the perturbations are sufficiently large to grow by gravitational instability. The next chapter will describe in detail how the large-scale structure we observe today is formed out of these fluctuations.

Chapter 2

Cosmological Perturbation Theory and Correlation Functions

Cosmological linear perturbation theory is one of the pillars for predictions of the temperature and polarization anisotropies of the cosmic microwave background. This is due to the fact that the temperature fluctuations are only of the order 10^{-5} and are thus well modeled by a linear perturbative approach. However, probes of the large-scale structure of the Universe like cosmic shear and galaxy redshift surveys use scales that are also in the nonlinear regime. A lot of effort was put into a perturbative approach that is still accurate in the mildly nonlinear or quasilinear regime (see the comprehensive review by Bernardeau et al. 2002, and references therein). Nevertheless, the nonlinear regime cannot be accessed with a perturbative approach since the description of the fluid equations breaks down. Several approaches try to cure this problem. Dark matter N-body simulations start from a Gaussian distribution of the density field and then evolve the density and velocity fields according to the Vlasov equation (which we introduce below). The caveat is that they are computationally costly and lack a physical interpretation of the process of structure formation via gravitational instability. They are also limited by the resolution of the simulation. Due to the large computational requirements, fitting functions were developed to interpolate between simulation results (most notably the fitting formulas for the dark matter power spectrum by Peacock & Dodds 1996; Smith et al. 2003). Another approach is the dark matter halo model which combines results from simulations for dark matter halos and theoretical models for gravitational clustering. We will discuss this model in detail in the next chapter.

Recently, we have seen a revival of perturbation theory mainly due to the feature of baryonic acoustic oscillations observed in the galaxy two-point correlation function (Eisenstein et al. 2005). The so-called baryonic acoustic peak is important at scales which essentially lie in the quasilinear regime. This regime can be modeled within 1% accuracy (Jeong & Komatsu 2006) using perturbation theory. In addition, the importance of baryonic acoustic oscillations to break parameter degeneracies has led to a remarkable progress in perturbation theory, e.g., in the development of renormalized perturbation theory and the renormalization group approach (Crocce & Scoccimarro 2006; McDonald 2007). Furthermore, these techniques may help to find a model which is also applicable in the nonlinear regime.

The outline of this chapter is as follows: In Sect. 2.1, we derive the basic equations governing cosmological structure formation and present a general perturbative solution scheme to these nonlinear equations. We present the concept and properties of n-point correlation functions in Sect. 2.2. In particular, we show the perturbative results for the two-, three- and four-point correlation function in lowest order of the density field. As perturbation theory breaks down in the nonlinear regime, we give fitting functions for the dark matter power spectrum and the dark matter bispectrum in Sect. 2.3 . Finally, in Sect. 2.4 we show the effect of radiation on structure formation, and introduce the transfer function which describes the transition of the radiation-dominated era to the matter-dominated era.

2.1 Perturbation Theory

This section provides the basic framework of cosmological perturbation theory in the matter-dominated regime. First, we derive the fundamental equations governing the process of structure formation, namely the fluid equations, from the collisionless Boltzmann equation which describes the conservation of the number of dark matter particles in a given phase-space element. The resulting fluid equations are highly nonlinear and are in general not analytically solvable. Nevertheless, it is possible to find a closed solution in the linear regime. For the nonlinear regime we apply a perturbative ansatz around this linear solution. Most of the presented results and further issues can be found in the review paper by Bernardeau et al. (2002) which provides a thorough introduction to this field.

2.1.1 The Vlasov Equation

When we describe the process of structure formation, we deal with a dynamical system of a large number of particles interacting only via gravitational forces. Here we formalize this problem and derive the basic differential equations, namely the continuity, the Poisson and the Euler equation. The discussion is based on the book by Peebles (1980) and on the well-known physics of classical fluid dynamics. A general introduction into this field is provided by Landau & Lifshitz (1959). Most of the ingredients needed for a description of structure formation can be found already in this work.

Weak field approximation

The underlying theory of cosmology is general relativity. Therefore, we need to formulate structure formation in this framework. Fortunately, we can apply Newtonian physics in regions of length R that are small compared to the Hubble length, i.e., $R \ll cH^{-1}$. The rest of the Universe can affect this region only through a tidal field ϕ. This behavior can be described using the *weak field approximation*

$$g_{\mu\nu} = \eta_{\mu\nu} + h_{\mu\nu} \,, \tag{2.1}$$

where $\eta_{\mu\nu}$ is the Minkowski metric of flat space-time (see Eq. A.1) and $h_{\mu\nu}$ is a small perturbation to this metric. Using this perturbed Minkowski metric, we can compute the components of the Einstein equation (1.9) assuming an ideal gas for the energy-momentum tensor in Eq. (1.11). As a result, we obtain the Poisson equation from the zero-zero-component of the Einstein equation:

$$\nabla_r^2 \phi = 4\pi G_N \left(\rho + \frac{3p}{c^2} \right) - \Lambda \,, \tag{2.2}$$

where ϕ is the gravitational potential and ∇_r denotes the nabla operator with respect to r, i.e., $\nabla_r = \partial/\partial\boldsymbol{r}$. The first term is the result we would also get using Newtonian physics from the start. In addition, we get two terms describing the influence of the pressure p and the cosmological constant Λ. In this section, we analyze cosmological structure formation after recombination, i.e., we are considering the limit $p \ll \rho c^2$. Then the Poisson equation simplifies to

$$\nabla_r^2 \phi = 4\pi G_N \rho - \Lambda \,. \tag{2.3}$$

One can show that the weak field approximation implies the non-relativistic limit. Now we want to derive the classical potential and equation of motion noting that the result of Eq. (2.3) is the Newtonian result plus a constant.

Newtonian approach

The Universe after recombination can be described as a system of N particles of mass m interacting only gravitationally. The particles themselves can be dark matter particles like WIMPs[1] or bound systems like dark matter halos. Note that it is not necessary to assume a certain particle species because the final equations are independent of the particle mass. The equation of motion of a single particle at position $\boldsymbol{r}$ is given by a superposition of the forces from all particles

$$\frac{\mathrm{d}\boldsymbol{v}}{\mathrm{d}t} = G_N m \sum_{i=1}^{N} \frac{\boldsymbol{r}_i - \boldsymbol{r}}{|\boldsymbol{r}_i - \boldsymbol{r}|^3} \,, \tag{2.4}$$

where $\boldsymbol{v}$ denotes the proper particle velocity and $\boldsymbol{r}_i$ the position of the i-th particle. Note that we assumed all particles to have the same mass m. By introducing the Newtonian gravitational potential

$$\phi(\boldsymbol{r}) = -G_N \int \mathrm{d}^3 r' \frac{\rho(\boldsymbol{r}')}{|\boldsymbol{r}' - \boldsymbol{r}|} \,, \tag{2.5}$$

we can write the equation of motion in the compact form

$$\frac{\mathrm{d}\boldsymbol{v}}{\mathrm{d}t} = -\nabla_r \phi(\boldsymbol{r}) \,. \tag{2.6}$$

---

[1]Weakly Interacting Massive Particles.

We already showed in Sect. 1.1.2 that the expansion of the Universe is governed by a time-dependent scale factor. It is a good practice to adopt *comoving coordinates* that stay constant for the normal Hubble expansion. They are defined as

$$\boldsymbol{r}(t) = a(t)\boldsymbol{x}\,, \tag{2.7}$$

where $\boldsymbol{x}$ denotes the comoving distance, and $a(t)$ is the scale factor of the Universe. In addition, we introduce the conformal time

$$\mathrm{d}t = a(\tau)\mathrm{d}\tau\,, \tag{2.8}$$

for notational convenience. Using conformal time coordinates the Friedmann equations (1.12) and (1.13) change to

$$Kc^2 = [\Omega_\mathrm{m}(\tau) + \Omega_\Lambda(\tau) - 1]\mathcal{H}^2\,, \tag{2.9}$$

$$\frac{\mathrm{d}\mathcal{H}}{\mathrm{d}\tau} = \left(\Omega_\Lambda(\tau) - \frac{\Omega_\mathrm{m}(\tau)}{2}\right)\mathcal{H}^2\,, \tag{2.10}$$

where we have defined the conformal Hubble rate $\mathcal{H} \equiv \mathrm{d}\ln a/\mathrm{d}\tau = Ha$. The dimensionless density parameters change accordingly to

$$\Omega_\mathrm{m}(\tau) = \frac{8\pi G_N}{3H^2}\bar{\rho} = \frac{8\pi G_N a^2}{3\mathcal{H}^2}\bar{\rho}\,, \tag{2.11}$$

$$\Omega_\Lambda(\tau) = \frac{\Lambda}{3H^2} = a^2\frac{\Lambda}{3\mathcal{H}^2}\,. \tag{2.12}$$

We define the dark matter density contrast

$$\delta(\boldsymbol{x}, \tau) \equiv \frac{\rho(\boldsymbol{x}, \tau) - \bar{\rho}(\tau)}{\bar{\rho}(\tau)}\,, \tag{2.13}$$

where $\bar{\rho}$ is the mean matter density of the Universe. Applying comoving coordinates, the Poisson equation (2.3) changes to

$$\nabla^2\phi = a^2(4\pi G_N\rho - \Lambda) = \mathcal{H}^2\left[\frac{3}{2}\Omega_\mathrm{m}(\tau)(1 + \delta) - 3\Omega_\Lambda(\tau)\right]\,, \tag{2.14}$$

where we used Eqs. (2.11), (2.12) and (2.13) in the second step. Here and in the following we will use the nabla operator in comoving coordinates, i.e., $\nabla_x \equiv \nabla = \partial/\partial\boldsymbol{x}$.

Performing the time derivative of Eq. (2.7), yields the proper velocity in terms of τ:

$$\boldsymbol{v}(\boldsymbol{x}, \tau) = \mathcal{H}\boldsymbol{x} + \boldsymbol{u}(\boldsymbol{x}, \tau)\,. \tag{2.15}$$

The first term on the right-hand side of this equation is the Hubble flow, whereas the second term describes departures from the mean expansion of the Universe. This is

the so-called *peculiar velocity* defined as $\boldsymbol{u} \equiv \dot{\boldsymbol{x}}$. We define the scaled cosmological gravitational potential by

$$\Phi(\boldsymbol{x}, \tau) \equiv \phi(\boldsymbol{x}, \tau) + \frac{1}{2} \frac{\mathrm{d}\mathcal{H}}{\mathrm{d}\tau} x^2 \,. \tag{2.16}$$

Using the identity

$$\nabla^2 \Phi(\boldsymbol{x}, \tau) = \nabla^2 \phi(\boldsymbol{x}, \tau) + 3 \frac{\mathrm{d}\mathcal{H}}{\mathrm{d}\tau} \,, \tag{2.17}$$

we find that the new potential fulfills the Poisson equation

$$\nabla^2 \Phi(\boldsymbol{x}, \tau) = \frac{3}{2} \Omega_{\mathrm{m}}(\tau) \mathcal{H}^2(\tau) \delta(\boldsymbol{x}, \tau) \,, \tag{2.18}$$

where we used the Poisson equation for ϕ in comoving coordinates (2.14) and the second Friedmann equation (2.10). Rewriting the equation of motion (2.6) in terms of the newly introduced variables, i.e., the peculiar velocity $\boldsymbol{u}$ (see Eq. 2.15) and the potential Φ (see Eq. 2.16), we get the following result

$$\frac{\mathrm{d}\boldsymbol{p}}{\mathrm{d}\tau} = -am\nabla\Phi(\boldsymbol{x}, \tau) \,, \tag{2.19}$$

where we defined the peculiar momentum

$$\boldsymbol{p} = am\boldsymbol{u} \,. \tag{2.20}$$

To study the motion of N dark matter particles analytically, one needs to solve N three-dimensional differential equations of the same type as Eq. (2.19). However, the huge number of particles makes it impossible to follow the motion of each individual particle. Therefore, we need to employ a different approach. A classical way out is to study the distribution function $f(\boldsymbol{x}, \boldsymbol{p}, \tau)$ of all particles rather than the individual equations. The distribution function is defined such that

$$\mathrm{d}N = f(\boldsymbol{x}, \boldsymbol{p}, \tau) \, \mathrm{d}^3 x \, \mathrm{d}^3 p \tag{2.21}$$

is the number of particles at time τ contained in the infinitesimal six-dimensional phase-space volume $\mathrm{d}^3 x \, \mathrm{d}^3 p$. The general Boltzmann equation describes the time evolution of this distribution function:

$$\frac{\mathrm{d}f}{\mathrm{d}t} = C_{\mathrm{coll}} \,, \tag{2.22}$$

where C_{coll} contains all possible collision terms. As we are considering collisionless dark matter, we can set this term to zero. Then the Boltzmann equation simplifies to the *Vlasov equation*:

$$\frac{\mathrm{d}f}{\mathrm{d}\tau} = \frac{\partial f}{\partial \tau} + \dot{\boldsymbol{x}} \cdot \nabla f + \dot{\boldsymbol{p}} \cdot \frac{\partial f}{\partial \boldsymbol{p}} = 0 \,. \tag{2.23}$$

This equation is a special case of Liouville's theorem which describes the conservation of the phase-space density $f(\boldsymbol{x}, \boldsymbol{p}, \tau)$ over time. As a consequence, particles contained

in an initial region move in phase-space such that the region will continue to occupy the same volume but with altered shape. Inserting the equations of motions (2.19) and (2.20) in the Vlasov equation yields

$$\frac{\partial f}{\partial \tau} + \frac{\boldsymbol{p}}{ma} \cdot \nabla f - am\nabla\Phi \cdot \frac{\partial f}{\partial \boldsymbol{p}} = 0 \, . \tag{2.24}$$

This equation is highly nonlinear which is induced by the potential Φ. This can be seen from the fact that the potential Φ depends through the Poisson equation (2.18) on the matter density. But the density is proportional to the integral over the distribution function f itself (see Eq. 2.25).

The common ansatz to solve the Vlasov equation (2.24) is to take velocity moments of the equation. The first three moments are defined as $\int \mathrm{d}^3 u$, $\int \mathrm{d}^3 u \, \boldsymbol{u}$ and $\int \mathrm{d}^3 u \, u_i u_j$ and higher-order moments can be defined accordingly. To identify the moments with physical quantities, we define the proper density as the zeroth moment:

$$\rho(\boldsymbol{x}, \tau) = ma^{-3} \int \mathrm{d}^3 p \, f(\boldsymbol{x}, \boldsymbol{p}, \tau) \, , \tag{2.25}$$

the peculiar velocity as the first moment:

$$\langle \boldsymbol{u}(\boldsymbol{x}, \tau) \rangle = \int \mathrm{d}^3 p \left(\frac{\boldsymbol{p}}{ma} \right) f(\boldsymbol{x}, \boldsymbol{p}, \tau) \bigg/ \int \mathrm{d}^3 p \, f(\boldsymbol{x}, \boldsymbol{p}, \tau) \, , \tag{2.26}$$

and the second velocity moment:

$$\langle u_i u_j \rangle \equiv [\langle u_i \rangle \langle u_j \rangle + \sigma_{ij}] = \int \mathrm{d}^3 p \left(\frac{p_i}{ma} \right) \left(\frac{p_j}{ma} \right) f(\boldsymbol{x}, \boldsymbol{p}, \tau) \bigg/ \int \mathrm{d}^3 p \, f(\boldsymbol{x}, \boldsymbol{p}, \tau) \, , \tag{2.27}$$

where σ_{ij} is the *stress tensor* which is defined as $\sigma_{ij} \equiv \langle u_i u_j \rangle - \langle u_i \rangle \langle u_j \rangle$. In the *single-stream approximation* one sets σ_{ij} and all higher-order velocity moments to zero. Multiple streams occur in cosmology at nonlinear scales, for example during the virialization process of a halo.

For notational convenience we will omit to write the average over the velocity $\langle \cdots \rangle$ in the following and simply denote $\langle \boldsymbol{u} \rangle \equiv \boldsymbol{u}$. Taking the zeroth moment of the Vlasov equation (2.24) yields

$$\frac{\partial}{\partial \tau} \int \mathrm{d}^3 p \, f + \nabla_i \int \mathrm{d}^3 p \, \frac{p_i}{ma} f - ma\nabla\Phi \cdot \int \mathrm{d}^3 p \, \frac{\partial f}{\partial \boldsymbol{p}} = 0 \, , \tag{2.28}$$

where $\nabla_i \equiv \partial/\partial x_i$ is the i-th component of the nabla operator and we assumed summation over multiple occurring indices. The third term vanishes because the distribution function is zero at infinity. Using the definitions (2.25) and (2.26), one obtains the *continuity equation*

$$\frac{\partial \delta}{\partial \tau} + \nabla \cdot [(1+\delta)\boldsymbol{u}] = 0 \, . \tag{2.29}$$

We analogously get the *Euler equation* by taking the first velocity moment of the Vlasov equation

$$\frac{\partial \boldsymbol{u}}{\partial \tau} + \mathcal{H}\boldsymbol{u} + (\boldsymbol{u} \cdot \nabla)\boldsymbol{u} = -\nabla\Phi - \frac{1}{\rho}\nabla_j(\rho\sigma_{ij}) \,, \tag{2.30}$$

where we used Eqs. (2.25), (2.26) and (2.27). In combination with the Poisson equation (2.18), the continuity and the Euler equation build the fundamental set of equations for our analytical study of structure formation.

A complementary approach to taking moments of the Vlasov equation is to assume an ideal fluid (see Peebles 1980), which is characterized by its density ρ and isotropic pressure p. The results of both methods are the same when using the equation of state $\rho\sigma_{ij} = \delta_{ij}p$. The Vlasov equation approach is more general in the sense that one also obtains differential equations for higher-order moments. Note that the moments of the Vlasov equation all have a similar feature: they couple the $(N-1)$-th moment to the N-th moment. For example, taking the second moment of the Vlasov equation one gets a differential equation for the stress tensor that is coupled to a third-order velocity tensor.

Up to now, there is no approach for solving the fluid equations for nonlinear scales, where the contribution from the stress tensor σ_{ij} becomes important. Recent studies try to use renormalized perturbation theory (see Crocce & Scoccimarro 2006) and a renormalization group approach (see McDonald 2007) to solve the fluid equations in the quasilinear regime. Maybe one can extend this kind of calculations also into the nonlinear regime, where multi-streaming is important. This would be a breakthrough in the study of structure formation. But it is more likely that perturbation theory will provide results that can be used as a startup configuration for subsequent N-body simulations.

2.1.2 Vorticity Perturbations

The peculiar velocity field $\boldsymbol{u}$, as any arbitrary (differentiable) vector field, can be decomposed into a divergence field $\theta = \nabla \cdot \boldsymbol{u}$ and a vorticity field $\boldsymbol{w} = \nabla \times \boldsymbol{u}$ which is know as *Helmholtz's theorem*. For a proof of the theorem we refer to the detailed discussion in Appendix B.2. In particular, the decomposition is helpful if one can neglect one of the components reducing the complexity of the fluid equations. This is indeed the case for the velocity of the cosmological fluid, as is shown in the following.

Taking the curl of the Euler equation (2.30), we obtain an evolution equation for the vorticity[2]

$$\frac{\partial \boldsymbol{w}}{\partial \tau} + \boldsymbol{w}\mathcal{H} - \nabla \times [\boldsymbol{u} \times \boldsymbol{w}] = -\nabla \times \left[\frac{1}{\rho}\nabla_j(\rho\sigma_{ij})\right] \,. \tag{2.31}$$

If we set $\sigma_{ij} = 0$, and start with the initial condition $\boldsymbol{w} = \boldsymbol{0}$ we get

$$\frac{\partial \boldsymbol{w}}{\partial \tau} = 0 \,, \tag{2.32}$$

---

[2]The result is obtained using the calculus identity $\boldsymbol{A} \times (\nabla \times \boldsymbol{A}) = \frac{1}{2}\nabla(\boldsymbol{A} \cdot \boldsymbol{A}) - (\boldsymbol{A} \cdot \nabla)\boldsymbol{A}$.

meaning $\boldsymbol{w}$ remains zero at all subsequent times even in the nonlinear regime. This conservation law is known as *Kelvin Circulation Theorem* in fluid mechanics (see e.g., Landau & Lifshitz 1959). In fact, the peculiar velocity field after the time of inflation is assumed to be irrotational. Therefore, we deal in cosmology with potential peculiar velocity flows that are characteristic for divergence fields. Note that this way of reasoning is only valid if we neglect the right-hand side of Eq. (2.31). At small scales, where one needs to include dissipative processes (heating, cooling and shock waves) this assumption breaks down. Nevertheless the large-scale behavior is unaffected by these effects.

Neglecting nonlinear terms, the vorticity equation simplifies to

$$\frac{\partial \boldsymbol{w}}{\partial \tau} + \boldsymbol{w}\mathcal{H} = 0 \tag{2.33}$$

with the solution $\boldsymbol{w}(\boldsymbol{x}, \tau) = \boldsymbol{F}(\boldsymbol{x}, 0)a^{-1}$, where $\boldsymbol{F}(\boldsymbol{x}, 0)$ is an arbitrary time-independent function. Hence, in the linear regime vorticity perturbations decay with the expansion of the Universe. That means that even if a non-vanishing contribution of vorticity modes exists in the primordial era, it will vanish in the linear regime with the expansion of the Universe.

Both effects lead us to the conclusion that we can safely neglect the vorticity of the velocity field. Nevertheless, we have to keep in mind the limitations of this assumption especially in the nonlinear regime of the density and velocity field.

2.1.3 Fluid Equations

To describe the evolution of the dark matter density field in general, one needs to solve the relativistic Boltzmann equation, i.e., the Vlasov equation. We made several approximations in the previous section: we assumed that the matter distribution can be approximated by a pressureless fluid, the peculiar velocity of the fluid is non-relativistic and the region of interest is much smaller than the Hubble distance cH^{-1}. Furthermore, we assume from now on that the stress tensor σ_{ij} is equal to zero. This is a good approximation if we are considering the linear to quasilinear regime of structure formation as discussed in the previous section. We saw that with these approximations it is possible to use a non-relativistic Newtonian approach. The pressureless fluid is then described by a coupled system of three equations: the continuity equation

$$\frac{\partial \delta}{\partial \tau} + \nabla \cdot [(1 + \delta)\boldsymbol{u}] = 0 \,, \tag{2.34}$$

the Euler equation

$$\frac{\partial \boldsymbol{u}}{\partial \tau} + \mathcal{H}\boldsymbol{u} + (\boldsymbol{u} \cdot \nabla)\boldsymbol{u} = -\nabla\Phi \,, \tag{2.35}$$

and the Poisson equation

$$\nabla^2 \Phi = \frac{3}{2}\Omega_{\mathrm{m}}(\tau)\mathcal{H}^2(\tau)\delta(\boldsymbol{x}, \tau) \,. \tag{2.36}$$

We can use a single scalar field $\theta = \nabla \cdot \boldsymbol{u}$ to describe the irrotational peculiar velocity field. By taking the divergence of the Euler equation (2.35), one can combine it with the Poisson equation (2.36). At the end, one is left with two coupled equations for the fields δ and θ:

$$\frac{\partial \delta}{\partial \tau} + \theta = -\nabla \cdot (\delta \boldsymbol{u}) \,, \tag{2.37}$$

$$\frac{\partial \theta}{\partial \tau} + \mathcal{H}\theta + \frac{3}{2}\Omega_{\mathrm{m}}\mathcal{H}^2\delta = -\nabla \cdot [(\boldsymbol{u} \cdot \nabla)\boldsymbol{u}] \,. \tag{2.38}$$

However, even with the inclusion of the aforementioned approximations, Eqs. (2.37) and (2.38) are still highly nonlinear. The nonlinear part is written on the right-hand side of the equations. In general, the equations are only solvable with a perturbative ansatz for the density contrast δ and the divergence of the velocity field θ. In this case, it is convenient to perform a Fourier transformation of the equations. But first we present the analytic solution in the linear regime of the fields in real space in the next section.

2.1.4 Linear Solution

Here we discuss the first-order or *linear solution* of the fluid equations which is applicable on large scales or at very early times in the history of the Universe, since in these cases we expect that the fluctuations in the fields are small compared to the homogeneous background. More specifically, we take the limit $|\delta| \ll 1$ and consider that also the peculiar velocity field $\boldsymbol{u}$ is sufficiently small (see Peebles 1980 for a more rigorous treatment). In this case we can neglect the nonlinear terms on the right-hand side of Eqs. (2.37) and (2.38) and we find

$$\frac{\partial \delta}{\partial \tau} + \theta = 0 \,, \tag{2.39}$$

$$\frac{\partial \theta}{\partial \tau} + \mathcal{H}\theta + \frac{3}{2}\Omega_{\mathrm{m}}\mathcal{H}^2\delta = 0 \,. \tag{2.40}$$

By taking the time derivative of Eq. (2.39) and then inserting Eq. (2.40), we find the following differential equation for the density contrast

$$\ddot{\delta} + \mathcal{H}\dot{\delta} = \frac{3}{2}\Omega_{\mathrm{m}}\mathcal{H}^2\delta \,, \tag{2.41}$$

where dots denote partial derivatives with respect to the conformal time. Noting that this equation has no derivatives with respect to $\boldsymbol{x}$, we perform a separation of variables with the ansatz $\delta(\boldsymbol{x}, \tau) = g(\boldsymbol{x})D(\tau)$. Then we can write Eq. (2.41) as ordinary second-order linear differential equation for the time-dependent function $D(\tau)$:

$$\frac{\mathrm{d}^2 D}{\mathrm{d}\tau^2} + \frac{\mathrm{d}D}{\mathrm{d}\tau}\mathcal{H} = \frac{3}{2}\Omega_{\mathrm{m}}\mathcal{H}^2 D \,. \tag{2.42}$$

Since Eq. (2.42) is a second-order differential equation, it has two independent solutions

$$\delta(\boldsymbol{x}, \tau) = D_+(\tau)A(\boldsymbol{x}) + D_-(\tau)B(\boldsymbol{x}) \,, \tag{2.43}$$

where $A(\boldsymbol{x})$ and $B(\boldsymbol{x})$ are arbitrary functions of position $\boldsymbol{x}$ fixed by the initial conditions. Plugging this result into Eq. (2.39), we find the solution for the divergence of the peculiar velocity field:

$$\theta(\boldsymbol{x}, \tau) = -\mathcal{H}[f(\Omega_{\rm m}, \Omega_\Lambda)A(\boldsymbol{x})D_+(\tau) + g(\Omega_{\rm m}, \Omega_\Lambda)B(\boldsymbol{x})D_-(\tau)] \,, \tag{2.44}$$

where the cosmology dependence is encoded in

$$f(\Omega_{\rm m}, \Omega_\Lambda) \equiv \frac{{\rm d}\ln D_+(\tau)}{{\rm d}\ln a} = \frac{1}{\mathcal{H}}\frac{{\rm d}\ln D_+(\tau)}{{\rm d}\tau} \,, \qquad g(\Omega_{\rm m}, \Omega_\Lambda) \equiv \frac{1}{\mathcal{H}}\frac{{\rm d}\ln D_-(\tau)}{{\rm d}\tau} \,. \tag{2.45}$$

For an EdS Universe one finds a simple closed solution to Eqs. (2.42) and (2.44):

$$D_+(a) = a \,, \qquad D_-(a) = a^{-3/2} \,, \tag{2.46}$$

and

$$f(1, 0) = 1 \,, \qquad g(1, 0) = -3/2 \,, \tag{2.47}$$

where we used that in this case $a \propto \tau^2$ and $\mathcal{H} \propto 2/\tau$. The function D_+ is the so-called *growth factor* because it describes a growing solution, whereas the second function D_- is a decaying solution meaning that it decreases as the Universe expands. Hence, in the following we neglect the decaying function.

For a general ΛCDM cosmology one finds the following solution (see Heath 1977):

$$
\begin{aligned}
D_+(a) &\propto H(a)H_0^2 \int_0^a \frac{{\rm d}a'}{[H(a')\,a']^3} \\
&= \frac{H(a)}{H_0} \int_0^a {\rm d}a' \left[1 + \Omega_{\rm m}\left(\frac{1}{a'} - 1\right) + \Omega_\Lambda(a'^2 - 1)\right]^{-3/2} \,.
\end{aligned} \tag{2.48}
$$

The integral has in general no analytic solution. However, an accurate fitting formula is given in Carroll et al. (1992):

$$D_+(a) = \frac{5}{2}a\,\Omega_{\rm m}(a) \left[\Omega_{\rm m}^{4/7}(a) - \Omega_\Lambda(a) + \left(1 + \frac{\Omega_{\rm m}(a)}{2}\right)\left(1 + \frac{\Omega_\Lambda(a)}{70}\right)\right]^{-1} \,. \tag{2.49}$$

It is common practice to normalize the growth factor to unity today. Therefore, we define a new normalized growth factor $D(a) \equiv D_+(a)/D_+(a = 1)$ that will be used from now on.

2.1.5 Formulation in Fourier Space

The whole idea behind transforming the equations into Fourier space is that derivatives and convolutions become simple algebraic operations. We show in the next section that the Fourier space transformation of the evolution equation is suitable for a perturbative solution. A perturbative approach in real space can be found in the pioneering work of Fry (1984).

We use the following convention for the continuous Fourier transformation

$$\tilde{\delta}(\boldsymbol{k}, \tau) = \int \mathrm{d}^3 x \, \delta(\boldsymbol{x}, \tau) \, \mathrm{e}^{\mathrm{i}\boldsymbol{k}\cdot\boldsymbol{x}}, \qquad \tilde{\theta}(\boldsymbol{k}, \tau) = \int \mathrm{d}^3 x \, \theta(\boldsymbol{x}, \tau) \, \mathrm{e}^{\mathrm{i}\boldsymbol{k}\cdot\boldsymbol{x}} \,. \tag{2.50}$$

Corresponding to the adopted Fourier transformation, the Dirac delta function acting in Fourier space is given by

$$\delta_{\mathrm{D}}(\boldsymbol{k}) = \int \frac{\mathrm{d}^3 x}{(2\pi)^3} \, \mathrm{e}^{\mathrm{i}\boldsymbol{k}\cdot\boldsymbol{x}} \,. \tag{2.51}$$

Employing these definitions, we transform the continuity equation (2.37) into Fourier space:

$$\begin{aligned}
\frac{\partial \tilde{\delta}}{\partial \tau}(\boldsymbol{k}, \tau) + \tilde{\theta}(\boldsymbol{k}, \tau) &= -\int \mathrm{d}^3 x \, \nabla(\delta\boldsymbol{u})(\boldsymbol{x}, \tau) \, \mathrm{e}^{\mathrm{i}\boldsymbol{k}\cdot\boldsymbol{x}} \\
&= -\int \mathrm{d}^3 x \, \mathrm{e}^{\mathrm{i}\boldsymbol{k}\cdot\boldsymbol{x}} \int \frac{\mathrm{d}^3 k_1}{(2\pi)^3} \int \frac{\mathrm{d}^3 k_2}{(2\pi)^3} \, \tilde{\delta}(\boldsymbol{k}_2, \tau) \tilde{u}_i(\boldsymbol{k}_1, \tau) \nabla_i \left(\mathrm{e}^{-\mathrm{i}(\boldsymbol{k}_1 + \boldsymbol{k}_2)\cdot\boldsymbol{x}} \right) \\
&= \int \frac{\mathrm{d}^3 k_1}{(2\pi)^3} \int \mathrm{d}^3 k_2 \, \tilde{\boldsymbol{u}}(\boldsymbol{k}_1, \tau) \cdot (\mathrm{i}\boldsymbol{k}_1 + \mathrm{i}\boldsymbol{k}_2) \tilde{\delta}(\boldsymbol{k}_2, \tau) \delta_{\mathrm{D}}(\boldsymbol{k} - \boldsymbol{k}_1 - \boldsymbol{k}_2) \,. \tag{2.52}
\end{aligned}$$

Here ∇_i and $\tilde{u}_i$ are the i-th components of the nabla operator and the Fourier transform of the peculiar velocity, respectively. We employ the Einstein summation convention, and sum over identical indices. In the second step we inserted the inverse Fourier transformation of the density contrast and the peculiar velocity, and performed the derivative in the last step. In addition, we used the definition of the Dirac delta function (see Eq. 2.51).

We argued in the previous sections that the rotational component of the velocity field can be neglected. Therefore, we are able to rewrite the right-hand side of Eq. (2.52) in terms of the divergence field only. In Fourier space we find for this field $\tilde{\theta}(\boldsymbol{k}, \tau) = -\mathrm{i}\boldsymbol{k} \cdot \tilde{\boldsymbol{u}}(\boldsymbol{k}, \tau)$. Note that this implies

$$\tilde{\boldsymbol{u}}(\boldsymbol{k}, \tau) = \frac{\mathrm{i}\boldsymbol{k}}{k^2} \tilde{\theta}(\boldsymbol{k}, \tau) \,. \tag{2.53}$$

The two scalar products in Eq. (2.52) can then simply be identified with the divergence field using Eq. (2.53):

$$\tilde{\boldsymbol{u}}(\boldsymbol{k}_1, \tau) \cdot (\mathrm{i}\boldsymbol{k}_1 + \mathrm{i}\boldsymbol{k}_2) = -\tilde{\theta}(\boldsymbol{k}_1, \tau) \left(1 + \frac{\boldsymbol{k}_1 \cdot \boldsymbol{k}_2}{k_1^2} \right) \,. \tag{2.54}$$

Combining Eq. (2.52) and Eq. (2.54), we finally find for the differential equation in Fourier space

$$\frac{\partial \tilde{\delta}}{\partial \tau}(\boldsymbol{k}, \tau) + \tilde{\theta}(\boldsymbol{k}, \tau) = -\int \frac{\mathrm{d}^3 k_1}{(2\pi)^3} \int \mathrm{d}^3 k_2\, \delta_{\mathrm{D}}(\boldsymbol{k} - \boldsymbol{k}_1 - \boldsymbol{k}_2)\alpha(\boldsymbol{k}_1, \boldsymbol{k}_2)\tilde{\theta}(\boldsymbol{k}_1, \tau)\tilde{\delta}(\boldsymbol{k}_2, \tau)\,,$$
(2.55)

where we introduced the function

$$\alpha(\boldsymbol{k}_1, \boldsymbol{k}_2) = \frac{(\boldsymbol{k}_1 + \boldsymbol{k}_2) \cdot \boldsymbol{k}_1}{k_1^2}\,.$$
(2.56)

Hence, we find a coupling between different Fourier modes mediated by the coupling function $\alpha(\boldsymbol{k}_1, \boldsymbol{k}_2)$. This is in contrast to linear perturbation theory, where the right-hand side is zero of Eq. (2.55) and there is no coupling between Fourier modes.

In an analogous way, one can solve the Euler equation (2.38). Again Fourier transforming the equation leads to

$$\frac{\partial \tilde{\theta}}{\partial \tau}(\boldsymbol{k}, \tau) + \mathcal{H}\tilde{\theta}(\boldsymbol{k}, \tau) + \frac{3}{2}\Omega_{\mathrm{m}}(\tau)\mathcal{H}^2\tilde{\delta}(\boldsymbol{k}, \tau) = -\int \mathrm{d}^3 x\, \nabla \cdot [(\boldsymbol{u} \cdot \nabla)\boldsymbol{u}](\boldsymbol{x}, \tau)\, \mathrm{e}^{\mathrm{i}\boldsymbol{k}\cdot\boldsymbol{x}}\,. \quad (2.57)$$

The only difficulty is to calculate the right-hand side of this equation in Fourier space:

$$-\int \mathrm{d}^3 x\, \nabla_i[(u_j\nabla_j)u_i](\boldsymbol{x}, \tau)\, \mathrm{e}^{\mathrm{i}\boldsymbol{k}\cdot\boldsymbol{x}}$$

$$= -\int \mathrm{d}^3 x\, \mathrm{e}^{\mathrm{i}\boldsymbol{k}\cdot\boldsymbol{x}} \int \frac{\mathrm{d}^3 k_1}{(2\pi)^3} \int \frac{\mathrm{d}^3 k_2}{(2\pi)^3}\, \tilde{u}_i(\boldsymbol{k}_1, \tau)\tilde{u}_j(\boldsymbol{k}_2, \tau)\nabla_i(\mathrm{e}^{-\mathrm{i}\boldsymbol{k}_2\cdot\boldsymbol{x}}\nabla_j\, \mathrm{e}^{-\mathrm{i}\boldsymbol{k}_1\cdot\boldsymbol{x}})$$

$$= -\int \frac{\mathrm{d}^3 k_1}{(2\pi)^3} \int \mathrm{d}^3 k_2\, [\tilde{\boldsymbol{u}}(\boldsymbol{k}_2, \tau) \cdot \mathrm{i}\boldsymbol{k}_1][\tilde{\boldsymbol{u}}(\boldsymbol{k}_1, \tau) \cdot (\mathrm{i}\boldsymbol{k}_1 + \mathrm{i}\boldsymbol{k}_2)]\delta_{\mathrm{D}}(\boldsymbol{k} - \boldsymbol{k}_{12})$$

$$= -\int \frac{\mathrm{d}^3 k_1}{(2\pi)^3} \int \mathrm{d}^3 k_2\, \tilde{\theta}(\boldsymbol{k}_1, \tau)\tilde{\theta}(\boldsymbol{k}_2, \tau)\left(1 + \frac{\boldsymbol{k}_1 \cdot \boldsymbol{k}_2}{k_1^2}\right)\frac{\boldsymbol{k}_1 \cdot \boldsymbol{k}_2}{k_2^2}\delta_{\mathrm{D}}(\boldsymbol{k} - \boldsymbol{k}_{12})\,, \quad (2.58)$$

where we used Eq. (2.53) in the last step. Furthermore, we introduced the abbreviation $\boldsymbol{k}_{12} \equiv \boldsymbol{k}_1 + \boldsymbol{k}_2$. As the integrand is symmetric under $(\boldsymbol{k}_1 \leftrightarrow \boldsymbol{k}_2)$ exchange[3], we get after symmetrizing the final result

$$\frac{\partial \tilde{\theta}}{\partial \tau}(\boldsymbol{k}, \tau) + \mathcal{H}\tilde{\theta}(\boldsymbol{k}, \tau) + \frac{3}{2}\Omega_{\mathrm{m}}(\tau)\mathcal{H}^2\tilde{\delta}(\boldsymbol{k}, \tau)$$

$$= -\int \frac{\mathrm{d}^3 k_1}{(2\pi)^3} \int \mathrm{d}^3 k_2\, \beta(\boldsymbol{k}_1, \boldsymbol{k}_2)\tilde{\theta}(\boldsymbol{k}_1, \tau)\tilde{\theta}(\boldsymbol{k}_2, \tau)\delta_{\mathrm{D}}(\boldsymbol{k} - \boldsymbol{k}_{12})\,, \quad (2.59)$$

where we introduced the second coupling function

$$\beta(\boldsymbol{k}_1, \boldsymbol{k}_2) = \frac{|\boldsymbol{k}_1 + \boldsymbol{k}_2|^2(\boldsymbol{k}_1 \cdot \boldsymbol{k}_2)}{2k_1^2 k_2^2}\,.$$
(2.60)

This function is by definition symmetric in its arguments in contrast to the previous coupling function $\alpha(\boldsymbol{k}_1, \boldsymbol{k}_2)$.

---

[3]Note that this is different from Eq. (2.52) because of the appearance of the product $\tilde{\theta}(\boldsymbol{k}_1)\tilde{\theta}(\boldsymbol{k}_2)$ in contrast to $\tilde{\theta}(\boldsymbol{k}_1)\tilde{\delta}(\boldsymbol{k}_2)$ in the integrand.

2.1.6 Perturbative Solution

So far we have only rephrased the problem of solving the coupled nonlinear fluid equations. We show in the following that we can separate out the time dependence in Eqs. (2.55) and (2.59) for an EdS background Universe. In this case the time dependence of the scale factor is simply $a \propto t^{2/3} \propto \tau^2$. The conformal expansion rate and its derivative are then given by $\mathcal{H} = 2/\tau$ and $\partial \mathcal{H}/\partial \tau = -\mathcal{H}^2/2$, respectively. We make the following perturbative ansatz for the fields

$$\tilde{\delta}(\boldsymbol{k}, \tau) = \sum_{n=1}^{\infty} a^n(\tau) \tilde{\delta}_n(\boldsymbol{k}), \qquad \tilde{\theta}(\boldsymbol{k}, \tau) = -\mathcal{H}(\tau) \sum_{n=1}^{\infty} a^n(\tau) \tilde{\theta}_n(\boldsymbol{k}), \qquad (2.61)$$

where $\tilde{\delta}_1$ and $\tilde{\theta}_1$ are linear in the initial density field, $\tilde{\delta}_2$ and $\tilde{\theta}_2$ are quadratic, etc. The ansatz is constructed such, that we reproduce for $n = 1$ the dependence of the linear density contrast on the scale factor. Note that we can already obtain the first-order solution by inserting the first term in the expansion of $\tilde{\delta}$ into the continuity equation (2.55) (neglecting the coupling term). The additional factor in front of the ansatz for $\tilde{\theta}$ then assures that $\tilde{\delta}_1 = \tilde{\theta}_1$. The equality of the first-order solution of the density contrast and velocity field will be the initial condition for the recursion relation of the general n-th-order perturbative solutions.

For the following discussion we need the first-order derivatives of both power series. They are given by

$$\frac{\partial \tilde{\delta}}{\partial \tau} = \mathcal{H} \sum_{n=1}^{\infty} n a^n \tilde{\delta}_n, \qquad \frac{\partial \tilde{\theta}}{\partial \tau} = -\mathcal{H}^2 \sum_{n=1}^{\infty} \left(n - \frac{1}{2} \right) a^n \tilde{\theta}_n. \qquad (2.62)$$

Now we insert the perturbative ansatz into Eq. (2.55). By comparison of coefficients of the scale factor a, one gets the relation

$$n \tilde{\delta}_n(\boldsymbol{k}) - \tilde{\theta}_n(\boldsymbol{k}) = A_n(\boldsymbol{k}), \qquad (2.63)$$

which is valid for $n > 1$. This can be done in a completely analogous way for Eq. (2.59) (note that $\Omega_{\mathrm{m}} = 1$) yielding

$$(2n + 1) \tilde{\theta}_n(\boldsymbol{k}) - 3 \tilde{\delta}_n(\boldsymbol{k}) = B_n(\boldsymbol{k}), \qquad (2.64)$$

which is again only valid for $n > 1$. The right-hand side of both equations is

$$A_n(\boldsymbol{k}) = \int \frac{\mathrm{d}^3 k_1}{(2\pi)^3} \int \mathrm{d}^3 k_2 \, \delta_{\mathrm{D}}(\boldsymbol{k} - \boldsymbol{k}_{12}) \alpha(\boldsymbol{k}_1, \boldsymbol{k}_2) \sum_{m=1}^{n-1} \tilde{\theta}_m(\boldsymbol{k}_1) \tilde{\delta}_{n-m}(\boldsymbol{k}_2), \qquad (2.65)$$

$$B_n(\boldsymbol{k}) = \int \frac{\mathrm{d}^3 k_1}{(2\pi)^3} \int \mathrm{d}^3 k_2 \, \delta_{\mathrm{D}}(\boldsymbol{k} - \boldsymbol{k}_{12}) 2\beta(\boldsymbol{k}_1, \boldsymbol{k}_2) \sum_{m=1}^{n-1} \tilde{\theta}_{n-m}(\boldsymbol{k}_1) \tilde{\theta}_m(\boldsymbol{k}_2), \qquad (2.66)$$

respectively. A solution to this linear system of equations is simply obtained by writing both equations in matrix notation

$$
\begin{pmatrix} n & -1 \\ -3 & 2n+1 \end{pmatrix} \begin{pmatrix} \tilde{\delta}_n \\ \tilde{\theta}_n \end{pmatrix} = \begin{pmatrix} A_n \\ B_n \end{pmatrix} , \tag{2.67}
$$

and solving for $\tilde{\delta}_n$ and $\tilde{\theta}_n$ by matrix inversion

$$
\begin{pmatrix} \tilde{\delta}_n \\ \tilde{\theta}_n \end{pmatrix} = \frac{1}{(2n+3)(n-1)} \begin{pmatrix} 2n+1 & 1 \\ 3 & n \end{pmatrix} \begin{pmatrix} A_n \\ B_n \end{pmatrix} . \tag{2.68}
$$

This is a recursion relation for the fields $\tilde{\delta}$ and $\tilde{\theta}$ giving the n-th order solution in terms of a product of two lower orders such that the sum of orders is equal to n. Or, in other words, lower-order results provide source terms for higher-order terms. This expansion is only valid if the orders in perturbation follow a hierarchical form, i.e., the contributions from higher orders get subsequently smaller. This ceases to be valid around the value of $\delta \simeq 1$. Furthermore, multi-streaming is induced at these nonlinear scales. Therefore, even the ideal fluid approximation breaks down. We discuss in the next chapter a possible solution to also model scales where $\delta > 1$.

For a general cosmological ΛCDM model it is impossible to find a separable solution to Eqs. (2.55) and (2.59). However, Scoccimarro et al. (1998) showed that it is possible to find a separable solution in any order if one makes an approximation that is valid at percentage level. In this case one indeed finds the same recursion relation as for the EdS case. The ansatz is changed according to

$$
\tilde{\delta}(\boldsymbol{k}, \tau) = \sum_{n=1}^{\infty} D^n(\tau) \tilde{\delta}_n(\boldsymbol{k}) , \qquad \tilde{\theta}(\boldsymbol{k}, \tau) = -\mathcal{H}(\tau) \sum_{n=1}^{\infty} D^n(\tau) \tilde{\theta}_n(\boldsymbol{k}) . \tag{2.69}
$$

Therefore, we find that the whole cosmological information (from the parameter Ω_Λ and Ω_{m}) is encoded in the growth function and the Hubble function.

2.1.7 Coupling Functions

One can find a more handy expression for the n-th order density contrast and the divergence of the peculiar velocity in Eq. (2.68) by defining:

$$
\tilde{\delta}_n(\boldsymbol{k}) = \int \frac{\mathrm{d}^3 q_1}{(2\pi)^3} \cdots \frac{\mathrm{d}^3 q_{n-1}}{(2\pi)^3} \int \mathrm{d}^3 q_n \, \delta_{\mathrm{D}}(\boldsymbol{k} - \boldsymbol{q}_{1\ldots n}) F_n(\boldsymbol{q}_1, \ldots, \boldsymbol{q}_n) \tilde{\delta}_1(\boldsymbol{q}_1) \cdots \tilde{\delta}_1(\boldsymbol{q}_n) ,
$$
$$
\tilde{\theta}_n(\boldsymbol{k}) = \int \frac{\mathrm{d}^3 q_1}{(2\pi)^3} \cdots \frac{\mathrm{d}^3 q_{n-1}}{(2\pi)^3} \int \mathrm{d}^3 q_n \, \delta_{\mathrm{D}}(\boldsymbol{k} - \boldsymbol{q}_{1\ldots n}) G_n(\boldsymbol{q}_1, \ldots, \boldsymbol{q}_n) \tilde{\delta}_1(\boldsymbol{q}_1) \cdots \tilde{\delta}_1(\boldsymbol{q}_n) .
$$
$$\tag{2.70}$$

Simply by inserting these definitions into the recursion relation (2.68), one finds a recursion relation for the n-th order coupling functions F_n and G_n (Jain & Bertschinger

1994):

$$
F_n(\boldsymbol{q}_1,\ldots,\boldsymbol{q}_n) = \sum_{m=1}^{n-1} \frac{G_m(\boldsymbol{q}_1,\ldots,\boldsymbol{q}_m)}{(2n+3)(n-1)} [(2n+1)\alpha(\boldsymbol{k}_1,\boldsymbol{k}_2)F_{n-m}(\boldsymbol{q}_{m+1},\ldots,\boldsymbol{q}_n)
$$
$$
+ 2\beta(\boldsymbol{k}_1,\boldsymbol{k}_2)G_{n-m}(\boldsymbol{q}_{m+1},\ldots,\boldsymbol{q}_n)], \tag{2.71}
$$

$$
G_n(\boldsymbol{q}_1,\ldots,\boldsymbol{q}_n) = \sum_{m=1}^{n-1} \frac{G_m(\boldsymbol{q}_1,\ldots,\boldsymbol{q}_m)}{(2n+3)(n-1)} [3\alpha(\boldsymbol{k}_1,\boldsymbol{k}_2)F_{n-m}(\boldsymbol{q}_{m+1},\ldots,\boldsymbol{q}_n)
$$
$$
+ 2n\beta(\boldsymbol{k}_1,\boldsymbol{k}_2)G_{n-m}(\boldsymbol{q}_{m+1},\ldots,\boldsymbol{q}_n)], \tag{2.72}
$$

where $\boldsymbol{k}_1 \equiv \boldsymbol{q}_1 + \ldots + \boldsymbol{q}_m$ and $\boldsymbol{k}_2 \equiv \boldsymbol{q}_{m+1} + \ldots + \boldsymbol{q}_n$. The initial conditions for these recursion relations are $F_1 \equiv 1$ and $G_1 \equiv 1$. The fundamental mode coupling functions $\alpha(\boldsymbol{k}_1,\boldsymbol{k}_2)$ and $\beta(\boldsymbol{k}_1,\boldsymbol{k}_2)$ are given by Eqs. (2.56) and (2.60), respectively. To get the functions $F_n^{(\mathrm{s})}$ and $G_n^{(\mathrm{s})}$ that are symmetric in its arguments, one must perform the following symmetrizing procedure

$$
F_n^{(\mathrm{s})}(\boldsymbol{q}_1,\ldots,\boldsymbol{q}_n) = \frac{1}{n!} \sum_{\pi} F_n(\boldsymbol{q}_{\pi(1)},\ldots,\boldsymbol{q}_{\pi(n)}), \tag{2.73}
$$

$$
G_n^{(\mathrm{s})}(\boldsymbol{q}_1,\ldots,\boldsymbol{q}_n) = \frac{1}{n!} \sum_{\pi} G_n(\boldsymbol{q}_{\pi(1)},\ldots,\boldsymbol{q}_{\pi(n)}), \tag{2.74}
$$

where the sum is taken over all possible permutations π of the set $\{1,\ldots,n\}$. These equations enable us to calculate the density contrast in the n-th order of perturbation theory by using the iterative equations for the coupling functions.

We present the explicit relations for the second- and third-order coupling functions as they are needed for the tree-level bispectrum and trispectrum (see Sect. 2.2.6). The calculation of the second-order coupling functions is straightforward. The result is

$$
F_2^{(\mathrm{s})}(\boldsymbol{q}_1,\boldsymbol{q}_2) = \frac{5}{7} + \frac{2}{7}\frac{(\boldsymbol{q}_1\cdot\boldsymbol{q}_2)^2}{q_1^2 q_2^2} + \frac{1}{2}\frac{\boldsymbol{q}_1\cdot\boldsymbol{q}_2}{q_1 q_2}\left(\frac{q_1}{q_2}+\frac{q_2}{q_1}\right), \tag{2.75}
$$

$$
G_2^{(\mathrm{s})}(\boldsymbol{q}_1,\boldsymbol{q}_2) = \frac{3}{7} + \frac{4}{7}\frac{(\boldsymbol{q}_1\cdot\boldsymbol{q}_2)^2}{q_1^2 q_2^2} + \frac{1}{2}\frac{\boldsymbol{q}_1\cdot\boldsymbol{q}_2}{q_1 q_2}\left(\frac{q_1}{q_2}+\frac{q_2}{q_1}\right). \tag{2.76}
$$

Note that for two identical vectors with opposite signs the second-order coupling functions vanish, i.e., $F_2^{(\mathrm{s})}(\boldsymbol{q},-\boldsymbol{q}) = G_2^{(\mathrm{s})}(\boldsymbol{q},-\boldsymbol{q}) = 0$. This is due to the fact that the first moment of the density contrast vanishes by definition $\langle\tilde{\delta}\rangle = 0$ (see Eq. 2.87). Therefore, the ensemble average of each term in the perturbative expansion needs to vanish, i.e., $\langle\tilde{\delta}_1\rangle = \langle\tilde{\delta}_2\rangle = \langle\tilde{\delta}_3\rangle = \ldots = 0$. The second-order coupling function is given by

$$
\langle\tilde{\delta}_2(\boldsymbol{k})\rangle = \frac{1}{(2\pi)^3} \int \mathrm{d}^3 k_1\,\mathrm{d}^3 k_2\,\delta_{\mathrm{D}}(\boldsymbol{k}-\boldsymbol{k}_{12})F_2^{(\mathrm{s})}(\boldsymbol{k}_1,\boldsymbol{k}_2)\langle\tilde{\delta}_1(\boldsymbol{k}_1)\tilde{\delta}_1(\boldsymbol{k}_2)\rangle
$$
$$
= \int \mathrm{d}^3 k_1\,\delta_{\mathrm{D}}(\boldsymbol{k}-\boldsymbol{k}_{12})F_2^{(\mathrm{s})}(-\boldsymbol{k}_2,\boldsymbol{k}_2)P(k_1) = 0, \tag{2.77}
$$

where we used the definition of the power spectrum (given in Eq. 2.112 below) in the second step. The uneven higher-order terms, i.e., $\langle \tilde{\delta}_3 \rangle$, $\langle \tilde{\delta}_5 \rangle$, ..., vanish trivially because the average is over an uneven number of Gaussian fields following Wick's theorem for Gaussian fields (see Sect. 2.2.5 below). In addition, the second-order coupling functions are divergent when one of the arguments goes to zero, i.e., $F_2(\boldsymbol{k}, \boldsymbol{q} \to \boldsymbol{0}) \to \infty$ and $G_2(\boldsymbol{k}, \boldsymbol{q} \to \boldsymbol{0}) \to \infty$.

The third-order coupling function is given by

$$F_3(\boldsymbol{q}_1, \boldsymbol{q}_2, \boldsymbol{q}_3) = \frac{1}{18}\Big\{7\alpha(\boldsymbol{q}_1, \boldsymbol{q}_{23})F_2(\boldsymbol{q}_2, \boldsymbol{q}_3) + 2\beta(\boldsymbol{q}_1, \boldsymbol{q}_{23})G_2(\boldsymbol{q}_2, \boldsymbol{q}_3)$$
$$+ [7\alpha(\boldsymbol{q}_{12}, \boldsymbol{q}_3) + 2\beta(\boldsymbol{q}_{12}, \boldsymbol{q}_3)]G_2(\boldsymbol{q}_1, \boldsymbol{q}_2)\Big\}, \tag{2.78}$$

where $\boldsymbol{q}_{ij} \equiv \boldsymbol{q}_i + \boldsymbol{q}_j$. Employing Eq. (2.73), we find the symmetric function

$$F_3^{(s)}(\boldsymbol{q}_1, \boldsymbol{q}_2, \boldsymbol{q}_3) =$$
$$\frac{7}{54}[\alpha(\boldsymbol{q}_1, \boldsymbol{q}_{23})F_2^{(s)}(\boldsymbol{q}_2, \boldsymbol{q}_3) + \alpha(\boldsymbol{q}_2, \boldsymbol{q}_{13})F_2^{(s)}(\boldsymbol{q}_1, \boldsymbol{q}_3) + \alpha(\boldsymbol{q}_3, \boldsymbol{q}_{12})F_2^{(s)}(\boldsymbol{q}_1, \boldsymbol{q}_2)]$$
$$+ \frac{4}{54}[\beta(\boldsymbol{q}_1, \boldsymbol{q}_{23})G_2^{(s)}(\boldsymbol{q}_2, \boldsymbol{q}_3) + \beta(\boldsymbol{q}_2, \boldsymbol{q}_{13})G_2^{(s)}(\boldsymbol{q}_1, \boldsymbol{q}_3) + \beta(\boldsymbol{q}_3, \boldsymbol{q}_{12})G_2^{(s)}(\boldsymbol{q}_1, \boldsymbol{q}_2)]$$
$$+ \frac{7}{54}[\alpha(\boldsymbol{q}_{12}, \boldsymbol{q}_3)G_2^{(s)}(\boldsymbol{q}_1, \boldsymbol{q}_2) + \alpha(\boldsymbol{q}_{13}, \boldsymbol{q}_2)G_2^{(s)}(\boldsymbol{q}_1, \boldsymbol{q}_3) + \alpha(\boldsymbol{q}_{23}, \boldsymbol{q}_1)G_2^{(s)}(\boldsymbol{q}_2, \boldsymbol{q}_3)]. \tag{2.79}$$

From now on the symmetry superscript "(s)" will be omitted because we will only deal with symmetric coupling functions. Note that the coupling function F_3 is parity symmetric, i.e.,

$$F_3(-\boldsymbol{q}_1, -\boldsymbol{q}_2, -\boldsymbol{q}_3) = F_3(\boldsymbol{q}_1, \boldsymbol{q}_2, \boldsymbol{q}_3). \tag{2.80}$$

For the calculations of the covariance of the power spectrum, as presented in Chapter 7, one only needs the configuration

$$F_3(\boldsymbol{q}_1, -\boldsymbol{q}_1, \boldsymbol{q}_2) = \frac{7}{54}[\alpha(\boldsymbol{q}_1, \boldsymbol{q}_-)F_2(-\boldsymbol{q}_1, \boldsymbol{q}_2) + \alpha(-\boldsymbol{q}_1, \boldsymbol{q}_+)F_2(\boldsymbol{q}_1, \boldsymbol{q}_2)]$$
$$+ \frac{4}{54}[\beta(\boldsymbol{q}_1, \boldsymbol{q}_-)G_2(-\boldsymbol{q}_1, \boldsymbol{q}_2) + \beta(-\boldsymbol{q}_1, \boldsymbol{q}_+)G_2(\boldsymbol{q}_1, \boldsymbol{q}_2)]$$
$$+ \frac{7}{54}[\alpha(\boldsymbol{q}_-, \boldsymbol{q}_1)G_2(-\boldsymbol{q}_1, \boldsymbol{q}_2) + \alpha(\boldsymbol{q}_+, -\boldsymbol{q}_1)G_2(\boldsymbol{q}_1, \boldsymbol{q}_2)], \tag{2.81}$$

where we have defined the difference of the vectors as $\boldsymbol{q}_- \equiv \boldsymbol{q}_2 - \boldsymbol{q}_1$ and the sum of the vectors as $\boldsymbol{q}_+ \equiv \boldsymbol{q}_1 + \boldsymbol{q}_2$.

We already mentioned in the previous section that it is possible to find a solution for an arbitrary cosmology if one makes a small approximation. In the literature one can find closed solutions for the second- and third-order coupling functions. The second-order coupling function changes to

$$F_2(\boldsymbol{q}_1, \boldsymbol{q}_2) = \frac{1}{2}(1 + \epsilon) + \frac{1}{2}\frac{\boldsymbol{q}_1 \cdot \boldsymbol{q}_2}{q_1 q_2}\left(\frac{q_1}{q_2} + \frac{q_2}{q_1}\right) + \left(\frac{1}{2} - \frac{\epsilon}{2}\right)\frac{(\boldsymbol{q}_1 \cdot \boldsymbol{q}_2)^2}{q_1^2 q_2^2}, \tag{2.82}$$

where $\epsilon \approx (3/7)\Omega_{\mathrm{m}}^{-2/63}$ for $\Omega_{\mathrm{m}} \gtrsim 0.1$ (Bernardeau et al. 2002). For a fiducial choice of $\Omega_{\mathrm{m}} = 0.3$, we get $\Omega_{\mathrm{m}}^{-2/63} \approx 1.039$ and thus $\epsilon \approx 3/7$. Hence, within a few percent correction to the first and last terms, the second-order coupling function is independent of cosmological parameters. In addition, one can show that also the influence of cosmological parameters on the third-order coupling function is small (Bernardeau et al. 2002).

2.2 Correlation Functions

In the previous sections we showed how the density contrast evolves with the expansion of the Universe. However, to predict density fluctuations at a certain time we need to know the initial conditions set after the time of inflation. These primordial fluctuations subsequently grow through gravitational instability to build the current large-scale structure. However, we do not have direct observational access to primordial fluctuations. In addition, we are not able to observe the evolution of single astronomical objects (for example a cluster of galaxies) due the large time-scales involved. Rather we observe the part of the Universe accessible through our past light cone at different snapshots or redshifts. The best we can hope is to infer statistical information of characteristic variables of the Universe like the density distribution. In other words, we assume that our observable Universe is a stochastic realization of an underlying continuous random field. Thus, we have to propose an ensemble of different realization of a random field, where each realization characterizes a different hypothetical Universe. The probability distribution function of attaining a certain realization is the functional $P[\phi]$. We can then try to build theoretical models which match the observed statistical properties of the random field. A detailed discussion of random fields can be found in the book by Adler (1981).

This section shall introduce the notion of correlation functions as a description of the statistical properties of the density field of the Universe.

2.2.1 Cosmological Random Fields

A random field is a set of functions $\{\phi : \mathbb{R}^N \rightarrow \mathbb{R}\}$, where an element is called a *realization* of the random field. The infinitesimal joint probability that the field at n considered positions lies within the interval ϕ_1 and $\phi_1 + \mathrm{d}\phi_1$, ϕ_2 and $\phi_2 + \mathrm{d}\phi_2$ etc., is given by

$$\mathrm{d}P = P(\phi_1, \phi_2, \ldots, \phi_n)\,\mathrm{d}\phi_1\,\mathrm{d}\phi_2 \cdots \mathrm{d}\phi_n\,, \tag{2.83}$$

where $\phi_1 = \phi(\boldsymbol{x}_1)$ etc., and this defines the n-point probability distribution function $P(\phi_1, \phi_2, \ldots, \phi_n)$. The moments of this probability distribution function are defined by taking the average over the ensemble:

$$\langle \phi_1^{m_1} \phi_2^{m_2} \cdots \phi_r^{m_r} \rangle = \int \mathrm{d}\phi_1\,\mathrm{d}\phi_2\,\cdots\mathrm{d}\phi_n\,\phi_1^{m_1}\phi_2^{m_2}\cdots\phi_r^{m_r}P(\phi_1, \phi_2, \ldots, \phi_n)\,, \tag{2.84}$$

where $r \leq n$ and $\{m_1, m_2, \ldots, m_r\} \in \mathbb{N}$. However, in general only the limit $n \to \infty$ ensures that the distribution function becomes the functional $P[\phi]$, providing a complete statistical description of the random field.

In practice it is impossible to calculate moments with the presented formalism because we only observe one realization of the whole ensemble of random fields. Hence, we need to consider *ergodic fields*, where we can replace the ensemble average by a volume average over different parts of the sky. To still fulfill the condition of statistical independence, the fields need to be causally disconnected. Thus, the experimental strategy is to observe different well-separated patches in the sky.

2.2.2 Gaussian Random Fields

In this section we discuss an important subclass of random fields, namely Gaussian random fields. For such fields we can explicitly write the form of the n-point probability distribution function. Assuming a zero-mean random field ($\langle \phi_i \rangle = 0$) the probability distribution is given by a multivariate Gaussian:

$$P(\phi_1, \phi_2, \ldots, \phi_n) = \frac{1}{\sqrt{(2\pi)^n \det(\mathcal{C})}} \exp\left(-\frac{1}{2} \sum_{i,j=1}^{n} \phi_i \mathcal{C}_{ij}^{-1} \phi_j\right), \qquad (2.85)$$

where the covariance matrix of the random field is $\mathcal{C}_{ij} \equiv \langle \phi_i \phi_j \rangle$.

Gaussian random fields play a key role in cosmology. Inflationary models predict that the primordial density fluctuations are randomly distributed. Using the *central limit theorem*, the combination of a large number of random processes results in a Gaussian distribution. Thus, the distribution of density fluctuations after inflation can be described by a Gaussian. In addition, Gaussian random fields are completely specified by the two-point correlation function. Both properties show the importance of Gaussian random fields in cosmological applications. However, the process of structure formation will inevitably induce nonlinearities. For example the formation of a galaxy cluster cannot be described by a Gaussian random field.

2.2.3 Density Correlation Functions

We apply in this section the formalism of random fields to the density contrast

$$\delta(\boldsymbol{x}, t) = \frac{\rho(\boldsymbol{x}, t) - \bar{\rho}(t)}{\bar{\rho}(t)}. \qquad (2.86)$$

In other words, we consider δ as a realization of a random field. Note that for notational convenience we drop the explicit time-dependence of the density contrast in the following. The first moment or mean of the density contrast vanishes by definition:

$$\langle \delta(\boldsymbol{x}) \rangle = \left\langle \frac{\rho(\boldsymbol{x}) - \bar{\rho}}{\bar{\rho}} \right\rangle = \frac{\langle \rho(\boldsymbol{x}) \rangle}{\bar{\rho}} - 1 = 0. \qquad (2.87)$$

We already mentioned that we need the information of all n-point correlation functions to determine the complete statistical properties of a general random field. In particular, it is convenient to define the correlation functions as the *connected* or *irreducible* part of the joint ensemble average which we label in the following by the subscript "c":

$$
\begin{aligned}
\xi(\boldsymbol{x}_1, \ldots, \boldsymbol{x}_n) \equiv \langle \delta(\boldsymbol{x}_1) \cdots \delta(\boldsymbol{x}_n) \rangle_{\mathrm{c}} = {} & \langle \delta(\boldsymbol{x}_1) \cdots \delta(\boldsymbol{x}_n) \rangle \\
& - [\langle \delta(\boldsymbol{x}_1) \delta(\boldsymbol{x}_2) \rangle_{\mathrm{c}} \langle \delta(\boldsymbol{x}_3) \cdots \delta(\boldsymbol{x}_n) \rangle_{\mathrm{c}} + \mathrm{perm.}] \\
& - [\langle \delta(\boldsymbol{x}_1) \delta(\boldsymbol{x}_2) \delta(\boldsymbol{x}_3) \rangle_{\mathrm{c}} \langle \delta(\boldsymbol{x}_4) \cdots \delta(\boldsymbol{x}_n) \rangle_{\mathrm{c}} + \mathrm{perm.}] - \ldots,
\end{aligned} \tag{2.88}
$$

where we used the fact that the first moment of the density contrast vanishes, i.e., $\langle \delta(\boldsymbol{x}_i) \rangle = 0$. Hence, all contributions from lower-order moments are removed for the connected moments. As an example we show the decomposition of the four-point density correlator in Fourier space which is needed for the discussion of the covariance matrix of the power spectrum:

$$
\langle \tilde{\delta}_1 \tilde{\delta}_2 \tilde{\delta}_3 \tilde{\delta}_4 \rangle = \langle \tilde{\delta}_1 \tilde{\delta}_2 \tilde{\delta}_3 \tilde{\delta}_4 \rangle_{\mathrm{c}} + \langle \tilde{\delta}_1 \tilde{\delta}_2 \rangle \langle \tilde{\delta}_3 \tilde{\delta}_4 \rangle + \langle \tilde{\delta}_1 \tilde{\delta}_3 \rangle \langle \tilde{\delta}_2 \tilde{\delta}_4 \rangle + \langle \tilde{\delta}_1 \tilde{\delta}_4 \rangle \langle \tilde{\delta}_2 \tilde{\delta}_3 \rangle, \tag{2.89}
$$

where $\tilde{\delta}_i \equiv \tilde{\delta}(\boldsymbol{k}_i)$ with $i = 1 \ldots 4$. Here and throughout we will use $\langle \tilde{\delta} \tilde{\delta} \rangle = \langle \tilde{\delta} \tilde{\delta} \rangle_{\mathrm{c}}$, since the first moment of the density field vanishes.

The first four connected moments of the density contrast field are

$$
\langle \delta(\boldsymbol{x}) \rangle_{\mathrm{c}} = 0, \tag{2.90}
$$

$$
\langle \delta(\boldsymbol{x}_1) \delta(\boldsymbol{x}_2) \rangle_{\mathrm{c}} \equiv \xi(\boldsymbol{x}_1, \boldsymbol{x}_2), \tag{2.91}
$$

$$
\langle \delta(\boldsymbol{x}_1) \delta(\boldsymbol{x}_2) \delta(\boldsymbol{x}_3) \rangle_{\mathrm{c}} \equiv \zeta(\boldsymbol{x}_1, \boldsymbol{x}_2, \boldsymbol{x}_3), \tag{2.92}
$$

$$
\langle \delta(\boldsymbol{x}_1) \delta(\boldsymbol{x}_2) \delta(\boldsymbol{x}_3) \delta(\boldsymbol{x}_4) \rangle_{\mathrm{c}} \equiv \eta(\boldsymbol{x}_1, \boldsymbol{x}_2, \boldsymbol{x}_3, \boldsymbol{x}_4), \tag{2.93}
$$

which define the two-point correlation function ξ, the three-point correlation function ζ and the four-point correlation function η. For a homogeneous random field the two-point correlation function depends only on the separation vector of the two points, i.e., $\xi(\boldsymbol{x}_1, \boldsymbol{x}_2) = \xi(\boldsymbol{x}_1 - \boldsymbol{x}_2)$. Analogously, assuming homogeneity, the three-point correlation function only depends on two vectors that build the two sides of the triangle, e.g., $\zeta(\boldsymbol{x}_1, \boldsymbol{x}_2, \boldsymbol{x}_3) = \zeta(\boldsymbol{x}_{12}, \boldsymbol{x}_{13})$, where $\boldsymbol{x}_{12} = \boldsymbol{x}_1 - \boldsymbol{x}_2$ and $\boldsymbol{x}_{13} = \boldsymbol{x}_1 - \boldsymbol{x}_3$. The same is true for the homogeneous four-point correlation function $\eta(\boldsymbol{x}_1, \boldsymbol{x}_2, \boldsymbol{x}_3, \boldsymbol{x}_4) = \eta(\boldsymbol{x}_{12}, \boldsymbol{x}_{23}, \boldsymbol{x}_{34})$, where $\boldsymbol{x}_{12}$, $\boldsymbol{x}_{23}$ and $\boldsymbol{x}_{34}$ are three sides of the quadrangle. If we considering in addition isotropic random fields the spectra depend only on the length of the corresponding sides.

Alternative Definition of Correlation Functions

We present in this section an intuitive alternative definition of the correlation functions following Peebles (1980).

Suppose we divide the continuous density field $\rho(\boldsymbol{x})$ into a discrete number of infinitesimal small cells $\mathrm{d}V_i$ such that each cell contains either one or no particle. The probability that we find a particle in a single volume $\mathrm{d}V$ is then

$$
\mathrm{d}P = \bar{\rho} \mathrm{d}V. \tag{2.94}
$$

The joint probability to find a pair of particles separated by the distance $\boldsymbol{x}_{12} = \boldsymbol{x}_1 - \boldsymbol{x}_2$, where one particle is in the volume $\mathrm{d}V_1$ and the other particle in the volume $\mathrm{d}V_2$ simply is

$$\mathrm{d}P = \bar{\rho}^2 \left[1 + \xi(x_{12})\right] \mathrm{d}V_1 \, \mathrm{d}V_2 \,. \tag{2.95}$$

Due to the assumed homogeneity and isotropy the correlation function depends only on the modulus of the distance. Considering a uniform Poisson point process, the joint probability is just the product of the individual probabilities of finding a particle in each volume (see Eq. 2.94):

$$\mathrm{d}P = \bar{\rho}^2 \mathrm{d}V_1 \, \mathrm{d}V_2 \,. \tag{2.96}$$

We note that in this case the correlation function vanishes, i.e., $\xi = 0$. Using this result, we interpret ξ as the excess probability over a random probability.

The definition of the two-point correlation function in Eqs. (2.91) and (2.95) is very similar. Considering the continuous density function $\rho(\boldsymbol{x})$, the probability to find a particle is

$$\mathrm{d}P = \rho(\boldsymbol{x})\mathrm{d}V \,. \tag{2.97}$$

This is characteristic for a *Poisson process*, where the probability density is a function of the position. The joint probability to find particles in two volume elements is

$$\mathrm{d}P = \rho(\boldsymbol{x}_1)\rho(\boldsymbol{x}_2)\mathrm{d}V_1 \, \mathrm{d}V_2 \,. \tag{2.98}$$

Averaging over the ensemble using Eq. (2.91) yields again

$$\mathrm{d}P = \bar{\rho}^2 \left[1 + \xi(x_{12})\right] \mathrm{d}V_1 \, \mathrm{d}V_2 \,, \tag{2.99}$$

where now $\xi(x_{12}) = \langle \delta(\boldsymbol{x}_1)\delta(\boldsymbol{x}_2) \rangle$.

We can easily generalize the discrete definition of the correlation function in Eq. (2.95) to a larger number of points. Considering three points, we find

$$\mathrm{d}P = \bar{\rho}^3 \left[1 + \xi(x_{12}) + \xi(x_{13}) + \xi(x_{23}) + \zeta(\boldsymbol{x}_1, \boldsymbol{x}_2, \boldsymbol{x}_3)\right] \mathrm{d}V_1 \, \mathrm{d}V_2 \, \mathrm{d}V_3 \,. \tag{2.100}$$

Hence, we can interpret the reduced three-point correlation function ζ as the excess correlation over the probability of finding a triplet described by the two-point correlation function. Finally, the probability of finding a quartet of points in four different cells is given by

$$\begin{aligned}
\mathrm{d}P = \bar{\rho}^4 [& 1 + \xi_{12} + \xi_{13} + \xi_{14} + \xi_{23} + \xi_{24} + \xi_{34} + \xi_{12}\xi_{34} + \xi_{13}\xi_{24} + \xi_{14}\xi_{23} \\
& + \zeta_{123} + \zeta_{124} + \zeta_{134} + \zeta_{234} + \eta_{1234}]\mathrm{d}V_1 \, \mathrm{d}V_2 \, \mathrm{d}V_3 \, \mathrm{d}V_4 \,,
\end{aligned} \tag{2.101}$$

where we used the compact notation $\xi_{ij} \equiv \xi(\boldsymbol{x}_i, \boldsymbol{x}_j)$, $\zeta_{ijk} \equiv \zeta(\boldsymbol{x}_i, \boldsymbol{x}_j, \boldsymbol{x}_k)$ and $\eta_{ijkl} \equiv \eta(\boldsymbol{x}_i, \boldsymbol{x}_j, \boldsymbol{x}_k, \boldsymbol{x}_l)$. The four-point correlation function can be interpreted as the excess correlation over the probability of finding a quartet described by the two-point and three-point correlation functions.

2.2.4 Power Spectra

We showed in Sect. 2.1 that the perturbative solution to the fluid equations is most easily done in Fourier space because we can use several convenient mathematical properties of the Fourier transformation. More specifically, the perturbative solution of the n-th order density contrast in Eq. (2.70) is given in Fourier space. Hence, to employ the presented perturbative formalism, we have to transform the correlation functions into Fourier space as well. The Fourier space counterparts of the correlation functions contain the same statistical information on the random field as the correlation functions. In particular, the *power spectrum* is the Fourier space counterpart of the two-point correlation function, the *bispectrum* of the three-point correlation function and the *trispectrum* of the four-point correlation function.

Here we use the same convention of the Fourier transform of the density contrast as in Sect. 2.1, i.e.,

$$\delta(\boldsymbol{x}) = \int \frac{\mathrm{d}^3 k}{(2\pi)^3}\, \tilde{\delta}(\boldsymbol{k})\, \mathrm{e}^{-\mathrm{i}\boldsymbol{k}\cdot\boldsymbol{x}}\,, \qquad \tilde{\delta}(\boldsymbol{k}) = \int \mathrm{d}^3 x\, \delta(\boldsymbol{x})\, \mathrm{e}^{\mathrm{i}\boldsymbol{k}\cdot\boldsymbol{x}}\,. \tag{2.102}$$

The tilde symbol denoting the Fourier transform will be omitted from now on.

Transforming the two-point correlation function into Fourier space yields

$$\begin{aligned}
\langle \delta(\boldsymbol{k})\delta(\boldsymbol{k}')\rangle &= \int \mathrm{d}^3 x\, \mathrm{e}^{\mathrm{i}\boldsymbol{k}\cdot\boldsymbol{x}} \int \mathrm{d}^3 x'\, \mathrm{e}^{\mathrm{i}\boldsymbol{k}'\cdot\boldsymbol{x}'} \langle \delta(\boldsymbol{x})\delta(\boldsymbol{x}')\rangle \\
&= \int \mathrm{d}^3 x\, \mathrm{e}^{\mathrm{i}(\boldsymbol{k}+\boldsymbol{k}')\cdot\boldsymbol{x}} \int \mathrm{d}^3 y\, \mathrm{e}^{\mathrm{i}\boldsymbol{k}'\cdot\boldsymbol{y}} \langle \delta(\boldsymbol{x})\delta(\boldsymbol{x}')\rangle \\
&= (2\pi)^3 \delta_{\mathrm{D}}(\boldsymbol{k}+\boldsymbol{k}')P(k)\,,
\end{aligned} \tag{2.103}$$

where we employed the substitution $\boldsymbol{x}' = \boldsymbol{x} + \boldsymbol{y}$ in the second step. Furthermore, we defined the power spectrum in the last step as

$$P(k) \equiv \int \mathrm{d}^3 y\, \mathrm{e}^{-\mathrm{i}\boldsymbol{k}\cdot\boldsymbol{y}}\, \xi(|\boldsymbol{y}|)\,. \tag{2.104}$$

In particular, we note that the power spectrum $P(k)$ and the correlation function $\xi(y)$ are Fourier transformation pairs. Performing the back-transformation yields the correlation function in dependence of the power spectrum:

$$\xi(y) = \int \frac{\mathrm{d}^3 k}{(2\pi)^3}\, P(k)\, \mathrm{e}^{\mathrm{i}\boldsymbol{k}\cdot\boldsymbol{y}} = 4\pi \int \frac{\mathrm{d}k}{(2\pi)^3}\, k^2 P(k) \frac{\sin(ky)}{ky}\,. \tag{2.105}$$

The angular integration in the second step is trivial because the power spectrum depends only on the modulus of the wave-vector k.

It is convenient to construct a dimensionless form of the power spectrum. We define the *dimensionless* or *reduced* power spectrum via the dispersion of the dark matter field (i.e., the correlation function for $y = 0$):

$$\sigma^2(z) = \langle \delta^2(\boldsymbol{x}, z)\rangle = \int \frac{\mathrm{d}^3 k}{(2\pi)^3}\, P(k, z) = \int \frac{\mathrm{d}k}{k}\, \Delta(k, z)\,. \tag{2.106}$$

Hence, the dimensionless power spectrum $\Delta(k, z)$ is the contribution to the variance per logarithmic interval in k:

$$\Delta(k, z) = \frac{k^3}{2\pi^2} P(k, z) \,. \tag{2.107}$$

Transforming the three-point correlation function into Fourier space yields

$$
\begin{aligned}
\langle \delta(\boldsymbol{k}_1)\delta(\boldsymbol{k}_2)\delta(\boldsymbol{k}_3) \rangle_{\mathrm{c}} &= \int \mathrm{d}^3x_1 \int \mathrm{d}^3x_2 \int \mathrm{d}^3x_3 \; \mathrm{e}^{\mathrm{i}(\boldsymbol{k}_1\cdot\boldsymbol{x}_1 + \boldsymbol{k}_2\cdot\boldsymbol{x}_2 + \boldsymbol{k}_3\cdot\boldsymbol{x}_3)} \langle \delta(\boldsymbol{x}_1)\delta(\boldsymbol{x}_2)\delta(\boldsymbol{x}_3) \rangle_{\mathrm{c}} \\
&= \int \mathrm{d}^3x_1 \int \mathrm{d}^3x_2 \int \mathrm{d}^3x_3 \; \mathrm{e}^{\mathrm{i}(\boldsymbol{k}_1\cdot\boldsymbol{x}_1 + \boldsymbol{k}_2\cdot\boldsymbol{x}_2 + \boldsymbol{k}_3\cdot\boldsymbol{x}_3)} \, \zeta(\boldsymbol{x}_{12}, \boldsymbol{x}_{13}) \\
&= \int \mathrm{d}^3x_1 \; \mathrm{e}^{\mathrm{i}\boldsymbol{x}_1\cdot(\boldsymbol{k}_1 + \boldsymbol{k}_2 + \boldsymbol{k}_3)} \int \mathrm{d}^3y \int \mathrm{d}^3z \; \mathrm{e}^{-\mathrm{i}\boldsymbol{k}_2\cdot\boldsymbol{y}} \, \mathrm{e}^{-\mathrm{i}\boldsymbol{k}_3\cdot\boldsymbol{z}} \, \zeta(\boldsymbol{y}, \boldsymbol{z}) \\
&= (2\pi)^3 \delta_{\mathrm{D}}(\boldsymbol{k}_1 + \boldsymbol{k}_2 + \boldsymbol{k}_3) B(\boldsymbol{k}_1, \boldsymbol{k}_2, \boldsymbol{k}_3) \,, \tag{2.108}
\end{aligned}
$$

where we assumed spatial homogeneity in the second step to parametrize the three-point correlation function with only two vectors that build up the triangle. Then we employed a change of variables $\boldsymbol{x}_{12} = \boldsymbol{x}_1 - \boldsymbol{x}_2 \equiv \boldsymbol{y}$ and $\boldsymbol{x}_{13} = \boldsymbol{x}_1 - \boldsymbol{x}_3 \equiv \boldsymbol{z}$ in the third step. Finally, the last step defines the relation between the three-point correlation function and the bispectrum:

$$B(\boldsymbol{k}_1, \boldsymbol{k}_2, \boldsymbol{k}_3) \equiv \int \mathrm{d}^3y \int \mathrm{d}^3z \; \mathrm{e}^{-\mathrm{i}\boldsymbol{k}_2\cdot\boldsymbol{y}} \, \mathrm{e}^{-\mathrm{i}\boldsymbol{k}_3\cdot\boldsymbol{z}} \, \zeta(\boldsymbol{y}, \boldsymbol{z}) \,. \tag{2.109}$$

Again, we note that the three-point correlation function and the bispectrum are Fourier transformation pairs. Furthermore, the bispectrum gives only a non-zero contribution if the wave-vectors form a closed triangle in Fourier space which is a result of the assumed homogeneity of the random fields.

Analogously, the trispectrum is

$$
\begin{aligned}
\langle \delta(\boldsymbol{k}_1)\delta(\boldsymbol{k}_2)\delta(\boldsymbol{k}_3)\delta(\boldsymbol{k}_4) \rangle_{\mathrm{c}} &= (2\pi)^3 \delta_{\mathrm{D}}(\boldsymbol{k}_1 + \boldsymbol{k}_2 + \boldsymbol{k}_3 + \boldsymbol{k}_4) \\
&\quad \times \int \mathrm{d}^3x \int \mathrm{d}^3y \int \mathrm{d}^3z \; \mathrm{e}^{-\mathrm{i}\boldsymbol{k}_1\cdot\boldsymbol{x}} \, \mathrm{e}^{-\mathrm{i}\boldsymbol{k}_2\cdot\boldsymbol{y}} \, \mathrm{e}^{-\mathrm{i}\boldsymbol{k}_3\cdot\boldsymbol{z}} \, \eta(\boldsymbol{x}, \boldsymbol{y}, \boldsymbol{z}) \\
&= (2\pi)^3 \delta_{\mathrm{D}}(\boldsymbol{k}_1 + \boldsymbol{k}_2 + \boldsymbol{k}_3 + \boldsymbol{k}_4) T(\boldsymbol{k}_1, \boldsymbol{k}_2, \boldsymbol{k}_3, \boldsymbol{k}_4) \,. \tag{2.110}
\end{aligned}
$$

Again, we employed spatial homogeneity to express the four-point correlation function in terms of three sides of the quadrilateral denoted by $\boldsymbol{x}$, $\boldsymbol{y}$ and $\boldsymbol{z}$.

2.2.5 Wick Theorem of Gaussian Random Fields

As already mentioned, Gaussian random fields are completely specified by their two-point correlation function or power spectrum. Here we show the consequences for

higher-order moments of Gaussian random fields. The moments of a Gaussian random field decompose in the following way:

$$\langle \delta(\boldsymbol{k}_1)\delta(\boldsymbol{k}_2)\cdots\delta(\boldsymbol{k}_{2p})\rangle = \sum_P \langle \delta(\boldsymbol{k}_1)\delta(\boldsymbol{k}_2)\rangle\langle \delta(\boldsymbol{k}_3)\delta(\boldsymbol{k}_4)\rangle\cdots\langle \delta(\boldsymbol{k}_{2p-1})\delta(\boldsymbol{k}_{2p})\rangle\,,$$

$$\langle \delta(\boldsymbol{k}_1)\delta(\boldsymbol{k}_2)\cdots\delta(\boldsymbol{k}_{2p+1})\rangle = 0\,, \tag{2.111}$$

which is known as *Wick's theorem* (see Bernardeau et al. 2002). The sum in the first equation runs over all P distinct permutations of the $2p$ indices. In other words, n-point correlation functions of Gaussian random fields resolve into products of two-point correlation functions if n is even, whereas n-point correlation functions are identical to zero if n is odd.

The Wick theorem clearly shows that for Gaussian fields the knowledge of the two-point correlation function or equivalently the power spectrum is sufficient to describe all statistical properties of the density field δ. However, non-Gaussian fields need to be described by the full hierarchy of connected moments. Applying the Wick theorem to Eq. (2.88), we find that all connected n-point functions for $n > 2$ are equal to zero for Gaussian fields. Hence, the connected moments intrinsically provide only the nonlinear statistical information of the random field.

2.2.6 Perturbative Results for the Spectra

We present here the expressions for the power spectrum, bispectrum and trispectrum using the perturbative approach as developed in Sect. 2.1. In particular, we give the results only in the lowest non-vanishing order of the perturbative expansion. When we derive the relations for the spectra we omit the dependence on the scale factor a.

Power Spectrum

The power spectrum of dark matter is defined as

$$\langle \delta(\boldsymbol{k}_1)\delta(\boldsymbol{k}_2)\rangle_{\mathrm{c}} = (2\pi)^3\delta_{\mathrm{D}}(\boldsymbol{k}_1 + \boldsymbol{k}_2)P(k_1)\,. \tag{2.112}$$

In linear perturbation theory we find for the power spectrum

$$P_{\mathrm{pt}}(k,a) = [D(a)]^2 P_{\mathrm{pt}}(k)\,, \tag{2.113}$$

where $P_{\mathrm{pt}}(k)$ is the power spectrum we observe today which is multiplied with the square of the growth factor to obtain the power spectrum at scale factor a.

The next non-vanishing order of perturbation theory is the *one-loop* power spectrum[4]. Writing the perturbative expansion following Eq. (2.69) for the power spectrum yields

$$\begin{aligned}
P(k) &= \langle(\delta_1 + \delta_2 + \delta_3 + \ldots)(\delta_1' + \delta_2' + \delta_3' + \ldots)\rangle \\
&= \langle\delta_1\delta_1'\rangle + \langle\delta_1\delta_2'\rangle + \langle\delta_2\delta_1'\rangle + \langle\delta_2\delta_2'\rangle + \langle\delta_1\delta_3'\rangle + \langle\delta_3\delta_1'\rangle + \mathcal{O}(\delta_1^6)
\end{aligned} \tag{2.114}$$

---

[4]In graph theory a one-loop term corresponds to a connected diagram with only one cycle, e.g., in Feynman diagrams.

with $\delta_i \equiv \delta(\boldsymbol{k}_i)$ and $\delta_i' \equiv \delta(\boldsymbol{k}_i')$. The second and third terms on the right-hand side are composed of an uneven number of Gaussian density fields and are thus equal to zero due to Wick's theorem (2.111). Therefore, we define the one-loop power spectrum as[5]

$$P_{\text{1-loop}}(k) = P_{13}(k) + P_{22}(k) \equiv 2\langle \delta_1 \delta_3 \rangle + \langle \delta_2 \delta_2 \rangle \,, \tag{2.115}$$

with the two contributions

$$P_{13}(k) = 6 P_{\text{pt}}(k) \int \frac{\mathrm{d}^3 q}{(2\pi)^3} \, P_{\text{pt}}(q) F_3(\boldsymbol{k}, \boldsymbol{q}, -\boldsymbol{q}) \,, \tag{2.116}$$

$$P_{22}(k) = 2 \int \frac{\mathrm{d}^3 q}{(2\pi)^3} \, P_{\text{pt}}(q) P_{\text{pt}}(|\boldsymbol{k} - \boldsymbol{q}|) [F_2(\boldsymbol{q}, \boldsymbol{k} - \boldsymbol{q})]^2 \,. \tag{2.117}$$

Introducing spherical coordinates we can write the integral in Eq. (2.116) as

$$P_{13}(k) = 12\pi P_{\text{pt}}(k) \int_0^\infty \frac{\mathrm{d}q}{(2\pi)^3} \, q^2 P_{\text{pt}}(q) \int_{-1}^1 \mathrm{d}\cos\theta \, F_3(\boldsymbol{k}, \boldsymbol{q}, -\boldsymbol{q}) \,, \tag{2.118}$$

where θ is the angle between the two vectors $\boldsymbol{k}$ and $\boldsymbol{q}$. In this case we can analytically perform the angular integration over the third-order coupling function given in Eq. (2.80):

$$\int_{-1}^1 \mathrm{d}\cos\theta \, F_3(\boldsymbol{k}, \boldsymbol{q}, -\boldsymbol{q}) = \frac{1}{6} \frac{1}{252} \left(\frac{k}{q}\right)^2 \left[100 \left(\frac{q}{k}\right)^2 - 158 + 12 \left(\frac{k}{q}\right)^2 - 42 \left(\frac{q}{k}\right)^4 \right.$$
$$\left. + \frac{3}{q^3 k^5} (q^2 - k^2)^3 (7q^2 + 2k^2) \ln\left(\frac{q+k}{|q-k|}\right) \right] \,, \tag{2.119}$$

and we reproduce the result of Jain & Bertschinger (1994)[6] and Jeong & Komatsu (2006).

Bispectrum

The dark matter bispectrum is defined as

$$\langle \delta(\boldsymbol{k}_1) \delta(\boldsymbol{k}_2) \delta(\boldsymbol{k}_3) \rangle_{\text{c}} = (2\pi)^3 \delta_{\text{D}}(\boldsymbol{k}_1 + \boldsymbol{k}_2 + \boldsymbol{k}_3) B(\boldsymbol{k}_1, \boldsymbol{k}_2, \boldsymbol{k}_3) \,. \tag{2.120}$$

Since the bispectrum vanishes for Gaussian random fields, it is the first intrinsically nonlinear moment.

Inserting the perturbative expansion (2.69) for each term results generally in an infinitely large sequence of correlators. The lowest non-vanishing order is the so-called *tree-level* contribution to the bispectrum. The name indicates that in a diagrammatic

---

[5]Note that the Dirac delta function in the definition of the two-point correlator (2.112) ensures that both wave-vectors are equal.

[6]However, in this work there is a missing factor k^2.

representation the graph has a tree-like structure (see Fig. 2.1). The next non-vanishing order is called *one-loop* contribution etc. We find for the tree-level correlator

$$\langle\delta(\boldsymbol{k}_1)\delta(\boldsymbol{k}_2)\delta(\boldsymbol{k}_3)\rangle_{\text{tree}} = \langle\delta_2(\boldsymbol{k}_1)\delta_1(\boldsymbol{k}_2)\delta_1(\boldsymbol{k}_3)\rangle + \langle\delta_1(\boldsymbol{k}_1)\delta_2(\boldsymbol{k}_2)\delta_1(\boldsymbol{k}_3)\rangle$$
$$+ \langle\delta_1(\boldsymbol{k}_1)\delta_1(\boldsymbol{k}_2)\delta_2(\boldsymbol{k}_3)\rangle. \tag{2.121}$$

Replacing the second-order density contrast with Eq. (2.70) results in

$$\langle\delta_2(\boldsymbol{k}_1)\delta_1(\boldsymbol{k}_2)\delta_1(\boldsymbol{k}_3)\rangle = \int \frac{\mathrm{d}^3 q_1}{(2\pi)^3} \int \mathrm{d}^3 q_2\, \delta_{\mathrm{D}}(\boldsymbol{k}_1 - \boldsymbol{q}_1 - \boldsymbol{q}_2) F_2(\boldsymbol{q}_1, \boldsymbol{q}_2)$$
$$\times \langle\delta_1(\boldsymbol{q}_1)\delta_1(\boldsymbol{q}_2)\delta_1(\boldsymbol{k}_2)\delta_1(\boldsymbol{k}_3)\rangle$$
$$= (2\pi)^3 \delta_{\mathrm{D}}(\boldsymbol{k}_1 + \boldsymbol{k}_2 + \boldsymbol{k}_3)[2F_2(\boldsymbol{k}_2, \boldsymbol{k}_3)P_{\mathrm{pt}}(k_2)P_{\mathrm{pt}}(k_3)], \tag{2.122}$$

where we applied Wick's theorem (2.111) to express the four-point correlator of Gaussian fields in terms of products of power spectra, and performed the two integrations over the Dirac delta functions. More specifically, the four-point correlator resolves into three two-point correlators, where one term is zero because of the identity $F_2(\boldsymbol{q}, -\boldsymbol{q}) = 0$. The other two terms are identical yielding the factor of 2 because we use the second-order coupling function given in Eq. (2.75) which is symmetric in its arguments. The results for the other two terms of the tree-level bispectrum are simply obtained by permutations of the arguments. Finally, the tree-level bispectrum is given by

$$B_{\mathrm{pt}}(\boldsymbol{k}_1, \boldsymbol{k}_2, \boldsymbol{k}_3) = 2F_2(\boldsymbol{k}_1, \boldsymbol{k}_2)P_1 P_2 + 2F_2(\boldsymbol{k}_1, \boldsymbol{k}_3)P_1 P_3 + 2F_2(\boldsymbol{k}_2, \boldsymbol{k}_3)P_2 P_3, \tag{2.123}$$

where $P_i \equiv P_{\mathrm{pt}}(k_i)$. We label from now on the first non-vanishing order of the bispectrum with the subscript "pt". We note that the general bispectrum obeys parity invariance (e.g., Smith et al. 2006)

$$B(\boldsymbol{k}_1, \boldsymbol{k}_2, \boldsymbol{k}_3) = B(-\boldsymbol{k}_1, -\boldsymbol{k}_2, -\boldsymbol{k}_3) \tag{2.124}$$

and we easily verify that also the tree-level bispectrum in Eq. (2.123) is parity symmetric.

Trispectrum

The dark matter trispectrum is defined as the connected four-point function in Fourier space:

$$\langle\delta(\boldsymbol{k}_1)\delta(\boldsymbol{k}_2)\delta(\boldsymbol{k}_3)\delta(\boldsymbol{k}_4)\rangle_{\mathrm{c}} = (2\pi)^3 \delta_{\mathrm{D}}(\boldsymbol{k}_{1234})T(\boldsymbol{k}_1, \boldsymbol{k}_2, \boldsymbol{k}_3, \boldsymbol{k}_4), \tag{2.125}$$

where $\boldsymbol{k}_{1234} \equiv \boldsymbol{k}_1 + \boldsymbol{k}_2 + \boldsymbol{k}_3 + \boldsymbol{k}_4$. We find that there are two different non-vanishing contributions to the tree level:

$$\langle\delta(\boldsymbol{k}_1)\delta(\boldsymbol{k}_2)\delta(\boldsymbol{k}_3)\delta(\boldsymbol{k}_4)\rangle_{\text{tree}} = \langle\delta_2(\boldsymbol{k}_1)\delta_2(\boldsymbol{k}_2)\delta_1(\boldsymbol{k}_3)\delta_1(\boldsymbol{k}_4)\rangle + \dots (6\text{ terms})$$
$$+ \langle\delta_3(\boldsymbol{k}_1)\delta_1(\boldsymbol{k}_2)\delta_1(\boldsymbol{k}_3)\delta_1(\boldsymbol{k}_4)\rangle + \dots (4\text{ terms}). \tag{2.126}$$

In total we find 6 terms of the first type and 4 terms for the second type. We wrote only the first term of each type and the remaining terms are simply obtained by permutations

of the arguments. All other contributions either vanish or are composed of higher-order terms in δ_1. Note that for the second type of terms we need the results from perturbation theory up to the third order.

The calculation of each term is a tedious but straightforward calculation. We use in this section the notation $P_i \equiv P_{\mathrm{pt}}(k_i)$, $P_{ij} \equiv P_{\mathrm{pt}}(|\boldsymbol{k}_i + \boldsymbol{k}_j|)$, $\boldsymbol{k}_{ij} \equiv \boldsymbol{k}_i + \boldsymbol{k}_j$ and $\boldsymbol{q}_{ij} \equiv \boldsymbol{q}_i + \boldsymbol{q}_j$. We obtain for the first term of the expansion

$$
\begin{aligned}
\langle \delta_2(\boldsymbol{k}_1)\delta_2(\boldsymbol{k}_2)\delta_1(\boldsymbol{k}_3)\delta_1(\boldsymbol{k}_4)\rangle &= \frac{1}{(2\pi)^6} \int \left[\prod_{i=1}^{4} \mathrm{d}^3 q_i\right] \delta_{\mathrm{D}}(\boldsymbol{k}_1 - \boldsymbol{q}_{12})\delta_{\mathrm{D}}(\boldsymbol{k}_2 - \boldsymbol{q}_{34})F_2(\boldsymbol{q}_1, \boldsymbol{q}_2) \\
&\quad \times F_2(\boldsymbol{q}_3, \boldsymbol{q}_4)\langle \delta_1(\boldsymbol{q}_1)\delta_1(\boldsymbol{q}_2)\delta_1(\boldsymbol{q}_3)\delta_1(\boldsymbol{q}_4)\delta_1(\boldsymbol{k}_3)\delta_1(\boldsymbol{k}_4)\rangle \\
&= (2\pi)^3 \delta_{\mathrm{D}}(\boldsymbol{k}_{1234})\{4P_3 P_4 [P_{13} F_2(\boldsymbol{k}_3, -\boldsymbol{k}_{13})F_2(\boldsymbol{k}_4, -\boldsymbol{k}_{24}) \\
&\quad + P_{14} F_2(\boldsymbol{k}_3, -\boldsymbol{k}_{23})F_2(\boldsymbol{k}_4, -\boldsymbol{k}_{14})]\}\,, \quad\quad (2.127)
\end{aligned}
$$

where the six-point correlator resolves into 15 terms consisting of power spectra products. Performing the integrations over the arising delta functions yields in the end 8 non-vanishing terms. Similarly, we find for the second type of terms

$$
\begin{aligned}
\langle \delta_3(\boldsymbol{k}_1)\delta_1(\boldsymbol{k}_2)\delta_1(\boldsymbol{k}_3)\delta_1(\boldsymbol{k}_4)\rangle &= \frac{1}{(2\pi)^6} \int \mathrm{d}^3 q_1\, \mathrm{d}^3 q_2\, \mathrm{d}^3 q_3\, \delta_{\mathrm{D}}(\boldsymbol{k}_1 - \boldsymbol{q}_{123})F_3(\boldsymbol{q}_1, \boldsymbol{q}_2, \boldsymbol{q}_3) \\
&\quad \times \langle \delta_1(\boldsymbol{q}_1)\delta_1(\boldsymbol{q}_2)\delta_1(\boldsymbol{q}_3)\delta_1(\boldsymbol{k}_2)\delta_1(\boldsymbol{k}_3)\delta_1(\boldsymbol{k}_4)\rangle \\
&= (2\pi)^3 \delta_{\mathrm{D}}(\boldsymbol{k}_{1234})\{6F_3(\boldsymbol{k}_2, \boldsymbol{k}_3, \boldsymbol{k}_4)P_2 P_3 P_4\}\,. \quad\quad (2.128)
\end{aligned}
$$

The other terms are easily obtained by permutations, however, we present here the complete result to avoid confusion with a short-hand notation. Combing the results of all terms from both types of correlations (Eqs. 2.127 and 2.128) yields the dark matter trispectrum in first non-vanishing order which is given by (Fry 1984):

$$
T_{\mathrm{pt}} = 4T_a + 6T_b\,, \quad\quad (2.129)
$$

where

$$
\begin{aligned}
T_a &= P_1 P_2 \left[P_{13} F_2(\boldsymbol{k}_1, -\boldsymbol{k}_{13})F_2(\boldsymbol{k}_2, \boldsymbol{k}_{13}) + P_{14} F_2(\boldsymbol{k}_1, -\boldsymbol{k}_{14})F_2(\boldsymbol{k}_2, \boldsymbol{k}_{14})\right] \\
&\quad + P_1 P_3 \left[P_{12} F_2(\boldsymbol{k}_1, -\boldsymbol{k}_{12})F_2(\boldsymbol{k}_3, \boldsymbol{k}_{12}) + P_{14} F_2(\boldsymbol{k}_1, -\boldsymbol{k}_{14})F_2(\boldsymbol{k}_3, \boldsymbol{k}_{14})\right] \\
&\quad + P_1 P_4 \left[P_{12} F_2(\boldsymbol{k}_1, -\boldsymbol{k}_{12})F_2(\boldsymbol{k}_4, \boldsymbol{k}_{12}) + P_{13} F_2(\boldsymbol{k}_1, -\boldsymbol{k}_{13})F_2(\boldsymbol{k}_4, \boldsymbol{k}_{13})\right] \\
&\quad + P_2 P_3 \left[P_{21} F_2(\boldsymbol{k}_2, -\boldsymbol{k}_{21})F_2(\boldsymbol{k}_3, \boldsymbol{k}_{21}) + P_{24} F_2(\boldsymbol{k}_2, -\boldsymbol{k}_{24})F_2(\boldsymbol{k}_3, \boldsymbol{k}_{24})\right] \\
&\quad + P_2 P_4 \left[P_{21} F_2(\boldsymbol{k}_2, -\boldsymbol{k}_{21})F_2(\boldsymbol{k}_4, \boldsymbol{k}_{21}) + P_{23} F_2(\boldsymbol{k}_2, -\boldsymbol{k}_{23})F_2(\boldsymbol{k}_4, \boldsymbol{k}_{23})\right] \\
&\quad + P_3 P_4 \left[P_{31} F_2(\boldsymbol{k}_3, -\boldsymbol{k}_{31})F_2(\boldsymbol{k}_4, \boldsymbol{k}_{31}) + P_{32} F_2(\boldsymbol{k}_3, -\boldsymbol{k}_{32})F_2(\boldsymbol{k}_4, \boldsymbol{k}_{32})\right]\,, \quad (2.130)
\end{aligned}
$$

and

$$
\begin{aligned}
T_b &= F_3(\boldsymbol{k}_1, \boldsymbol{k}_2, \boldsymbol{k}_3)P_1 P_2 P_3 + F_3(\boldsymbol{k}_2, \boldsymbol{k}_3, \boldsymbol{k}_4)P_2 P_3 P_4 \\
&\quad + F_3(\boldsymbol{k}_3, \boldsymbol{k}_4, \boldsymbol{k}_1)P_3 P_4 P_1 + F_3(\boldsymbol{k}_4, \boldsymbol{k}_1, \boldsymbol{k}_2)P_4 P_1 P_2\,. \quad\quad (2.131)
\end{aligned}
$$

For the covariance matrix of the power spectrum, as we will discuss in detail in Chapter 7, one only needs the parallelogram configuration of the trispectrum, which imposes the conditions $\boldsymbol{k}_2 = -\boldsymbol{k}_1$ and $\boldsymbol{k}_4 = -\boldsymbol{k}_3$ on the wave-vectors. At first glance, it seems that the terms proportional to $F_2(\boldsymbol{k}_i, \pm\boldsymbol{k}_{12})$ in Eq. (2.130) are divergent for the parallelogram configuration because $\boldsymbol{k}_{12} \to \boldsymbol{0}$. Fortunately, the divergences of the first four terms cancel in this limit as shown in Appendix B.3. In this case the trispectrum given by Eqs. (2.129), (2.130) and (2.131) simplifies to

$$
\begin{aligned}
T_{\mathrm{pt|pc}} = {}& 4P_1^2 \left\{ [F_2(\boldsymbol{k}_1, -\boldsymbol{k}_+)]^2 P_+ + [F_2(\boldsymbol{k}_1, \boldsymbol{k}_-)]^2 P_- \right\} \\
& + 4P_3^2 \left\{ [F_2(\boldsymbol{k}_3, -\boldsymbol{k}_+)]^2 P_+ + [F_2(\boldsymbol{k}_3, -\boldsymbol{k}_-)]^2 P_- \right\} \\
& + 8P_1 P_3 [F_2(\boldsymbol{k}_1, -\boldsymbol{k}_+) F_2(\boldsymbol{k}_3, -\boldsymbol{k}_+) P_+ + F_2(\boldsymbol{k}_1, \boldsymbol{k}_-) F_2(\boldsymbol{k}_3, -\boldsymbol{k}_-) P_-] \\
& + 12[P_1^2 P_3 F_3(\boldsymbol{k}_1, -\boldsymbol{k}_1, \boldsymbol{k}_3) + P_1 P_3^2 F_3(\boldsymbol{k}_1, \boldsymbol{k}_3, -\boldsymbol{k}_3)] \,,
\end{aligned}
\tag{2.132}
$$

where we used the compact notation $T_{\mathrm{pt|pc}} \equiv T_{\mathrm{pt}}(\boldsymbol{k}_1, -\boldsymbol{k}_1, \boldsymbol{k}_3, -\boldsymbol{k}_3)$, $\boldsymbol{k}_- \equiv \boldsymbol{k}_3 - \boldsymbol{k}_1$, $\boldsymbol{k}_+ \equiv \boldsymbol{k}_1 + \boldsymbol{k}_3$, $P_- \equiv P_{\mathrm{pt}}(|\boldsymbol{k}_-|)$ and $P_+ \equiv P_{\mathrm{pt}}(|\boldsymbol{k}_+|)$.

General Correlation Function

The calculation of higher-order spectra than the trispectrum is a very tedious algebraic exercise. An alleviation to this repetitive calculation is to use a diagrammatic approach as presented in Scoccimarro & Frieman (1996). This method is already well developed in classical field theory (e.g., Feynman diagrams) and allows to easily read off the result for each perturbative term. In addition, topologically equivalent diagrams need to be calculated only once. We show the diagrams of the tree-level terms of the power spectrum, bispectrum and trispectrum in Fig. 2.1. Each diagram contains n vertices and $n-1$ lines connecting them. Each link carries a power spectrum of the particular wave-number. We can infer from the figure that the scaling of the n-point tree-level correlation function T_n is

$$
T_n \propto (P_{\mathrm{pt}})^{n-1} \,,
\tag{2.133}
$$

which is a consequence of Wick's theorem.

2.3 Fitting Functions

We present in this section the fitting functions of the nonlinear power spectrum and bispectrum.

2.3.1 Nonlinear Power Spectrum

We showed that theoretical models of the power spectrum break down at nonlinear scales. Hence, we need to rely on results obtained from N-body simulations or analytical models like the halo model. Using the results from many simulations, one can develop fitting functions that are dependent on the adopted cosmological model. Here we
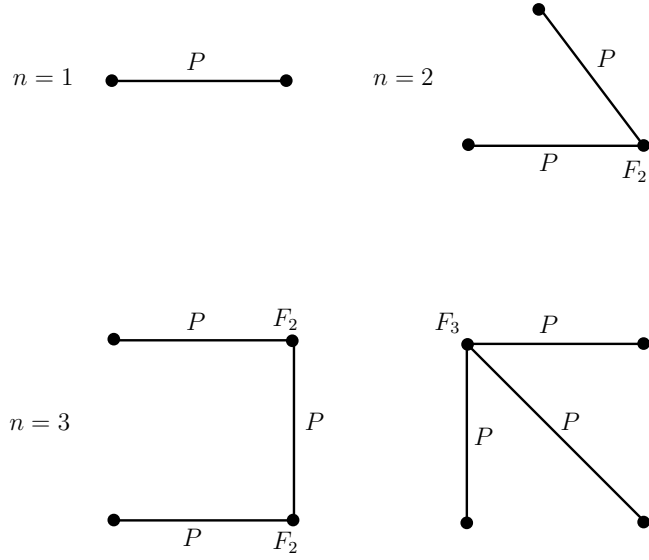
Figure 2.1: Graphical representation of the tree-level power spectrum, bispectrum and trispectrum. The trispectrum consists of two topologically different contributions, the so-called snake and star terms. The bullets correspond to different positions $\boldsymbol{k}_1$, $\boldsymbol{k}_2$, ... Each vertex with n outgoing lines gets a factor of F_n, and each link carries a power spectrum of the particular wave-number. Furthermore, at each vertex momentum conservation is imposed, i.e., $\boldsymbol{k}_1 + \ldots + \boldsymbol{k}_n = 0$. A comprehensive treatment of the diagrammatical representation in the context of cosmological perturbation theory is given in Scoccimarro & Frieman (1996).

describe the widely used fitting function from Peacock & Dodds (1996). There is an improved fitting function by Smith et al. (2003) based on the dark matter halo model.

The main idea is that the nonlinear power spectrum is connected to the linear one through the transformation

$$\Delta_{\mathrm{nl}}(k_{\mathrm{nl}}) = f_{\mathrm{nl}}[\Delta_{\mathrm{nl}}(k_{\mathrm{l}})]\,, \qquad k_{\mathrm{nl}} = k_{\mathrm{l}}[1 + \Delta_{\mathrm{nl}}(k_{\mathrm{nl}})]^{1/3}\,, \tag{2.134}$$

where "nl" refers to nonlinear and "l" to linear scales, respectively, and $\Delta(k)$ is the reduced power spectrum as defined in Eq. (2.107). The function f_{nl} has the form

$$f_{\mathrm{nl}}(x) = x \left[\frac{1 + B\beta x + (Ax)^{\alpha\beta}}{1 + ([Ax]^\alpha g^3(\Omega)/[V\sqrt{x}])^\beta} \right]^{1/\beta}\,, \tag{2.135}$$

where the parameters are fitted to simulations. The growth function $g(\Omega)$ is described by the fitting function from Carroll et al. (1992) given in Eq. (2.49). The resulting parameters are

$$A = 0.482(1 + n_{\mathrm{eff}}/3)^{-0.947}\,, \qquad B = 0.226(1 + n_{\mathrm{eff}}/3)^{-1.778}\,,$$
$$\alpha = 3.310(1 + n_{\mathrm{eff}}/3)^{-0.244}\,, \qquad \beta = 0.862(1 + n_{\mathrm{eff}}/3)^{-0.287}\,,$$
$$V = 11.55(1 + n_{\mathrm{eff}}/3)^{-0.423}\,,$$

where the effective spectral index of the power spectrum is taken at $n_{\text{eff}} = n_{\text{eff}}(k' = k/2)$. The fit function in Eq. (2.135) has the asymptotic behavior

$$f_{\text{nl}}(x) = \begin{cases} x & \text{for } x \ll 1\,, \\ x^{3/2} & \text{for } x \gg 1\,. \end{cases} \tag{2.136}$$

This scaling ensures that for large scales the fitting function resembles the result from perturbation theory, i.e., the linear power spectrum, and on small scales we recover the result of stable clustering. The *stable clustering hypothesis* states that on very small scales where the clustering process reaches virial equilibrium the mean velocity between particle pairs exactly cancel the Hubble expansion.

2.3.2 Nonlinear Bispectrum

For the fitting function of the nonlinear bispectrum it is convenient to define the reduced bispectrum, which shows a reduced scale dependence compared to the bispectrum itself:

$$Q(\boldsymbol{k}_1, \boldsymbol{k}_2, \boldsymbol{k}_3) = \frac{B(\boldsymbol{k}_1, \boldsymbol{k}_2, \boldsymbol{k}_3)}{P_1 P_2 + P_1 P_3 + P_2 P_3}\,, \tag{2.137}$$

where $P_i \equiv P(k_i)$. Recalling that the bispectrum is only non-zero for closed triangles in Fourier space, we can parametrize the bispectrum by the length of two sides of the triangle and the angle θ between them. First we want to discuss the configuration dependence of the reduced bispectrum in tree-level perturbation theory which depends mostly on the second-order coupling function given in Eq. (2.75). The coupling function is composed of three different terms and we give in the following an interpretation of each term. The first term gives an isotropic contribution that is independent of the configuration of the bispectrum. The middle term arises from the gradient of the density field in the direction of the flow $(\boldsymbol{u} \cdot \nabla \delta)$ as given on the right-hand side of the continuity equation (2.37). The last term arises from the gradient of the velocity divergence in direction of the flow $(\nabla \cdot (\boldsymbol{u} \cdot \nabla)\boldsymbol{u})$ in the modified Euler equation (2.38). Hence, we conclude that the configuration dependence of the bispectrum reflects the anisotropy of structures and flows generated by gravitational instability. We show in the left panel of Fig. 2.2 the reduced tree-level bispectrum as a function of the angle θ for a fixed ratio of the two wave-vectors such that $k_1 = k_2/2$. We choose four different values of k_2 as indicated in the figure that cover the small-scale and large-scale behavior of the reduced bispectrum. All curves show a similar behavior, i.e., a minimum at $\theta \approx 0.6\pi$ and the curves are maximal for collinear configuration $(\theta = 0, \pi)$. The enhancement of correlations for collinear configurations reflects the fact that density and velocity divergence gradients generated by gravitational instability are preferentially oriented parallel to the flow. This particular feature can be seen in the large-scale distribution of galaxies (see Fig. 1.2) and in the distribution of cold dark matter as obtained in simulations which builds a filamentary structure.

Numerical simulations indicate that on small scales the bispectrum is nearly independent of θ and approaches a constant value (Scoccimarro et al. 1998). This constant is approximately equal to the collinear configuration on large scales. Using these results Scoccimarro & Frieman (1999) developed a semi-analytic ansatz that they called *hyper-extended perturbation theory* (HEPT) for the strongly nonlinear regime of the bispectrum. They conjectured that in the strongly nonlinear regime or hierarchical limit ($|\delta| \gg 1$) the reduced bispectrum Q is equal to the collinear configuration Q in tree-level perturbation theory. To calculate the reduced bispectrum in HEPT we choose
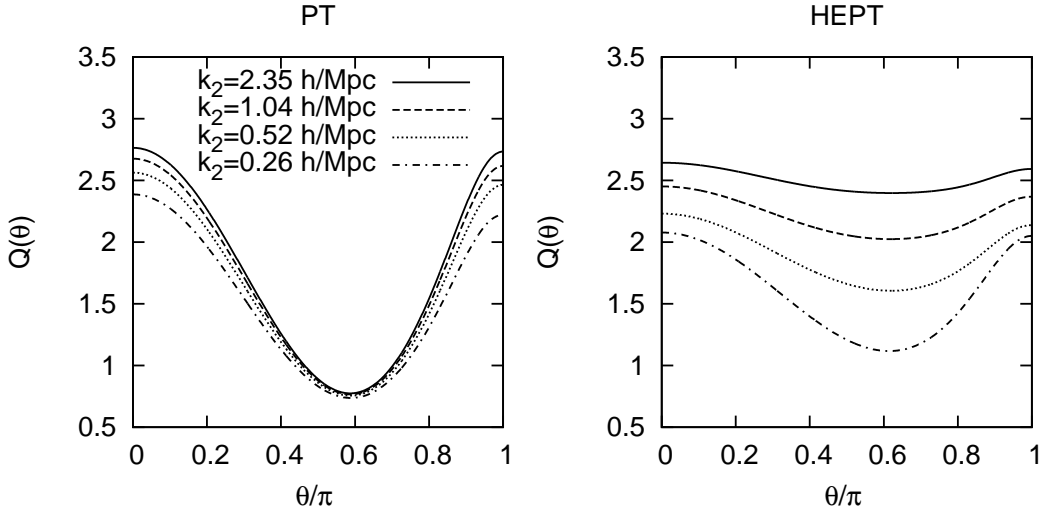

Figure 2.2: Reduced bispectrum in dependence of the angle θ between the two wave-vectors $\boldsymbol{k}_1$ and $\boldsymbol{k}_2$. We show the predictions for four different values of k_2 as indicated in the figure and choose k_1 according to $k_1 = k_2/2$. The left panel shows the predictions from tree-level perturbation theory and the right panel shows the result of the HEPT fitting formula.

$\boldsymbol{k}_1 = \boldsymbol{k}_2 \equiv \boldsymbol{q}$ and $\boldsymbol{k}_3 = -2\boldsymbol{q}$ since in tree-level perturbation theory the collinear value of Q depends only very weakly on the ratio $r_{12} = k_1/k_2$. Then we find for the reduced bispectrum in tree-level perturbation theory

$$Q_{\mathrm{pt}}(q) = \frac{B_{\mathrm{pt}}(\boldsymbol{q}, \boldsymbol{q}, -2\boldsymbol{q})}{[P_{\mathrm{pt}}(q)]^2 + 2P_{\mathrm{pt}}(q)P_{\mathrm{pt}}(2q)} \, . \tag{2.138}$$

Using a scale-free power spectrum ansatz $P_{\mathrm{pt}}(k) \propto k^n$, where n denotes the spectral index, we find

$$Q(n) = \frac{4 - 2^n}{1 + 2^{n+1}} \, . \tag{2.139}$$

Analogous to the nonlinear power spectrum, one can now interpolate between the perturbative (weakly nonlinear regime) and the hierarchical regime (strongly nonlinear regime). To get the behavior of the bispectrum for intermediate scales, one uses N-body

simulations. For a ΛCDM cosmology Scoccimarro & Couchman (2001) calculated a fitting formula that can be used for all scales and fits the results of N-body simulations to an accuracy of 15 per cent. The fitting function replaces the second-order coupling function defined in Eq. (2.75) which is used in the definition of the linear bispectrum in Eq. (2.123) with the effective coupling function

$$F_2^{\text{eff}}(\boldsymbol{k}_1, \boldsymbol{k}_2) = \frac{5}{7}a(n_{\text{eff}}, k_1)a(n_{\text{eff}}, k_2) + \frac{1}{2}\frac{\boldsymbol{k}_1 \cdot \boldsymbol{k}_2}{|\boldsymbol{k}_1||\boldsymbol{k}_2|}b(n_{\text{eff}}, k_1)b(n_{\text{eff}}, k_2)\left(\frac{k_1}{k_2} + \frac{k_2}{k_1}\right)$$
$$+ \frac{2}{7}\frac{(\boldsymbol{k}_1 \cdot \boldsymbol{k}_2)^2}{k_1^2 k_2^2}c(n_{\text{eff}}, k_1)c(n_{\text{eff}}, k_2)\,, \qquad (2.140)$$

where the fitting parameters are given by

$$a(n_{\text{eff}}, k) = \frac{1 + \sigma_8^{-0.2}(z)\sqrt{0.7Q(n_{\text{eff}})}(q/4)^{n_{\text{eff}}+3.5}}{1 + (q/4)^{n_{\text{eff}}+3.5}}\,, \qquad (2.141)$$

$$b(n_{\text{eff}}, k) = \frac{1 + 0.4(n_{\text{eff}} + 3)q^{n_{\text{eff}}+3}}{1 + q^{n_{\text{eff}}+3.5}}\,, \qquad (2.142)$$

$$c(n_{\text{eff}}, k) = \frac{1 + 4.5[1.5 + (n_{\text{eff}} + 3)^4]^{-1}(2q)^{n_{\text{eff}}+3}}{1 + (2q)^{n_{\text{eff}}+3.5}}\,, \qquad (2.143)$$

and where we defined the ratio $q = k/k_{\text{nl}}$. The nonlinear wave-number k_{nl} is defined as the scale where the dimensionless power spectrum is equal to 1, i.e., $\Delta(k_{\text{nl}}, z) = 1$. Note that this is a different definition for the nonlinear wave-number as in Eq. (2.134). Both the nonlinear wave-number and the normalization of the power spectrum are redshift dependent, where $\sigma_8(z) = D(z)\sigma_8$. For large scales ($k \ll k_{\text{nl}}$) the fitting function converges to $a = b = c = 1$ which is the result from tree-level perturbation theory. For small scales ($k \gg k_{\text{nl}}$) we find $b = c = 0$ and $a = \sigma_8^{-0.2}(z)\sqrt{0.7Q(n_{\text{eff}})}$ which resembles the behavior of the bispectrum in the strongly nonlinear regime as given in Eq. (2.139).

In the right panel of Fig. 2.2 we show the results of the reduced bispectrum in HEPT. Compared to the results of perturbation theory the scale dependence is clearly reduced. On the smallest scales the reduced bispectrum approaches a constant value which is not predicted by tree-level perturbation theory.

2.4 Transfer Function

Up to now, we discussed only perturbations in the matter-dominated regime that are smaller than the comoving horizon (recall that we are then able to use a simple Newtonian approach). However, in the radiation-dominated regime we have to include pressure terms originating from the coupled photon-baryon fluid. Hence, for baryonic perturbations in the radiation-dominated regime we have to include pressure terms in the description of the fluid equations. Also the behavior of the dark matter perturbations is changed in the radiation-dominated phase because the scale-dependence of the

mean background density is different compared to the matter-dominated phase. In addition, we show the behavior of perturbations that are larger than the horizon of the Hubble expansion. A common approach is to include all of these different effects in a scale-dependent function, the so-called transfer function.

2.4.1 Jeans Equation

When we include pressure, the Euler equation changes to

$$\frac{\partial \boldsymbol{u}}{\partial \tau} + \mathcal{H}\boldsymbol{u} + (\boldsymbol{u} \cdot \nabla)\boldsymbol{u} = -\frac{1}{\rho}\nabla p - \nabla\Phi \,. \tag{2.144}$$

Taking the divergence of this equation and only keeping terms linear in $\boldsymbol{u}$ yields

$$\frac{\partial \theta}{\partial \tau} + \mathcal{H}\theta + \frac{3}{2}\mathcal{H}^2\Omega_{\mathrm{m}}\delta = -\frac{1}{\rho}\nabla^2 p \,. \tag{2.145}$$

To relate the pressure to the density, we perform a Taylor expansion of the pressure around the mean background density. Up to linear order in ρ we find

$$p(\rho) = p(\bar{\rho}) + \frac{\mathrm{d}p}{\mathrm{d}\rho}\bigg|_{\rho=\bar{\rho}} (\rho - \bar{\rho}) \equiv p(\bar{\rho}) + c_{\mathrm{s}}^2\bar{\rho}\delta \tag{2.146}$$

where we defined the sound speed in the second step. Then we find for the derivative

$$\frac{\mathrm{d}p}{\mathrm{d}\rho} = c_{\mathrm{s}}^2 \,, \tag{2.147}$$

and we can rewrite the pressure term as

$$\nabla^2 p = \bar{\rho}c_{\mathrm{s}}^2\nabla^2\delta \,. \tag{2.148}$$

Combining Eqs. (2.39), (2.145) and (2.148), we find the equation of the linear growth of fluctuations including pressure (compare with the pressureless differential equation in 2.42):

$$\frac{\partial^2\delta}{\partial\tau^2} + \mathcal{H}\frac{\partial\delta}{\partial\tau} = 4\pi G\bar{\rho}a^2\delta + c_{\mathrm{s}}^2\nabla^2\delta \,. \tag{2.149}$$

Transforming the differential equation into Fourier space results in

$$\frac{\partial^2\delta}{\partial\tau^2} + \mathcal{H}\frac{\partial\delta}{\partial\tau} = \left[4\pi G\bar{\rho}a^2 - c_{\mathrm{s}}^2 k^2\right]\delta \,. \tag{2.150}$$

The right-hand side of this equation shows that we have two competing effects: gravity leading to an amplification of the density perturbation (see discussion on the linear growth factor) and an opposing pressure term. It depends on the wave-length of the perturbations which of both effects is dominant. Large-scale fluctuations are unaffected by pressure effects as $k \to 0$, whereas for small-scale fluctuations the pressure term is

the dominant contribution. For small-scale fluctuations the solutions to Eq. (2.150) are oscillating functions. Both effects compensate each other for perturbations with the characteristic *Jeans wave-length*:

$$\lambda_{\mathrm{J}} = \sqrt{\frac{\pi}{G\bar{\rho}}}c_{\mathrm{s}}\,. \tag{2.151}$$

For modes with $\lambda > \lambda_{\mathrm{J}}$ gravity is dominating the right-hand side of Eq. (2.150). In particular, taking the limit $\lambda \gg \lambda_{\mathrm{J}}$, we retain the solution of the linear growth factor given in Eq. (2.48). On the other hand, modes with $\lambda < \lambda_{\mathrm{J}}$ are affected by the pressure term, and the perturbations begin to oscillate like acoustic waves with sound velocity c_{s}.

2.4.2 Matter Perturbations in a Radiation-Dominated Background

The radiation component has also an effect on the matter density perturbations. To study this effect, we need to solve Eq. (2.149) neglecting the pressure term and using for the mean density the sum of the matter and radiation density. Rewriting the equation in terms of the new variable $y = a/a_{\mathrm{eq}}$ yields

$$\frac{\partial^2 \delta}{\partial y^2} + \frac{2 + 3y}{2y(1 + y)}\frac{\partial \delta}{\partial y} - \frac{3}{2y(1 + y)}\delta = 0\,. \tag{2.152}$$

The growing solution to this equation is given by

$$D(a) = \frac{a}{a_{\mathrm{eq}}} + \frac{2}{3}\,. \tag{2.153}$$

During radiation domination, we have $y \ll 1$ and the growth of matter perturbation effectively stops and goes to a constant, which is the so-called *Meszaros effect*. However, in the matter-dominated regime, where $y \gg 1$, we retain the solution of the linear growth factor in the EdS Universe discussed in Sect. 2.1.4.

2.4.3 General Fluctuation

For the following discussion we consider the evolution of a single fluctuation of wave-length λ during the transition of the radiation- to the matter-dominated phase of the Universe. Therefore, we can neglect any contribution from a cosmological constant that is only dominating the expansion of the Universe at late times.

At first, we consider the evolution of a single perturbation in the collisionless cold dark matter density component. As long as the wave-length is larger than the comoving horizon (see definition in Eq. 1.56), i.e., $\lambda > r_{\mathrm{h}}$, the perturbation is unaffected by causal physics like pressure of the baryon-photon fluid. A general relativistic consideration shows that the density contrast grows like $\delta \propto a^2$ for these *superhorizon fluctuations*.

When the perturbation *enters* the horizon[7] in the radiation-dominated era, the growth of the density contrast stops due to the Meszaros effect. The perturbation starts to grow again at the time of matter-radiation equality with $\delta \propto a$. In summary, small-scale perturbations are suppressed relative to large-scale fluctuations. To quantify the suppression, we consider two different perturbations: the first enters the horizon at a_{enter} in the radiation-dominated era and the second only in the matter-dominated era. Then the former one is reduced by a factor $(a_{\text{enter}}/a_{\text{eq}})^2$ in comparison to the latter one.

Considering a perturbation in the baryonic density component is more complicated because we need to include the effect of pressure. At early times, the evolution follows that of the matter component: a superhorizon fluctuation first grows and then stagnates when it enters the horizon. However, if $\lambda < \lambda_{\text{J}}$ then the perturbation starts to oscillate like an acoustic wave. This oscillation originates from the competing effects of pressure in the photon-baryon fluid and the gravitational instability: gravitational forces cause the baryons to fall into their potential wells, whereas the radiation pressure drags them out if the fluctuation is smaller than λ_{J}, i.e., if the pressure is strong enough. Then the baryons fall into their potential wells and the cycle starts again leading to oscillations in the form of acoustic waves. In addition, the amplitude of the oscillation is reduced by *Silk damping*. This reduction is caused by the diffusion of photons which drag the baryons with them. After the time of recombination photons and baryons decouple. In this case, we can neglect pressure effects and the baryonic perturbation grows like the dark matter perturbation.

We discussed here only the basic effects on matter and baryonic perturbations in the radiation- and matter-dominated phase of the Universe. A detailed analysis needs to be done in the framework a general relativity (see the book of Dodelson 2003, which focuses on the derivation of the CMB anisotropy power spectrum). In principle, one needs to solve the (coupled) relativistic Boltzmann equation for each of the components: photons, baryons, cold dark matter, massive neutrinos, etc. However, in general, this can only be done numerically. A number of relativistic Boltzmann codes is publically available (for example the CMBFAST code introduced by Seljak & Zaldarriaga 1996 and the CAMB software presented in Lewis et al. 2000).

To account for the scale-dependent effects occurring during horizon crossing and matter-radiation transition, we define the *transfer function*:

$$\frac{\delta(k, a=1)}{\delta(k_{\text{LS}}, a=1)} \equiv T(k)\frac{\delta(k, a_{\text{i}})}{\delta(k_{\text{LS}}, a_{\text{i}})} \tag{2.154}$$

where k_{LS} is a sufficiently large perturbation that entered the horizon only in the matter-dominated phase and thus has not been affected by growth suppression. In addition, we consider an initial time or scale factor a_{i} such that all perturbations are outside the horizon. Building the ratio of an arbitrary fluctuation with wave-number k

---

[7]More correctly, the horizon grows with the expansion of the Universe and thus there is a time where the horizon size is equal to the size of the perturbation. Then we say that the perturbation entered the horizon.

to a large-scale fluctuation which never entered the horizon, we can quantify the growth suppression of $\delta(k)$. Hence, the transfer function describes the change of this ratio from an early initial time to today. Note that the transfer function is independent on the reference variables a_{i} and k_{LS}. Using this formalism, we easily see that for large scales the transfer function goes to 1 as $k \rightarrow k_{\mathrm{LS}}$. On the other hand, the behavior for small scales can be inferred from the condition that a perturbation δ entered the horizon in the radiation-dominated era:

$$\lambda = r_{\mathrm{h}}(a_{\mathrm{enter}}) \approx \frac{c}{a_{\mathrm{enter}} H(a_{\mathrm{enter}})} \,. \tag{2.155}$$

For $a \ll a_{\mathrm{eq}}$, the second Friedmann equation (1.22) yields $H(a) \propto a^{-2}$ and thus $k \propto a_{\mathrm{enter}}^{-1}$. Hence, as the suppression of modes for small scales is $(a_{\mathrm{enter}}/a_{\mathrm{eq}})^2$, we find $T(k) \propto k^{-2}$.

A widely used transfer function for cold dark matter perturbations is (Bardeen et al. 1986)

$$T(k) = \frac{\ln(1 + 2.34q)}{2.34q} \left[1 + 3.89q + (16.1q)^2 + (5.46q)^3 + (6.71q)^4\right]^{-1/4} \,, \tag{2.156}$$

with the dimensionless variable $q = [k/(h\,\mathrm{Mpc}^{-1})]\Gamma^{-1}$, and where Γ is the *shape parameter*. The shape parameter reflects the characteristic scale of the horizon size at matter-radiation equality. For a Universe without baryons the shape parameter is simply

$$\Gamma = \Omega_{\mathrm{m}} h \,. \tag{2.157}$$

This equations is modified in the presence of baryons (Sugiyama 1995)

$$\Gamma = \Omega_{\mathrm{m}} h \exp[-\Omega_{\mathrm{b}}(1 + \sqrt{2h}/\Omega_{\mathrm{m}})] \,. \tag{2.158}$$

This equation fails if Ω_{b} is too large and the transfer function develops oscillations. For these situations it is better to use the improved Eisenstein and Hu fitting function (Eisenstein & Hu 1998, 1999).

2.4.4 Power Spectrum

So far, we considered only the late-time behavior of the linear power spectrum. With the help of the transfer function, we have access to the primordial power spectrum P_{prim} set up after inflation:

$$P_{\mathrm{pt}}(k) = A P_{\mathrm{prim}}(k) T^2(k) \,, \tag{2.159}$$

where A is the amplitude of the power spectrum. We still need to specify the primordial power spectrum. Most models of structure formation assume Gaussian initial conditions for the primordial fluctuations after inflation. In this case, the power spectrum contains all statistical information on the density field. However, recently there is a growing interest in constraining primordial non-Gaussianity as predicted by some inflationary

models, and which is potentially strong enough to be observed. Naturally we can study this effect by considering higher-order correlation functions. Hence, it is very important to put tight limits on the observed level of non-Gaussianity. The best limits come from CMB measurements (Komatsu et al. 2009).

Right after the time of inflation basically all perturbation modes were larger than the horizon. Hence, without a characteristic length scale the primordial spectrum needs to be of the form of a power law, i.e., $P_{\mathrm{prim}} \propto k^{n_{\mathrm{s}}}$, where n_{s} is the *spectral index* of the primordial spectrum. Inflationary models provide estimates for this power-law index. One can show that the spectral is fixed by the slow roll parameters (ϵ and η) of inflation given in Eq. (1.67) such that (Peacock 1999)

$$n_{\mathrm{s}} = 1 - 6\epsilon + 2\eta \, . \tag{2.160}$$

For most models in which the potential of the inflaton is a smooth function we have $|\epsilon| = |\eta|$. Thus, a prediction of inflation is to have a *tilted* primordial power spectrum which is characterized by a spectral index which is slightly smaller than 1. A special case is the primordial power spectrum for $n_{\mathrm{s}} = 1$ which is the so-called *Harrison-Zel'dovich spectrum*.

We showed in Sect. 2.1.4 that the late-time evolution of the density contrast is in linear perturbation theory proportional to the growth function, i.e., $\delta(\boldsymbol{k}, a) = D(a)\delta(\boldsymbol{k})$. Then, the power spectrum at redshift z or scale factor a is

$$P_{\mathrm{pt}}(k, a) = A k^{n_{\mathrm{s}}} T^2(k) D^2(a) \, . \tag{2.161}$$

The amplitude A of the power spectrum still needs to be fixed. This amplitude cannot be predicted from theory but needs to be determined from observations of the power spectrum at a certain redshift. One particular way[8] is to use the result that we measure today that the variance of number counts of galaxies in spheres of radius $R = 8\,h^{-1}\,\mathrm{Mpc}$ is about unity, i.e., $\sigma_{8,\mathrm{gal}}^2 \approx 1$. To apply this result for the dark matter power spectrum, we need to translate the variance to the variance in the dark matter fluctuations σ_8^2. However, we need to include the difference in the clustering of dark matter and galaxies known as the *galaxy bias*. On large scales we can assume that we have a simple linear deterministic bias factor leading to $\sigma_{8,\mathrm{gal}}^2 = b^2 \sigma_8^2$, where $\sigma_8^2 \equiv \sigma^2(R = 8\,h^{-1}\,\mathrm{Mpc})$ is the variance of the dark matter fluctuations which is given by

$$\sigma_8^2 = \int \frac{\mathrm{d}^3 k}{(2\pi)^3} \, |W_8(k)|^2 \, P_{\mathrm{pt}}(k, a=1) = \frac{A}{(2\pi)^2} \int \mathrm{d}k \, k^2 \, W_8^2(k) T^2(k) k^{n_{\mathrm{s}}} \, , \tag{2.162}$$

where $W_8(k)$ is the top-hat filter function in Fourier space at scale $R = 8\,h^{-1}\,\mathrm{Mpc}$ given in Eq. (B.23). In addition, we inserted the power spectrum (2.161) and performed the angular integration in the second step. Hence, the amplitude of the power spectrum is fixed by

$$A = \sigma_8^2 \Big/ \left[\frac{1}{(2\pi)^2} \int \mathrm{d}k \, k^2 \, W_8^2(k) T^2(k) k^{n_{\mathrm{s}}} \right] \, . \tag{2.163}$$

---

[8]The CMB community uses another method to fix the amplitude of the power spectrum (e.g., Dodelson 2003).

Today most cosmological probes like measurements of the cosmic shear two-point correlation functions (Fu et al. 2008), of the CMB anisotropy spectrum (Komatsu et al. 2009) and of the abundance of galaxy clusters (e.g., the forecast of the constraints which are expected to be obtained from the XMM-Newton Cluster Survey[9] is given in Sahlén et al. 2008), find values around $\sigma_8 \approx 0.8$. However, the measurements show strong degeneracies between σ_8 and Ω_{m}.

The asymptotic behavior of the Fourier-mode dependence of the power spectrum is determined by the asymptotic behavior of the transfer function and is given by

$$P_{\mathrm{pt}}(k) = \begin{cases} k & \text{for small } k\,, \\ k^{-3} & \text{for large } k\,. \end{cases} \tag{2.164}$$

On large scales the density fluctuations are not suppressed and the power spectrum traces the scale-dependence of the primordial power spectrum. Using the behavior of the transfer function on small scales, we find that the power spectrum decreases $\propto k^{-3}$. Imprinted in the linear power spectrum is the characteristic size of the horizon at a_{eq}, where we see the turnover in the power spectrum.

---

[9]X-ray Multi-Mirror Mission.

Chapter 3

The Dark Matter Halo Model

So far we discussed the linear and the quasilinear regime of the dark matter density field which is well described by cosmological perturbation theory (see Chapter 2). As we already mentioned, the perturbative expansion breaks down when the density contrast becomes close to unity marking the onset of the nonlinear regime of the density field. This is a problem because many interesting astrophysical objects like groups and clusters of galaxies are nonlinear objects. The study of the nonlinear regime is usually examined with numerical simulations. However, we will go another way and adopt an analytic model which combines results from simulations and theoretical models of gravitational clustering. This approach allows us to predict the form of correlation functions in the linear and the nonlinear regime in a fairly accurate way. The main idea is that dark matter is only distributed in spherically symmetric dark matter halos. The clustering of dark matter which is described by the density contrast is then fully replaced by the clustering of halos and their individual properties. This is a powerful model because the properties of dark matter halos are well constrained by simulations.

The idea to explain gravitational clustering with an analytic approach has a long history. The first models were already developed in the 1950s and they described galaxy clustering as a superposition of randomly distributed objects with a range of masses and density profile models (Neyman & Scott 1952; Peebles 1974; McClelland & Silk 1977). Recently, the remarkable results of high-resolution dark matter N-body simulations for the abundance of halos (halo mass function), the density run around a halo of mass m (halo density profile) and the clustering of halos (halo bias) have renewed the interest in analytic models. Especially, the concept of halo clustering was not contained in the original models. Combining the new results from simulations and theoretical results of perturbation theory yields the *halo model*, independently developed by Seljak (2000), Ma & Fry (2000) and Scoccimarro et al. (2001). In principle, the halo model can be extended and/or updated by the inclusion of new results from simulations.

The outline of this chapter is as follows: First, we introduce the spherical collapse model in Sect. 3.1 which provides the necessary conditions for the formation of dark matter halos. In Sect. 3.2, the number density of virialized objects of mass m, the so-called halo mass function, is introduced. The universal radial density profile of a halo is discussed in Sect. 3.3. The clustering of halos is the topic of Sect. 3.4, where we introduce the halo bias. Finally, using the properties of dark matter halos as building

blocks, we derive in Sect. 3.5 the halo model correlation functions and their Fourier space counterparts. In particular, we provide expressions for the power spectrum, the bispectrum and the trispectrum that are needed for the rest of this thesis.

3.1 Spherical Collapse Model

In this section we analyze the formation of nonlinear objects like galaxies and clusters of galaxies as they break away from the general Hubble expansion of the Universe. We use the *spherical collapse model* as a description of the necessary conditions for the formation of dark matter halos. In this picture, halos originate from the spherical collapse of small perturbations in the surrounding background matter. This is an overly simplistic model that gives only a rough guideline for the formation of halos as the formation of halos is not spherical. Nevertheless, simulations use the results from the spherical collapse model to select virialized objects and get reasonable results compared to observations.

The dynamics of a gravitating shell of radius $r(t)$ of a spherical mass distribution is governed by the Newtonian differential equation

$$\frac{\mathrm{d}^2}{\mathrm{d}t^2}\, r(t) = -\frac{G_N M}{r^2(t)}\,, \tag{3.1}$$

where M is the mass contained in the spherical shell and G_N is Newton's constant. The first integral of the equation of motion is given by

$$\left(\frac{\mathrm{d}r(t)}{\mathrm{d}t}\right)^2 = \frac{2G_N M}{r(t)} + E\,, \tag{3.2}$$

where we used the fact that the mass is time independent and E is the constant of integration. Clearly, for $E > 0$ the shell will expand forever as the kinetic energy is always larger than the potential energy. However, when $E < 0$ there is a turning point and the shell will only expand until a maximal radius and then contract again. As we are interested in the spherical collapse and the building of virialized objects, we consider the case where $E < 0$ in the following. The solution to Eq. (3.1) for the radius r and the time t is given by the cycloid solution

$$r(\theta) = A(1 - \cos\theta)\,, \tag{3.3}$$
$$t(\theta) = B(\theta - \sin\theta)\,, \tag{3.4}$$

where A and B are constant parameters. Plugging this ansatz into Eq. (3.1) gives the constraint

$$A^3 = G_N M B^2\,. \tag{3.5}$$

In the following we consider three different cases for the parameter θ and show the results for the radius of the sphere and the corresponding time using Eqs. (3.3) and (3.4). We find

- $\theta = 0 \quad \rightarrow \quad r = 0\,; \quad t = 0\,,$

- $\theta_{\text{ta}} = \pi \quad \rightarrow \quad r_{\text{ta}} = 2A\,; \quad t_{\text{ta}} = \pi B\,,$

- $\theta_{\text{coll}} = 2\pi \quad \rightarrow \quad r_{\text{coll}} = 0\,; \quad t_{\text{coll}} = 2\pi B\,.$

These relations demonstrate that the parametric solution describes a sphere which is expanding until it reaches a maximal radius at *turnaround* (subscript "ta"). This is followed by a contraction which results formally in a vanishing minimal radius at *collapse* (subscript "coll"), i.e, $r_{\text{coll}} = 0$. Note that the three different values of θ denote a time evolution because the time is increasing as θ is increasing. Expanding the parametric solution given by Eqs. (3.3) and (3.4) in a power series for $\theta \ll 1$ and keeping terms up to $\mathcal{O}(\theta^5)$, we find the radius in the linear regime:

$$r_{\text{lin}} \simeq \frac{A}{2} \left(\frac{6t}{B} \right)^{2/3} \left[1 - \frac{1}{20} \left(\frac{6t}{B} \right)^{2/3} \right]\,. \tag{3.6}$$

The corresponding density in the linear regime then simply follows from

$$\rho_{\text{lin}} = \frac{3M}{4\pi r_{\text{lin}}^3} \simeq \frac{1}{6\pi G_N t^2} \left[1 + \frac{3}{20} \left(\frac{6t}{B} \right)^{2/3} \right]\,, \tag{3.7}$$

where we performed a Taylor expansion for small times t keeping only the lowest-order term and used the constraint (3.5) in the second step. Note that the pre-factor corresponds to the mean density in an EdS Universe since $\bar{\rho}_{\text{EdS}} = \rho_{\text{crit}} = 3H^2/(8\pi G_N)$ with $H = 2/(3t)$. Hence, we can identify the linear density contrast as the second term in square brackets by using the relation $\rho = \bar{\rho}(1 + \delta)$:

$$\delta_{\text{lin}} = \frac{3}{20} \left(\frac{6t}{B} \right)^{2/3}\,. \tag{3.8}$$

Results for a flat ΛCDM model are discussed at the end of this section. Note that the results of the linear spherical collapse model in Eq. (3.8) agree with the results of linear perturbation theory where the perturbation grows proportional to the scale factor, i.e., $\delta_{\text{lin}} \propto a \propto t^{2/3}$.

The general density which is also valid in the nonlinear regime is given by

$$\rho_{\text{nl}} = \frac{3M}{4\pi r^3} = \frac{3}{4\pi} \frac{M}{A^3(1 - \cos\theta)^3} = \frac{1}{6\pi G_N t^2} \frac{9(\theta - \sin\theta)^2}{2(1 - \cos\theta)^3}\,, \tag{3.9}$$

where we inserted the parametric solution for the radius given in Eq. (3.3) in the second step and used the constraint (3.5) in combination with the parametric solution for the time (3.4) in the last step. By noting that the pre-factor is again the mean background density we identify the nonlinear density contrast as

$$\delta_{\text{nl}} = \frac{9}{2} \frac{(\theta - \sin\theta)^2}{(1 - \cos\theta)^3} - 1\,. \tag{3.10}$$

We are now able to calculate the linear and nonlinear density contrast using Eqs. (3.8) and (3.10), respectively, for the two particular times at turnaround and collapse. At turnaround we find

$$\delta_{\text{lin}}^{(\text{ta})} \simeq 1.06 \,; \qquad \delta_{\text{nl}}^{(\text{ta})} = \frac{9}{16}\pi^2 - 1 \simeq 4.55 \,, \tag{3.11}$$

and the ratio of the density to the mean density is

$$\frac{\rho_{\text{nl}}^{(\text{ta})}}{\bar{\rho}^{(\text{ta})}} = 1 + \delta_{\text{nl}}^{(\text{ta})} = \frac{9}{16}\pi^2 \simeq 5.55 \,. \tag{3.12}$$

Hence, at turnaround the sphere is 5.55 times more dense than the mean background density of the Universe. Since the perturbative result of the linear density ratio $(\rho_{\text{lin}}^{(\text{ta})}/\bar{\rho}^{(\text{ta})} = 2.06)$ contrast underestimates the general density contrast by more than 50 per cent, we are already in the nonlinear regime.

After turnaround the spherical region begins to contract until it collapses formally to a point of infinite density. However, this will not occur in reality because we neglected dissipative physics in the simplified model above. The kinetic energy of the infalling matter will be transferred into a random motion of the mass particles which is called *violent relaxation*. This random motion leads to a virialization where the spherical region reaches a constant *virial radius* r_{vir} corresponding to a finite density. This radius can be estimated using the virial theorem

$$U_{\text{vir}} = -2T_{\text{vir}} \,, \tag{3.13}$$

where U denotes the potential energy and T the kinetic energy. At the point of turnaround the kinetic energy of the shell vanishes, i.e., $T_{\text{ta}} = 0$. Conservation of the total energy yields $E_{\text{vir}} = T_{\text{vir}} + U_{\text{vir}} = U_{\text{vir}}/2 = E_{\text{ta}} = U_{\text{ta}}$, where we used the virial theorem in the second step. This leads to a relation of the potential energy at virialization and turnaround, i.e., $U_{\text{vir}} = 2U_{\text{ta}}$. As $U \propto 1/r$ we find that the radius of objects at virialization is half as large as the maximal radius, i.e., $r_{\text{vir}} = r_{\text{ta}}/2$. This enables us to calculate the density of a virialized object in terms of the density at turnaround as $\rho_{\text{nl}}^{(\text{vir})} = 8\rho_{\text{nl}}^{(\text{ta})}$. In addition, we need to compute the background density at collapse

$$\bar{\rho}(t_{\text{vir}}) = \frac{1}{6\pi G_N t_{\text{vir}}^2} = \frac{\bar{\rho}(t_{\text{ta}})}{4} \,, \tag{3.14}$$

where used $t_{\text{vir}} \equiv t_{\text{coll}} = 2t_{\text{ta}}$ in the second step. Finally, we find for the density contrast at collapse

$$\delta_{\text{nl}}^{(\text{vir})} = \frac{\rho_{\text{nl}}^{(\text{vir})}}{\bar{\rho}^{(\text{vir})}} - 1 = 32\frac{\rho_{\text{nl}}^{(\text{ta})}}{\bar{\rho}^{(\text{ta})}} - 1 = 18\pi^2 - 1 \,, \tag{3.15}$$

where we inserted Eq. (3.12) for the density ratio at turnaround in the last step. Therefore the density ratio at virialization is

$$\Delta_{\text{vir}} \equiv \frac{\rho_{\text{nl}}^{(\text{vir})}}{\bar{\rho}^{(\text{vir})}} = 1 + \delta_{\text{nl}}^{(\text{vir})} = 18\pi^2 \simeq 178 \,. \tag{3.16}$$

Hence, in the spherical collapse model, virialized objects are characterized by a density that is roughly 180 times larger than the mean background density. The linear density contrast at collapse is easily calculated because Eq. (3.8) is still applicable. Inserting the time of collapse $t_{\rm coll} = 2\pi B$ yields

$$\delta_{\rm lin}^{\rm (coll)} = \frac{3}{20}(12\pi)^{2/3} \simeq 1.686\,. \tag{3.17}$$

Thus, a linear density contrast of 1.69 marks roughly the point where the virialization of a spherical halo occurs. We will label the corresponding linear density contrast at collapse with $\delta_{\rm c}$ in the following.

In summary, the spherical collapse model provides two important numbers: the linear density contrast at the time of collapse $\delta_{\rm c}$ and the density ratio of a virialized halo $\Delta_{\rm vir} = \rho_{\rm vir}/\bar{\rho}$. If we consider virialized objects today we take $\bar{\rho} = \rho_{\rm crit}\Omega_{\rm m}$ which is the mean matter density today. For an EdS Universe we obtained for both parameters

$$\delta_{\rm c}^{\rm (EdS)} \simeq 1.686\,, \tag{3.18}$$

$$\Delta_{\rm vir}^{\rm (EdS)} = 18\pi^2 \simeq 178\,. \tag{3.19}$$

Note that for a general cosmological model both parameters are redshift- and cosmology-dependent. Calculations for a flat cosmological ΛCDM model in Henry (2000), where $\Omega_{\rm m} + \Omega_\Lambda = 1$, give the following results

$$\delta_{\rm c}(z) = \delta_{\rm c}^{\rm (EdS)}[1 - 0.0123\ln(1 + x^3)]\,, \tag{3.20}$$

$$\Delta_{\rm vir}(z) = \Delta_{\rm vir}^{\rm (EdS)}(1 + 0.4093x^{2.71572})\,, \tag{3.21}$$

where the redshift and cosmology dependence is encoded in the parameter x with

$$x \equiv \frac{(\Omega_{\rm m}^{-1} - 1)^{1/3}}{1 + z}\,. \tag{3.22}$$

Note that the value of the threshold $\delta_{\rm c}$ is only weakly dependent on cosmology. Therefore we use the EdS value in Eq. (3.18) for the subsequent calculations. However, for the density ratio we use the redshift and cosmology dependence as given in Eq. (3.21) in the following which is valid for a flat ΛCDM model.

3.2 Halo Mass Function

Using the results of the spherical collapse model presented in the previous section, we want to calculate the *mass function* of virialized objects such as dark matter halos or galaxy clusters. More precisely, we want to obtain an equation for the comoving number density of objects at redshift z with masses in the range m and $m + {\rm d}m$. We derived in the previous section that a virialized object is characterized by a linear density contrast larger than a threshold density contrast such that $\delta_{\rm lin} > \delta_{\rm c} \simeq 1.69$.

First we present the pioneering work by Press-Schechter (see Press & Schechter 1974) on the mass function in Sect. 3.2.1 which showed good agreement with observations at that time. However, high-resolution N-body simulations showed that the Press-Schechter mass function while capturing the rough features of the simulation fails in detail. In the advent of precision cosmology we need more reliable models for the mass function. We present such improved models in Sect. 3.2.2 including the most used parametrization, namely the Sheth-Tormen mass function (Sheth & Tormen 1999).

3.2.1 Press-Schechter Model

The Press-Schechter approach to calculate the mass function of virialized objects is based on the assumption that objects form in the so-called *hierarchical clustering* or *bottom-up* picture. In this case small structures form first and then subsequently merge to form larger structures.

We can assign a characteristic length scale R to a halo of mass m defined as the comoving radius of a homogeneous sphere with mean matter density $\bar{\rho}$

$$\frac{4\pi}{3} R^3 \bar{\rho} = m \,, \qquad R(m) = \left(\frac{3m}{4\pi\bar{\rho}} \right)^{1/3} \,. \tag{3.23}$$

The mean density contrast within this volume needs to be larger than δ_c to form a virialized structure. Therefore, we will smooth the density contrast δ over the characteristic scale R with a filter function. We are free to choose the form of this filter function. Here we will adopt a top-hat function defined in Eq. (B.22). Appendix B.5 provides a complete description of the smoothing of Gaussian density fields. For an initially Gaussian random field, as assumed for simple inflationary models, the probability of finding the smoothed density contrast δ is given by

$$p_R(\delta) = \frac{\exp[-\delta^2/2\sigma_R^2(m)]}{\sqrt{2\pi\sigma_R^2(m)}} \,, \tag{3.24}$$

where the variance of scale R is denoted by $\sigma_R^2(m)$ and is given by

$$\sigma_R^2(m) = \int \frac{\mathrm{d}k}{k} \frac{k^3 P_\mathrm{pt}(k, z=0)}{2\pi^2} |W_R(k)|^2 \,, \tag{3.25}$$

where $W_R(k)$ is the filter function in Fourier space and $P_\mathrm{pt}(k, z=0)$ is the linear power spectrum at redshift $z = 0$. Note that $\sigma_R^2(m)$ is a monotonically decreasing function of the halo mass m.

The fraction of the Universe contained in virialized objects with mass larger than m ($\delta > \delta_\mathrm{c}$) is estimated as

$$F_>(m) = \int_{\delta_\mathrm{c}}^{\infty} p_R(\delta) \mathrm{d}\delta = \frac{1}{2} \operatorname{erfc} \left[\frac{\delta_\mathrm{c}}{\sqrt{2}\sigma_R(m)} \right] \,, \tag{3.26}$$

where $\mathrm{erfc}(x)$ is the complementary error function. However, there is a serious problem with this approach as the considered mass of bound objects goes to zero. In this case the total fraction should be 1, whereas the Press-Schechter approach gives a fraction of $1/2$, i.e.,

$$F_>(0) = \frac{1}{2}\,\mathrm{erfc}\left[\frac{\delta_c}{\sqrt{2}\sigma_{R=0}(m=0)}\right] = \frac{1}{2}\,, \tag{3.27}$$

where we used the fact that the top-hat function is $W_R(0) = 1$ for $R = 0$ and thus $\sigma_R^2(m) \to \infty$. To solve this problem, Press & Schechter simply multiplied the final result in Eq. (3.29) below with the missing factor of 2. We convert the fraction (3.26) to the fraction of the cosmic volume filled with halos with masses between m and $m + \mathrm{d}m$ using

$$f(m) = -\frac{\partial F_>}{\partial m}\mathrm{d}m\,, \tag{3.28}$$

where we introduced a minus sign since $F_>(m)$ is a decreasing function of m. The number density $n(m)$ per comoving volume is obtained by dividing Eq. (3.28) with the mean occupied volume V of a halo with mass m

$$n(m)\mathrm{d}m = \frac{f(m)}{V} = -\bar{\rho}\frac{\partial F_>}{\partial m}\frac{\mathrm{d}m}{m}\,, \tag{3.29}$$

where $\bar{\rho}$ is the mean comoving density. Finally, after performing the partial derivative in Eq. (3.29) we find the halo mass function

$$\frac{\mathrm{d}n}{\mathrm{d}m} \equiv n_{\mathrm{PS}}(m) = -2\frac{\bar{\rho}}{m}\frac{\delta_c}{\sigma^2}\frac{\mathrm{e}^{-\delta_c^2/2\sigma^2}}{\sqrt{2\pi}}\frac{\mathrm{d}\sigma}{\mathrm{d}m} = \frac{\bar{\rho}}{m}\frac{\mathrm{e}^{-\delta_c^2/2\sigma^2}}{\sqrt{2\pi}}\frac{\delta_c}{\sigma^3}\left|\frac{\mathrm{d}\sigma^2}{\mathrm{d}m}\right|\,, \tag{3.30}$$

where we emphasized the equality of $\mathrm{d}n/\mathrm{d}m$ and $n(m)$ in the first step as both notations are used in the literature. In addition, we use from now on the compact notation $\sigma_R \equiv \sigma$ and only write the mass dependence when necessary. The ad-hoc factor of 2 can be derived from extended Press-Schechter theory (e.g., Zentner 2007). The dependence of the mass function on cosmological parameters enters through the variance σ^2 which depends on the linear power spectrum (see Eq. 3.25) and through the mean density of the Universe which depends on Ω_{m}.

To get insight into the behavior of the mass function, it is useful to consider a scale-free power spectrum as we can then find an analytical expression for the mass function. For a scale-free power spectrum $P(k) \propto k^n$ we find that the variance is given by $\sigma^2(m) = (m/m_*)^{-\frac{n+3}{3}}\delta_c^2$. Here we write the result in terms of the nonlinear mass scale m_* defined as

$$\sigma^2(m_*) = \delta_c^2\,, \tag{3.31}$$

which provides a natural way to divide the mass function into two regimes. We find

$$n_{\mathrm{PS}}(m) = \frac{A}{m^2}\left(\frac{m}{m_*}\right)^{(3+n)/6}\exp\left[-\frac{1}{2}\left(\frac{m}{m_*}\right)^{1+n/3}\right]\,, \tag{3.32}$$
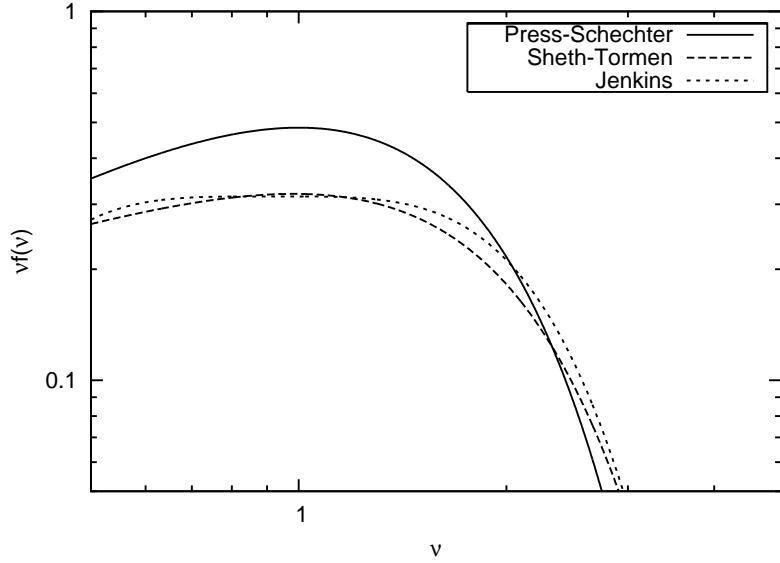
Figure 3.1: Comparison of the different halo mass function parametrizations. Shown is the multiplicity function $\nu f(\nu)$ (see Eq. 3.33 for the connection to the mass function) against the dimensionless variable ν. The solid line shows the Press-Schechter mass function in Eq. (3.35), the dashed line the Sheth-Tormen mass function in Eq. (3.36) and the dotted line the Jenkins mass function in Eq. (3.37).

where $A = \frac{\bar{\rho}}{\sqrt{2\pi}}\left(\frac{3+n}{3}\right)$. For $m \ll m_*$ we find $n_{\mathrm{PS}}(m) \propto m^{-2}m^{(3+n)/6}$ meaning that at low masses the mass function diverges like a power law. For large masses the exponential takes over leading to a cutoff for masses $m \gtrsim m_*$.

Up to now the expression for the mass function is limited to the current time $z = 0$. If we want to know the mass function of halos at a specific redshift z we simply need to modify the variance as $\sigma^2(m, z) = D^2(z)\sigma^2(m)$, where we used the redshift dependence of the linear power spectrum (see Eq. 2.48 for the expression of the growth factor $D(z)$).

3.2.2 General Halo Mass Function

We can write the differential number density of halos in the following compact form

$$n(m, z) = \frac{\bar{\rho}}{m^2}\nu f(\nu)\frac{\mathrm{d}\ln\nu}{\mathrm{d}\ln m}\,,\tag{3.33}$$

where we defined the dimensionless variable ν as

$$\nu = \frac{\delta_{\mathrm{c}}(z)}{D(z)\sigma(m)}\,.\tag{3.34}$$

Thus, part of the mass function can be expressed by the multiplicity function $\nu f(\nu)$, which has a universal shape, i.e., independent on cosmological parameters and redshift.

The universal shape is one of the main nontrivial results from simulations. However, there is very recent indication of a redshift dependence of the multiplicity function as reported in Tinker et al. (2008).

In the literature one finds a number of different parametrizations of the multiplicity function. The most popular ones are

- Press-Schechter mass function (Press & Schechter 1974)

$$\nu f(\nu) = \sqrt{\frac{2}{\pi}} \nu \exp(-\nu^2/2) \,. \tag{3.35}$$

- Sheth-Tormen mass function (Sheth & Tormen 1999)

$$\nu f(\nu) = A \sqrt{\frac{2}{\pi}} [1 + (q\nu^2)^{-p}] \sqrt{q\nu^2} \exp(-q\nu^2/2) \,, \tag{3.36}$$

  where the two parameters are given by $q = 0.707$ and $p = 0.3$ and A denotes the amplitude of the mass function that is fixed by mass conservation as shown in Eq. (3.38) below.

- Jenkins mass function (Jenkins et al. 2001)

$$\nu f(\nu) = 0.315 \exp(-|\ln \sigma^{-1} + 0.61|^{3.8}) \,. \tag{3.37}$$

The Sheth-Tormen and Jenkins functions are directly fitted to numerical simulations. For small ν we find $\nu f(\nu) \propto \nu^{0.4}$ for the Sheth-Tormen mass function and $\nu f(\nu) \propto \nu$ for the Press-Schechter mass function. This limit corresponds to small halo masses because the variance is largest for small masses. We present the three different multiplicity functions in Fig. 3.1. The largest difference is seen for small ν (or small m) which thus affects the small scales of the halo model spectra. This will be explained in detail in Sect. 3.3.

In the following we will focus on the Sheth-Tormen mass function as it provides the best agreement with simulations. In addition, it was shown to be connected to a physical model that describes an ellipsoidal mass collapse in contrast to a spherical mass collapse (see Sheth et al. 2001). The amplitude A in Eq. (3.36) is determined by assuming mass conservation, such that the integral over the mass function times the halo mass gives the mean density of the Universe:

$$\frac{1}{\bar{\rho}} \int_0^\infty n(m,z) m \, \mathrm{d}m = \int_0^\infty f(\nu) \, \mathrm{d}\nu = 1 \,, \tag{3.38}$$

where we have used the definition of the mass function in terms of the variable ν as in Eq. (3.33) in the first step. The integral can be solved analytically for $p < 1/2$ and we obtain for the amplitude

$$A(p) = \left[1 + 2^{-p} \Gamma\left(\frac{1}{2} - p\right) \Big/ \sqrt{\pi} \right]^{-1} \,, \tag{3.39}$$

where $\Gamma(x)$ is the Gamma function. Note that the amplitude only depends on the parameter p. For our fiducial choice of $p = 0.3$ the amplitude is $A = 0.322$. The general form of the Sheth-Tormen mass function contains the Press-Schechter mass function as a special case choosing the parameters $p = 0$ and $q = 1$. In this case we get $A = 0.5$ resembling the result in Eq. (3.35).

3.3 Halo Density Profile

The next ingredient we need for our halo model description of dark matter clustering is the *halo density profile*. Especially high-resolution dark matter N-body simulations are suited to determine the density profiles of halos. A nontrivial result from different simulations is that they find an approximately *universal* form of the mass profile, i.e., independent of the halo mass. However, different groups report a different functional form of the universal density profile. Ongoing theoretical work and improved simulations are needed to test the universality of the density profile and its functional form. In addition, the results from simulations can be compared to mass estimates from rotation curves of galaxies, weak lensing and X-ray observations of clusters. However, the observations still need to be improved to give tight constraints on the form of the density profile.

The simplest analytic model is the *singular isothermal sphere*, which describes a spherically symmetric, self-gravitating system of non-interacting particles. The kinetic energy of the particles is $E_{\mathrm{kin}} = k_B T$, where T is the temperature and k_B denotes the Boltzmann constant. The density profile is then given by

$$\rho(r) = \frac{\sigma_v^2}{2\pi G_N r^2} \,, \tag{3.40}$$

where σ_v is the velocity dispersion of the particles

$$\sigma_v^2 = \frac{k_B T}{m} \,. \tag{3.41}$$

However, results from improved N-body simulations indicate that the halo density profile is described by a broken power law. As already mentioned there are a number of different profiles and we give only the most important ones in the following:

- Navarro-Frenk-White (NFW) (see Navarro et al. 1996)

$$\rho(r) = \frac{\rho_{\mathrm{s}}}{(r/r_{\mathrm{s}})[1 + (r/r_{\mathrm{s}})]^2} \,, \tag{3.42}$$

- M99 (see Moore et al. 1999)

$$\rho(r) = \frac{\rho_{\mathrm{s}}}{(r/r_{\mathrm{s}})^{3/2}[1 + (r/r_{\mathrm{s}})^{3/2}]} \,, \tag{3.43}$$

- Hernquist (see Hernquist 1990)

$$\rho(r) = \frac{\rho_{\rm s}}{(r/r_{\rm s})[1 + (r/r_{\rm s})]^3} \,, \tag{3.44}$$

- Einasto (see e.g., Gao et al. 2008)

$$\rho(r) = \rho_{\rm s} \exp\left\{ -\frac{2}{\alpha}\left[\left(\frac{r}{r_{\rm s}}\right)^{\alpha} - 1\right]\right\} \,, \tag{3.45}$$

where $\rho_{\rm s}$ is the central density parameter and $r_{\rm s}$ the scale radius. The scale radius divides the density profile into its inner and outer part that have a different power-law behavior. The NFW and M99 density profiles differ only on small scales ($r \lesssim r_{\rm s}$). For large radii ($r \gg r_{\rm s}$, i.e., the outer profile) they have the same asymptotic behavior $\rho(r) \propto r^{-3}$. Most of the results from simulations agree on this scaling behavior of the outer profile. However, the form of the inner profile is still under debate as high-resolution simulations are needed. The newest results from the Millennium Run simulation prefer the Einasto parametrization for the inner part of the profile and they constrain the parameter α in (3.45) to be approximately 0.15 with a weak mass dependence (Neto et al. 2007). The four different profiles are plotted in Fig. 3.2 as a function of the radius. We can clearly see the different scaling of the inner and outer part of the profiles. The difference between the NFW profile and the Einasto profile is most significant for the inner part of the profiles.

The density profiles are usually expressed in terms of the halo mass, which can be derived from the density through

$$m = \int {\rm d}^3 r \, \rho(\boldsymbol{r}) = \int_0^{r_{\rm vir}} {\rm d}r \, 4\pi r^2 \rho(r) \,, \tag{3.46}$$

where we assumed a spherical symmetric profile in the second step. In addition, we introduced a cutoff radius $r_{\rm vir}$, the so-called *virial radius* which defines the virial mass of a halo, i.e., the mass of a halo in virial equilibrium. The virial radius can be easily computed from

$$r_{\rm vir}(z) = \left(\frac{3}{4\pi}\frac{m}{\Delta_{\rm vir}(z)\bar{\rho}}\right)^{1/3} \,, \tag{3.47}$$

where $\Delta_{\rm vir}$ is the ratio of the density of a virialized halo to the mean density and is calculated using the spherical collapse model. For a ΛCDM model we found that $\Delta_{\rm vir}$ is redshift dependent as given in Eq. (3.21). In the literature one can find several different definitions of the cutoff radius and therefore of a virial mass of a halo. Instead of using $\Delta_{\rm vir}$ in Eq. (3.47) one can find the EdS inspired values (compare with Eq. 3.16)

$$\Delta_{200} = 200 \,, \qquad \Delta_{180} = 180 \,, \tag{3.48}$$

independent of cosmology and redshift. The NFW paper even used the combination $\Delta_{200}\rho_{\rm crit}$ instead of the product of $\Delta_{\rm vir}$ with the mean background density. All these
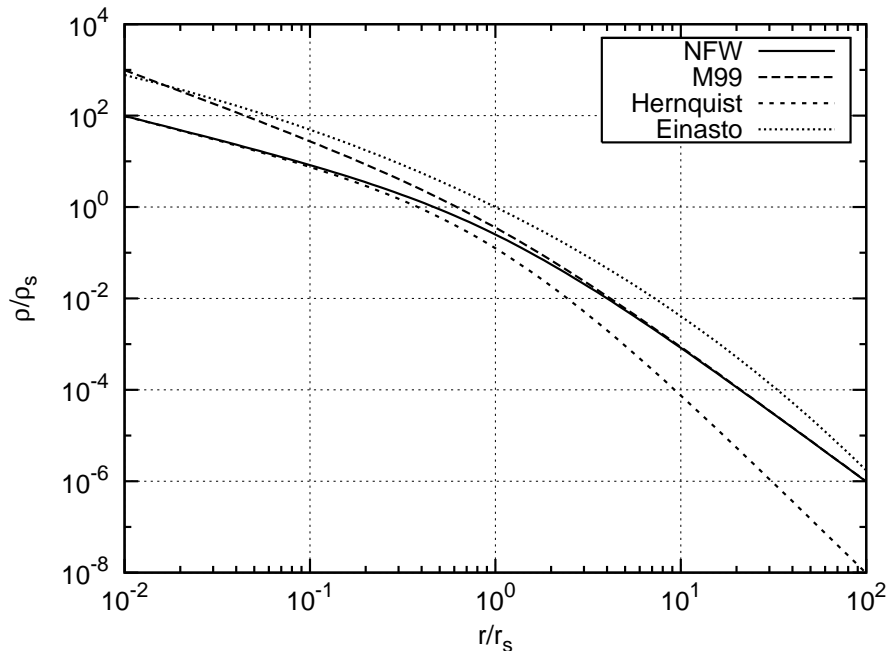
Figure 3.2: Different functional forms of the dark matter density profile in terms of the scaled density ρ/ρ_s as a function of the scaled radius r/r_s. We plot the NFW- (solid line), the M99- (long-dashed line), the Hernquist- (short-dashed line) and the Einasto profile (dotted line) as given in Eqs. (3.42), (3.43), (3.44) and (3.45), respectively. Current numerical simulations favor the NFW-profile or the Einasto profile. At $r/r_s = 1$ the transition from the power-law behavior of the inner to the outer part of the profile is clearly visible.

different combinations show that it is up to now not exactly clear what is the best way to define a halo. Hence, caution is needed before interpreting results from simulations because one needs to know their virial radius definition.

Formally one needs to integrate Eq. (3.46) up to infinity, but the mass of the M99 and the NFW profile is logarithmically divergent for large radii. Therefore one needs to introduce an arbitrary cutoff radius. Here we will adopt r_{vir} as a cutoff radius to be consistent with the results from the spherical collapse model. Strictly speaking the results of different simulations for the density profile are only tested for radii smaller than the virial radius. The Hernquist profile is constructed in a way that it cures this problem. For large r the density is proportional to r^{-4} so that it is not divergent.

The integration in Eq. (3.46) can be done analytically for the NFW and M99 profiles yielding

- NFW

$$m = 4\pi\rho_s r_s^3 \left[\ln(1+c) - \frac{c}{1+c}\right] \equiv \frac{4\pi\rho_s r_s^3}{f(c)}, \qquad (3.49)$$

- M99

$$m = 4\pi\rho_{\mathrm{s}}r_{\mathrm{s}}^3 \left[\frac{2\ln(1 + c^{3/2})}{3} \right] \equiv \frac{4\pi\rho_{\mathrm{s}}r_{\mathrm{s}}^3}{g(c)} \,, \qquad (3.50)$$

where we have defined the *halo concentration parameter*

$$c \equiv r_{\mathrm{vir}}/r_{\mathrm{s}} \,. \qquad (3.51)$$

For convenience we defined the function in square brackets as $1/f(c)$ and $1/g(c)$, respectively. Finally, we rewrite the NFW profile defined in Eq. (3.42) as

$$\rho(r, m) = \frac{m}{4\pi} \frac{c^3 f(c)}{r_{\mathrm{vir}}^3} \frac{1}{x(1 + x)^2} \,, \qquad (3.52)$$

where we replaced ρ_{s} using Eq. (3.49) and defined $x \equiv c\,r/r_{\mathrm{vir}}$. Hence, we parametrized the density profile with the virial mass (or equivalently the virial radius) and the concentration parameter. For the formulation of the halo model correlation functions it is convenient to define the normalized density profile

$$u(\boldsymbol{r}, m) \equiv \frac{\rho(\boldsymbol{r}, m)}{m} \,, \qquad (3.53)$$

where $\int \mathrm{d}^3r\, u(\boldsymbol{r}, m) = 1$.

In the following, we will need the expression of the density profile in Fourier space because we want to calculate the halo model power spectrum defined as the Fourier space counterpart of the two-point correlation function and also higher-order spectra. We find for the normalized dark matter density profile

$$\tilde{u}(\boldsymbol{k}, m) = \frac{\int \mathrm{d}^3r\, \rho(\boldsymbol{r}, m)\mathrm{e}^{\mathrm{i}\boldsymbol{k}\cdot\boldsymbol{r}}}{\int \mathrm{d}^3r\, \rho(\boldsymbol{r}, m)} \,. \qquad (3.54)$$

For spherical symmetric profiles we can perform the angular integration and the equation simplifies to

$$\tilde{u}(k, m) = \int_0^{r_{\mathrm{vir}}} \mathrm{d}r\, 4\pi r^2 \frac{\sin(kr)}{kr} \frac{\rho(r, m)}{m} \,, \qquad (3.55)$$

where $r = |\boldsymbol{r}|$. Note that we need to truncate the integration at the virial radius r_{vir} to be consistent with the definition of the halo mass in Eq. (3.46). For the NFW profile in Eq. (3.52) it is then possible to find a closed solution given by

$$\tilde{u}(k, m) = f(c) \Bigg[\sin\eta \left\{ \mathrm{Si}[\eta(1 + c)] - \mathrm{Si}(\eta) \right\} + \cos\eta \left\{ \mathrm{Ci}[\eta(1 + c)] - \mathrm{Ci}(\eta) \right\}$$

$$- \frac{\sin(\eta c)}{\eta(1 + c)} \Bigg] \,, \qquad (3.56)$$

where the sine- and cosine-integrals are defined as

$$\mathrm{Si}(x) = \int_0^x \mathrm{d}t\, \frac{\sin t}{t} \,, \qquad \mathrm{Ci}(x) = -\int_x^\infty \mathrm{d}t\, \frac{\cos t}{t} \,, \qquad (3.57)$$

and we introduced $\eta = kr_{\mathrm{vir}}/c$. The profile has the asymptotic behavior $\tilde{u}(k, m) \to 1$ for large scales which is easily verified using the limit $k \to 0$ in Eq. (3.54). Going to smaller scales the amplitude begins to decrease, i.e., $\tilde{u}(k, m) \lesssim 1$. This decline begins earlier for high-mass halos compared to small-mass halos. Finally, for small scales the profile goes asymptotically as $\tilde{u}(k, m) \propto k^{-2}$. We derive this result in the following. First we take the limit of Eq. (3.56) for small halo masses, which results in large concentrations (see Eq. 3.62 below). Thus, for the limit $c \gg 1$ we find (Scoccimarro et al. 2001)

$$\tilde{u}(k, m) = (\ln c)^{-1} \left[-\sin\eta \, \mathrm{si}(\eta) - \cos\eta \, \mathrm{Ci}(\eta) \right] , \tag{3.58}$$

where we defined $\mathrm{si}(x) \equiv \mathrm{Si}(x) - \pi/2$, and used the fact that $\mathrm{Si}(\infty) = \pi/2$ and $\mathrm{Ci}(\infty) = 0$. Now taking the limit for small scales, i.e., $\eta \gg 1$ (note that k grows faster than c) we find

$$\tilde{u}(k, m) \simeq (\ln c)^{-1} \left[\frac{\sin^2\eta}{\eta^2} + \frac{\cos^2\eta}{\eta^2} \right] = (\ln c)^{-1} \eta^{-2} \propto k^{-2} , \tag{3.59}$$

where we used the asymptotic expansion of the sine- and cosine-integrals for $x \gg 1$. The expansion is given by

$$\mathrm{si}(x) = -\frac{\cos x}{x} \left(1 - \frac{2!}{x^2} + \frac{4!}{x^4} - \dots \right) - \frac{\sin x}{x^2} \left(1 - \frac{3!}{x^2} + \frac{5!}{x^4} - \dots \right) , \tag{3.60}$$

$$\mathrm{Ci}(x) = \frac{\sin x}{x} \left(1 - \frac{2!}{x^2} + \frac{4!}{x^4} - \dots \right) - \frac{\cos x}{x^2} \left(1 - \frac{3!}{x^2} + \frac{5!}{x^4} - \dots \right) , \tag{3.61}$$

which is found by successive partial integrations of the functions in Eq. (3.57).

We show the normalized density profile in Fourier space in Fig. 3.3 as a function of the wave-number k for six different halo masses ranging from $m = 10^{11} \, h^{-1} \, M_\odot$ to $m = 10^{16} \, h^{-1} \, M_\odot$. The plot shows that massive halos contribute power only on large scales, whereas smaller halos contribute power also on small scales.

3.3.1 Halo Concentration Parameter

The halo model spectra are strongly dependent on the concentration parameter defined in Eq. (3.51). In order to get an equation for the concentration one must again resort to N-body simulations. The general result is that high-mass halos are less concentrated than low-mass halos. A good fitting formula for the mass- and redshift-dependence of the concentration of NFW halos is given by Bullock et al. (2001)

$$c(m, z) = \frac{c_0}{1 + z} \left[\frac{m}{m_*(z = 0)} \right]^{-\alpha} , \tag{3.62}$$

with the parameters $c_0 = 9$ and $\alpha = 0.13$. On the other hand, Takada & Jain (2003) used $c_0 = 10$ and $\alpha = 0.2$ instead which gave better results for a halo model applied to estimate higher-order weak lensing correlation functions. We already introduced the
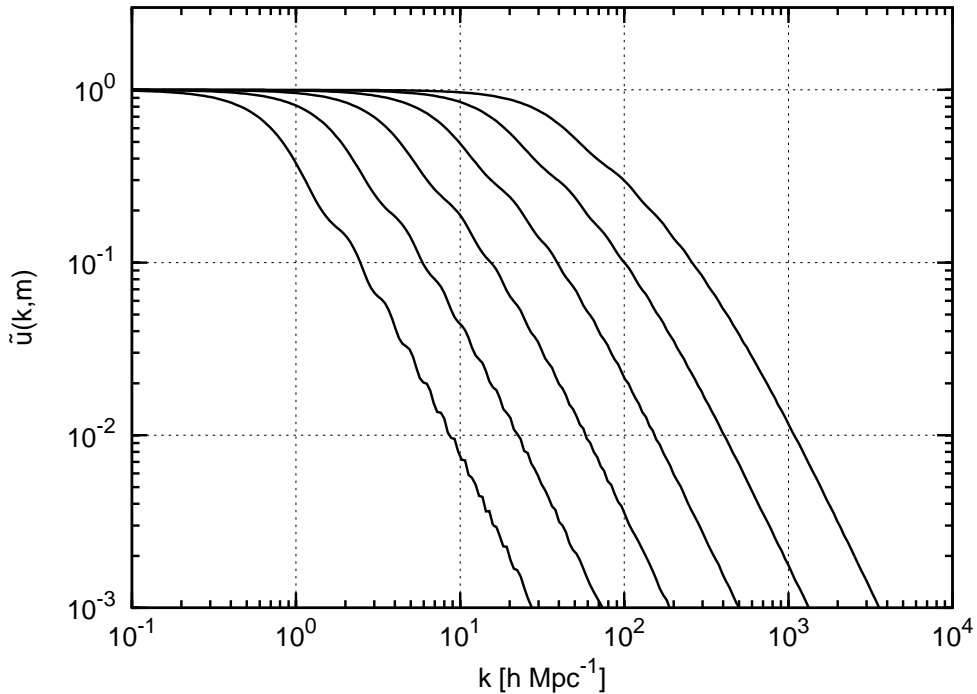
Figure 3.3: Fourier transform of the normalized NFW dark matter density profile $\tilde{u}(k, m)$ as defined in Eq. (3.56) against the wave-number k for six different halo masses m. Shown is the important halo mass range from $m = 10^{11}\, h^{-1}\, M_\odot$ at the right to $m = 10^{16}\, h^{-1}\, M_\odot$ at the left.

mass m_* in Eq. (3.31) which is defined by $\nu = 1$. In the next section we will demonstrate the influence of m_* on the halo bias.

Simulations show that different halos of the same mass have a distribution of concentrations which is well fitted by a log-normal distribution with dispersion $\sigma_{\ln c}$

$$p(c|m)\mathrm{d}c = \frac{1}{\sqrt{2\pi\sigma_{\ln c}^2}} \exp\left[-\frac{(\ln c - \ln \bar{c})^2}{2\sigma_{\ln c}^2}\right] \mathrm{d}\ln c\,, \tag{3.63}$$

where $\bar{c} \equiv \bar{c}(m, z)$ is the mean concentration parameter given by Eq. (3.62). The width of this distribution is obtained from simulations to be $\sigma_{\ln c} \approx 0.2 - 0.4$ (for example Bullock et al. 2001). Note that the width of the distribution is independent of the halo mass.

3.4 Halo Bias

Cosmological structure formation models predict that the clustering of dark matter halos is different from the clustering of the general dark matter background. Here

we will quantitatively discuss this so-called *halo bias*. Understanding halo bias is an important step forward to infer the bias between galaxy and dark matter clustering as dark matter halos are the environment for the formation of galaxies.

In this section we will sometimes use the short-hand notation $s_i \equiv \sigma^2(m_i)$. In addition, we consider here that the variance $\sigma^2(m)$ is constant in time and make the linear collapse density contrast time dependent, i.e., $\delta_c \rightarrow \delta_c(z) = \delta_c/D(z)$. This is justified by the fact that the mass function depends only on the ratio ν of both quantities (see for example Eq. 3.36).

We consider a halo of mass m_2 at time δ_2 ($\delta_i \equiv \delta_c(z_i)$) corresponding to a redshift z_2. The fraction of mass that was in halos of mass m_1 at an earlier time at redshift z_1 (where $z_1 > z_2$ or equivalently $\delta_1 > \delta_2$) is given by the *conditional mass function*:

$$f(s_1, \delta_1 | s_2, \delta_2) \frac{\mathrm{d}s_1}{\mathrm{d}m_1} \mathrm{d}m_1 = \frac{\delta_1 - \delta_2}{\sqrt{2\pi}(s_1 - s_2)^{3/2}} \exp\left[-\frac{(\delta_1 - \delta_2)^2}{2(s_1 - s_2)}\right] \frac{\mathrm{d}s_1}{\mathrm{d}m_1} \mathrm{d}m_1 , \qquad (3.64)$$

where $m_1 < m_2$ and thus $s_2 < s_1$. The mass m_2 is growing through merger and accretion of the surrounding halos. This relation can be derived from *extended Press-Schechter theory* (see the pioneering work of Bond et al. 1991; Lacey & Cole 1993, and the comprehensive review by Zentner 2007) and is the basis for the following derivation of the halo bias.

Now we want to use the conditional mass function to relate the density contrast of halos δ_h to the dark matter density contrast δ. The presented approach was first developed by Mo & White (1996) and Mo et al. (1997). We consider a region of mass M and volume V that has a corresponding density of

$$\rho = M/V = \bar{\rho}(1 + \delta) . \qquad (3.65)$$

The region is assumed to be massive enough to fulfill the condition $\sigma^2(M) \ll \sigma^2(M_*) = \delta_c^2$, so that we can take the approximate limit $\sigma^2(M) \rightarrow 0$. This region will become a halo in the future. With this setup we can describe the fraction of mass in halos of mass m that collapse at time δ_c contained in the region of mass M with the density contrast δ. This quantity is given by the approximate form of the conditional mass function in Eq. (3.64):

$$f(m, \delta_c | M, \delta) \frac{\mathrm{d}\sigma^2}{\mathrm{d}m} \approx \frac{\delta_c - \delta_{\mathrm{lin}}(\delta)}{\sqrt{2\pi}\sigma^3(m)} \exp\left[-\frac{(\delta_c - \delta_{\mathrm{lin}}(\delta))^2}{2\sigma^2(m)}\right] \frac{\mathrm{d}\sigma^2}{\mathrm{d}m} . \qquad (3.66)$$

Here $\delta_{\mathrm{lin}}(\delta)$ is the linear collapse density contrast for the region of mass M characterized by the density contrast δ. From this expression the average number of halos with mass m in a region of mass M is given by

$$N(m | M, \delta) = \frac{M}{m} f(m, \delta_c | M, \delta) \left|\frac{\mathrm{d}\sigma^2}{\mathrm{d}m}\right| . \qquad (3.67)$$

We can then define the halo density contrast in analogy to the dark matter density contrast as the ratio of the number density of halos of mass m contained in a region of mass M to the general number density of halos provided by the halo mass function, i.e.,

$$1 + \delta_{\mathrm{h}} = \frac{N(m|M,\delta)}{V} \frac{1}{n(m)} . \tag{3.68}$$

Inserting the number of halos, Eq. (3.67), and using Eq. (3.65) we find

$$1 + \delta_{\mathrm{h}} = \frac{\bar{\rho}}{m} \frac{f(m,\delta_{\mathrm{c}}|M,\delta)}{n(m)} (1+\delta) \left| \frac{\mathrm{d}\sigma^2}{\mathrm{d}m} \right| . \tag{3.69}$$

For $\delta \ll 1$ we can expand the function f in Eq. (3.66) in a Taylor series:

$$f(m,\delta_{\mathrm{c}}|M,\delta) = \left[\delta_{\mathrm{c}} + (\nu^2 - 1)\delta_{\mathrm{lin}}(\delta) + \frac{\nu^2(\nu^2-3)}{\delta_{\mathrm{c}}} \frac{\delta_{\mathrm{lin}}^2(\delta)}{2} + \dots \right] \frac{\mathrm{e}^{-\nu^2/2}}{\sqrt{2\pi}} \frac{1}{\sigma^3(m)} \tag{3.70}$$

where we used the definition of ν in Eq. (3.34). Inserting the Press-Schechter mass function (3.30) and the expansion (3.70) into Eq. (3.69) yields

$$1 + \delta_{\mathrm{h}} = (1+\delta) \left[1 + \frac{\nu^2 - 1}{\delta_{\mathrm{c}}} \delta_{\mathrm{lin}}(\delta) + \frac{\nu^2(\nu^2-3)}{2\delta_c^2} \delta_{\mathrm{lin}}^2(\delta) + \dots \right] . \tag{3.71}$$

From the spherical collapse model we find

$$\delta(\delta_{\mathrm{lin}}) = \delta_{\mathrm{lin}} + \frac{a_2}{2} \delta_{\mathrm{lin}}^2 + \frac{a_3}{3!} \delta_{\mathrm{lin}}^3 + \dots , \tag{3.72}$$

where the coefficients a_i are given in the Appendix B.1. Up to quadratic order in δ this equation can be inverted to:

$$\delta_{\mathrm{lin}}(\delta) \simeq \delta - \frac{a_2}{2} \delta^2 + \mathcal{O}(\delta^3) . \tag{3.73}$$

Inserting this into Eq. (3.71) yields the desired relation between δ_{h} and δ:

$$1 + \delta_{\mathrm{h}} \simeq (1+\delta) \left[1 + \left(\delta - \frac{a_2}{2} \delta^2 \right) \frac{\nu^2 - 1}{\delta_{\mathrm{c}}} + \frac{\nu^2(\nu^2-3)}{2\delta_{\mathrm{c}}^2} \delta^2 + \dots \right] . \tag{3.74}$$

Furthermore, we introduce the halo bias functions $b_i^{\mathrm{h}}(m)$ as coefficients of a power-series expansion of δ_{h}:

$$\delta_{\mathrm{h}}(\delta) \equiv \delta_{\mathrm{h}}(\boldsymbol{x};m) = b_1^{\mathrm{h}}(m)\delta(\boldsymbol{x}) + \frac{b_2^{\mathrm{h}}(m)}{2} \delta^2(\boldsymbol{x}) + \frac{b_3^{\mathrm{h}}(m)}{6} \delta^3(\boldsymbol{x}) + \dots \tag{3.75}$$

We can identify each term by comparing equal orders of δ in Eq. (3.74) with Eq. (3.75). Using this approach we find the bias between halos and the surrounding dark matter:

$$b_1^{\mathrm{h}}(m) \equiv 1 + \frac{\nu^2 - 1}{\delta_{\mathrm{c}}} , \tag{3.76}$$

$$b_2^{\mathrm{h}}(m) \equiv 2 \left(1 - \frac{a_2}{2} \right) \frac{\nu^2 - 1}{\delta_{\mathrm{c}}} + \frac{\nu^2(\nu^2-3)}{\delta_{\mathrm{c}}^2} . \tag{3.77}$$

These expressions represent the linear and quadratic bias of halos with respect to the underlying dark matter field. There is a characteristic mass associated with the linear bias factor. If $\nu = 1$ the correspondence between the underlying dark matter field and halo clustering is unbiased in linear order, i.e., $b_1^{\mathrm{h}}(m) = 1$. The corresponding mass is called m_*, and can be calculated from $\delta_{\mathrm{c}} = \sigma(m_*)$. This characteristic mass is also important for the description of the halo concentration as we saw in Sect. 3.3.1. For $m > m_*$ (i.e., $\nu > 1$) the linear bias factor is $b_1^{\mathrm{h}}(m) > 1$ meaning these halos are biased. But halos with $m < m_*$ are anti-biased, i.e., $b_1^{\mathrm{h}}(m) < 1$. Similarly we find for the quadratic bias factor that $b_2^{\mathrm{h}}(m) < 0$ for $m \lesssim m_*$ and $b_2^{\mathrm{h}}(m) > 0$ for $m \gtrsim m_*$. The presented formalism allows us to calculate halo bias factors of any order.

The discussion of the halo bias was up to now limited to the Press-Schechter mass function. The above calculation can be used for any given mass function, but one needs to use the corresponding conditional mass function. Here we are especially interested in the Sheth-Tormen mass function which is directly fitted to numerical simulations. The linear and quadratic bias functions are then dependent on the parameters q and p of the Sheth-Tormen mass function in Eq. (3.36). In this case, the result for the first three orders of the halo bias expansion are (see Scoccimarro et al. 2001)

$$b_1^{\mathrm{h}}(m) = 1 + \epsilon_1 + E_1 \,, \tag{3.78}$$

$$b_2^{\mathrm{h}}(m) = 2 \left(1 - \frac{a_2}{2}\right)(\epsilon_1 + E_1) + \epsilon_2 + E_2 \,, \tag{3.79}$$

$$b_3^{\mathrm{h}}(m) = 6 \left(-\frac{a_2}{2} + \frac{a_3}{6}\right)(\epsilon_1 + E_1) + 3(1 - a_2)(\epsilon_2 + E_2) + \epsilon_3 + E_3 \,, \tag{3.80}$$

where

$$\epsilon_1 = \frac{q\nu^2 - 1}{\delta_{\mathrm{c}}} \,, \qquad \epsilon_2 = \frac{q\nu^2}{\delta_{\mathrm{c}}}\left(\frac{q\nu^2 - 3}{\delta_{\mathrm{c}}}\right) \,, \qquad \epsilon_3 = \frac{q\nu^2}{\delta_{\mathrm{c}}^3}(q^2\nu^4 - 6q\nu^2 + 3) \,, \tag{3.81}$$

and

$$E_1 = \frac{2p}{1 + (q\nu^2)^p}\frac{1}{\delta_{\mathrm{c}}} \,, \qquad E_2 = \left(\frac{1 + 2p}{\delta_{\mathrm{c}}} + 2\epsilon_1\right)E_1 \,, \tag{3.82}$$

$$E_3 = \left(\frac{4(p^2 - 1) + 6pq\nu^2}{\delta_{\mathrm{c}}^2} + 3\epsilon_1^2\right)E_1 \,. \tag{3.83}$$

For the Press-Schechter mass function the parameters are $p = 0$ and $q = 1$. In this case E_1 and therefore also E_2 vanish and we reproduce the result of the corresponding bias factors in Eqs. (3.76) and (3.77). A general bias factor $b_i^{\mathrm{h}}(m)$ obeys the following consistency relations (Scoccimarro et al. 2001)

$$\frac{1}{\bar{\rho}}\int \mathrm{d}m\, m\, n(m)b_i^{\mathrm{h}}(m) = \int_0^\infty \mathrm{d}\nu\, f(\nu)b_i^{\mathrm{h}}(\nu) = \begin{cases} 1 & \text{for } i = 1 \,, \\ 0 & \text{for } i > 1 \,. \end{cases} \tag{3.84}$$
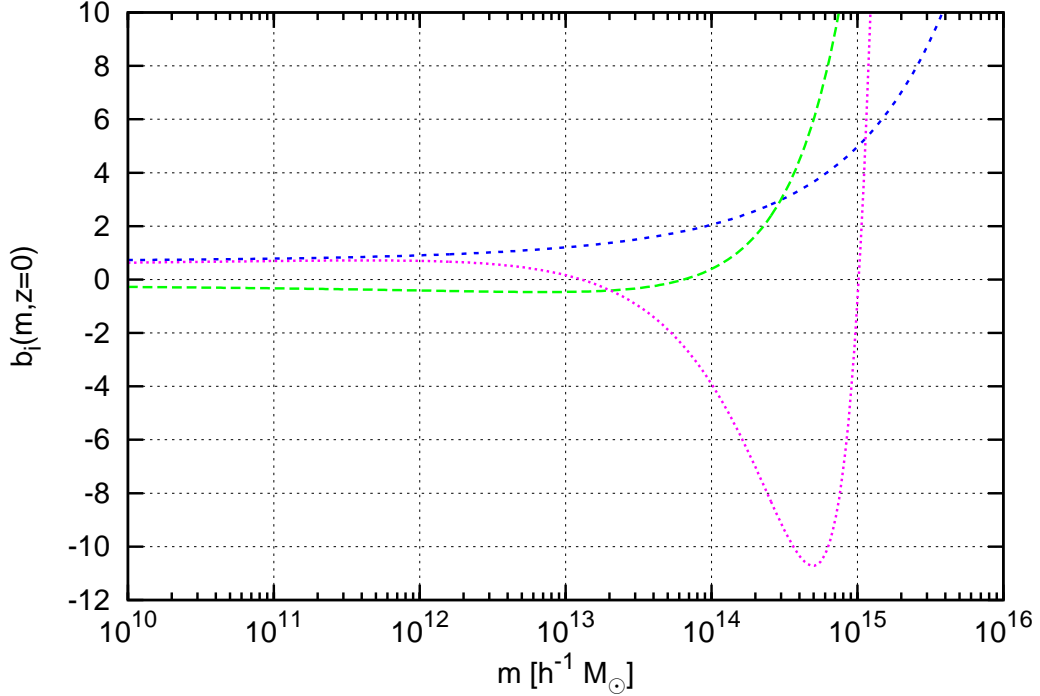
Figure 3.4: First three orders of the halo bias factor expansion in Eq. (3.75) calculated using the Sheth-Tormen mass function at redshift $z = 0$ as a function of the halo mass. The solid line shows the linear halo bias $b_1^h(m)$ (see Eq. 3.78), the dashed line $b_2^h(m)$ (see Eq. 3.79) and the dotted line $b_3^h(m)$ (see Eq. 3.80).

We can easily show that these relations are fulfilled for the first three halo bias factors of the Press-Schechter mass function using the following identities

$$\int_0^\infty d\nu \, f(\nu) = 1 \,, \qquad \int_0^\infty d\nu \, \nu^2 f(\nu) = 1 \,, \qquad (3.85)$$

$$\int_0^\infty d\nu \, \nu^4 f(\nu) = 3 \,, \qquad \int_0^\infty d\nu \, \nu^6 f(\nu) = 15 \,. \qquad (3.86)$$

The consistency relations are important for the formulation of the halo model. The halo model correlation functions should resemble the results of lowest-order non-vanishing perturbation theory on large scales. We will discuss this issue in Sect. 3.5 where we construct halo model spectra.

We depict the halo bias factors b_1^h, b_2^h and b_3^h in Fig. 3.4 using the Sheth-Tormen mass function plotted against the halo mass. The higher-order halo bias factors need to have a zero crossing to fulfill the integral constraint in Eq. (3.84) as seen in the figure.

3.5 Halo Model Correlation Functions

The aim of this section is to derive equations for the two-point, three-point and four-point correlation functions of the dark matter field using the properties of dark matter halos obtained from simulations. We presented the results for the spherical collapse model, the halo mass function, the halo density profile and the halo bias in the previous sections. All these different ingredients are now combined to the dark matter halo model to predict the statistical properties of the dark matter density field. Transforming the equations for the correlation functions into Fourier space, yields the corresponding Fourier space counterparts, i.e., the power spectrum, the bispectrum and the trispectrum. The general approach for the calculation of n-point spectra is the so-called Scherrer-Bertschinger formalism (Scherrer & Bertschinger 1991) developed for a density field that is composed of a superposition of discrete seed masses (here halo masses). The alternative approach replaces the ensemble average with an integral over the joint probability density distribution (PDF) (McClelland & Silk 1977; Smith & Watts 2005; Smith et al. 2006) which is the way we derive the correlation functions in the following.

3.5.1 Two-Point Correlation Function

The two-point auto-correlation function is defined as

$$\xi(\boldsymbol{x}, \boldsymbol{y}) = \langle \delta(\boldsymbol{x})\delta(\boldsymbol{y}) \rangle \,, \tag{3.87}$$

where we considered a general anisotropic and inhomogeneous density field. For a homogeneous and isotropic random field we find

$$\xi(r) = \langle \delta(\boldsymbol{x})\delta(\boldsymbol{y}) \rangle \,, \tag{3.88}$$

where $r = |\boldsymbol{y} - \boldsymbol{x}|$. Rewriting Eq. (3.87) in terms of the density ρ, using the relation

$$\rho(\boldsymbol{r}) = \bar{\rho}[1 + \delta(\boldsymbol{r})] \,, \tag{3.89}$$

yields

$$\langle \rho(\boldsymbol{x})\rho(\boldsymbol{y}) \rangle = \bar{\rho}^2[1 + \xi(\boldsymbol{x}, \boldsymbol{y})] \,. \tag{3.90}$$

Similarly, one can define the two-point cross-correlation function as

$$\langle \rho_a(\boldsymbol{x})\rho_b(\boldsymbol{y}) \rangle = \langle \rho_a \rangle \langle \rho_b \rangle [1 + \xi_{ab}(\boldsymbol{x}, \boldsymbol{y})] \,, \tag{3.91}$$

which describes the correlation between two different continuous functions ρ_a and ρ_b.

The halo model assumes that all matter is bound to dark matter halos. The density field at a position $\boldsymbol{x}$ can then simply be obtained from a superposition of all halos:

$$\rho(\boldsymbol{x}) = \sum_{i=1}^{N} \rho(\boldsymbol{x} - \boldsymbol{x}_i, m_i) = \sum_{i=1}^{N} m_i u(\boldsymbol{x} - \boldsymbol{x}_i, m_i) \,, \tag{3.92}$$

where we used the definition of the normalized density profile $u(\boldsymbol{x}, m)$ given by Eq. (3.53) in the second step. Here N is the total number of halos, m_i and $\boldsymbol{x}_i$ are the mass and the position of the center of the i-th halo, respectively.

Stochastic Approach

We characterize each halo by a set of stochastical parameters: here we consider the position of the i-th halo center $\boldsymbol{x}_i$ and the mass of the i-th halo m_i. Making the assumption of triaxial halos we would get additional parameters describing the orientation of the halo (see Smith & Watts 2005). The ensemble average needed for the calculation of the correlation functions is then given by an integral over all N halo positions and halo masses that form the density field weighted by the PDF. In addition, we sum over the probability for obtaining the N halos given a volume V which we label by $p(N|V)$. Hence, the ensemble average over some quantity F is given by

$$\langle F \rangle \equiv \sum_j p(N_j|V) \left[\int \prod_{i=1}^{N_j} \mathrm{d}^3 x_i \, \mathrm{d}m_i \right] p(\boldsymbol{x}_1, \ldots, \boldsymbol{x}_{N_j}; m_1, \ldots, m_{N_j}|N_j) F, \qquad (3.93)$$

where $p(\boldsymbol{x}_1, \ldots, \boldsymbol{x}_{N_j}; m_1, \ldots, m_{N_j}|N_j)$ is the PDF of the stochastical parameters given the number of N_j halos. For a large volume the probability $p(N|V)$ is very sharply peaked around $N = \bar{n}_\mathrm{h} V$, where $\bar{n}_\mathrm{h}$ is the mean number density of halos. In this case, we can replace $P(N|V)$ with a Kronecker delta function and find for the ensemble average

$$\langle F \rangle \equiv \left[\int \prod_{i=1}^{N} \mathrm{d}^3 x_i \, \mathrm{d}m_i \right] p(\boldsymbol{x}_1, \ldots, \boldsymbol{x}_N; m_1, \ldots, m_N|N) F. \qquad (3.94)$$

In the following, we restrict our analysis to this case only. For a single halo, we assume that the halo mass and halo position are independent random variables. Then we have

$$p(\boldsymbol{x}_1; m_1) = p(\boldsymbol{x}_1) p(m_1) = \frac{1}{V} \frac{n(m)}{\bar{n}_\mathrm{h}}, \qquad (3.95)$$

where $n(m)$ is the halo mass function which is the number density of halos per unit mass. Then the first moment of the density field is

$$\langle \rho(\boldsymbol{r}) \rangle = \sum_{i=1}^{N} \langle m_i u(\boldsymbol{r} - \boldsymbol{x}_i) \rangle = \frac{N}{V \bar{n}_\mathrm{h}} \int \mathrm{d}m \, n(m) m \int \mathrm{d}^3 x \, u(\boldsymbol{r} - \boldsymbol{x}, m) = \bar{\rho}, \qquad (3.96)$$

where we used Eq. (3.92) in the first step to express the density field by a discrete sum over halos, and then applied the ensemble average given in Eq. (3.94). In addition, we used the normalization of the mass function (see Eq. 3.38) and the fact that u is normalized to unity. Similarly, the two-point correlation function of the density field is

$$\langle \rho(\boldsymbol{r}_1) \rho(\boldsymbol{r}_2) \rangle = \sum_{i,j}^{N} \langle m_i m_j u(\boldsymbol{r}_1 - \boldsymbol{x}_i, m_i) u(\boldsymbol{r}_2 - \boldsymbol{x}_j, m_j) \rangle. \qquad (3.97)$$

From now on, we use the following notation convention: the vector $\boldsymbol{r}_i$ labels the considered position of the density field and $\boldsymbol{x}_i$ labels the position of the i-th halo center.

We split the double sum into a sum over correlations in a single halo ($i = j$) and into a sum over correlations in two distinct halos ($i \neq j$):

$$
\begin{aligned}
\langle \rho(\boldsymbol{r}_1)\rho(\boldsymbol{r}_2) \rangle &= \sum_i^N \langle m_i^2 u(\boldsymbol{r}_1 - \boldsymbol{x}_i, m_i)u(\boldsymbol{r}_2 - \boldsymbol{x}_i, m_i) \rangle \\
&\quad + \sum_{i \neq j}^N \langle m_i m_j u(\boldsymbol{r}_1 - \boldsymbol{x}_i, m_i)u(\boldsymbol{r}_2 - \boldsymbol{x}_j, m_j) \rangle \\
&= \frac{N}{V\bar{n}_{\mathrm{h}}} \int \mathrm{d}m\, n(m)m^2 \int \mathrm{d}^3 x\, u(\boldsymbol{r}_1 - \boldsymbol{x}, m)u(\boldsymbol{r}_2 - \boldsymbol{x}, m) \\
&\quad + N(N-1) \int \mathrm{d}m_1\, \mathrm{d}m_2\, \mathrm{d}^3 x_1\, \mathrm{d}^3 x_2\, m_1 m_2 u(\boldsymbol{r}_1 - \boldsymbol{x}_1, m_1)u(\boldsymbol{r}_2 - \boldsymbol{x}_2, m_2) \\
&\quad \times p(\boldsymbol{x}_1, \boldsymbol{x}_2; m_1, m_2)\,,
\end{aligned}
\tag{3.98}
$$

where the joint probability of two distinct halos is

$$
\begin{aligned}
p(\boldsymbol{x}_1, \boldsymbol{x}_2; m_1, m_2) &= p(\boldsymbol{x}_1; m_1)p(\boldsymbol{x}_2; m_2)\left[1 + \xi_{\mathrm{hh}}(\boldsymbol{x}_1, \boldsymbol{x}_2; m_1, m_2)\right] \\
&= \frac{n(m_1)n(m_2)}{\bar{n}_{\mathrm{h}}^2} \frac{1}{V^2}\left[1 + \xi_{\mathrm{hh}}(\boldsymbol{x}_1, \boldsymbol{x}_2; m_1, m_2)\right]\,.
\end{aligned}
\tag{3.99}
$$

Here $\xi_{\mathrm{hh}}(\boldsymbol{x}_1, \boldsymbol{x}_2; m_1, m_2)$ is the two-point correlation function of halo centers. Assuming that the number of halos is large ($N \gg 1$), the second term in Eq. (3.98) becomes

$$
\begin{aligned}
\int \mathrm{d}m_1\, \mathrm{d}m_2\, \mathrm{d}^3 x_1\, \mathrm{d}^3 x_2\, n(m_1)n(m_2)m_1 m_2 u(\boldsymbol{r}_1 - \boldsymbol{x}_1, m_1)u(\boldsymbol{r}_2 - \boldsymbol{x}_2, m_2) \\
\times \left[1 + \xi_{\mathrm{hh}}(\boldsymbol{x}_1, \boldsymbol{x}_2; m_1, m_2)\right]\,.
\end{aligned}
\tag{3.100}
$$

Finally, we apply Eq. (3.90) to rewrite the density correlator (3.98) in terms of the two-point correlation function yielding

$$
\xi_{\text{1-h}}(\boldsymbol{r}_1, \boldsymbol{r}_2) = \int \mathrm{d}m\, n(m)\left(\frac{m}{\bar{\rho}}\right)^2 \int \mathrm{d}^3 x\, u(\boldsymbol{r}_1 - \boldsymbol{x}, m)u(\boldsymbol{r}_2 - \boldsymbol{x}, m)\,,
\tag{3.101}
$$

$$
\begin{aligned}
\xi_{\text{2-h}}(\boldsymbol{r}_1, \boldsymbol{r}_2) &= \int \mathrm{d}m_1\, \mathrm{d}m_2\, \mathrm{d}^3 x_1\, \mathrm{d}^3 x_2\, n(m_1)n(m_2)\left(\frac{m_1}{\bar{\rho}}\right)\left(\frac{m_2}{\bar{\rho}}\right) \\
&\quad \times u(\boldsymbol{r}_1 - \boldsymbol{x}_1, m_1)u(\boldsymbol{r}_2 - \boldsymbol{x}_2, m_2)\xi_{\mathrm{hh}}(\boldsymbol{x}_1, \boldsymbol{x}_2; m_1, m_2)\,.
\end{aligned}
\tag{3.102}
$$

The first term is due to density correlations in a single halo and is therefore found in the literature as *one-halo term*. The second term is due to density correlations in two different halos and is referred to as *two-halo term*. The geometric interpretation of the two terms is shown in Figs. 3.5 and 3.6.

3.5.2 Power Spectrum

Since the two separate halo contributions to the two-point correlation function involve convolutions of the normalized density profiles and for the two-halo term also with
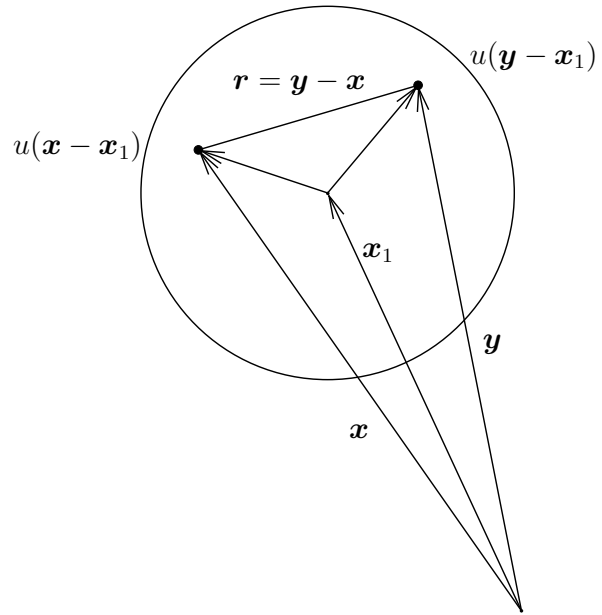
Figure 3.5: Shown is the one-halo contribution to the two-point correlation function. The halo center is labeled by $\boldsymbol{x}_1$. The filled black circles show two different positions labeled by the position vectors $\boldsymbol{x}$ and $\boldsymbol{y}$ for the calculations of the correlation. The two points are separated by the vector $\boldsymbol{r}$. They probe the normalized density profile u at two different positions in the same halo.
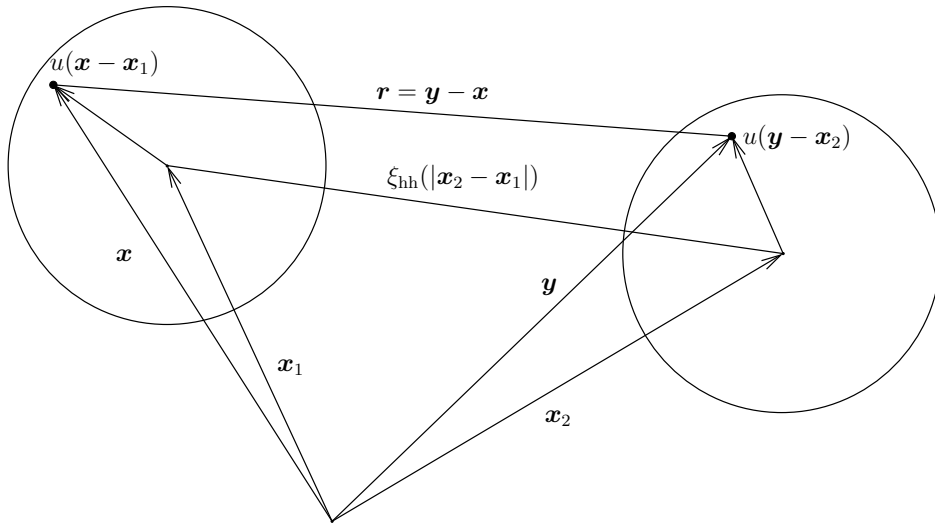

Figure 3.6: Shown is the two-halo contribution to the two-point correlation function. We consider again two points as in Fig. 3.5 but now in two different halos. Therefore, we have to include the clustering of halos described by the correlation ξ_{hh} of the two halo centers $\boldsymbol{x}_1$ and $\boldsymbol{x}_2$.

the halo correlation function, it is easier to work in Fourier space. In this case, the convolutions become simple multiplications. Fourier transforming Eqs. (3.101) and (3.102) yields

$$P_{\text{1-h}}(k) = \int \mathrm{d}m\, n(m) \left(\frac{m}{\bar{\rho}}\right)^2 |\tilde{u}(k,m)|^2 \,, \tag{3.103}$$

$$P_{\text{2-h}}(k) = \int \mathrm{d}m_1\, n(m_1) \left(\frac{m_1}{\bar{\rho}}\right) \tilde{u}(k,m_1) \int \mathrm{d}m_2\, n(m_2) \left(\frac{m_2}{\bar{\rho}}\right) \tilde{u}(k,m_2)$$
$$\times\, P_{\text{hh}}(k; m_1, m_2) \,, \tag{3.104}$$

where $P_{\text{hh}}(k; m_1, m_2)$ is the power spectrum of halo centers. This can be related to the underlying dark matter power spectrum using the concept of the halo bias introduced in Sect. 3.4. We find from transforming the halo-bias expansion given in Eq. (3.75) into Fourier space

$$P_{\text{hh}}(k; m_1, m_2) \equiv \langle \delta_{\text{h}}(k, m_1)\delta_{\text{h}}(k, m_2)\rangle = b_1^{\text{h}}(m_1)b_1^{\text{h}}(m_2)P_{\text{pt}}(k) + \mathcal{O}(\delta_{\text{lin}}^4)\,, \tag{3.105}$$

where the first term is the lowest-order contribution and depends on the linear power spectrum $P_{\text{pt}}(k)$. In principle this relation is only applicable on large scales. Going to smaller scales the one-loop power spectrum and higher orders contribute to the power spectrum of halo centers. Nevertheless, we use only the lowest-order contribution because on small scales the one-halo term is dominant. Applying Eq. (3.105) the two-halo term is

$$P_{\text{2-h}}(k) = \int \mathrm{d}m_1\, n(m_1) \left(\frac{m_1}{\bar{\rho}}\right) \tilde{u}(k,m_1)b_1^{\text{h}}(m_1)$$
$$\times \int \mathrm{d}m_2\, n(m_2) \left(\frac{m_2}{\bar{\rho}}\right) \tilde{u}(k,m_2)b_1^{\text{h}}(m_2)P_{\text{pt}}(k)\,. \tag{3.106}$$

3.5.3 Three-Point Correlation Function

The three-point correlation function is defined as

$$\zeta(\boldsymbol{r}_1, \boldsymbol{r}_2, \boldsymbol{r}_3) \equiv \langle \delta(\boldsymbol{r}_1)\delta(\boldsymbol{r}_2)\delta(\boldsymbol{r}_3)\rangle\,. \tag{3.107}$$

We can relate this to the three-point correlation function of the density field using Eq. (3.89) and find

$$\langle \rho_1\rho_2\rho_3\rangle = \bar{\rho}^3[1 + \langle\delta_1\delta_2\rangle + \langle\delta_1\delta_3\rangle + \langle\delta_2\delta_3\rangle + \langle\delta_1\delta_2\delta_3\rangle]\,. \tag{3.108}$$

Here we employed the short-hand notation $\rho_1 \equiv \rho(\boldsymbol{r}_1)$ and $\delta_1 \equiv \delta(\boldsymbol{r}_1)$, etc. Inserting the halo model representation of the density field given in Eq. (3.92) yields

$$\langle \rho_1\rho_2\rho_3\rangle = \sum_{i,j,k}^{N} \langle m_i m_j m_k u(\boldsymbol{r}_1 - \boldsymbol{x}_i, m_i)u(\boldsymbol{r}_2 - \boldsymbol{x}_j, m_j)u(\boldsymbol{r}_3 - \boldsymbol{x}_k, m_k)\rangle\,. \tag{3.109}$$

Again, we split the triple sum into three terms: contributions from a single halo $(i = j = k)$, contributions from two distinct halos $(i \neq j)$ and contributions from three distinct halos $(i \neq j \neq k)$:

$$
\begin{aligned}
\langle \rho_1 \rho_2 \rho_3 \rangle = & \sum_{i=1}^{N} \langle m_i^3 u(\boldsymbol{r}_1 - \boldsymbol{x}_i, m_i) u(\boldsymbol{r}_2 - \boldsymbol{x}_i, m_i) u(\boldsymbol{r}_3 - \boldsymbol{x}_i, m_i) \rangle \\
& + \sum_{i \neq j}^{N} \Big[\langle m_i^2 m_j u(\boldsymbol{r}_1 - \boldsymbol{x}_i, m_i) u(\boldsymbol{r}_2 - \boldsymbol{x}_i, m_i) u(\boldsymbol{r}_3 - \boldsymbol{x}_j, m_j) \rangle \\
& + \langle m_i^2 m_j u(\boldsymbol{r}_1 - \boldsymbol{x}_i, m_i) u(\boldsymbol{r}_2 - \boldsymbol{x}_j, m_j) u(\boldsymbol{r}_3 - \boldsymbol{x}_i, m_i) \rangle \\
& + \langle m_i^2 m_j u(\boldsymbol{r}_1 - \boldsymbol{x}_j, m_j) u(\boldsymbol{r}_2 - \boldsymbol{x}_i, m_i) u(\boldsymbol{r}_3 - \boldsymbol{x}_i, m_i) \rangle \Big] \\
& + \sum_{i \neq j \neq k}^{N} \langle m_i m_j m_k u(\boldsymbol{r}_1 - \boldsymbol{x}_i, m_i) u(\boldsymbol{r}_2 - \boldsymbol{x}_j, m_j) u(\boldsymbol{r}_3 - \boldsymbol{x}_k, m_k) \rangle \\
\equiv & \; \Gamma_{\text{1-h}}(\boldsymbol{r}_1, \boldsymbol{r}_2, \boldsymbol{r}_3) + \Gamma_{\text{2-h}}(\boldsymbol{r}_1, \boldsymbol{r}_2, \boldsymbol{r}_3) + \Gamma_{\text{3-h}}(\boldsymbol{r}_1, \boldsymbol{r}_2, \boldsymbol{r}_3) \,. \qquad (3.110)
\end{aligned}
$$

Using the ensemble average in Eq. (3.94), the one-halo term of the three-point density correlator becomes

$$
\Gamma_{\text{1-h}} = \int \mathrm{d}m \, n(m) m^3 \int \mathrm{d}^3 x \, u(\boldsymbol{r}_1 - \boldsymbol{x}, m) u(\boldsymbol{r}_2 - \boldsymbol{x}, m) u(\boldsymbol{r}_3 - \boldsymbol{x}, m) \,. \qquad (3.111)
$$

The two-halo term is

$$
\begin{aligned}
\Gamma_{\text{2-h}} = & \; N(N-1) \int \mathrm{d}m_1 \, \mathrm{d}m_2 \, \mathrm{d}^3 x_1 \, \mathrm{d}^3 x_2 \, m_1^2 m_2 \\
& \times u(\boldsymbol{r}_1 - \boldsymbol{x}_1, m_1) u(\boldsymbol{r}_2 - \boldsymbol{x}_1, m_1) u(\boldsymbol{r}_3 - \boldsymbol{x}_2, m_2) p(\boldsymbol{x}_1, \boldsymbol{x}_2; m_1, m_2) + \text{cyc.} \\
= & \; \bar{\rho}^3 \left[\xi_{\text{1-h}}(\boldsymbol{r}_1, \boldsymbol{r}_2) + \xi_{\text{1-h}}(\boldsymbol{r}_2, \boldsymbol{r}_3) + \xi_{\text{1-h}}(\boldsymbol{r}_1, \boldsymbol{r}_3) \right] \\
& + \Big[\int \mathrm{d}m_1 \, \mathrm{d}m_2 \, \mathrm{d}^3 x_1 \, \mathrm{d}^3 x_2 \, n(m_1) n(m_2) m_1^2 m_2 u(\boldsymbol{r}_1 - \boldsymbol{x}_1, m_1) \\
& \times u(\boldsymbol{r}_2 - \boldsymbol{x}_1, m_1) u(\boldsymbol{r}_3 - \boldsymbol{x}_2, m_2) \xi_{\text{hh}}(\boldsymbol{x}_1, \boldsymbol{x}_2; m_1, m_2) + \text{cyc.} \Big] \,, \qquad (3.112)
\end{aligned}
$$

where we used Eq. (3.99) to rewrite the joint probability in the second step. The one-halo term of the two-point correlation function turns up because of the position-independent term in Eq. (3.99). This allows us to perform the integration $\int \mathrm{d}^3 x_2 \, u(\boldsymbol{r}_3 - \boldsymbol{x}_2, m_2)$ which is equal to 1 because we used the normalized density profile. Then we identify the remaining part with the result of the one-halo term of the two-point correlation function given in Eq. (3.101). There are two analogous terms that are given by cyclic permutations of the positions of the halo centers in the halo density profiles. More specifically, we replace the set $\{\boldsymbol{x}_1, \boldsymbol{x}_1, \boldsymbol{x}_2\}$ by $\{\boldsymbol{x}_1, \boldsymbol{x}_2, \boldsymbol{x}_1\}$ and $\{\boldsymbol{x}_2, \boldsymbol{x}_1, \boldsymbol{x}_1\}$ in the

argument of the three normalized density profiles. Finally, the three-halo term is

$$
\Gamma_{\text{3-h}} = N(N-1)(N-2) \int \prod_{i=1}^{3} \mathrm{d}m_i \, \mathrm{d}^3 x_i \, p(\boldsymbol{x}_1, \boldsymbol{x}_2, \boldsymbol{x}_3; m_1, m_2, m_3) m_1 m_2 m_3
$$
$$
\times u(\boldsymbol{r}_1 - \boldsymbol{x}_1, m_1) u(\boldsymbol{r}_2 - \boldsymbol{x}_2, m_2) u(\boldsymbol{r}_3 - \boldsymbol{x}_3, m_3) \,, \tag{3.113}
$$

where the joint PDF for the characteristics of three halos is

$$
p(1, 2, 3) = p(1)p(2)p(3) \left[1 + \xi_{\text{hh}}(1, 2) + \xi_{\text{hh}}(2, 3) + \xi_{\text{hh}}(3, 1) + \zeta_{\text{hhh}}(1, 2, 3) \right] \,, \tag{3.114}
$$

where we used the compact notation $p(i) \equiv p(\boldsymbol{x}_i; m_i)$, $\xi_{\text{hh}}(i, j) \equiv \xi_{\text{hh}}(\boldsymbol{x}_i, \boldsymbol{x}_j)$ and $\zeta_{\text{hh}}(1, 2, 3) \equiv \xi_{\text{hhh}}(\boldsymbol{x}_1, \boldsymbol{x}_2, \boldsymbol{x}_3)$. Then the three-halo term is

$$
\Gamma_{\text{3-h}} = \bar{\rho}^3 \left[1 + \xi_{\text{2-h}}(\boldsymbol{r}_1, \boldsymbol{r}_2) + \xi_{\text{2-h}}(\boldsymbol{r}_2, \boldsymbol{r}_3) + \xi_{\text{2-h}}(\boldsymbol{r}_1, \boldsymbol{r}_3) \right]
$$
$$
+ \int \prod_{i=1}^{3} [\mathrm{d}m_i \, \mathrm{d}^3 x_i \, n(m_i) m_i u(\boldsymbol{r}_i - \boldsymbol{x}_i, m_i)] \zeta_{\text{hhh}}(1, 2, 3) \,, \tag{3.115}
$$

where we used the expression for the two-halo term of the two-point correlation function given in Eq. (3.102). Rewriting all halo functions in terms of the density contrast using Eq. (3.108) yields

$$
\zeta(\boldsymbol{r}_1, \boldsymbol{r}_2, \boldsymbol{r}_3) \equiv \zeta_{\text{1-h}}(\boldsymbol{r}_1, \boldsymbol{r}_2, \boldsymbol{r}_3) + \zeta_{\text{2-h}}(\boldsymbol{r}_1, \boldsymbol{r}_2, \boldsymbol{r}_3) + \zeta_{\text{3-h}}(\boldsymbol{r}_1, \boldsymbol{r}_2, \boldsymbol{r}_3) \,, \tag{3.116}
$$

where

$$
\zeta_{\text{1-h}}(\boldsymbol{r}_1, \boldsymbol{r}_2, \boldsymbol{r}_3) = \int \mathrm{d}m \, n(m) \left(\frac{m}{\bar{\rho}} \right)^3 \int \mathrm{d}^3 x \, u(\boldsymbol{r}_1 - \boldsymbol{x}, m) u(\boldsymbol{r}_2 - \boldsymbol{x}, m) u(\boldsymbol{r}_3 - \boldsymbol{x}, m) \,, \tag{3.117}
$$

$$
\zeta_{\text{2-h}}(\boldsymbol{r}_1, \boldsymbol{r}_2, \boldsymbol{r}_3) = \int \mathrm{d}m_1 \, \mathrm{d}m_2 \, \mathrm{d}^3 x_1 \, \mathrm{d}^3 x_2 \, n(m_1) n(m_2) \left(\frac{m_1}{\bar{\rho}} \right)^2 \left(\frac{m_2}{\bar{\rho}} \right)
$$
$$
\times u(\boldsymbol{r}_1 - \boldsymbol{x}_1, m_1) u(\boldsymbol{r}_2 - \boldsymbol{x}_1, m_1) u(\boldsymbol{r}_3 - \boldsymbol{x}_2, m_2) \xi_{\text{hh}}(1, 2) + \text{cyc.} \,, \tag{3.118}
$$

$$
\zeta_{\text{3-h}}(\boldsymbol{r}_1, \boldsymbol{r}_2, \boldsymbol{r}_3) = \int \prod_{i=1}^{3} [\mathrm{d}m_i \, \mathrm{d}^3 x_i \, n(m_i) \left(\frac{m_i}{\bar{\rho}} \right) u(\boldsymbol{r}_i - \boldsymbol{x}_i, m_i)] \zeta_{\text{hhh}}(1, 2, 3) \,. \tag{3.119}
$$

We note that the additional one- and two-halo terms of the two-point correlation function in Eqs. (3.112) and (3.115) exactly cancel with the terms in Eq. (3.108) leaving only the reduced three-point correlation function.

3.5.4 Bispectrum

Fourier transforming the halo model three-point correlation function which is composed of the three halo terms in Eqs. (3.117), (3.118) and (3.119) using the relation between

the three-point correlation function and the bispectrum defined in Eq. (2.109) yields

$$B_{\text{1-h}} = \int \mathrm{d}m\, n(m) \left(\frac{m}{\rho}\right)^3 \left[\prod_{i=1}^{3} \tilde{u}(\boldsymbol{k}_i, m)\right], \tag{3.120}$$

$$B_{\text{2-h}} = P_{\text{pt}}(k_2) \left[\int \mathrm{d}m_1\, n(m_1) \left(\frac{m_1}{\bar\rho}\right)^2 b_1^{\text{h}}(m_1)\tilde{u}(\boldsymbol{k}_1, m_1)\tilde{u}(\boldsymbol{k}_3, m_1)\right]$$
$$\times \left[\int \mathrm{d}m_2\, n(m_2) \left(\frac{m_2}{\bar\rho}\right) b_1^{\text{h}}(m_2)\tilde{u}(\boldsymbol{k}_2, m_2)\right] + \text{cyc.}\{\boldsymbol{k}_1, \boldsymbol{k}_3, \boldsymbol{k}_2\}, \tag{3.121}$$

$$B_{\text{3-h}} = \int \prod_{i=1}^{3} \left[\mathrm{d}m_i\, n(m_i) \left(\frac{m_i}{\bar\rho}\right) \tilde{u}(\boldsymbol{k}_i, m_i)\right] B_{\text{hhh}}(\boldsymbol{k}_1, \boldsymbol{k}_2, \boldsymbol{k}_3; m_1, m_2, m_3). \tag{3.122}$$

We used Eq. (3.105) for the two-halo term of the bispectrum to replace the power spectrum of halo centers with the dark matter power spectrum times the two first-order halo bias factors. Note that the bispectrum is only non-zero for closed triangles in Fourier space owing to the assumed homogeneity (see the definition of the three-point correlator in Eq. 2.108).

The bispectrum of halo centers in lowest non-vanishing order of the linear density contrast is given by (Matarrese et al. 1997)

$$\begin{aligned}
B_{\text{hhh}}(\boldsymbol{k}_1, \boldsymbol{k}_2, \boldsymbol{k}_3; m_1, m_2, m_3) &= b_1^{\text{h}}(m_1)b_1^{\text{h}}(m_2)b_1^{\text{h}}(m_3)B_{\text{pt}}(\boldsymbol{k}_1, \boldsymbol{k}_2, \boldsymbol{k}_3) \\
&\quad + [b_1^{\text{h}}(m_1)b_1^{\text{h}}(m_2)b_2^{\text{h}}(m_3)P_1 P_2 + \text{perm.}] + \mathcal{O}(\delta_{\text{lin}}^6) \\
&\simeq b_1^{\text{h}}(m_1)b_1^{\text{h}}(m_2)b_1^{\text{h}}(m_3)B_{\text{pt}}(\boldsymbol{k}_1, \boldsymbol{k}_2, \boldsymbol{k}_3),
\end{aligned} \tag{3.123}$$

with $P_i \equiv P_{\text{pt}}(k_i)$. Note that in the second step we neglected all terms proportional to the second-order halo bias factor as they only provide a small contribution (Ma & Fry 2000). This is justified by the fact that on large scales the contribution to the three-halo term of the bispectrum is zero due to the consistency relation for b_2^{h} in Eq. (3.84). Furthermore, smaller scales are dominated by the two-halo and one-halo term. In this case the three-halo term of the dark matter bispectrum is

$$B_{\text{3-h}} = B_{\text{pt}}(\boldsymbol{k}_1, \boldsymbol{k}_2, \boldsymbol{k}_3) \int \prod_{i=1}^{3} \left[\mathrm{d}m_i\, n(m_i)b_1^{\text{h}}(m_i) \left(\frac{m_i}{\bar\rho}\right) \tilde{u}(\boldsymbol{k}_i, m_i)\right]. \tag{3.124}$$

3.5.5 Building Blocks for Dark Matter Halo Model Spectra

One can build general n-point spectra with the halo model function defined by (Cooray & Hu 2001)

$$I_{ij}(k_1, \ldots, k_j) = \int \mathrm{d}m\, n(m) \left(\frac{m}{\bar\rho}\right)^j b_i^{\text{h}}(m)[\tilde{u}(k_1, m) \cdots \tilde{u}(k_j, m)]. \tag{3.125}$$

A halo concentration distribution can be easily incorporated into this model by

$$I_{ij}(k_1, \ldots, k_j) = \int \int \mathrm{d}m \, \mathrm{d}c \, p(c|m) n(m) \left(\frac{m}{\bar{\rho}}\right)^j b_i^{\mathrm{h}}(m) [\tilde{u}(k_1, m, c) \cdots \tilde{u}(k_j, m, c)] \,, \tag{3.126}$$

where the log-normal distribution of the concentration parameter was introduced in Eq. (3.63).

Using the building blocks the halo model power spectrum is

$$P(k) = I_{02}(k, k) + [I_{11}(k)]^2 P_{\mathrm{pt}}(k) \,. \tag{3.127}$$

Furthermore, we can write the bispectrum in the following compact form:

$$B_{\text{1-h}} = I_{03}(k_1, k_2, k_3) \,, \tag{3.128}$$

$$B_{\text{2-h}} = P_1 I_{11}(k_1) I_{12}(k_2, k_3) + P_2 I_{11}(k_2) I_{12}(k_3, k_1) + P_3 I_{11}(k_3) I_{12}(k_1, k_2) \,, \tag{3.129}$$

$$B_{\text{3-h}} = B_{\mathrm{pt}}(\boldsymbol{k}_1, \boldsymbol{k}_2, \boldsymbol{k}_3) I_{11}(k_1) I_{11}(k_2) I_{11}(k_3) \,, \tag{3.130}$$

with $P_i \equiv P_{\mathrm{pt}}(k_i)$. For general n-point spectra we find the same simple behavior for the one-halo term

$$T_{\text{1-h}}^{(n)}(\boldsymbol{k}_1, \ldots, \boldsymbol{k}_n) = I_{0n}(k_1, \ldots, k_n) \,. \tag{3.131}$$

3.5.6 Trispectrum

The halo model trispectrum which is the Fourier space counterpart of the four-point correlation function consists of four terms: the one-halo, two-halo, three-halo and four-halo terms (see Cooray & Hu 2001; Cooray & Sheth 2002):

$$T = T_{\text{1-h}} + T_{\text{2-h}} + T_{\text{3-h}} + T_{\text{4-h}} \,. \tag{3.132}$$

The different terms are shown schematically in Fig. 3.7. We see the correlation between different halo centers for the two-, three- and four-halo terms. For the two- and three-halo terms we need to account for the possible orderings of the points.

By adopting the machinery presented explicitly for the two- and three-point correlation functions, we are able to calculate the different terms of the halo model four-point correlation function which are then transformed into Fourier space using Eq. (2.110) to obtain the trispectrum. The trispectrum is only non-zero when the wave-vectors from a closed quadrilateral in Fourier space. We will leave out the explicit calculation and only show the results. It is easy to guess the form of the one- and four-halo term given by

$$T_{\text{1-h}} = \int \mathrm{d}m \, n(m) \left(\frac{m}{\bar{\rho}}\right)^4 \left[\prod_{i=1}^{4} \tilde{u}(\boldsymbol{k}_i, m)\right] \,, \tag{3.133}$$

$$T_{\text{4-h}} = \int \left[\prod_{i=1}^{4} \mathrm{d}m_i \, n(m_i) \left(\frac{m_i}{\bar{\rho}}\right) \tilde{u}(\boldsymbol{k}_i, m_i)\right] T_{\mathrm{hhhh}}(1, 2, 3, 4) \,, \tag{3.134}$$
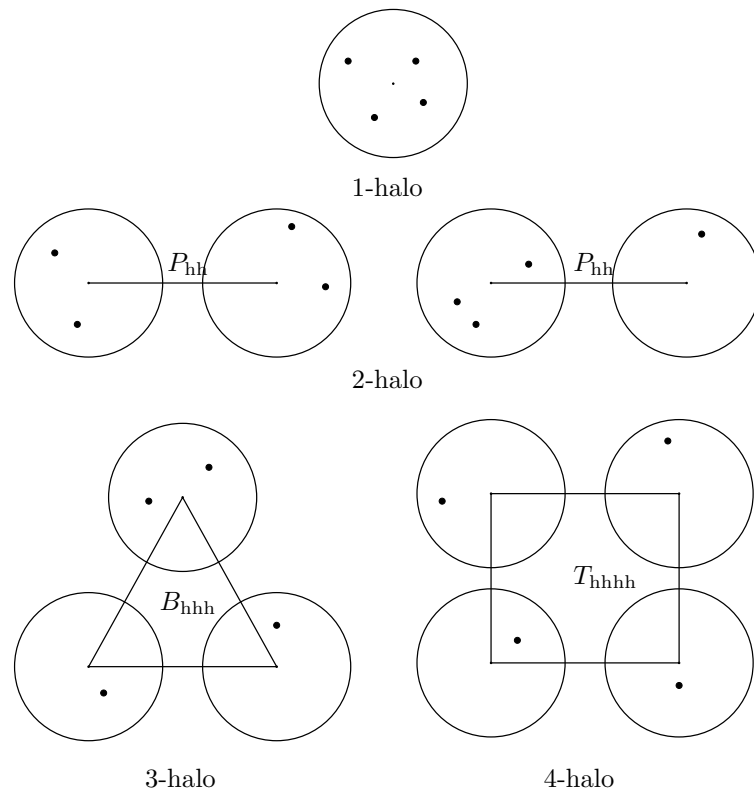
Figure 3.7: Diagrammatic plot of the halo model trispectrum. Shown are the different halo contributions, namely one-halo, two-halo, three-halo and four-halo term. On large scales the mass is distributed in four different halos, and thus the four-halo term is dominant. In the intermediate regime the three-halo and the two-halo term become dominant. On small scales most of the mass is situated in only one halo. The straight lines represent the correlation of halo centers. Using the halo bias description they can be linked to the underlying dark matter spectra.

where we used $T_{\mathrm{hhhh}}(1,2,3,4) \equiv T_{\mathrm{hhhh}}(\boldsymbol{k}_1, \boldsymbol{k}_2, \boldsymbol{k}_3, \boldsymbol{k}_4; m_1, m_2, m_3, m_4)$. For the one-halo term that is dominant on small scales one gets:

$$T_{\text{1-h}} = I_{04}(k_1, k_2, k_3, k_4)\,, \tag{3.135}$$

and for the four-halo term we need the trispectrum of halo centers.

$$\begin{aligned}
T_{\mathrm{hhhh}}(1,2,3,4) &= b_1^{\mathrm{h}}(m_1)b_1^{\mathrm{h}}(m_2)b_1^{\mathrm{h}}(m_3)b_1^{\mathrm{h}}(m_4)T_{\mathrm{pt}}(\boldsymbol{k}_1, \boldsymbol{k}_2, \boldsymbol{k}_3, \boldsymbol{k}_4) \\
&\quad + [b_1(m_1)b_1^{\mathrm{h}}(m_2)b_1^{\mathrm{h}}(m_3)b_3^{\mathrm{h}}(m_4)P_1 P_2 P_3 + \text{perm.}] + \mathcal{O}(\delta_{\mathrm{lin}}^8) \\
&\simeq T_{\mathrm{pt}}(\boldsymbol{k}_1, \boldsymbol{k}_2, \boldsymbol{k}_3, \boldsymbol{k}_4)\left[\prod_{i=1}^{4} b_1^{\mathrm{h}}(m_i)\right]\,,
\end{aligned} \tag{3.136}$$

where T_{pt} is the lowest-order perturbation theory contribution of the trispectrum as given in Eqs. (2.130) and (2.131). Here we again neglected higher-order bias factors in the second step since on large scales b_3^{h} is zero due to the consistency relation in Eq. (3.84). Hence, the four-halo term is given by

$$T_{\text{4-h}} = T_{\mathrm{pt}}(\boldsymbol{k}_1, \boldsymbol{k}_2, \boldsymbol{k}_3, \boldsymbol{k}_4) \int \left[\prod_{i=1}^{4} \mathrm{d}m_i\, n(m_i)\left(\frac{m_i}{\bar{\rho}}\right) b_1^{\mathrm{h}}(m_i)\tilde{u}(\boldsymbol{k}_i, m_i)\right]\,, \tag{3.137}$$

or in terms of the building blocks

$$T_{\text{4-h}} = I_{11}(k_1)I_{11}(k_2)I_{11}(k_3)I_{11}(k_4)T_{\mathrm{pt}}(\boldsymbol{k}_1, \boldsymbol{k}_2, \boldsymbol{k}_3, \boldsymbol{k}_4)\,. \tag{3.138}$$

The two-halo term is given by two separate contributions, since there are two possible combinations to distribute four points in two halos: three points in the first and one in the second halo or two points in each halo. We denote the first contribution by T_{31} and the second by T_{22}, respectively. Hence, the two-halo term is

$$T_{\text{2-h}} = T_{31} + T_{22}\,, \tag{3.139}$$

with

$$\begin{aligned}
T_{31} &= \frac{1}{\bar{\rho}^4} \int \mathrm{d}m_1\, \mathrm{d}m_2\, n(m_1)n(m_2)m_1 m_2^3\, \tilde{u}(\boldsymbol{k}_1, m_1)\tilde{u}(\boldsymbol{k}_2, m_2)\tilde{u}(\boldsymbol{k}_3, m_2)\tilde{u}(\boldsymbol{k}_4, m_2) \\
&\quad \times P_{\mathrm{hh}}(k_1; m_1, m_2) + \text{cyc.}\{\boldsymbol{k}_1, \boldsymbol{k}_2, \boldsymbol{k}_3, \boldsymbol{k}_4\}\,, \tag{3.140} \\
T_{22} &= \frac{1}{\bar{\rho}^4} \int \mathrm{d}m_1\, \mathrm{d}m_2\, n(m_1)n(m_2)m_1^2 m_2^2\, \tilde{u}(\boldsymbol{k}_1, m_1)\tilde{u}(\boldsymbol{k}_2, m_1)\tilde{u}(\boldsymbol{k}_3, m_2)\tilde{u}(\boldsymbol{k}_4, m_2) \\
&\quad \times P_{\mathrm{hh}}(|\boldsymbol{k}_1 + \boldsymbol{k}_2|; m_1, m_2) + \text{cyc.}\{\boldsymbol{k}_1, \boldsymbol{k}_2, \boldsymbol{k}_3, \boldsymbol{k}_4\}\,. \tag{3.141}
\end{aligned}$$

Here P_{hh} is the halo center power spectrum of the two halos. Including the cyclic permutations, T_{31} consists of four terms and T_{22} of three terms. Inserting Eq. (3.105)
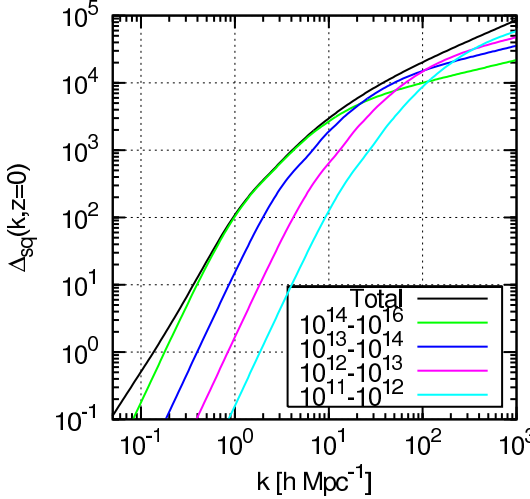
Figure 3.8: Mass contributions of the "square-configuration" of the dark matter trispectrum defined in Eq. (3.146) at redshift $z = 0$. Shown is the effect on the one-halo term from halos in the mass range of $10^{14} \, h^{-1} \, M_\odot < m < 10^{16} \, h^{-1} \, M_\odot$, $10^{13} \, h^{-1} \, M_\odot < m < 10^{14} \, h^{-1} \, M_\odot$, $10^{12} \, h^{-1} \, M_\odot < m < 10^{13} \, h^{-1} \, M_\odot$ and $10^{11} \, h^{-1} \, M_\odot < m < 10^{12} \, h^{-1} \, M_\odot$ as indicated by the line color. The black line shows the total trispectrum.

for the power spectrum of halos, we can write both equations in terms of the building blocks:

$$
\begin{aligned}
T_{31} &= P_1 I_{11}(k_1) I_{13}(k_2, k_3, k_4) + P_2 I_{11}(k_2) I_{13}(k_3, k_4, k_1) \\
&\quad + P_3 I_{11}(k_3) I_{13}(k_4, k_1, k_2) + P_4 I_{11}(k_4) I_{13}(k_1, k_2, k_3) \,, \quad (3.142) \\
T_{22} &= P_{1+2} I_{12}(k_1, k_2) I_{12}(k_3, k_4) + P_{1+3} I_{12}(k_1, k_3) I_{12}(k_2, k_4) \\
&\quad + P_{1+4} I_{12}(k_1, k_4) I_{12}(k_2, k_3) \,, \quad (3.143)
\end{aligned}
$$

where we used the compact notation $P_i \equiv P_{\mathrm{pt}}(k_i)$ and $P_{i+j} \equiv P_{\mathrm{pt}}(|\boldsymbol{k}_i + \boldsymbol{k}_j|)$.

Similarly, the three-halo term is

$$
\begin{aligned}
T_{\text{3-h}} = \frac{1}{\bar{\rho}^4} \int \Big[\prod_{i=1}^3 \mathrm{d}m_i \, n(m_i) \Big] m_1 m_2 m_3^2 \, \tilde{u}(\boldsymbol{k}_1, m_1) \tilde{u}(\boldsymbol{k}_2, m_2) \tilde{u}(\boldsymbol{k}_3, m_3) \tilde{u}(\boldsymbol{k}_4, m_3) \\
\times B_{\mathrm{hhh}}(\boldsymbol{k}_1, \boldsymbol{k}_2, \boldsymbol{k}_3 + \boldsymbol{k}_4; m_1, m_2, m_3) + \mathrm{cyc.}\{\boldsymbol{k}_1, \boldsymbol{k}_2, \boldsymbol{k}_3, \boldsymbol{k}_4\} \,, \quad (3.144)
\end{aligned}
$$

where B_{hhh} describes the correlation of the three halo centers given in Eq. (3.123). In terms of the building blocks we find then

$$
\begin{aligned}
T_{\text{3-h}} = {}& I_{11}(k_1) I_{11}(k_2) B_{\mathrm{pt}}(\boldsymbol{k}_1, \boldsymbol{k}_2, \boldsymbol{k}_{34}) I_{12}(k_3, k_4) + I_{11}(k_3) I_{11}(k_4) B_{\mathrm{pt}}(\boldsymbol{k}_3, \boldsymbol{k}_4, \boldsymbol{k}_{12}) I_{12}(k_1, k_2) \\
& + I_{11}(k_2) I_{11}(k_4) B_{\mathrm{pt}}(\boldsymbol{k}_2, \boldsymbol{k}_4, \boldsymbol{k}_{13}) I_{12}(k_1, k_3) + I_{11}(k_2) I_{11}(k_3) B_{\mathrm{pt}}(\boldsymbol{k}_2, \boldsymbol{k}_3, \boldsymbol{k}_{14}) I_{12}(k_1, k_4) \\
& + I_{11}(k_1) I_{11}(k_4) B_{\mathrm{pt}}(\boldsymbol{k}_1, \boldsymbol{k}_4, \boldsymbol{k}_{23}) I_{12}(k_2, k_3) + I_{11}(k_1) I_{11}(k_3) B_{\mathrm{pt}}(\boldsymbol{k}_1, \boldsymbol{k}_3, \boldsymbol{k}_{24}) I_{12}(k_2, k_4)
\end{aligned}
$$
$$(3.145)$$

with $\boldsymbol{k}_{ij} = \boldsymbol{k}_i + \boldsymbol{k}_j$.

We show the total dark matter trispectrum in Fig. 3.8 and additionally the different mass contributions to the one-halo term. To make a two-dimensional plot, we define the square configuration of the trispectrum by

$$
\Delta_{\mathrm{sq}}(k) \equiv \frac{k^3}{2\pi^2} \left[T(\boldsymbol{k}_1, -\boldsymbol{k}_1, \boldsymbol{k}_2, -\boldsymbol{k}_2) \right]^{1/3} \,, \quad (3.146)
$$

where $\boldsymbol{k}_1 \cdot \boldsymbol{k}_2 = 0$ and $|\boldsymbol{k}_1| = |\boldsymbol{k}_2| \equiv k$. Up to $k \simeq 20\,h\,\mathrm{Mpc}^{-1}$ the trispectrum is dominated by the most massive halos ($10^{14}\,h^{-1}\,M_\odot < m < 10^{16}\,h^{-1}\,M_\odot$). On the other hand, the small-scale trispectrum ($k \gtrsim 300\,h\,\mathrm{Mpc}^{-1}$) is dominated by small mass halos in the interval $10^{11}\,h^{-1}\,M_\odot < m < 10^{12}\,h^{-1}\,M_\odot$.

Chapter 4

Halo Model for Galaxy Clustering

The angular correlation function of galaxies is one of the basic observables for constraining cosmological models. Observational results from large galaxy surveys like the SDSS (Sloan Digital Sky Survey)[1] or the 2dF-survey report that the angular galaxy correlation function is well described by a simple power law over a wide range of scales[2]. As the angular correlation function is a projection of the three-dimensional correlation function also the three-dimensional galaxy correlation function and its Fourier counterpart, the galaxy power spectrum, are described by a power law. However, the dark matter power spectrum cannot be described by a single power law. Thus, theoretical and observational work need to clarify the scale-dependent difference between galaxy and dark matter clustering, which is also known as the *galaxy-dark matter bias*. Additionally, experiments find that the galaxy correlation function is strongly dependent on color. For example on small scales, red galaxies have a steeper correlation function than blue galaxies. Hence, the bias also depends on the type of the considered galaxies.

Due to its complementary and unique features compared to the dark matter correlation function, it is important to find reliable theoretical models for the galaxy correlation function. Also, historically the galaxy correlation function was measured first as it basically traces the light distribution of the Universe which is directly measurable. However, theoretical models are mostly available for the dark matter correlation function, and thus careful modeling of the bias influenced by non-linear physics is needed. In addition, galaxy redshift surveys observe galaxies in redshift space and thus need to include the effect of peculiar velocities of galaxies on the correlation function which lead to the so-called *redshift-space distortions*. Leaving this complication aside we need to know the physics of galaxy formation to model the bias. The basic picture for the formation of galaxies (see the pioneering work of White & Rees 1978) is that baryonic gas can only cool and form stars if it is in potential wells, for example provided by virialized dark matter halos. In this picture, more massive halos contain on average more galaxies than less massive halos as they allow more gas to cool. In addition, we

---

[1] `www.sdss.org`

[2] Recent results in Zehavi et al. (2004) show small deviations from a power law, in particular a change of the slope at $r \sim 1 - 2 \, h^{-1} \, \mathrm{Mpc}$. With the same number of parameters as a power law the halo model for galaxy clustering provides a significantly better fit which is one of the reasons for its popularity. Note that we assume here that the parameters of the dark model halo are fixed by the results of simulations.

assume a threshold mass above which the formation of galaxies in halos is possible. This is due to the fact that the gravitational potential of the halo needs to be strong enough to oppose the energy feedback from supernova explosions which follow an initial burst of star formation. In summary, the physics of galaxy formation involves the following processes: gas cooling, star formation, stellar evolution, stellar feedback etc. Recent N-body simulations start to include baryons into their dissipationless dark matter simulations. The challenge is to model all these effects to provide realistic density and velocity fields at each redshift output. However, these simulations are very time-consuming and face fundamental problems, for example the so-called *overcooling problem* that the stellar masses of the galaxies in the simulation outputs are larger than the ones in observed galaxies (see for example Nagai & Kravtsov 2004). Moreover, these simulations can cover only small comoving volumes due to the large computational requirements and are thus strongly affected by sample variance. Therefore, precision forecasts from simulations including baryons are not expected in the near future. This explains the need for analytic models like the halo model which provides an interplay between theoretical results and results from simulations. Furthermore, halo model calculations are much faster to perform than simulations and thus permit the rapid exploration of a large parameter space. Contrary to the partly problematic results of baryonic simulations, dissipationless dark matter simulations provide much more stable and reliable results. We expect to have precision forecasts from dark matter-only simulations in the near future replacing the dark matter halo model calculations. On the other hand, the halo model turns out to be a suited model to describe galaxy clustering – on large scales only the clustering between different dark matter halos play an important role – on small scales gas-dynamics, radiative cooling and star formation influence the distribution of galaxies within halos. Therefore, it naturally splits the problem of modeling the galaxy correlation function into the well-known properties of dark matter halos and the theory of galaxy formation on small scales.

In this chapter, we want to model the correlation functions of galaxies using the methods of the dark matter halo model as described in the previous chapter. The halo model for dark matter can be easily extended to account for this case. We present these extensions in the following and comment on their limitations.

The outline of this chapter is as follows: In Sect. 4.1, we introduce the basic extensions of the halo model for dark matter such that it can be used to describe galaxy clustering. After we established the new formalism, we show the results of the galaxy power spectrum in Sect. 4.2. Section 4.3 provides a short introduction of the general form of the galaxy-dark matter cross-spectra using the halo model and shows the results of the cross-power spectrum. In Sect. 4.4, we derive the expressions for the galaxy-dark matter cross-bispectrum that is probed by galaxy-galaxy-galaxy lensing surveys. We then derive the expression for the cross-trispectrum in Sect. 4.5 that is needed for the calculation of the errors of the galaxy-galaxy lensing signal. Finally, in Sect. 4.6 we present the results of a concentration parameter distribution for the galaxy and cross-spectra and compare them with the corresponding dark matter spectra.

4.1 Building Blocks for Galaxy Clustering

We presented the building blocks of dark matter clustering, i.e., the spherical collapse model, the halo mass function, the clustering of halos and the halo density profile in the previous chapter. Here we show the extensions of the dark matter halo model, namely the building blocks for galaxy clustering.

In the introduction of this chapter we argued that galaxies form only in the environment of dark matter halos as they allow the gas to cool[3]. To incorporate galaxies into the halo model one replaces the weighting by the halo mass m with the weighting of the number of galaxies by the so-called *halo occupation distribution* (HOD) $P(N|m)$, which is the conditional probability that a halo of mass m contains N galaxies. Note that we make the assumption that the HOD depends only on the halo mass and is independent of the environment of the halo, i.e., if the halo is situated in low-density or high-density regions. Furthermore, we assume that the first galaxy within each halo above a *threshold mass* is placed at the center of the halo. Subsequent galaxies are placed around the halo center following the galaxy distribution profile $u_{\mathrm{g}}(\boldsymbol{r}, m)$:

$$u_{\mathrm{g}}(\boldsymbol{r}, m) \equiv \frac{\rho_{\mathrm{g}}(\boldsymbol{r})}{\int \mathrm{d}^3 r \, \rho_{\mathrm{g}}(\boldsymbol{r})} \,, \tag{4.1}$$

where ρ_{g} describes the average spatial distribution of these galaxies around the halo center which is normalized by the expected number of galaxies. The form of this profile can be approximated by the distribution of dark matter subhalos because galaxies condense in these subhalos. Substructure or subhalos originate in massive halos via the hierarchical merging and accretion of smaller progenitors. We need to accurately know the distribution of the dark matter substructure to estimate the subhalo profile which is beyond the resolution limit of most simulations. In addition, galaxy density profiles are almost certainly different from dark matter density profiles due to *tidal stripping* which introduces a radial bias as the effect is stronger near the core of the host halo and weaker near the virial radius (see Nagai & Kravtsov 2005). In particular, it is possible to model a difference in both profiles by adopting different parameters for the concentration-mass relation of the NFW profile in Eq. (3.62). To simplify things, we assume that the dark matter and the galaxy density distribution follow the same density profile, i.e., in terms of the normalized profile in Fourier space $\tilde{u}_{\mathrm{dm}}(k, m) = \tilde{u}_{\mathrm{g}}(k, m) \equiv \tilde{u}(k, m)$. However, in the following sections we formulate the equations without assuming equal density profiles to distinguish between terms coming from dark matter and galaxy clustering.

We also need to replace the mean mass density in the dark matter halo model in Eq. (3.38) by the mean number density of galaxies to correctly normalize the spectra. The mean galaxy number density is given by the completeness relation

$$\bar{n}_{\mathrm{g}} = \int \mathrm{d}m \, n(m) \langle N(m) \rangle \,. \tag{4.2}$$

---

[3]Recall that the halo model assumes that all mass is contained in dark matter halos.

In summary, the changes from the dark matter halo model to the halo model including galaxies are from a technical point of view only minor. The properties of the dark matter halos which contain the galaxies and the clustering between the halos are unchanged compared to the dark matter spectra. For the case of halos that contain only satellite galaxies, we can simply extend the construction of n-point spectra of dark matter clustering in Eq. (3.125) by using the following galaxy building blocks

$$G_{ij}^{\mathrm{nc}}(k_1, \ldots, k_j) = \int \mathrm{d}m\, n(m) \frac{\langle N^{(j)}(m) \rangle}{\bar{n}_{\mathrm{g}}^j} b_i^{\mathrm{h}}(m) [\tilde{u}_{\mathrm{g}}(k_1, m) \cdots \tilde{u}_{\mathrm{g}}(k_j, m)], \qquad (4.3)$$

and the correlations of halo centers as before. The superscript "nc" indicates that we assume that the halos contain only satellite galaxies. We derive the building blocks for the realistic case of an additional central galaxy contribution in Sect. 4.1.2 below considering a specific HOD parametrization. The result in Eq. (4.3) is just an adaptation of the results from the previous chapter with the replacements

$$m^j \to \langle N^{(j)}(m) \rangle, \qquad \bar{\rho}^j \to \bar{n}_{\mathrm{g}}^j. \qquad (4.4)$$

The j-th factorial moment of the HOD is defined as

$$\langle N^{(j)}(m) \rangle \equiv \left\langle \prod_{l=1}^{j} (N + 1 - l)(m) \right\rangle = \sum_{N=0}^{\infty} N(N-1) \cdots N(N+1-j) P(N|m), \quad (4.5)$$

where we replaced in the second step the ensemble average by an average of the conditional probability $P(N|m)$. Of particular interest for the subsequent analysis are the first three factorial moments that characterize the spectra we use below. The first factorial moment is given by

$$\langle N^{(1)}(m) \rangle = \langle N(m) \rangle \equiv \sum_{N=0}^{\infty} N P(N|m), \qquad (4.6)$$

and is for example probed by the one-halo term of the cross-power spectrum. The second factorial moment is

$$\langle N^{(2)}(m) \rangle = \langle N(N-1)(m) \rangle \equiv \sum_{N=0}^{\infty} N(N-1) P(N|m) \qquad (4.7)$$

which describes the mean number of possible pairings of two galaxies (counting each pair twice) probed for example by the one-halo term of the galaxy power spectrum and the third factorial moment

$$\langle N^{(3)}(m) \rangle = \langle N(N-1)(N-2)(m) \rangle \equiv \sum_{N=0}^{\infty} N(N-1)(N-2) P(N|m). \qquad (4.8)$$

quantifies the mean number of possible galaxy triplets (counting each triplet 6 times) as probed for example by the one-halo term of the galaxy bispectrum. Higher-order

correlation functions probe also higher-order moments of the HOD in this formalism and they are defined accordingly. Note that the probability is normalized such that $\sum_{N=0}^{\infty} P(N|m) = 1$. Note that by using the factorial moments we neglect self-correlations of galaxy pairs, triplets, etc., which lead to shot noise terms. We need to add these shot noise terms because in contrast to the continuous dark matter field the observed galaxy distribution is a discrete field.

The only missing component for calculating galaxy spectra explicitly is a model for the HOD. The next section provides a comprehensive description of the HOD including its parametrization. Using these results we are able to model the galaxy auto- and galaxy-dark matter cross-spectra at arbitrary order. The results up to the fourth order which are needed for the rest of this thesis will be presented in subsequent sections.

4.1.1 Halo Occupation Distribution

The HOD formalism has emerged as one of the most powerful frameworks for modeling galaxy clustering in recent years. As it is a model for understanding galaxy clustering, it can also be used to constrain the bias between dark matter and galaxies which depends on the physics of galaxy formation that is rather poorly understood. Referring to Berlind & Weinberg (2002) the HOD is composed of three different components: the conditional probability distribution $P(N|m)$ that a halo of virial mass m contains N galaxies, the radial distribution of galaxies in their host halo, and the relative velocity dispersion of galaxies. As the latter two parts are usually assumed to follow the dark matter case, we will put the emphasis on the first component, i.e., the conditional halo probability distribution. Most notably the HOD framework provides a complete description of the bias factor as mentioned by Berlind & Weinberg (2002). To achieve this goal we need to determine the information contained in all factorial moments of the HOD. Note that by defining the HOD we assume a luminosity threshold to select specific galaxy samples.

Furthermore, we can define representations of the HOD corresponding to specific galaxy samples that are defined by luminosity, color, morphology etc. One can for example separate the contributions from red and blue galaxies (defined according to their stellar composition) to the average total number of galaxies:

$$\langle N(m) \rangle = \langle N_{\text{blue}}(m) \rangle + \langle N_{\text{red}}(m) \rangle . \tag{4.9}$$

Having defined the mathematical properties of the HOD we will now focus on its determination. The HOD is obtained from N-body simulations[4] or fitted to results from galaxy surveys. The simulations find for the first moment of the HOD an extended plateau at low halo masses, where there is on average only 1 galaxy inside the halo,

---

[4]There are three types of simulations: simulations resolving subhalos which are supposed to be good tracers of the galaxy positions, dark matter N-body simulations that populate the dark matter halos with galaxies using semi-analytic models of galaxy formation and simulations that include the coupled baryonic-dark matter differential equations.

i.e., $\langle N(m) \rangle \simeq 1$. Considering a halo threshold mass of $m = 10^{11} \, h^{-1} M_\odot$ the plateau extends to $m = 10^{13} \, h^{-1} M_\odot$. For $m > 10^{13} \, h^{-1} M_\odot$ the halo is populated by satellite galaxies which are well described by a power law in halo mass. Note that the stated halo masses shift accordingly with increasing of the threshold mass.

Results of different simulations for higher-order moments of the HOD find that the distribution $P(N|m)$ is sub-Poissonian (that is, the distribution is narrower than a Poisson distribution, or more precisely the corresponding variance is smaller than the variance of a Poisson distribution) around the threshold mass and Poissonian[5] for large host halo masses. Several simple functions have been considered for the shape of the HOD distribution, and we present now the two most important ones.

The first results to model higher-order moments of the HOD were done using halo model fits to results of the APM (Automatic Plate Measuring Facility) galaxy survey (Scoccimarro et al. 2001). They assumed that the HOD is described by a binomial distribution, in which case higher orders are completely specified by the first and second moments of this distribution. In addition, they relate the second-order moment to the first-order moment by introducing the function $\alpha(m)$ which fulfills

$$\langle N(N-1)(m) \rangle \equiv \alpha^2(m) \langle N(m) \rangle^2 \, , \qquad (4.10)$$

and is given by

$$\alpha(m) = \begin{cases} 1 & \text{for } m \geq 10^{13} \, h^{-1} M_\odot \, , \\ \log_{10} \left(\sqrt{m/m_{11}} \right) & \text{for } m < 10^{13} \, h^{-1} M_\odot \, . \end{cases} \qquad (4.11)$$

In this model the threshold mass is $m_{11} = 10^{11} \, h^{-1} M_\odot$. The function $\alpha(m)$ describes the departure from a Poisson distribution of the HOD. We see that for large masses the galaxies follow a Poisson distribution, but for small masses there are deviations from the Poisson statistics.

The second approach developed by Kravtsov et al. (2004) separates the number of galaxies in halos into two different contributions: *central galaxies* hosting the dark matter halo and a number of *satellite galaxies* that subsequently populate the halo. The motivation for this decomposition comes partly from results of simulations and studies of central elliptical galaxies in groups and clusters which are often considered as a separate population from the rest of the galaxies in the observed group or cluster[6]. This separation turns out to naturally reproduce the observed sub-Poissonian behavior for small masses where the correlations of central galaxies dominate, as well as the change to the Poissonian behavior for large masses where satellite correlations dominate.

---

[5] For a Poisson distributed random variable X the ensemble average of X is equal to the variance of X, i.e., $\langle X \rangle = \langle X^2 \rangle - \langle X \rangle^2$.

[6] The galaxy sitting in the center of the cluster is in the majority of cases the most luminous and massive one in the cluster and therefore called the *brightest cluster galaxy* (BCG). These galaxies are generally old ellipticals and except for those undergoing major mergers, they lie at the bottom of the cluster potential well and close to the X-ray emission peak.

Furthermore, Kravtsov et al. assume that each halo hosts one central galaxy only if it has a mass above the *minimal mass* $m_{\min}$. Below this minimal mass there will not be enough cold gas to form galaxies as mentioned before. Therefore, the number of central galaxies $N_{\mathrm{cen}}(m)$ can be approximated by a step function:

$$N_{\mathrm{cen}}(m) = \Theta(m - m_{\min}),\tag{4.12}$$

where $\Theta(m)$ is the Heaviside step function. In practice flux-limited galaxy samples are defined by a lower luminosity threshold $L_{\min}$ rather than a minimal host halo mass. Therefore, we need to find a conversion of $L_{\min}$ to $m_{\min}$. The stochastic nature of galaxy formation induces scatter in the central galaxy luminosity at a fixed halo mass m which is well modeled by a log-normal distribution. This scatter in the luminosity translates into a scatter in the host halo mass. We can model the scatter by convolving the step function with a log-normal distribution of variance $\sigma_{\ln m}^2$ and zero mean. The result is[7] (e.g., Zheng et al. 2007)

$$\langle N_{\mathrm{cen}}(m) \rangle = \frac{1}{2} \, \mathrm{erfc} \left[\frac{\ln(m_{\min}/m)}{\sqrt{2}\sigma_{\ln m}} \right].\tag{4.13}$$

This more realistic modeling comes at the expense of an additional parameter, i.e., the dispersion $\sigma_{\ln m}$. Using this approach, on average half of the halos in the sample with a mass of $m = m_{\min}$ host a central galaxy.

After the placement of the central galaxy the halo is populated by satellite galaxies. The mean number of satellite galaxies follows approximately a Poisson distribution, where the first moment is well described by

$$\langle N_{\mathrm{sat}}(m) \rangle = \left(\frac{m}{m_1} \right)^{\beta} \Theta(m - m_{\min}),\tag{4.14}$$

where we use a simple power law with the amplitude and slope as free parameters. Here m_1 is linearly related to the minimal mass, i.e., $m_1 = A_{\mathrm{s}} m_{\min}$ with the parameter $A_{\mathrm{s}} > 1$. In summary, the HOD is characterized by four parameters: the minimal mass $m_{\min}$ above which halos are populated with galaxies, the scatter of the mean number of central galaxies $\sigma_{\ln m}$, and the two parameters β and A_{s} that specify the power law of satellite galaxies. Note that the minimal mass is not a free parameter but is fixed by matching the mean number density in Eq. (4.2) to that of a given survey sample defined by a minimal luminosity. Recent simulations indicate (Zheng et al. 2005) that at low masses the mean number of satellite galaxies drops below the power-law extrapolation from high masses. This behavior is well modeled by introducing an additional cut-off parameter m_0 that can differ from the minimal mass of central galaxies. Then the first moment of the satellite galaxies in Eq. (4.14) is replaced by

$$\langle N_{\mathrm{sat}}(m) \rangle = \left(\frac{m - m_0}{m_1'} \right)^{\beta} \Theta(m - m_0),\tag{4.15}$$

---

[7]Sometimes the dispersion $\sigma_{\ln m}$ is defined including a factor $\sqrt{2}$.

with the two new parameters m_1' and m_0. As this results only in a minor change in the galaxy power spectrum we will adopt the four-parameter model.

Combining the contributions from the central and satellite galaxies we get the total number of galaxies, i.e., $N = N_{\mathrm{cen}} + N_{\mathrm{sat}}$. Using the different statistical properties of centrals and satellites, we are able to relate higher-order factorial moments of the total number of galaxies to first-order moments of central and satellite galaxies. We show explicitly the results of the first four orders of the HOD:

$$\langle N(N-1)\rangle = \langle N_{\mathrm{sat}}(N_{\mathrm{sat}}-1)\rangle + \langle N_{\mathrm{cen}}(N_{\mathrm{cen}}-1)\rangle + 2\langle N_{\mathrm{cen}}N_{\mathrm{sat}}\rangle$$
$$= \langle N_{\mathrm{sat}}\rangle^2 + 2\langle N_{\mathrm{cen}}\rangle\langle N_{\mathrm{sat}}\rangle\,, \tag{4.16}$$
$$\langle N(N-1)(N-2)\rangle = \langle N_{\mathrm{sat}}\rangle^3 + 3\langle N_{\mathrm{cen}}\rangle\langle N_{\mathrm{sat}}\rangle^2\,, \tag{4.17}$$
$$\langle N(N-1)(N-2)(N-3)\rangle = \langle N_{\mathrm{sat}}\rangle^4 + 4\langle N_{\mathrm{cen}}\rangle\langle N_{\mathrm{sat}}\rangle^3\,. \tag{4.18}$$

The distribution of central galaxies can be described by a nearest-integer or Bernoulli distribution as halos contain either one central galaxy or none. Therefore, all factorial moments involving only central galaxies vanish. The factorial moments of satellites are easily calculated remembering that they follow a Poisson distribution, e.g., $\langle N_{\mathrm{sat}}(N_{\mathrm{sat}}-1)\rangle = \langle N_{\mathrm{sat}}\rangle^2$. Furthermore, we need to deal with terms involving cross-correlations of central and satellite species. These are easily determined, since by definition $N_{\mathrm{cen}} = 0$ implies that also $N_{\mathrm{sat}} = 0$. Thus, the cross-correlations split into the averages of the individual components, e.g., $\langle N_{\mathrm{cen}}N_{\mathrm{sat}}\rangle = \langle N_{\mathrm{cen}}\rangle\langle N_{\mathrm{sat}}\rangle$.

Using the approach of separating contributions from central and satellite galaxies is much simpler than assuming a binomial distribution because we need only the first moment of each species to calculate higher-order moments. The Poissonian nature of the satellite HOD which is the key ingredient of the model was tested in Kravtsov et al. (2004) up to the third-order moment, and observational results verify this behavior, e.g., Yang et al. (2005).

We still need to specify our input parameters for the HOD model which are provided by results from simulations and observations. Hydrodynamic N-body simulations and pure dark matter N-body simulations resolving subhalos find that the satellite HOD is approximately proportional to the mass of the host halo, i.e., $\beta \approx 1$. Note that in this case $m = m_1$ is the characteristic mass where a halo hosts on average one satellite galaxy. All parameters for the fiducial model of the HOD we use in our analysis are summarized in Table A.1 (*Model A*). The minimal mass of $m_{\mathrm{min}} = 10^{12}\,h^{-1}\,M_\odot$ corresponds to a mean number density of galaxies of $\bar{n}_{\mathrm{g}} = 4.96 \times 10^{-3}\,h^3\,\mathrm{Mpc}^{-3}$. Note that the parameters describing the HOD (β, A_{s} and $\sigma_{\ln m}$) are cosmology- and redshift-independent. However, one expects a dependence on cosmological parameters that has not yet been quantified and is possibly small. One would need a large ensemble of hydrodynamical simulations with varying cosmological models to test for this case which has not been done up to now. The form of the first moment of the HOD using the fiducial model is shown in Fig. 4.1. One clearly sees the smoothed-out step function from the contribution of central galaxies and the power-law behavior of satellite galaxies. Also shown is the dimensionless form of the halo mass function for the two redshifts $z = 0$ and $z = 1$
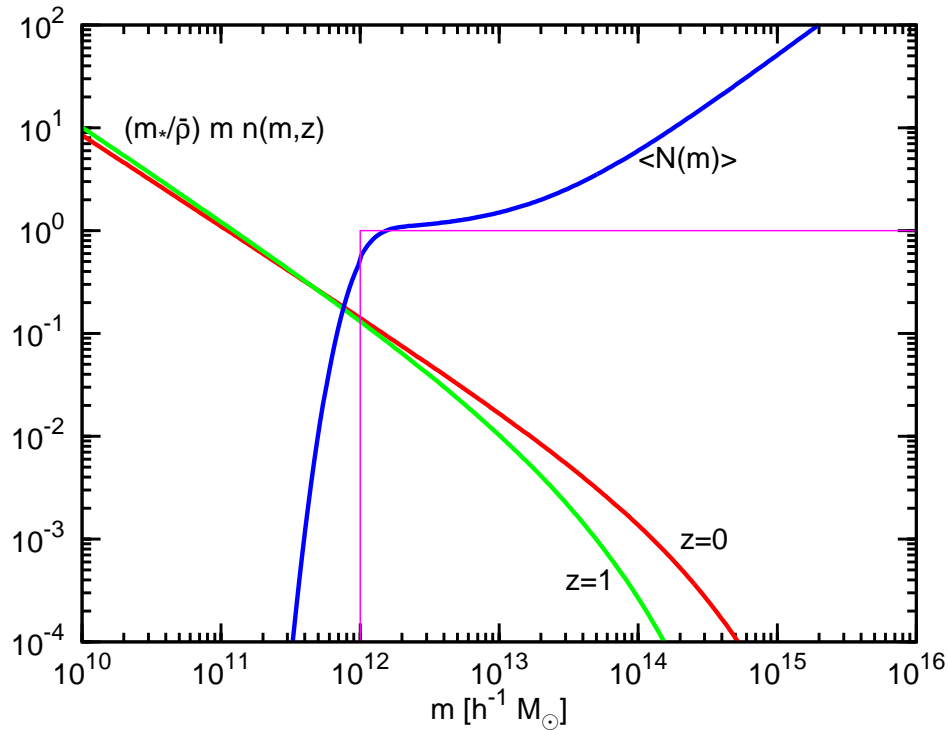
Figure 4.1: First moment of the HOD, i.e., $\langle N(m) \rangle$ using the parameters of the fiducial model (see *Model A* in Table A.1) as a function of halo mass showing the individual contributions of central and satellite galaxies (see Eqs. 4.13 and 4.14, respectively). One can clearly distinguish the contributions from central galaxies around the threshold mass $m_{\min} = 10^{12} \, h^{-1} \, M_\odot$ (we also show a pure step function in magenta) and the power-law behavior of the satellite galaxies for large masses. Also shown is the dimensionless form of the halo mass function for the redshifts $z = 0$ and $z = 1$ which bracket the range essentially probed by weak gravitational lensing observations.

which correspond approximately to the redshift range used for current cosmic shear experiments. We see that the number density of halos drops off significantly for masses around $m = 10^{14} \, h^{-1} \, M_\odot$ and $m = 10^{15} \, h^{-1} \, M_\odot$ for $z = 1$ and $z = 0$, respectively. Shifting the threshold mass for the central galaxy to higher masses will move the HOD to higher masses. As the halo mass function has an exponential cutoff for high-mass halos, the satellite galaxies contribution will be suppressed.

Dependence of the HOD on Galaxy Color

Results from observations and simulations indicate that the HOD is strongly dependent on galaxy color. Hence, different samples that are divided by color, e.g., in blue and red galaxies, should yield a different form of the HOD. Fits to results from semi-analytic models of galaxy formation (see for example Kauffmann et al. 1999) yield the following

power laws for red and blue galaxies, which are parametrized in Sheth & Diaferio (2001):

$$\langle N_{\mathrm{blue}}(m) \rangle = 0.7 \left(\frac{m}{m_{\mathrm{blue}}} \right)^{\alpha_{\mathrm{b}}}, \qquad \langle N_{\mathrm{red}}(m) \rangle = \left(\frac{m}{m_{\mathrm{red}}} \right)^{\alpha_{\mathrm{r}}}. \tag{4.19}$$

For blue galaxies the power-law index is given by

$$\alpha_{\mathrm{b}} = \begin{cases} 0 & \text{for } m_{\mathrm{min}} \leq m \leq m_{\mathrm{blue}}, \\ 0.8 & \text{for } m > m_{\mathrm{blue}}, \end{cases} \tag{4.20}$$

where we introduced the threshold mass $m_{\mathrm{min}} = 10^{11}\, h^{-1}\, M_{\odot}$ and the cutoff for blue galaxies $m_{\mathrm{blue}} = 4 \times 10^{12}\, h^{-1}\, M_{\odot}$. For red galaxies the power-law index is

$$\alpha_{\mathrm{r}} = 0.9, \quad \text{for } m \geq m_{\mathrm{min}}, \tag{4.21}$$

where $m_{\mathrm{red}} = 2.5 \times 10^{12}\, h^{-1}\, M_{\odot}$. The total number of galaxies is then the sum of blue and red galaxies, i.e.,

$$\langle N(m) \rangle = \langle N_{\mathrm{blue}}(m) \rangle + \langle N_{\mathrm{red}}(m) \rangle. \tag{4.22}$$

Note that these relations follow the HOD approach of Scoccimarro et al. outlined in the previous section and are not applicable for the Kravtsov et al. formalism which distinguishes between the contributions from central and satellite galaxies. For high halo masses the red galaxy HOD is steeper than the one for blue galaxies.

The parametrization of the HOD is not unique. A recent description of the HOD of early- and late-type galaxies can be found in Zheng et al. (2005).

4.1.2 Central Galaxy Correlations

For the calculation of higher-order moments of the HOD we use the Kravtsov et al. method described in detail in Sect. 4.1.1 which distinguishes between two different galaxy populations in halos.

Since the first galaxy in each halo is placed at the center of the host halo, terms involving correlations with central galaxies are reduced by a factor of one density profile compared to terms involving correlations with only satellite galaxies (see detailed discussion in Appendix B.7). In the following we will adopt the compact notation $\langle N_{\mathrm{sat}}(m) \rangle \equiv \bar{N}_{\mathrm{sat}}$ and $\langle N_{\mathrm{cen}}(m) \rangle \equiv \bar{N}_{\mathrm{cen}}$. Including correlations with central galaxies we need to perform the following replacements in the building blocks of Eq. (4.3):

$$\langle N^{(j)}(m) \rangle \left[\prod_{i=1}^{j} \tilde{u}_{\mathrm{g}}(k_i, m) \right] \rightarrow$$

$$S_j(k_1, \ldots, k_j, m) = \left[\prod_{i=1}^{j} \tilde{u}_{\mathrm{g}}(k_i, m) \right] \left[\bar{N}_{\mathrm{sat}}^{j} + (\bar{N}_{\mathrm{sat}})^{j-1} \sum_{i=1}^{j} \frac{1}{\tilde{u}_{\mathrm{g}}(k_i, m)} \right], \tag{4.23}$$
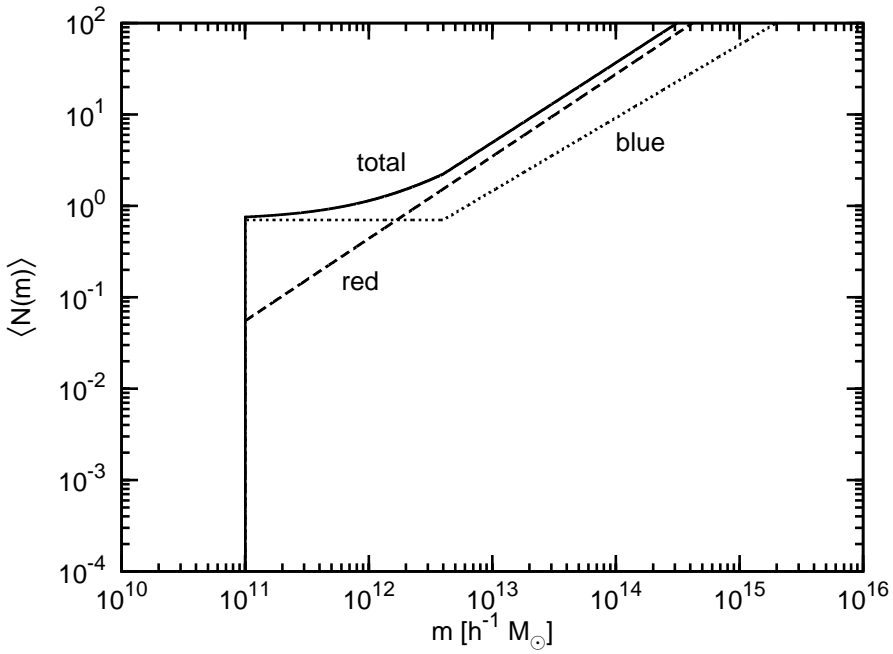
Figure 4.2: Color dependence of the average number of galaxies as a function of halo mass. We use the parametrizations of Eq. (4.19) for red galaxies (dashed line) and for blue galaxies (dotted line) with the corresponding power-law indices (see Eqs. 4.20 and 4.21). In addition, we depict the sum of red and blue galaxies (solid line).

where we used the definition of the j-th factorial moment as given in Eq. (4.5). The first term in square brackets represents the j satellite-only correlations and the second term the correlations of $(j-1)$ satellite galaxies with one central galaxy. We have to change the building blocks defined in Eq. (4.3) accordingly:

$$G_{ij}(k_1, \ldots, k_j) = \int \mathrm{d}m\, n(m)\, \frac{S_j(k_1, \ldots, k_j, m)}{\bar{n}_{\mathrm{g}}^j}\, b_i^{\mathrm{h}}(m)\,. \qquad (4.24)$$

These are the building blocks we will employ in our subsequent predictions of the spectra.

4.2 Galaxy Power Spectrum

In this section we derive the explicit form of the galaxy power spectrum using the halo model formalism.

The galaxy power spectrum is defined by the two-point correlator

$$\langle \delta_{\mathrm{g}}(\boldsymbol{k}) \delta_{\mathrm{g}}(\boldsymbol{k}') \rangle = (2\pi)^3 \delta_{\mathrm{D}}(\boldsymbol{k} + \boldsymbol{k}') P^{\mathrm{gg}}(k)\,. \qquad (4.25)$$

The one-halo term of the galaxy power spectrum is weighted by the mean number of pairs (including repetition) and in order to correctly normalize the equation we divide by

the square of the mean number density of galaxies. Considering a halo which contains only satellite galaxies we find

$$P^{\mathrm{gg}}_{\text{1-h (nc)}}(k) = \int \mathrm{d}m\, n(m) \frac{\langle N(N-1)(m)\rangle}{\bar{n}^2_{\mathrm{g}}} \tilde{u}^2_{\mathrm{g}}(k,m)\,. \tag{4.26}$$

and we label this contribution with the subscript "(nc)" in the following. When we furthermore assume that the first galaxy in each halo is placed at the center of the host halo, terms involving correlations with central galaxies are reduced by a factor of one density profile compared to terms involving correlations with only satellite galaxies (see discussion in Appendix B.7). Under this assumption the one-halo term of the galaxy power spectrum is given by

$$P^{\mathrm{gg}}_{\text{1-h}}(k) = \int \mathrm{d}m\, n(m) \left[\frac{[\bar{N}_{\mathrm{sat}}\tilde{u}_{\mathrm{g}}(k,m)]^2 + 2\bar{N}_{\mathrm{cen}}\bar{N}_{\mathrm{sat}}\tilde{u}_{\mathrm{g}}(k,m)}{\bar{n}^2_{\mathrm{g}}} \right]\,, \tag{4.27}$$

where we used Eq. (4.16) to relate the second-order moment of the HOD to the first-order moments of satellite and central galaxies. The first term in the integrand originates from satellite-satellite correlations and the second from central-satellite correlations. Note that there is no central-central correlation because each halo contains only one central galaxy. Similarly, the two-halo term is given by

$$P^{\mathrm{gg}}_{\text{2-h (nc)}}(k) = \left[\int \mathrm{d}m\, n(m) \frac{\langle N(m)\rangle}{\bar{n}_{\mathrm{g}}} \tilde{u}_{\mathrm{g}}(k,m) b^{\mathrm{h}}_1(m) \right]^2 P_{\mathrm{pt}}(k)\,. \tag{4.28}$$

Assuming that each halo contains a central galaxy, the two-halo term is given by

$$P^{\mathrm{gg}}_{\text{2-h}}(k) = \left[\int \mathrm{d}m\, n(m) \frac{\left[\bar{N}_{\mathrm{cen}} + \bar{N}_{\mathrm{sat}}\tilde{u}_{\mathrm{g}}(k,m)\right]}{\bar{n}_{\mathrm{g}}} b^{\mathrm{h}}_1(m) \right]^2 P_{\mathrm{pt}}(k)\,, \tag{4.29}$$

where we have satellite-satellite, central-satellite and central-central correlations. The first term in square brackets is sometimes neglected because the contribution of central galaxies only dominates the two-halo term on small scales where the one-halo term is anyway larger than the two-halo term. This is due to the fact that on small scales the dominant contribution comes from small mass halos, which is discussed in detail at the end of this section. The total galaxy power spectrum is the sum of the one- and two-halo terms

$$P^{\mathrm{gg}}(k) = P^{\mathrm{gg}}_{\text{1-h}}(k) + P^{\mathrm{gg}}_{\text{2-h}}(k)\,. \tag{4.30}$$

Using the building blocks, introduced in Eq. (4.24), we can write both terms in the compact form

$$P^{\mathrm{gg}}(k) = G_{02}(k,k) + P_{\mathrm{pt}}(k)[G_{11}(k)]^2\,. \tag{4.31}$$

where

$$G_{11}(k) = \int \mathrm{d}m\, n(m) \frac{\left[\bar{N}_{\mathrm{cen}} + \bar{N}_{\mathrm{sat}}\tilde{u}_{\mathrm{g}}(k,m)\right]}{\bar{n}_{\mathrm{g}}} b^{\mathrm{h}}_1(m) \tag{4.32}$$

and

$$G_{02}(k, k) = \int dm \, n(m) \frac{\left[\bar{N}_{\text{sat}} \tilde{u}_{\text{g}}(k, m) \right]^2 + 2 \bar{N}_{\text{cen}} \bar{N}_{\text{sat}} \tilde{u}_{\text{g}}(k, m)}{\bar{n}_{\text{g}}^2} \, . \tag{4.33}$$

Note that for large scales $(k \ll k_{\text{nl}})$[8] the one-halo term (4.27) does not go to zero but converges to a constant scale-independent white noise spectrum since $\tilde{u}(k, m) \to 1$ in this case. As the linear power spectrum is proportional to k at small k, the constant one-halo term eventually gives the dominant contribution making the halo model inconsistent with linear perturbation theory on the largest scales[9]. In the review paper by Cooray & Sheth (2002), we find an ansatz to solve this problem by using *compensated density profiles* which are constructed such that $\tilde{u}(k, m) = \tilde{u}_{\text{g}}(k, m) \to 0$ at small k. However, in this case there will be no power on large scales, since the two-halo term also depends on the density profile. Thus, this weakness of the halo model remains and it is not clear how to solve this problem. On the other hand, the two-halo term (4.29) is in accordance with the results from perturbation theory since on large scales we find $P_{\text{2-h}}^{\text{gg}}(k) = b^2 P_{\text{pt}}(k)$, where b is the linear bias factor defined by the large-scale limit of G_{11} in Eq. (4.32).

In the presented formalism several processes have been neglected. First of all, we did not account for the effect of *halo exclusion*. Different halos in simulations are never separated by distances smaller than the sum of their virial radii since otherwise they would have been linked to one larger halo. This effect is not included in our description of the two-halo terms of the dark matter and galaxy power spectra. To correct for this effect, we need to exclude overlapping halos in the two-halo terms. Secondly, simulations indicate that the halo bias is scale-dependent, whereas the halo model calculation in Sect. 3.4 predicts a scale-independent halo bias (see for example the Press-Schechter halo bias in Eq. 3.76). One possibility is to determine the scale-dependent bias factor directly from simulations. However, then we would need to use the nonlinear dark matter power spectrum for the clustering of halo centers that is obtained from simulations for consistency instead of P_{pt}. The drawback of using simulations to obtain the halo bias is that there is no simple way to generalize the results to higher-order spectra, like the galaxy bispectrum. In addition, the cosmology dependence of the scale-dependent halo bias is not well tested. A detailed description of all these effects can be found in the appendix of Tinker et al. (2005). We refrain from using these halo model extensions because they are only valid and tested at the two-point level. As we mainly aim at modeling higher-order correlation functions there is no simple extension of this formalism. Also, all these corrections are only important for the transition of the two-halo to the one-halo term at intermediate scales. In particular, the nonlinear part which is probed by the one-halo term is unaffected by these corrections.

The dimensionless galaxy power spectrum (see definition of dimensionless power

---

[8]Here, k_{nl} is the nonlinear wave-number defined as the scale where the dimensionless power spectrum is 1.

[9]Note that the one-halo term of the dark matter power spectrum (see Eq. 3.103) suffers from the same inconsistency.
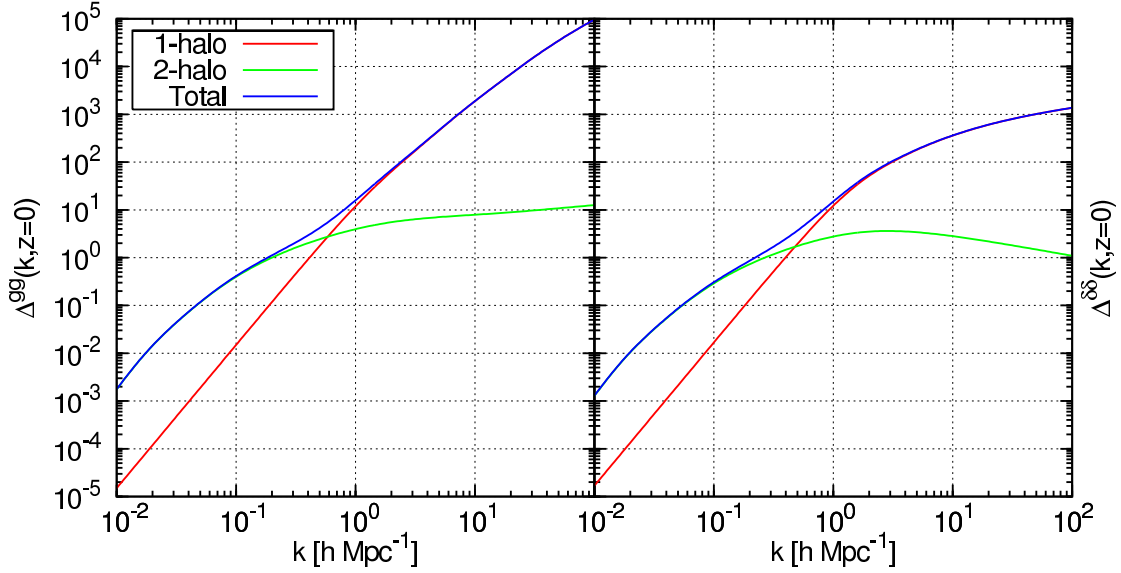
Figure 4.3: The plot shows in the left panel the dimensionless galaxy power spectrum defined in Eq. (2.107) and in the right panel the dark matter power spectrum against wave-number k at redshift $z = 0$. Both plots show the separate contributions from the one- and two-halo terms to the total power spectrum.

spectrum in Eq. 2.107) is plotted in the left panel of Fig. 4.3 and the right panel shows the dimensionless dark matter power spectrum for comparison. Both panels show the one- and the two-halo term contributions to the corresponding total power spectrum for $z = 0$. The first point to note is the approximate power-law behavior of the galaxy power spectrum over the whole range of scales. The change from the large-scale regime described by the two-halo term to the small-scale regime dominated by the one-halo term at around $k \simeq 0.5\,h\,\mathrm{Mpc}^{-1}$ is not well modeled by our halo model method and results in a small dip in the total power spectrum. The dark matter power spectrum is clearly not described by a single power law. Furthermore, we note both power spectra have a similar amplitude on large scales. The ratio of the dark matter and galaxy power spectrum will be quantified in Sect. 4.3.3 where we introduce the scale-dependent bias between galaxy and dark matter clustering.

In summary, the halo model reproduces the observed power-law behavior of the galaxy power spectrum. The origin of this behavior is best seen by comparing the one- and two-halo terms of the galaxy power spectrum in Eqs. (4.27) and (4.29) to the dark matter power spectrum in Eqs. (3.103) and (3.106). Both power spectra are similar if the radial distribution of galaxies trace the dark matter density profile, the HOD is described by a Poisson distribution over the whole mass range (i.e., there is no minimal mass) and the first moment of satellites, $\bar{N}_{\mathrm{sat}}$, depends linearly on the host halo mass. The only difference left between the power spectra is the different normalization either by the mean galaxy density or by the mean dark matter density.

To illustrate the importance of specific assumptions made in the galaxy halo model, we show in the left panel of Fig. 4.4 the one- and the two-halo terms of the dimensionless

power spectrum by dropping specific assumptions as indicated in the figure caption. We find that the one- and two-halo term drop below the "real" galaxy power spectrum on small scales if the halos contain only satellite galaxies. This is due to the fact that on small scales the normalized halo density profile begins to decrease from unity as we showed in Fig. 3.3. In particular, central galaxy correlations are dominant on small scales because they are weighted by only one density profile. Therefore, the suppression of the halo terms due to the density profile on small scales is reduced for central galaxy correlations. If we further assume that the HOD distribution is Poissonian for all halo masses and in addition neglect the threshold mass for the central galaxy, we obtain a one-halo term which is proportional to the one-halo term of the power spectrum in the right panel of Fig. 4.3.

The right panel in Fig. 4.4 depicts the mass contributions to the one-halo term from halos divided into certain mass ranges as indicated in the figure. On large scales the dominant contributions come from high-mass halos $10^{14} \, h^{-1} \, M_\odot < m < 10^{16} \, h^{-1} \, M_\odot$. Going to smaller scales, also smaller mass halos begin to dominate. On the smallest scales the largest contributions come from low-mass halos. This is due to the fact that low-mass halos contain only a very small number of galaxies, which enhances the probability to have central-satellite correlations in the one-halo term. Note that for the right panel of Fig. 4.4 we changed the minimal mass to $m_{\min} = 10^{11} \, h^{-1} \, M_\odot$. Reducing $m_{\min}$ leads to a higher number density of galaxies $\bar{n}_{\mathrm{g}}$ resulting in a suppression of the one-halo term which is normalized by the inverse square of the number density.

4.3 Galaxy-Dark Matter Cross-Spectra

The cross-power spectra of galaxies and the underlying dark matter field reveal statistical information about galaxies and their local environment, namely the dark matter halos. The lowest-order statistic is the second-order correlation, i.e., the cross-power spectrum. The projected two-point cross-spectrum has been probed by a number of galaxy-galaxy lensing studies and also by studies of the magnification bias of background galaxies. Furthermore, it is beneficial to study higher-order spectra which contain independent information about the relation between galaxies and dark matter that is not contained in the two-point level. Therefore, it is natural to study the next higher-order spectrum, namely the galaxy-dark matter cross-bispectra[10]. Recently, Schneider & Watts (2005) introduced the projected form of these cross-bispectra that are probed in studies of galaxy-galaxy-galaxy lensing. Furthermore, the covariance of the cross-power spectrum estimator depends on the four-point spectrum, the cross-trispectrum. Similar to the galaxy power spectrum, there exists no theoretical model from first principles for the cross-power spectrum. This is due to the nonlinear physics of galaxy formation. Especially higher-order cross-spectra have not yet been tested in simulations and thus there are no fitting functions available that could be used to calculate them for a given

---

[10]One can build two cross-bispectra, namely the dark-matter-dark-matter-galaxy and the galaxy-galaxy-dark matter bispectra.
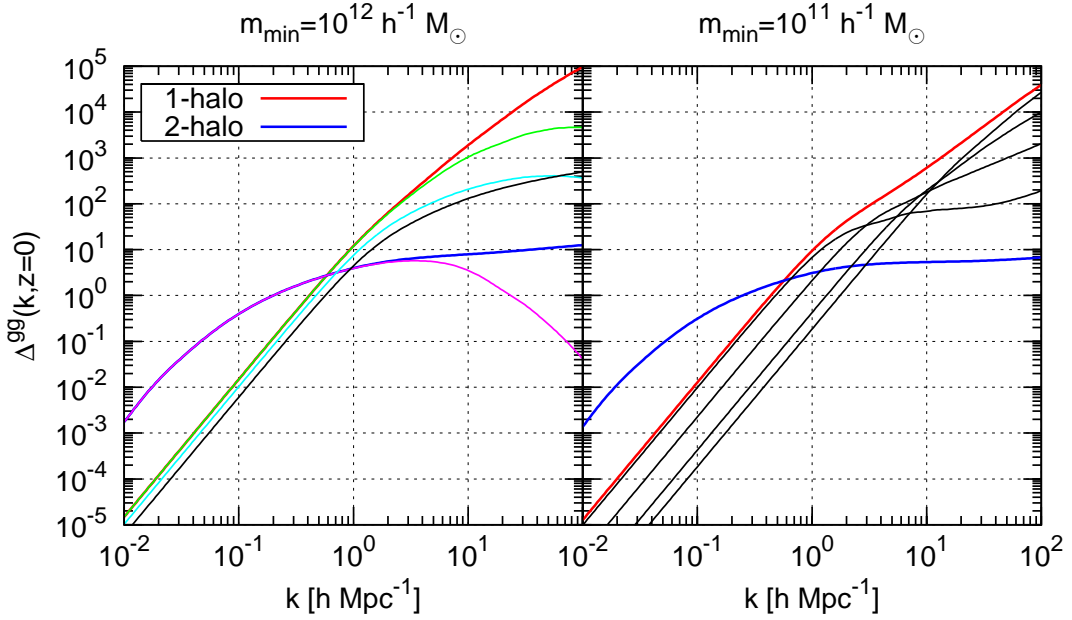
Figure 4.4: Dimensionless galaxy power spectrum at redshift $z = 0$. The left panel depicts the influences on the one- (red line) and two-halo terms (blue line) by neglecting particular assumptions of the galaxy halo model. First the green and the magenta curve show the results for the one-halo and two-halo terms if we consider halos that contain only satellite galaxies. The light blue curve shows the effect of additionally neglecting the sub-Poissonian nature of the HOD at low halo masses. Finally, the black curve shows the effect of neglecting the threshold mass for building galaxies. The right panel shows the contributions to the one-halo term (red line) as thin black lines from halos in a particular mass range: for large scales ($k \lesssim 1\,h\,\mathrm{Mpc}^{-1}$) the dominant contribution comes from the most massive halos in the range $10^{14}\,h^{-1}\,M_\odot < m < 10^{16}\,h^{-1}\,M_\odot$. The contribution for the mass ranges $10^{13}\,h^{-1}\,M_\odot < m < 10^{14}\,h^{-1}\,M_\odot$, $10^{12}\,h^{-1}\,M_\odot < m < 10^{13}\,h^{-1}\,M_\odot$ and $10^{11}\,h^{-1}\,M_\odot < m < 10^{12}\,h^{-1}\,M_\odot$ becomes successively smaller. However, on the smallest scales ($k \simeq 10^2\,h\,\mathrm{Mpc}^{-1}$) this behavior is reversed and the dominant contribution comes from small mass halos. For both panels we used the fiducial model (see *Model A* in Table A.1) but for the right panel we changed the minimal mass from $m_{\min} = 10^{12}\,h^{-1}\,M_\odot$ to $m_{\min} = 10^{11}\,h^{-1}\,M_\odot$ which reduces the power spectrum.

cosmological model. Here we employ the halo model formalism for dark matter and galaxy clustering as developed in the previous sections. Encouraged by the agreement of the results from the halo model and simulations on the two-point level (e.g., Zehavi et al. 2004) we want to extend it to the three- and four-point levels which are needed for galaxy-galaxy-galaxy lensing (see Chapter 6) and to quantify the errors for galaxy-galaxy lensing (see Chapter 7), respectively.

The halo model for dark matter and galaxy clustering can be combined to calculate the cross-spectra without introducing new concepts. More precisely, the cross-spectra in any order can be constructed using the building blocks of the dark matter spectra in Eq. (3.125) and the building blocks of galaxy clustering in Eq. (4.24) discussed in the previous sections.

4.3.1 Galaxy-Dark Matter Cross-Power Spectrum

The cross-power spectrum $P^{\delta g}(k)$ is defined as the two-point correlator of the dark matter and the galaxy density contrast, i.e.,

$$\langle \delta(\boldsymbol{k}) \delta_{\mathrm{g}}(\boldsymbol{k}') \rangle = (2\pi)^3 \delta_{\mathrm{D}}(\boldsymbol{k} + \boldsymbol{k}') P^{\delta g}(k) \, . \tag{4.34}$$

We present the explicit form of the cross-power spectrum making use of the clustering formalism of galaxies and dark matter developed above. The one-halo term is given as

$$P^{\delta g\,(\mathrm{nc})}_{\mathrm{1\text{-}h}}(k) = \int \mathrm{d}m\, n(m) \left(\frac{m}{\bar{\rho}} \right) \frac{\langle N(m) \rangle}{\bar{n}_{\mathrm{g}}} \tilde{u}_{\mathrm{dm}}(k, m) \tilde{u}_{\mathrm{g}}(k, m) \, . \tag{4.35}$$

When we place one galaxy in the center of the halo the result is

$$P^{\delta g}_{\mathrm{1\text{-}h}}(k) = \int \mathrm{d}m\, n(m) \left(\frac{m}{\bar{\rho}} \right) \tilde{u}_{\mathrm{dm}}(k, m) \left[\frac{\bar{N}_{\mathrm{cen}} + \bar{N}_{\mathrm{sat}} \tilde{u}_{\mathrm{g}}(k, m)}{\bar{n}_{\mathrm{g}}} \right] \, . \tag{4.36}$$

Similarly, we find for the two-halo term including central galaxies

$$P^{\delta g}_{\mathrm{2\text{-}h}}(k) = P_{\mathrm{pt}}(k) \left[\int \mathrm{d}m\, n(m) \left(\frac{m}{\bar{\rho}} \right) \tilde{u}_{\mathrm{dm}}(k, m) b^{\mathrm{h}}_1(m) \right]$$
$$\times \left[\int \mathrm{d}m\, n(m) \frac{\left[\bar{N}_{\mathrm{cen}} + \bar{N}_{\mathrm{sat}} \tilde{u}_{\mathrm{g}}(k, m) \right]}{\bar{n}_{\mathrm{g}}} b^{\mathrm{h}}_1(m) \right] \, . \tag{4.37}$$

Using the building blocks for the dark matter and galaxy spectra we can write the two-halo term in the compact notation

$$P^{\delta g}_{\mathrm{2\text{-}h}}(k) = I_{11}(k) G_{11}(k) P_{\mathrm{pt}}(k) \, , \tag{4.38}$$

where we used Eq. (4.32) and

$$I_{11}(k) = \int \mathrm{d}m\, n(m) \left(\frac{m}{\bar{\rho}} \right) \tilde{u}_{\mathrm{dm}}(k, m) b^{\mathrm{h}}_1(m) \, . \tag{4.39}$$
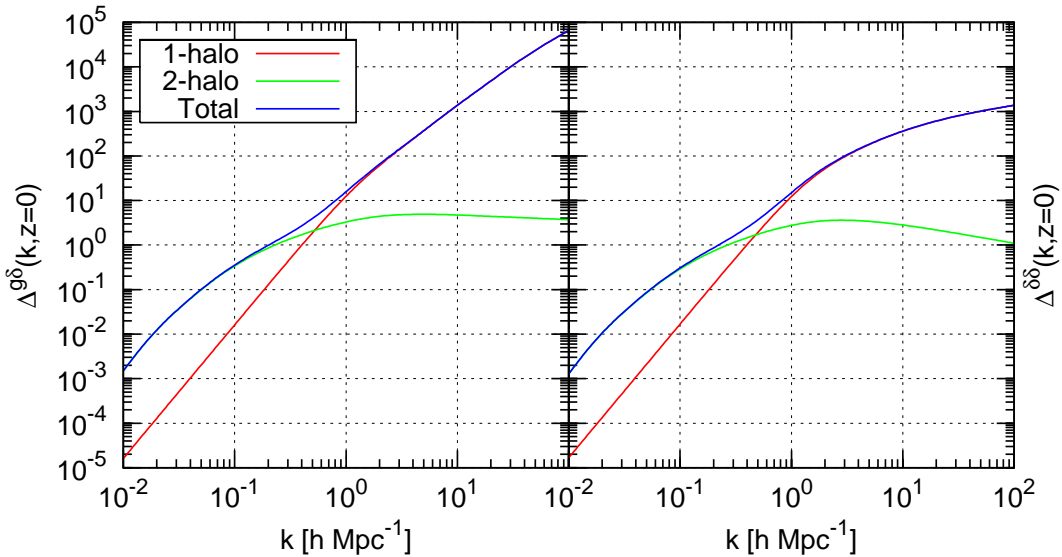
Figure 4.5: The plot shows the dimensionless galaxy-dark matter cross-power spectrum (left panel) and the dark matter power spectrum (right panel) against wave-number k at redshift $z = 0$. Both plots show the separate contribution from the one- and two-halo term to the total power spectrum.

The total cross-power spectrum is then the sum of the one- and two-halo terms

$$P^{\delta g}(k) = P^{\delta g}_{1\text{-h}}(k) + P^{\delta g}_{2\text{-h}}(k)\,. \tag{4.40}$$

The dimensionless cross-power spectrum is shown in the left panel of Fig. 4.5. The right panel depicts the dimensionless dark matter power spectrum for comparison. The cross-power spectrum is well described by a single power law and is very similar to the galaxy power spectrum. This is due to the fact that both power spectra have the same dependence on the normalized density profile if galaxies follow the dark matter profile. In addition, they are both influenced by the low-mass cutoff $m_{\min}$. We will analyze the ratio of both spectra in detail in Sect. 4.3.3 where we discuss scale-dependent bias.

4.3.2 Large-Scale Galaxy Bias Parameters

The theoretical prediction of the bias between galaxy and dark matter clustering from first principles is not feasible up to now because the bias is in general nonlinear and stochastical. But on sufficiently large scales one can assume that galaxy formation is a local process and thus depends only on the local matter density field. Hence, in this case there is a local mapping of the dark matter density contrast to the galaxy density contrast

$$\delta_{\rm g}(\boldsymbol{x}) \equiv f[\delta(\boldsymbol{x})]\,, \tag{4.41}$$

where the function f describes the mapping. As on large scales $|\delta| \ll 1$, one can expand the galaxy overdensity $\delta_{\rm g}$ at comoving position $\boldsymbol{x}$ in a Taylor series (see Fry & Gaztanaga

1993) around $\delta = 0$ of the underlying matter overdensity, i.e.,

$$\delta_{\mathrm{g}}(\boldsymbol{x}) = b_1^{\mathrm{L}}\delta(\boldsymbol{x}) + \frac{b_2^{\mathrm{L}}}{2}\delta^2(\boldsymbol{x}) + \frac{b_3^{\mathrm{L}}}{6}\delta^3(\boldsymbol{x}) + \dots,$$ (4.42)

where we introduced the constant first-, second- and third-order bias parameters b_1^{L}, b_2^{L} and b_3^{L}, respectively. The bias parameters are defined by the derivatives of the mapping function:

$$b_i^{\mathrm{L}} \equiv \left.\frac{\mathrm{d}^i}{\mathrm{d}\delta^i}f(\delta)\right|_{\delta=0}.$$ (4.43)

Transforming Eq. (4.42) into Fourier space yields

$$\delta_{\mathrm{g}}(\boldsymbol{k}) = b_1^{\mathrm{L}}\delta(\boldsymbol{k}) + \frac{b_2^{\mathrm{L}}}{2}\int\frac{\mathrm{d}^3 q_1}{(2\pi)^3}\,\delta(\boldsymbol{q}_1)\delta(\boldsymbol{k}-\boldsymbol{q}_1)$$
$$+ \frac{b_3^{\mathrm{L}}}{6}\int\frac{\mathrm{d}^3 q_1}{(2\pi)^3}\int\frac{\mathrm{d}^3 q_2}{(2\pi)^3}\,\delta(\boldsymbol{q}_1)\delta(\boldsymbol{q}_2)\delta(\boldsymbol{k}-\boldsymbol{q}_1-\boldsymbol{q}_2) + \dots$$ (4.44)

Using this expression, we can easily calculate the galaxy two-point correlator to lowest order in δ and we find for the galaxy power spectrum (see definition in Eq. 4.25)

$$P^{\mathrm{gg}}(k) = \left(b_1^{\mathrm{L}}\right)^2 P_{\mathrm{pt}}(k).$$ (4.45)

The cross-power spectrum defined in Eq. (4.34) is accordingly

$$P^{\delta\mathrm{g}}(k) = b_1^{\mathrm{L}}P_{\mathrm{pt}}(k).$$ (4.46)

Similarly, we find for the galaxy bispectrum (Matarrese et al. 1997)

$$B^{\mathrm{ggg}}(k_1, k_2, k_3) = (b_1^{\mathrm{L}})^3 B_{\mathrm{pt}}(k_1, k_2, k_3) + (b_1^{\mathrm{L}})^2 b_2^{\mathrm{L}}\left[P_{\mathrm{pt}}(k_1)P_{\mathrm{pt}}(k_2) + P_{\mathrm{pt}}(k_1)P_{\mathrm{pt}}(k_3)\right.$$
$$\left. + P_{\mathrm{pt}}(k_2)P_{\mathrm{pt}}(k_3)\right].$$ (4.47)

Note that we define the galaxy bispectrum in Eq. (4.54) below.

The framework of the galaxy halo model allows us to calculate these large-scale bias parameters. On large scales the n-point spectra are dominated by the n-point halo correlation function between the n halo centers. As the normalized density profile goes asymptotically to $\tilde{u}_{\mathrm{g}}(k = 0, m) \to 1$, we find for the i-th order large-scale galaxy bias factor (Scoccimarro et al. 2001)

$$b_i^{\mathrm{L}}(z) = \frac{1}{\bar{n}_{\mathrm{g}}}\int\mathrm{d}m\,n(m, z)\langle N(m)\rangle b_i^{\mathrm{h}}(m),$$ (4.48)

where b_i^{h} is the bias between halos and the underlying dark matter field and we explicitly wrote the redshift dependence. This equation allows the determination of the large-scale galaxy bias parameters from the well-known halo bias parameters that are extensively tested in dissipationless simulations. This method circumvents the modeling of galaxy

clustering to compute the bias parameters. For example setting $\tilde{u}_{\mathrm{g}}(k, m) \to 1$ in Eq. (4.29) yields

$$P_{2\text{-h}}^{\mathrm{gg}}(k, z) = \left[b_1^{\mathrm{L}}(z)\right]^2 P_{\mathrm{pt}}(k, z) \tag{4.49}$$

with the first-order bias parameter

$$b_1^{\mathrm{L}}(z) = \frac{1}{\bar{n}_{\mathrm{g}}} \int \mathrm{d}m\, n(m, z)[\bar{N}_{\mathrm{sat}} + \bar{N}_{\mathrm{cen}}]\, b_1^{\mathrm{h}}(m) \,. \tag{4.50}$$

Similar we can derive the results for the higher-order bias parameters which fulfill Eq. (4.48).

4.3.3 Scale-Dependent Power Spectrum Bias

In the previous section we explored the large-scale bias between galaxies and the dark matter field. Here, we extend this concept with the help of the halo model now to small scales. On large scales the bias goes to a constant value as described by Eq. (4.48). However, on small scales the bias factor is non-monotonic and scale-dependent, as will be shown below.

The relation between the galaxy and the dark matter power spectra can be parametrized by

$$P^{\mathrm{gg}}(k, w) = b^2(k, w)P^{\delta\delta}(k, w) \,, \tag{4.51}$$

where $b(k, w)$ is the in general scale- and redshift-dependent bias parameter where the redshift dependence is encoded in the comoving distance, i.e., $w \equiv w(z)$. Similarly, the relation between the cross- and the dark matter power spectra is given by

$$P^{\delta\mathrm{g}}(k, w) = b(k, w)r(k, w)P^{\delta\delta}(k, w) \,, \tag{4.52}$$

where we additionally introduced the scale- and redshift-dependent *galaxy-mass correlation coefficient* $r(k, w)$. For large scales the bias factor is described by the *linear deterministic bias*, where $b(k, w) \to b_1^{\mathrm{L}}(w)$, and the correlation coefficient goes to 1. This follows from the large-scale solutions in Eqs. (4.45) and (4.46). We build the following ratios

$$b(k, w) = \sqrt{\frac{P^{\mathrm{gg}}(k, w)}{P^{\delta\delta}(k, w)}} \,, \qquad \frac{b(k, w)}{r(k, w)} = \frac{P^{\mathrm{gg}}(k, w)}{P^{\delta\mathrm{g}}(k, w)} \,, \tag{4.53}$$

and present them in dependence of the wave-number k in Fig. 4.6. The figure shows both quantities for three different minimal masses. The galaxy bias and the ratio b/r resemble the linear deterministic bias on large scales. On small scales the galaxy bias becomes highly scale-dependent, whereas the ratio of the galaxy and cross-power spectra is nearly constant over the scales considered. We note that a higher threshold mass results in a smaller number density $\bar{n}_{\mathrm{g}}$ which leads to an enhancement of the galaxy power spectrum.
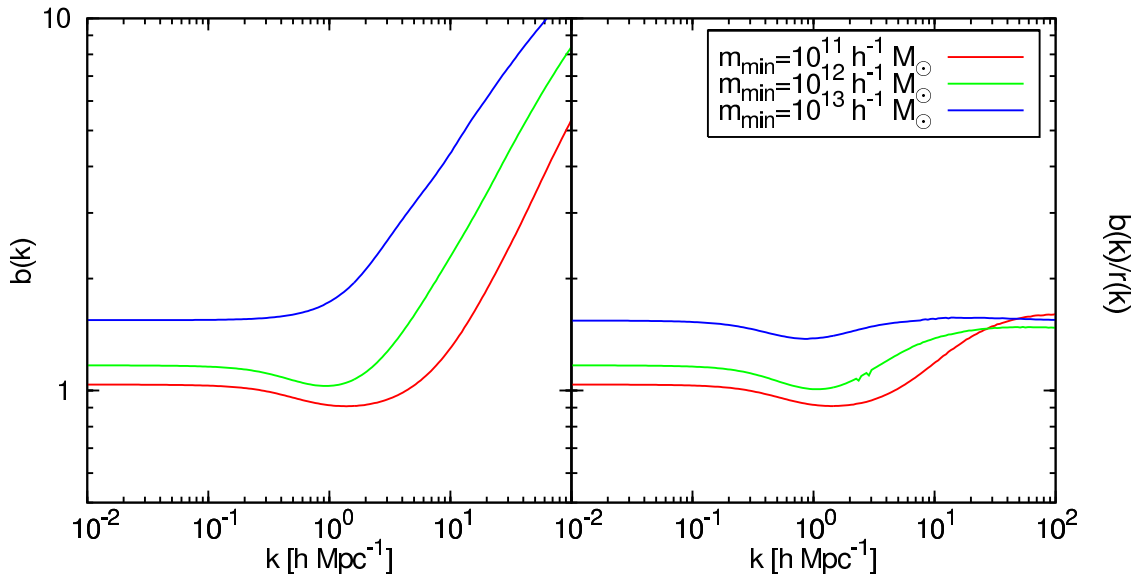
Figure 4.6: The left panel shows the scale-dependent bias between galaxies and dark matter. The right panel shows the ratio of the galaxy power spectrum to the cross-power spectrum (see definitions in Eq. 4.53). Both functions are evaluated at $z = 0$ and shown for three different threshold masses $m_{\min}$ as indicated in the figure.

4.4 Galaxy Auto- and Cross-Bispectrum

The power of the halo model is best demonstrated by considering higher-order correlation functions. This section provides the halo model description of the galaxy bispectrum and its cross-spectra with the dark matter field. The bispectrum is the lowest-order statistic that describes non-Gaussianity and is thus of particular interest. The galaxy auto-bispectrum is probed in galaxy redshift surveys. The projected cross-bispectrum is probed in surveys that measure galaxy-galaxy-galaxy lensing. This section provides the basic equations for the three-dimensional bispectra following the halo model approach. The projected spectra can then easily be obtained by using Limber's approximation (see Eq. 5.65 in the next chapter).

The galaxy auto-bispectrum is defined by the connected three-point correlator

$$\langle \delta_{\mathrm{g}}(\boldsymbol{k}_1)\delta_{\mathrm{g}}(\boldsymbol{k}_2)\delta_{\mathrm{g}}(\boldsymbol{k}_3)\rangle_{\mathrm{c}} = (2\pi)^3 \delta_{\mathrm{D}}(\boldsymbol{k}_1 + \boldsymbol{k}_2 + \boldsymbol{k}_3)B^{\mathrm{ggg}}(\boldsymbol{k}_1, \boldsymbol{k}_2, \boldsymbol{k}_3). \qquad (4.54)$$

Owing to the assumed homogeneity and isotropy of the Universe, we can parametrize the bispectrum with the length of the three sides that build a triangle in Fourier space such that $B^{\mathrm{ggg}}(\boldsymbol{k}_1, \boldsymbol{k}_2, \boldsymbol{k}_3) \to B^{\mathrm{ggg}}(k_1, k_2, k_3)$.

Generalizing the result of Eq. (3.120) for the one-halo term of the dark matter bispectrum yields for the one-halo term of the galaxy bispectrum

$$B^{\mathrm{ggg}}_{\mathrm{1\text{-}h\,(nc)}}(k_1, k_2, k_3) = \int \mathrm{d}m\, n(m) \frac{\langle N(N-1)(N-2)(m)\rangle}{\bar{n}_{\mathrm{g}}^3} \prod_{i=1}^{3} \tilde{u}_{\mathrm{g}}(k_i, m). \qquad (4.55)$$

This weighting changes if we place a galaxy in the center of each halo above a certain mass (for details see Appendix B.7):

$$B_{\text{1-h}}^{\text{ggg}}(k_1, k_2, k_3) = \frac{1}{\bar{n}_{\text{g}}^3} \int \mathrm{d}m \, n(m) \left[\bar{N}_{\text{sat}}^3 + \bar{N}_{\text{cen}} \bar{N}_{\text{sat}}^2 \left(\sum_{i=1}^3 \frac{1}{\tilde{u}_{\text{g}}(k_i, m)} \right) \right] \prod_{i=1}^3 \tilde{u}_{\text{g}}(k_i, m) \, , \tag{4.56}$$

where the two terms in square brackets correspond to the two possible triplet correlations, i.e., satellite-satellite-satellite correlations and central-satellite-satellite correlations, respectively. For the two-halo term we find by adopting the halo model of galaxy clustering to Eq. (3.129)

$$\begin{aligned} B_{\text{2-h}}^{\text{ggg}}(k_1, k_2, k_3) = {} & G_{11}(k_1)G_{12}(k_2, k_3)P_{\text{pt}}(k_1) + G_{11}(k_3)G_{12}(k_2, k_1)P_{\text{pt}}(k_3) \\ & + G_{11}(k_2)G_{12}(k_1, k_3)P_{\text{pt}}(k_2) \, , \end{aligned} \tag{4.57}$$

where we used the definition of $G_{11}(k)$ in Eq. (4.32) and we introduced the function

$$\begin{aligned} G_{12}(k_1, k_2) = {} & \frac{1}{\bar{n}_{\text{g}}^2} \int \mathrm{d}m \, n(m) \left[\bar{N}_{\text{sat}}^2 + \bar{N}_{\text{cen}} \bar{N}_{\text{sat}} \left(\frac{1}{\tilde{u}_{\text{g}}(k_1, m)} + \frac{1}{\tilde{u}_{\text{g}}(k_2, m)} \right) \right] \\ & \times \tilde{u}_{\text{g}}(k_1, m)\tilde{u}_{\text{g}}(k_2, m)b_1^{\text{h}}(m) \, . \end{aligned} \tag{4.58}$$

This function describes the two-point correlation of galaxies in one of the halos weighted by the halo bias factor between the two halo centers. Finally, the three halo term is (compare with Eq. 3.130 for dark matter)

$$B_{\text{3-h}}^{\text{ggg}}(k_1, k_2, k_3) = G_{11}(k_1)G_{11}(k_2)G_{11}(k_3)B_{\text{pt}}(k_1, k_2, k_3) \, . \tag{4.59}$$

Note that we neglect terms involving the second-order halo bias factor as they provide on most scales only a small correction (Ma & Fry 2000; Takada & Jain 2003). Furthermore, the perturbative expansion of the correlation function of halo centers breaks down on nonlinear scales (Smith et al. 2007) and thus one needs more elaborated models than our presented approach.

In addition to the dark matter and galaxy auto-correlation functions, we can define two cross-correlation functions, namely the galaxy-galaxy-dark matter bispectrum

$$\langle \delta_{\text{g}}(\boldsymbol{k}_1)\delta_{\text{g}}(\boldsymbol{k}_2)\delta(\boldsymbol{k}_3) \rangle_{\text{c}} = (2\pi)^3 \delta_{\text{D}}(\boldsymbol{k}_1 + \boldsymbol{k}_2 + \boldsymbol{k}_3)B^{\text{gg}\delta}(\boldsymbol{k}_1, \boldsymbol{k}_2; \boldsymbol{k}_3) \, , \tag{4.60}$$

and the dark matter-dark matter-galaxy bispectrum

$$\langle \delta(\boldsymbol{k}_1)\delta(\boldsymbol{k}_2)\delta_{\text{g}}(\boldsymbol{k}_3) \rangle_{\text{c}} = (2\pi)^3 \delta_{\text{D}}(\boldsymbol{k}_1 + \boldsymbol{k}_2 + \boldsymbol{k}_3)B^{\delta\delta\text{g}}(\boldsymbol{k}_1, \boldsymbol{k}_2; \boldsymbol{k}_3) \, . \tag{4.61}$$

For the first function we denote with k_1 and k_2 the two galaxies and with k_3 the dark matter position. On the other hand, for the second function we label k_1 and k_2 as dark matter particles and k_3 as a galaxy position. The semicolon indicates the symmetry of the function under permutations of its arguments, i.e., $B^{\text{gg}\delta}(\boldsymbol{k}_1, \boldsymbol{k}_2; \boldsymbol{k}_3) = B^{\text{gg}\delta}(\boldsymbol{k}_2, \boldsymbol{k}_1; \boldsymbol{k}_3)$ and $B^{\delta\delta\text{g}}(\boldsymbol{k}_1, \boldsymbol{k}_2; \boldsymbol{k}_3) = B^{\delta\delta\text{g}}(\boldsymbol{k}_2, \boldsymbol{k}_1; \boldsymbol{k}_3)$.

First we show the halo terms for the galaxy-galaxy-dark matter bispectrum. The one-halo term is given by the cross-correlation of two galaxy positions with one position in the dark matter field. The weighting by the mean number of galaxy pairs is replaced equivalently to the one-halo term of the power spectrum when we include central galaxies (see also Eq. B.34 in the Appendix B.7). In addition the dark matter contribution has the same weighting as in the one-halo term of the cross-power spectrum in Eq. (4.36). Combining both weightings yields

$$B_{\text{1-h}}^{\text{gg}\delta}(k_1, k_2; k_3) = \int dm\, n(m) \frac{1}{\bar{n}_{\text{g}}^2} \left[\bar{N}_{\text{sat}}^2 + \bar{N}_{\text{cen}} \bar{N}_{\text{sat}} \left(\frac{1}{\tilde{u}_{\text{g}}(k_1, m)} + \frac{1}{\tilde{u}_{\text{g}}(k_2, m)} \right) \right]$$
$$\times \left(\frac{m}{\bar{\rho}} \right) \tilde{u}_{\text{g}}(k_1, m) \tilde{u}_{\text{g}}(k_2, m) \tilde{u}_{\text{dm}}(k_3, m) \,, \tag{4.62}$$

where the two terms in the integrand represent satellite-satellite-dark matter correlations and central-satellite-dark matter correlations. The two-halo term of the galaxy bispectrum in Eq. (4.57) can be easily extended to the galaxy-galaxy-matter cross-bispectrum:

$$B_{\text{2-h}}^{\text{gg}\delta}(k_1, k_2; k_3) = G_{11}(k_1) \mathcal{G}_{12}^{\text{gg}\delta}(k_2; k_3) P_{\text{pt}}(k_1) + I_{11}(k_3) G_{12}(k_2, k_1) P_{\text{pt}}(k_3)$$
$$+ G_{11}(k_2) \mathcal{G}_{12}^{\text{gg}\delta}(k_1; k_3) P_{\text{pt}}(k_2) \,, \tag{4.63}$$

where we defined the cross-function

$$\mathcal{G}_{12}^{\text{gg}\delta}(k_1; k_2) = \frac{1}{\bar{n}_{\text{g}}} \int dm\, n(m) \left[\bar{N}_{\text{sat}}(m) \tilde{u}_{\text{g}}(k_1, m) + \bar{N}_{\text{cen}}(m) \right]$$
$$\times \left(\frac{m}{\bar{\rho}} \right) \tilde{u}_{\text{dm}}(k_2, m) b_1^{\text{h}}(m) \,. \tag{4.64}$$

Note that the first-order halo bias appears because we express the halo power spectrum in terms of the linear dark matter power spectrum. The first term in Eq. (4.63) corresponds to a correlation of a single galaxy in one halo with a galaxy and dark matter position in a second halo, where P_{pt} describes the correlation between the two halo centers. The other two terms are then obtained by permutations of the three wave-numbers, which then also leads to a change in the building blocks. For example in the second term we have a two-point correlation of two galaxies in one halo with a dark matter position in the second halo. Finally, the three-halo term is (compare with Eq. 4.59)

$$B_{\text{3-h}}^{\text{gg}\delta}(k_1, k_2; k_3) = G_{11}(k_1) G_{11}(k_2) I_{11}(k_3) B_{\text{pt}}(k_1, k_2, k_3) \,. \tag{4.65}$$

In accordance with the derivation of the halo model representation of $B^{\text{gg}\delta}$ we can extend this model to $B^{\delta\delta\text{g}}$. The one-halo term is given by

$$B_{\text{1-h}}^{\delta\delta\text{g}}(k_1, k_2; k_3) = \int dm\, n(m) \left(\frac{m}{\bar{\rho}} \right)^2 \tilde{u}_{\text{dm}}(k_1, m) \tilde{u}_{\text{dm}}(k_2, m)$$
$$\times \frac{1}{\bar{n}_{\text{g}}} \left[\bar{N}_{\text{sat}} \tilde{u}_{\text{g}}(k_3, m) + \bar{N}_{\text{cen}} \right] \,, \tag{4.66}$$

where we the first term represents dark matter-dark matter-central correlations and the second term dark matter-dark matter-satellite correlations. The two-halo term is

$$B_{\text{2-h}}^{\delta\delta\text{g}}(k_1, k_2; k_3) = I_{11}(k_1)\mathcal{G}_{12}^{\text{g}\delta}(k_3; k_2)P_{\text{pt}}(k_1) + G_{11}(k_3)I_{12}(k_2, k_1)P_{\text{pt}}(k_3)$$
$$+ I_{11}(k_2)\mathcal{G}_{12}^{\text{g}\delta}(k_3; k_1)P_{\text{pt}}(k_2). \tag{4.67}$$

Note that the order of the three wave-numbers is different compared to Eq. (4.63) because of the cross-function in Eq. (4.64) which is not symmetric in its arguments. Finally, the three-halo term is

$$B_{\text{3-h}}^{\delta\delta\text{g}}(k_1, k_2; k_3) = I_{11}(k_1)I_{11}(k_2)G_{11}(k_3)B_{\text{pt}}(k_1, k_2, k_3). \tag{4.68}$$

4.4.1 Reduced Bispectra

For the three-point correlation function $\zeta(\boldsymbol{x}_1, \boldsymbol{x}_2, \boldsymbol{x}_3)$ it is useful to define the following dimensionless hierarchical or *reduced* three-point correlation function (see Appendix B.4 for more information)

$$Q(\boldsymbol{x}_1, \boldsymbol{x}_2, \boldsymbol{x}_3) = \frac{\zeta(\boldsymbol{x}_1, \boldsymbol{x}_2, \boldsymbol{x}_3)}{\xi_{12}\xi_{13} + \xi_{12}\xi_{23} + \xi_{13}\xi_{23}}, \tag{4.69}$$

where $\xi_{ij} \equiv \xi(\boldsymbol{x}_i, \boldsymbol{x}_j)$ is the two-point correlation function. If the value of Q is constant then we find after transforming this relation into Fourier space

$$Q = \frac{B(\boldsymbol{k}_1, \boldsymbol{k}_2, \boldsymbol{k}_3)}{P(\boldsymbol{k}_1)P(\boldsymbol{k}_2) + P(\boldsymbol{k}_1)P(\boldsymbol{k}_3) + P(\boldsymbol{k}_2)P(\boldsymbol{k}_3)}, \tag{4.70}$$

with the same value of Q. To study the scale dependence of the bispectrum, it is thus convenient to extend the equation to

$$Q(\boldsymbol{k}_1, \boldsymbol{k}_2, \boldsymbol{k}_3) \equiv \frac{B(\boldsymbol{k}_1, \boldsymbol{k}_2, \boldsymbol{k}_3)}{P(\boldsymbol{k}_1)P(\boldsymbol{k}_2) + P(\boldsymbol{k}_1)P(\boldsymbol{k}_3) + P(\boldsymbol{k}_2)P(\boldsymbol{k}_3)}. \tag{4.71}$$

Note that by assuming isotropy and homogeneity we can parametrize the reduced bispectrum by the modulus of the two triangle sides and the angle between them, i.e., $Q(\boldsymbol{k}_1, \boldsymbol{k}_2, \boldsymbol{k}_3) \to Q(k_1, k_2, \cos\theta)$ where θ is the angle between $\boldsymbol{k}_1$ and $\boldsymbol{k}_2$. On large scales perturbation theory predicts that the bispectrum scales as $B_{\text{pt}} \propto P_{\text{pt}}^2$ (see Eq. 2.123) and Q converges to a constant. On small scales, the *hierarchical ansatz* also predicts that the bispectrum is proportional to the power spectrum squared. It is not clear if higher-order correlation functions follow the hierarchical ansatz in detail. However, even if the bispectrum follows only roughly the hierarchical ansatz the reduced bispectrum has a much weaker scale dependence than the bispectrum itself. We will use Eq. (4.71) for dark matter and galaxy clustering by simply using the corresponding bispectrum and power spectra. Note that we use the nonlinear bispectrum and power spectra to consistently calculate the reduced bispectrum. A generalization of this concept yields
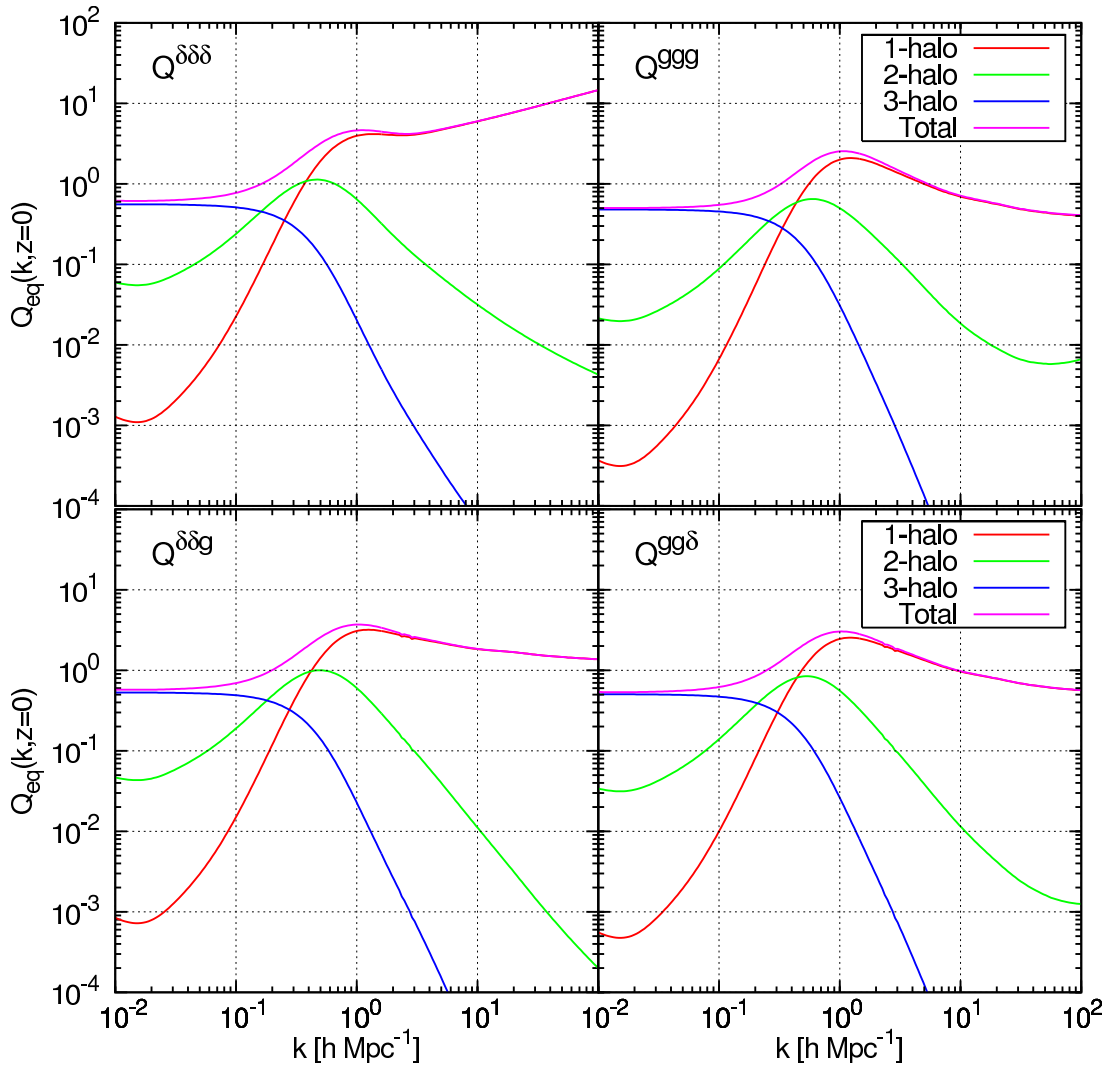
Figure 4.7: Reduced halo model bispectrum Q_{eq} in equilateral configuration (see text for detailed information) as a function of wave-number k at redshift $z = 0$. The two upper panels show the auto-spectra defined in Eq. (4.71): on the left side the dark matter bispectrum and on the right side the galaxy bispectrum. The two lower panels depict the cross-spectra: on the left side the dark matter-dark matter-galaxy as defined in Eq. (4.73) and on the right side the galaxy-galaxy-dark matter bispectrum of Eq. (4.72). All plots show the individual contributions from the one-, two- and three-halo terms to the total bispectrum as indicated in the plots. The three bispectra which include galaxy correlations show a similar scale dependence. The bump feature at intermediate scales ($k \simeq 1\,h\,\text{Mpc}^{-1}$) might be related to our simple halo model implementation (see text for further details).

for the two cross-bispectra

$$Q^{\mathrm{gg}\delta}(\boldsymbol{k}_1, \boldsymbol{k}_2; \boldsymbol{k}_3) = \frac{B^{\mathrm{gg}\delta}(\boldsymbol{k}_1, \boldsymbol{k}_2; \boldsymbol{k}_3)}{P^{\delta\mathrm{g}}(\boldsymbol{k}_1)P^{\delta\mathrm{g}}(\boldsymbol{k}_2) + P^{\mathrm{gg}}(\boldsymbol{k}_1)P^{\delta\mathrm{g}}(\boldsymbol{k}_3) + P^{\mathrm{gg}}(\boldsymbol{k}_2)P^{\delta\mathrm{g}}(\boldsymbol{k}_3)} \,, \qquad (4.72)$$

$$Q^{\delta\delta\mathrm{g}}(\boldsymbol{k}_1, \boldsymbol{k}_2; \boldsymbol{k}_3) = \frac{B^{\delta\delta\mathrm{g}}(\boldsymbol{k}_1, \boldsymbol{k}_2; \boldsymbol{k}_3)}{P^{\delta\mathrm{g}}(\boldsymbol{k}_1)P^{\delta\mathrm{g}}(\boldsymbol{k}_2) + P^{\delta\delta}(\boldsymbol{k}_1)P^{\delta\mathrm{g}}(\boldsymbol{k}_3) + P^{\delta\delta}(\boldsymbol{k}_2)P^{\delta\mathrm{g}}(\boldsymbol{k}_3)} \,. \qquad (4.73)$$

Again we assume isotropy and homogeneity to parametrize the reduced bispectra by k_1, k_2 and the angle between the corresponding vectors. Furthermore, to make a two-dimensional plot of the bispectrum, we define the *equilateral configuration* of the reduced bispectrum $Q_{\mathrm{eq}}(k, z)$ where $k_1 = k_2 = k_3 \equiv k$ and thus the angle between $\boldsymbol{k}_1$ and $\boldsymbol{k}_2$ is $\theta = \pi/3$.

We depict the reduced auto-bispectra in the two upper panels of Fig. 4.7 in dependence of the wave-number k. The upper left panel shows the dark matter bispectrum and the upper right panel the galaxy bispectrum. On the two lower panels we show the cross-spectra, where the lower left panel is the dark matter-dark matter-galaxy bispectrum and the lower right panel the galaxy-galaxy-dark matter bispectrum. The reduced dark matter bispectrum is increasing for small scales, whereas the three reduced bispectra including galaxy correlations are decreasing for small scales. This is in general agreement with the results of the dark matter bispectrum in the literature (Scoccimarro et al. 2001; Ma & Fry 2000; Cooray & Sheth 2002). The bump feature in the bispectrum at intermediate scales ($k \propto 1\,h\,\mathrm{Mpc}^{-1}$) is probably related to inaccuracies in the halo model as reported in Takada & Jain (2003) where they analyzed the three-point correlation function. Partly the feature is a result of halo exclusion which is not included in our halo model. In real space the bump is around $1\,\mathrm{Mpc}$ which is of the order of the virial radius of massive halos that make a significant contribution to the mass integrals in this regime. Hence, our halo model might overestimate the contributions from the two- and three-halo terms at these scales. The bump feature is persistent in the plots of the galaxy bispectrum and the cross-bispectra. The other uncertainty in the halo model is related to the truncation of the integration of the density profile $\tilde{u}(k, m)$ in Eq. (3.55) at the virial radius. Ma & Fry (2000) showed that using the density profile without a cutoff results in bispectra without a bump feature. However, this would violate mass conservation. Including both effects Takada & Jain showed that the maximum in Q nearly vanishes. In summary, we should be cautious with the results of the halo model as presented here at intermediate scales.

4.4.2 Scale-Dependent Bispectrum Bias

In analogy to the galaxy bias factor in Eq. (4.53) we introduce the third-order scale- and redshift-dependent bias parameter b_3 and two galaxy-mass correlation coefficients r_1 and r_2 to get a relation of the galaxy auto-bispectrum and the two cross-bispectra to the dark matter bispectrum. We follow here the definitions of the work of Schneider &
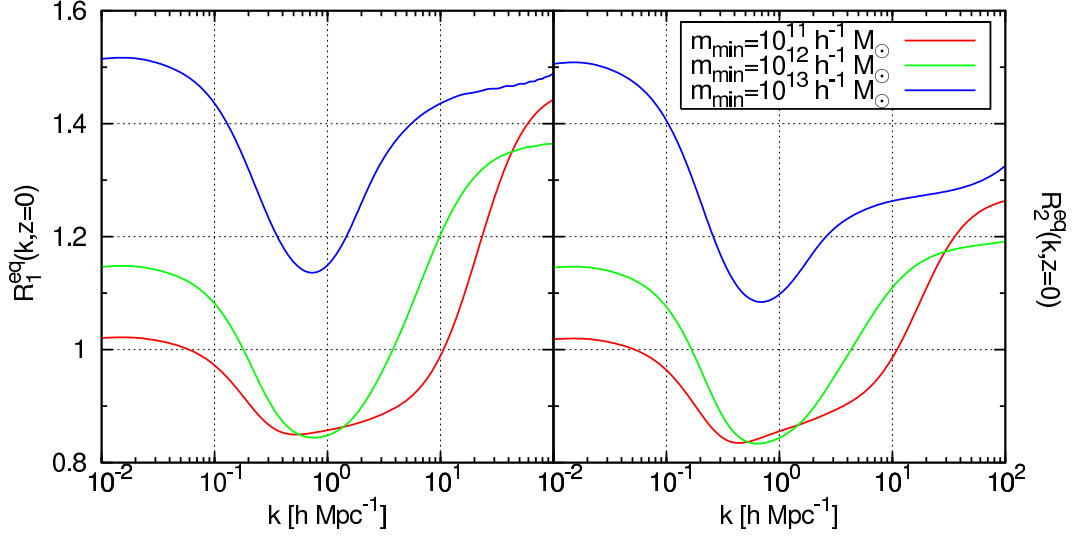
Figure 4.8: Ratios of the galaxy bispectrum to the two cross-bispectra in dependence of the scale k at redshift $z = 0$ and for equilateral triangles. The ratios are shown for three different minimal masses, i.e., $m_{\min} = 10^{11}\,h^{-1}\,M_\odot$, $m_{\min} = 10^{12}\,h^{-1}\,M_\odot$ and $m_{\min} = 10^{13}\,h^{-1}\,M_\odot$ as indicated by the line color. The left panel shows the ratio R_1^{eq} and the right panel shows the ratio R_2^{eq} (see definitions in Eq. 4.78).

Watts (2005):

$$B^{\mathrm{ggg}}(\boldsymbol{k}_1, \boldsymbol{k}_2, \boldsymbol{k}_3; w) = \left[b_3^3 B^{\delta\delta\delta}\right](\boldsymbol{k}_1, \boldsymbol{k}_2, \boldsymbol{k}_3; w)\,, \tag{4.74}$$

$$B^{\mathrm{gg}\delta}(\boldsymbol{k}_1, \boldsymbol{k}_2; \boldsymbol{k}_3; w) = \left[b_3^2 r_2 B^{\delta\delta\delta}\right](\boldsymbol{k}_1, \boldsymbol{k}_2; \boldsymbol{k}_3; w)\,, \tag{4.75}$$

$$B^{\delta\delta\mathrm{g}}(\boldsymbol{k}_1, \boldsymbol{k}_2; \boldsymbol{k}_3; w) = \left[b_3 r_1 B^{\delta\delta\delta}\right](\boldsymbol{k}_1, \boldsymbol{k}_2; \boldsymbol{k}_3; w)\,. \tag{4.76}$$

Using these relations we build the following ratios

$$b_3 = (B^{\mathrm{ggg}}/B^{\delta\delta\delta})^{1/3}\,, \tag{4.77}$$

$$R_2 \equiv \frac{b_3}{r_2} = \frac{B^{\mathrm{ggg}}}{B^{\mathrm{gg}\delta}}\,, \qquad R_1 \equiv \frac{b_3}{\sqrt{r_1}} = \sqrt{\frac{B^{\mathrm{ggg}}}{B^{\delta\delta\mathrm{g}}}}\,, \tag{4.78}$$

$$r_1 = \frac{B^{\delta\delta\mathrm{g}}}{B^{\delta\delta\delta}}\left(\frac{B^{\delta\delta\delta}}{B^{\mathrm{ggg}}}\right)^{1/3}\,, \qquad r_2 = \frac{B^{\mathrm{gg}\delta}}{B^{\delta\delta\delta}}\left(\frac{B^{\delta\delta\delta}}{B^{\mathrm{ggg}}}\right)^{2/3}\,, \tag{4.79}$$

where we suppressed the dependence on the scales and comoving distance. Note that for the bispectrum the bias parameter and the correlation coefficients depend on the considered triangle configuration in Fourier space. For large scales the bias again converges to the case of the linear deterministic bias, i.e., $b_3 \to b_1^{\mathrm{L}}$ and $r_1 = r_2 = 1$. We label the ratios in Eqs. (4.77), (4.78) and (4.79) with the superscript "eq" when we consider equilateral triangle configurations of the Fourier modes in the following.

The results for the equilateral configuration of the two cross-correlation coefficients are shown in Fig. 4.8 and in Fig. 4.10 for the third-order bias parameter. All ratios are shown
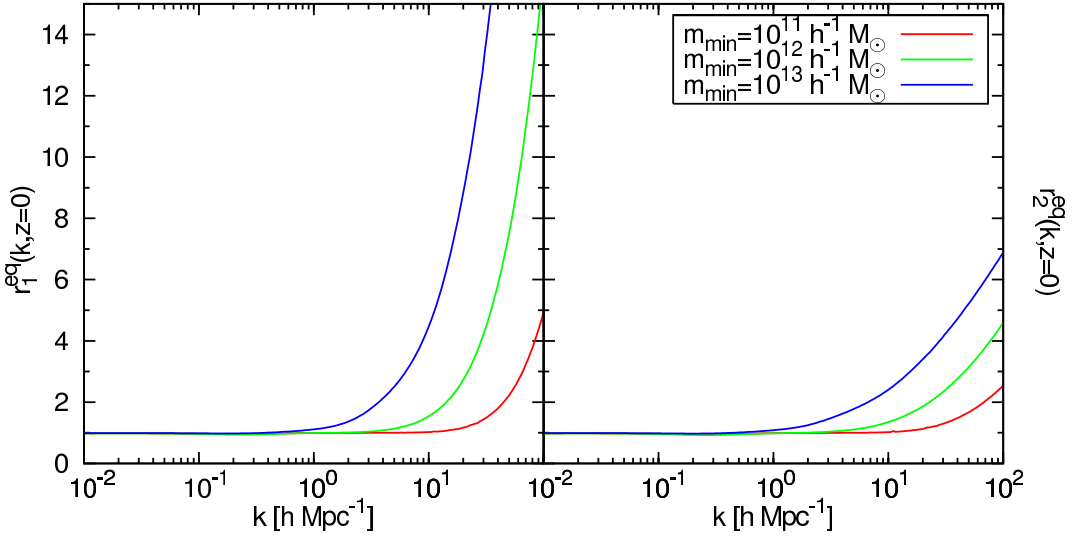
Figure 4.9: Correlation coefficients r_1 and r_2 as a function of the scale k at redshift $z = 0$ and for equilateral triangles. We plot the same minimal masses as in Fig. 4.8. The left panel shows the ratio r_1^{eq} and the right panel shows the ratio r_2^{eq} (see definitions in Eq. 4.79).

for three different threshold masses, i.e., $m_{\min} = 10^{11}\,h^{-1}\,M_\odot$, $m_{\min} = 10^{12}\,h^{-1}\,M_\odot$ and $m_{\min} = 10^{13}\,h^{-1}\,M_\odot$. The left panel of Fig. 4.8 depicts the ratio R_1^{eq} and the right panel shows R_2^{eq} defined in Eq. (4.78). Both ratios have a very similar behavior on all scales noting that we use a linear ordinate. On large scales both ratios resemble the large-scale bias parameter b_1^{L}, whereas on small scales R_2^{eq} shows a weaker scale dependence than R_1^{eq}. The reason for this behavior is that on small scales the central-satellite correlations of the one-halo terms in Eqs. (4.56), (4.62) and (4.66) dominate the different bispectra. In this regime all integrals are the same (if we consider that the HOD of centrals is a step function) and we find for the ratio of both correlation parameters $R_2^{\mathrm{eq}}/R_1^{\mathrm{eq}} = \sqrt{3}/2 \approx 0.87$. More specifically the two cross-bispectra probe different moments of the HOD which leads to the difference in the small-scale regime. We see that at the characteristic scale of $k \simeq 1\,h\,\mathrm{Mpc}^{-1}$ both correlation parameters attain a minimum. Again, we have to be careful with the interpretation at this particular scale because it is sensitive to the halo-biasing scheme for which we use only a simple model. Furthermore, we note that for $10 < k/(h\,\mathrm{Mpc}^{-1}) < 1$ the increase in the correlation function is due to the satellite-satellite-satellite correlations of the one-halo terms. Around $k = 10\,h\,\mathrm{Mpc}^{-1}$ the slope gets flatter which is induced by the transition to the dominance of central-satellite-satellite correlations.

In Fig. 4.9 we depict the ratio r_1^{eq} (left panel) and r_2^{eq} (right panel) defined in Eq. (4.78) as a function of k. On large scales we recover the case of the linear deterministic bias where both ratios $r_1^{\mathrm{eq}} = r_2^{\mathrm{eq}} = 1$, whereas on small scales r_1^{eq} shows a stronger scale dependence than r_2^{eq}.

The third-order bias parameter b_3 shows a similar behavior compared to the power spectrum bias factor in the left panel of Fig. 4.6. The major difference is the weaker
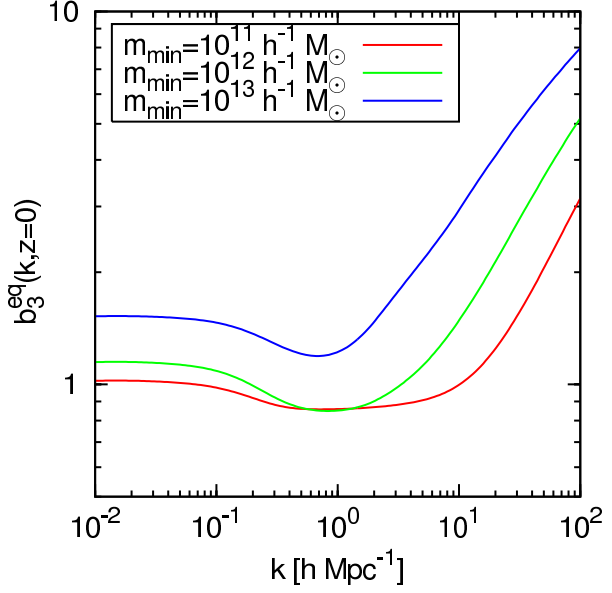
Figure 4.10: The figure depicts the third-order scale-dependent bias parameter of the bispectrum in dependence of the wavenumber k at redshift $z = 0$ and for equilateral triangles as defined in Eq. (4.77). We show the results for three different minimal masses, i.e., $m_{min} = 10^{11}\,h^{-1}\,M_\odot$, $m_{min} = 10^{12}\,h^{-1}\,M_\odot$ and $m_{min} = 10^{13}\,h^{-1}\,M_\odot$ as indicated by the line color. The third-order bias parameter has a similar scale dependence compared to the results of the power spectrum bias factor depicted in the left panel of Fig. 4.6.

scale-dependence of b_3 on small scales.

4.5 Cross-Trispectrum

We define the matter-galaxy-matter-galaxy cross-trispectrum as

$$\langle \delta(\boldsymbol{k}_1)\delta_{\mathrm g}(\boldsymbol{k}_2)\delta(\boldsymbol{k}_3)\delta_{\mathrm g}(\boldsymbol{k}_4)\rangle_{\mathrm c} \equiv (2\pi)^3 \delta_{\mathrm D}(\boldsymbol{k}_1 + \boldsymbol{k}_2 + \boldsymbol{k}_3 + \boldsymbol{k}_4) T^{\delta\mathrm{g}\delta\mathrm{g}}(\boldsymbol{k}_1, \boldsymbol{k}_2, \boldsymbol{k}_3, \boldsymbol{k}_4)\,, \quad (4.80)$$

where $\boldsymbol{k}_1$ and $\boldsymbol{k}_3$ are assigned to the dark matter and $\boldsymbol{k}_2$ and $\boldsymbol{k}_4$ to the galaxy field. Note that this definition of the cross-trispectrum is symmetric under exchanging $\boldsymbol{k}_1$ and $\boldsymbol{k}_3$, and $\boldsymbol{k}_2$ and $\boldsymbol{k}_4$. The cross-trispectrum quantifies the error matrix for the cross-power spectrum estimator or, in the projected case, the covariance matrix for galaxy-galaxy lensing. Since we need only parallelogram configurations (this will be the topic of Chapter 7, in particular see Eq. 7.73) for the calculation of the covariance matrix, we present our model of the cross-trispectrum only for this particular case. We parametrize the trispectrum with the length of the two sides of the parallelogram k_1 and k_2 and the angle θ between them, i.e.,

$$T^{\delta\mathrm{g}\delta\mathrm{g}}(\boldsymbol{k}_1, -\boldsymbol{k}_1, \boldsymbol{k}_2, -\boldsymbol{k}_2) \equiv T^{\delta\mathrm{g}\delta\mathrm{g}}_{\mathrm{pc}}(k_1, k_2, \cos\theta)\,, \quad (4.81)$$

with $\cos\theta = \boldsymbol{k}_1 \cdot \boldsymbol{k}_2/(k_1 k_2)$. We reiterate that this configuration is symmetric under permutations of k_1 and k_2, i.e., $T^{\delta\mathrm{g}\delta\mathrm{g}}_{\mathrm{pc}}(k_1, k_2, \cos\theta) = T^{\delta\mathrm{g}\delta\mathrm{g}}_{\mathrm{pc}}(k_2, k_1, \cos\theta)$. In the following we will drop the subscript "pc" labeling our parallelogram configuration.

To model the cross-trispectrum, we extend the halo model results of the dark matter trispectrum. Again we neglect all terms involving the second- and third-order halo bias factors as they provide only small contributions. We obtained in the previous

chapter the following expression for the one-halo term of the dark matter trispectrum in parallelogram configuration

$$T_{\text{1-h}}^{\delta\delta\delta\delta}(k_1, k_2) = \int dm\, n(m) \left(\frac{m}{\bar{\rho}}\right)^4 \tilde{u}_{\text{dm}}^2(k_1, m)\tilde{u}_{\text{dm}}^2(k_2, m)\,, \qquad (4.82)$$

which is independent of the angle between the two vectors. Generalizing this result to the cross-trispectrum yields

$$T_{\text{1-h}}^{\delta g \delta g}(k_1, k_2) = \int dm\, n(m) \left(\frac{m}{\bar{\rho}}\right)^2 \frac{\langle N(N-1)(m)\rangle}{\bar{n}_{\text{g}}^2}$$
$$\times\, \tilde{u}_{\text{dm}}(k_1, m)\tilde{u}_{\text{dm}}(k_2, m)\tilde{u}_{\text{g}}(k_1, m)\tilde{u}_{\text{g}}(k_2, m)\,, \qquad (4.83)$$

Including a central galaxy population instead of a pure satellite population the weighting of the number of pairs changes to (see also Eq. B.34)

$$T_{\text{1-h}}^{\delta g \delta g}(k_1, k_2) = \int dm\, n(m) \left(\frac{m}{\bar{\rho}}\right)^2 \tilde{u}_{\text{dm}}(k_1, m)\tilde{u}_{\text{dm}}(k_2, m)$$
$$\times\, \frac{1}{\bar{n}_{\text{g}}^2} \left\{ \bar{N}_{\text{sat}}^2 \tilde{u}_{\text{g}}(k_1, m)\tilde{u}_{\text{g}}(k_2, m) + \bar{N}_{\text{sat}}\bar{N}_{\text{cen}}[\tilde{u}_{\text{g}}(k_1, m) + \tilde{u}_{\text{g}}(k_2, m)] \right\}\,. $$
$$(4.84)$$

The two-halo term is composed of two different terms

$$T_{\text{2-h}}^{\delta g \delta g}(k_1, k_2, \cos\theta) = T_{(31)}^{\delta g \delta g}(k_1, k_2, \cos\theta) + T_{(22)}^{\delta g \delta g}(k_1, k_2, \cos\theta)\,. \qquad (4.85)$$

The first term describes a correlation of particles (galaxies/dark matter) which are contained in two halos where three particles are in one halo and the fourth particle is in the other halo. A generalization of the corresponding dark matter relation in Eq. (7.66) gives

$$T_{(31)}^{\delta g \delta g}(k_1, k_2, \cos\theta) = P_1 \mathcal{G}_{13}^{g\delta g}(k_1, k_2, k_2) I_{11}(k_1) + P_1 \mathcal{G}_{13}^{\delta g \delta}(k_2, k_2, k_1) G_{11}(k_1)$$
$$+ P_2 \mathcal{G}_{13}^{g\delta g}(k_2, k_1, k_1) I_{11}(k_2) + P_2 \mathcal{G}_{13}^{\delta g \delta}(k_1, k_1, k_2) G_{11}(k_2)\,, \qquad (4.86)$$

where $P_i \equiv P_{\text{pt}}(k_i)$ and we need the cross-correlations of galaxy-matter-galaxy $\mathcal{G}_{13}^{g\delta g}$ and matter-galaxy-matter $\mathcal{G}_{13}^{\delta g \delta}$, respectively. They are defined by

$$\mathcal{G}_{13}^{g\delta g}(k_1, k_2, k_2) = \int dm\, n(m) \left(\frac{m}{\bar{\rho}}\right) \tilde{u}_{\text{dm}}(k_2, m) b_1^{\text{h}}(m)$$
$$\times\, \frac{1}{\bar{n}_{\text{g}}^2} \left[\bar{N}_{\text{sat}}^2 \tilde{u}_{\text{g}}(k_1, m)\tilde{u}_{\text{g}}(k_2, m) + \bar{N}_{\text{cen}}\bar{N}_{\text{sat}}[\tilde{u}_{\text{g}}(k_1, m) + \tilde{u}_{\text{g}}(k_2, m)] \right]\,, $$
$$(4.87)$$

$$\mathcal{G}_{13}^{\delta g \delta}(k_1, k_1, k_2) = \int dm\, n(m) \left(\frac{m}{\bar{\rho}}\right)^2 \tilde{u}_{\text{dm}}(k_1, m)\tilde{u}_{\text{dm}}(k_2, m) b_1^{\text{h}}(m)$$
$$\times\, \frac{1}{\bar{n}_{\text{g}}} \left[\bar{N}_{\text{sat}} \tilde{u}_{\text{g}}(k_1, m) + \bar{N}_{\text{cen}} \right]\,. \qquad (4.88)$$

The second contribution to the two-halo term (4.85) corresponds to the situation where each halo contains two particles. From the corresponding dark matter relation (3.139) we deduce

$$T^{\delta g \delta g}_{(22)} = P^+_{12} I_{12}(k_1, k_2) G_{12}(k_1, k_2) + P^-_{12} \mathcal{G}^{g\delta}_{12}(k_2; k_1) \mathcal{G}^{g\delta}_{12}(k_1; k_2) \,, \tag{4.89}$$

with $P^+_{12} \equiv P_{\rm pt}(|\boldsymbol{k}_1 + \boldsymbol{k}_2|)$ and $P^-_{12} \equiv P_{\rm pt}(|\boldsymbol{k}_1 - \boldsymbol{k}_2|)$ and $\mathcal{G}^{g\delta}_{12}$ is given in Eq. (4.64). Starting from Eq. (3.145) the three-halo term of the cross-trispectrum is given by

$$\begin{aligned}
T^{\delta g \delta g}_{\rm 3\text{-}h}(k_1, k_2, \cos\theta) = {} & G_{11}(k_1) G_{11}(k_2) I_{12}(k_1, k_2) B_{\rm pt}(\boldsymbol{k}_1, \boldsymbol{k}_2, -\boldsymbol{k}_1 - \boldsymbol{k}_2) \\
& + G_{11}(k_1) I_{11}(k_2) \mathcal{G}^{g\delta}_{12}(k_2; k_1) B_{\rm pt}(\boldsymbol{k}_1, -\boldsymbol{k}_2, \boldsymbol{k}_2 - \boldsymbol{k}_1) \\
& + I_{11}(k_1) G_{11}(k_2) \mathcal{G}^{g\delta}_{12}(k_1; k_2) B_{\rm pt}(\boldsymbol{k}_1, -\boldsymbol{k}_2, \boldsymbol{k}_2 - \boldsymbol{k}_1) \\
& + I_{11}(k_1) I_{11}(k_2) G_{12}(k_1, k_2) B_{\rm pt}(\boldsymbol{k}_1, \boldsymbol{k}_2, -\boldsymbol{k}_1 - \boldsymbol{k}_2) \,.
\end{aligned} \tag{4.90}$$

Finally, the four-halo term in Eq. (3.137) changes to

$$T^{\delta g \delta g}_{\rm 4\text{-}h}(k_1, k_2, \cos\theta) = I_{11}(k_1) I_{11}(k_2) G_{11}(k_1) G_{11}(k_2) T_{\rm pt}(\boldsymbol{k}_1, -\boldsymbol{k}_1, \boldsymbol{k}_2, -\boldsymbol{k}_2) \,. \tag{4.91}$$

Note that the perturbation theory trispectrum depends for this configuration only on k_1, k_2 and $\cos\theta$ and it is given in Eqs. (2.129)-(2.131).

4.5.1 Reduced Trispectrum

Again it is useful to introduce the reduced cross-trispectrum which shows a weaker scale-dependence. It is defined as (see Appendix B.4)

$$Q^{\delta g \delta g}(\boldsymbol{k}_1, \boldsymbol{k}_2, \boldsymbol{k}_3, \boldsymbol{k}_4) \equiv \frac{T^{\delta g \delta g}(\boldsymbol{k}_1, \boldsymbol{k}_2, \boldsymbol{k}_3, \boldsymbol{k}_4)}{d_{\rm snake}(\boldsymbol{k}_1, \boldsymbol{k}_2; \boldsymbol{k}_3, \boldsymbol{k}_4) + d_{\rm star}(\boldsymbol{k}_1, \boldsymbol{k}_2; \boldsymbol{k}_3, \boldsymbol{k}_4)} \,, \tag{4.92}$$

where $d_{\rm snake}$ and $d_{\rm star}$ are the two topologically different contributions of the hierarchical model of the trispectrum which we showed in Fig. 2.1. A special case of the cross-trispectrum which is useful for plotting is the *square configuration*, where all sides have equal length and the angle between two vectors is $\pi/2$, more precisely

$$T^{\delta g \delta g}_{\rm sq}(k) \equiv T^{\delta g \delta g}_{\rm pc}(k, k, \cos\theta = 0) \,. \tag{4.93}$$

Using this configuration we define the dimensionless trispectrum

$$\Delta_{\rm sq}(k) \equiv \frac{k^3}{2\pi^2} \left[T^{\delta g \delta g}_{\rm sq}(k) \right]^{1/3} \,, \tag{4.94}$$

and the reduced trispectrum

$$Q^{\delta g \delta g}_{\rm sq}(k) = \frac{T^{\delta g \delta g}_{\rm sq}(k)}{d^{\rm (sq)}_{\rm snake}(k) + d^{\rm (sq)}_{\rm star}(k)} \,. \tag{4.95}$$
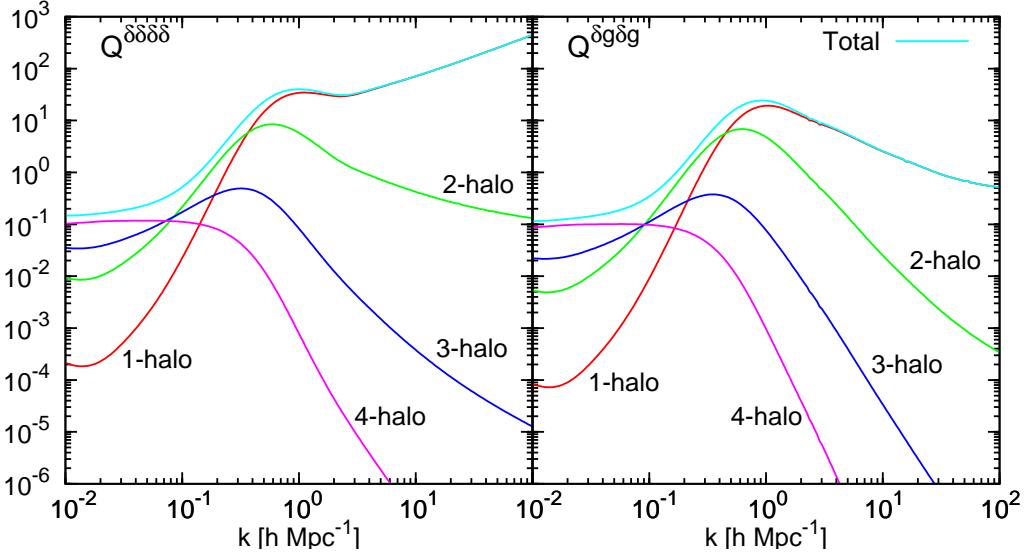
Figure 4.11: Reduced trispectrum in the square configuration at redshift $z = 0$ splitted into the individual contributions from the one-halo, two-halo, three-halo and four-halo term. The left panel depicts the reduced dark matter trispectrum and the right panel the reduced cross-trispectrum defined in Eq. (4.95).

For the square configuration the terms in the denominator are given by

$$d_{\mathrm{snake}}^{(\mathrm{sq})}(k) = \left\{ 2P^{\delta \mathrm{g}}(\sqrt{2}k) + P^{\mathrm{gg}}(\sqrt{2}k) + P^{\delta\delta}(\sqrt{2}k) \right\} [P^{\delta \mathrm{g}}(k)]^2$$
$$+ 4P^{\delta \mathrm{g}}(\sqrt{2}k)P^{\delta\delta}(k)P^{\mathrm{gg}}(k) , \tag{4.96}$$

$$d_{\mathrm{star}}^{(\mathrm{sq})}(k) = 2P^{\mathrm{gg}}(k)[P^{\delta \mathrm{g}}(k)]^2 + 2P^{\delta\delta}(k)[P^{\delta \mathrm{g}}(k)]^2 . \tag{4.97}$$

On large scales we find

$$Q^{\delta \mathrm{g} \delta \mathrm{g}}(k) = \frac{b^2 \, T_{\mathrm{pt}}(k, x = 0)}{(2b + b^2 + 1 + 4b^3)P_{\mathrm{pt}}(\sqrt{2}k)P_{\mathrm{pt}}^2(k) + 2b^2(b^2 + 1)P_{\mathrm{pt}}^3(k)} , \tag{4.98}$$

where we used the notation $b \equiv b_1^{\mathrm{L}}$. For the case of unbiased galaxies ($b = 1$) we resemble the result for the reduced dark matter trispectrum (see Cooray & Sheth 2002):

$$Q^{\delta\delta\delta\delta}(k) = \frac{T_{\mathrm{pt}}(k, x = 0)}{8P_{\mathrm{pt}}(\sqrt{2}k)P_{\mathrm{pt}}^2(k) + 4P_{\mathrm{pt}}^3(k)} . \tag{4.99}$$

The two reduced trispectra are shown in Fig. 4.11 splitted into the four halo terms. The left panel depicts the dark matter trispectrum and the right panel the cross-trispectrum. Compared to the reduced cross-bispectrum in Fig. 4.7 the general behavior of the cross-trispectrum is very similar. For large scales it is smaller than 1 and then
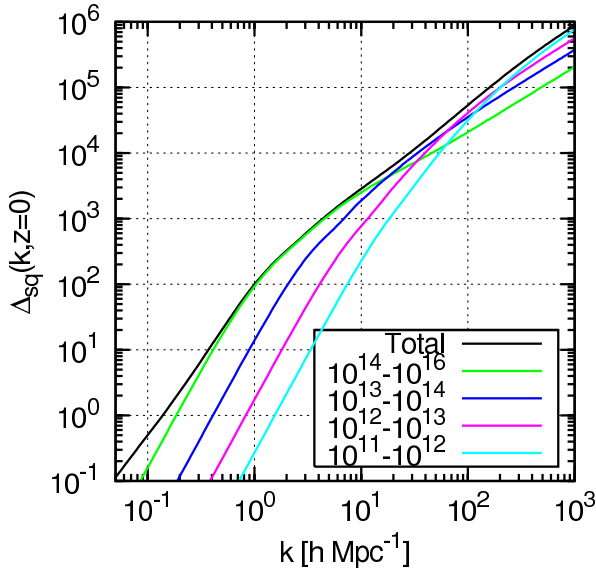
Figure 4.12: Mass contributions to the cross-trispectrum in square configuration defined in Eq. (4.94) at redshift $z = 0$. Shown is the effect on the one-halo term from halos in certain mass intervals as indicated by the line color. Note that the black line shows the total cross-trispectrum including all halo terms which explains the deviation of the green line to the black line on large scales. Compared to the results of the galaxy power spectrum in the right panel of Fig. 4.4, the trispectrum is dominated by higher mass halos.

rises until $k \simeq 1\,h\,\mathrm{Mpc}^{-1}$ where it slowly decreases for small scales. On large scales the reduced trispectrum goes to a constant that is different from that for the reduced bispectrum. The peak at $k \simeq 1\,h\,\mathrm{Mpc}^{-1}$ is approximately one magnitude larger than for the cross-bispectrum, whereas on small scales it drops below 1. On the other hand, the dark matter trispectrum is rising for small scales in the same way as the dark matter bispectrum depicted in the upper left-hand panel of Fig. 4.7.

In Fig. 4.12 we show the different mass contributions to the one-halo term of the cross-trispectrum defined in Eq. (4.94). As expected, the dimensionless cross-trispectrum is dominated by more massive halos compared to the results of the galaxy power spectrum in Fig. 4.4 because it has a stronger mass-weighting. This can be seen for example by comparing the mass factors of the one-halo terms in Eqs. (4.82) and (4.27).

4.6 Inclusion of a Stochastic Concentration Parameter

In this section we explore the effect of a stochastical concentration parameter on the power spectrum, bispectrum and trispectrum. We already discussed that halos of the same mass have a distribution of concentrations which is well described by a log-normal distribution around the mean concentration with dispersion $\sigma_{\ln c}$. In particular, we want to study the impact on the dark matter, galaxy and cross-spectra. The stochastical concentration parameter has an impact on the density profile of dark matter and galaxies. Since the density profile affects the spectra mostly on small scales we only need to analyze the influence on the one-halo terms of the spectra. In all subsequent figures we show the effect on the relevant dark matter spectrum in the left panel for reference. To quantify the influence of a concentration parameter distribution we define the ratio of the one-halo term including a stochastic concentration to the one-halo term with a deterministic concentration. For the one-halo term of the power spectrum we define the
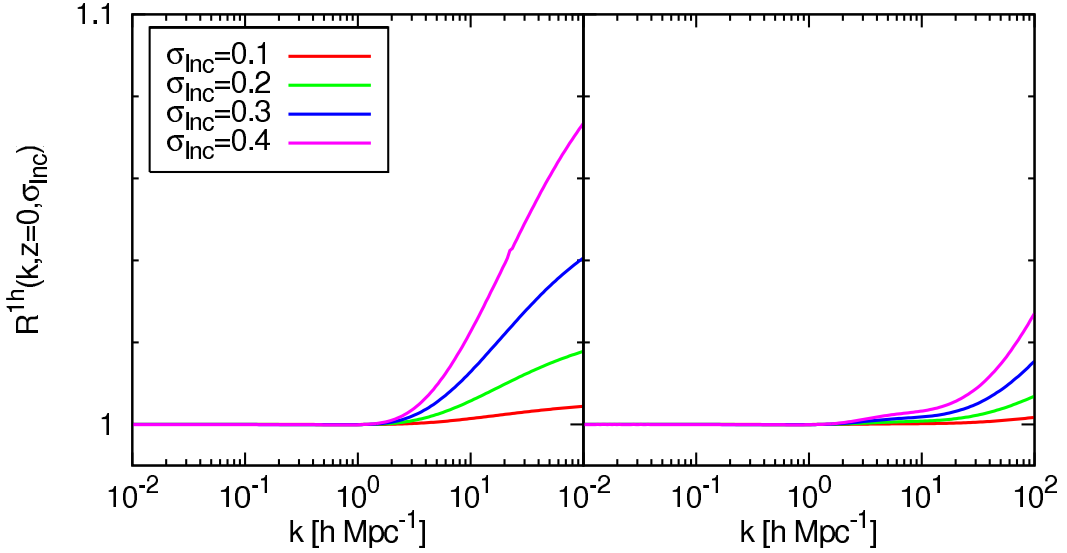
Figure 4.13: Ratio of the one-halo term of the power spectrum including a concentration parameter distribution to the one-halo term with a deterministic concentration parameter as a function of the wave-number. On the left panel we show the ratio for the dark matter power spectrum and on the right panel the ratio for the galaxy power spectrum. We display the results for four different concentration parameter dispersion, i.e., $\sigma_{\ln c} \in \{0.1, 0.2, 0.3, 0.4\}$ indicated by the different line color. Note that a ratio of 1 corresponds to perfect agreement between both spectra.

ratio

$$R^{1h}(k, z; \sigma_{\ln c}) \equiv \frac{\Delta^{1h}(k, z; \sigma_{\ln c})}{\Delta^{1h}(k, z; \sigma_{\ln c} = 0)} \, . \tag{4.100}$$

The result is depicted in Fig. 4.13, where we have plotted the ratio as a function of the wave-number. We show the results for four different choices of the concentration dispersion, i.e., $\sigma_{\ln c} \in \{0.1, 0.2, 0.3, 0.4\}$. Results from simulations prefer values around $\sigma_{\ln c} = 0.2$–0.3 (see Jing 2000 and the recent results from the millennium run in Neto et al. 2007[11]). These values are bracketed by the two extremes of a low and high value of the dispersion. A higher concentration dispersion leads also to an enhanced power spectrum on small scales. We see that the influence of a concentration distribution starts around $k \simeq 1\,h\,\mathrm{Mpc}^{-1}$ for both panels. However, the impact of the dispersion is negligible also on small scales, especially for the galaxy power spectrum.

We define analogously the ratio of the one-halo term of the bispectrum as

$$R_{\mathrm{eq}}^{1h}(k, z; \sigma_{\ln c}) \equiv \frac{\Delta_{\mathrm{eq}}^{1h}(k, z; \sigma_{\ln c})}{\Delta_{\mathrm{eq}}^{1h}(k, z; \sigma_{\ln c} = 0)} \, , \tag{4.101}$$

---

[11]Note that they quote best-fit values for a log-normal distribution with base 10. Therefore one needs to transform the dispersion using $\sigma_{\ln c} = \ln(10)\sigma_{\log_{10} c}$.

where we defined the dimensionless form of the bispectrum for equilateral triangles

$$\Delta_{\mathrm{eq}}(k, z) \equiv \frac{k^3}{2\pi^2} \sqrt{B(k, k, k, z)} \,. \qquad (4.102)$$

The results of the ratio for the one-halo term of the bispectrum are shown in Fig. 4.14 as a function of the wave-number. On the upper left panel we depict the dark matter bispectrum and on the upper right panel the galaxy bispectrum. The dark matter bispectrum ratio grows in the extreme case of $\sigma_{\ln c} = 0.4$ to $R_{\mathrm{eq}}^{1\mathrm{h}} = 1.5$ for the smallest considered scale of $k = 10^2 \, h \, \mathrm{Mpc}^{-1}$. For $\sigma_{\ln c} = 0.2$ we find $R_{\mathrm{eq}}^{1\mathrm{h}} = 1.1$ and for $\sigma_{\ln c} = 0.3$ the ratio is $R_{\mathrm{eq}}^{1\mathrm{h}} = 1.26$ for the smallest scale. On the other hand, we find smaller ratios for the galaxy bispectrum, i.e., $R_{\mathrm{eq}}^{1\mathrm{h}} = 1.05$ for $\sigma_{\ln c} = 0.2$ and $R_{\mathrm{eq}}^{1\mathrm{h}} = 1.1$ for $\sigma_{\ln c} = 0.3$. Clearly, the influence of a stochastic concentration parameter is less pronounced for the galaxy bispectrum. This is expected since on small scales the galaxy bispectrum is dominated by central-satellite-satellite correlations in Eq. (4.56) which are weighted by one density profile less compared to the dark matter density profile. Hence, the galaxy bispectrum is less affected by the enhancement of the density profile due to the log-normal distribution of the concentration parameter. Thus on the smallest scales we have the approximate relation that the ratio of the dispersion for $\sigma_{\ln c} = 0.2$ and $\sigma_{\ln c} = 0.3$ for dark matter corresponds to $\sigma_{\ln c} = 0.3$ and $\sigma_{\ln c} = 0.4$ for galaxy clustering, respectively. We find similar results for the two cross-bispectra (not shown) which is due to the fact that the bispectra including galaxy correlations have on small scales the same dependence on the density profiles.

Finally, we define the ratio for the one-halo term of the dark matter and cross-trispectrum

$$R_{\mathrm{sq}}^{1\mathrm{h}}(k, z; \sigma_{\ln c}) \equiv \frac{\Delta_{\mathrm{sq}}^{1\mathrm{h}}(k, z; \sigma_{\ln c})}{\Delta_{\mathrm{sq}}^{1\mathrm{h}}(k, z; \sigma_{\ln c} = 0)} \,, \qquad (4.103)$$

where we used the definition of the dimensionless trispectrum in Eq. (4.94). The results are shown in Fig. 4.14 in dependence of the Fourier mode, where the lower left panel shows the predictions of the dark matter trispectrum and the lower right panel the results for the galaxy-dark matter cross-trispectrum. Compared to the predictions in Fig. 4.14 the influence of a stochastic concentration is enhanced. This is due to the fact that the trispectrum is weighted by four density profiles in contrast to the bispectrum which is only weighted by three density profiles. We find $R_{\mathrm{sq}}^{1\mathrm{h}} = 1.16$ for dark matter and $R_{\mathrm{sq}}^{1\mathrm{h}} = 1.08$ for the cross-trispectrum for $\sigma_{\ln c} = 0.2$ at the smallest scale. Furthermore, we find for $\sigma_{\ln c} = 0.3$, $R_{\mathrm{sq}}^{1\mathrm{h}} = 1.4$ for the dark matter and $R_{\mathrm{sq}}^{1\mathrm{h}} = 1.2$ the cross-trispectrum, respectively.

In summary, we find that the inclusion of a concentration parameter distribution is less important for galaxy and galaxy-dark matter cross-spectra compared to dark matter spectra. We showed this effect for the power spectrum, bispectrum and trispectrum. The effect is most important for the trispectrum.
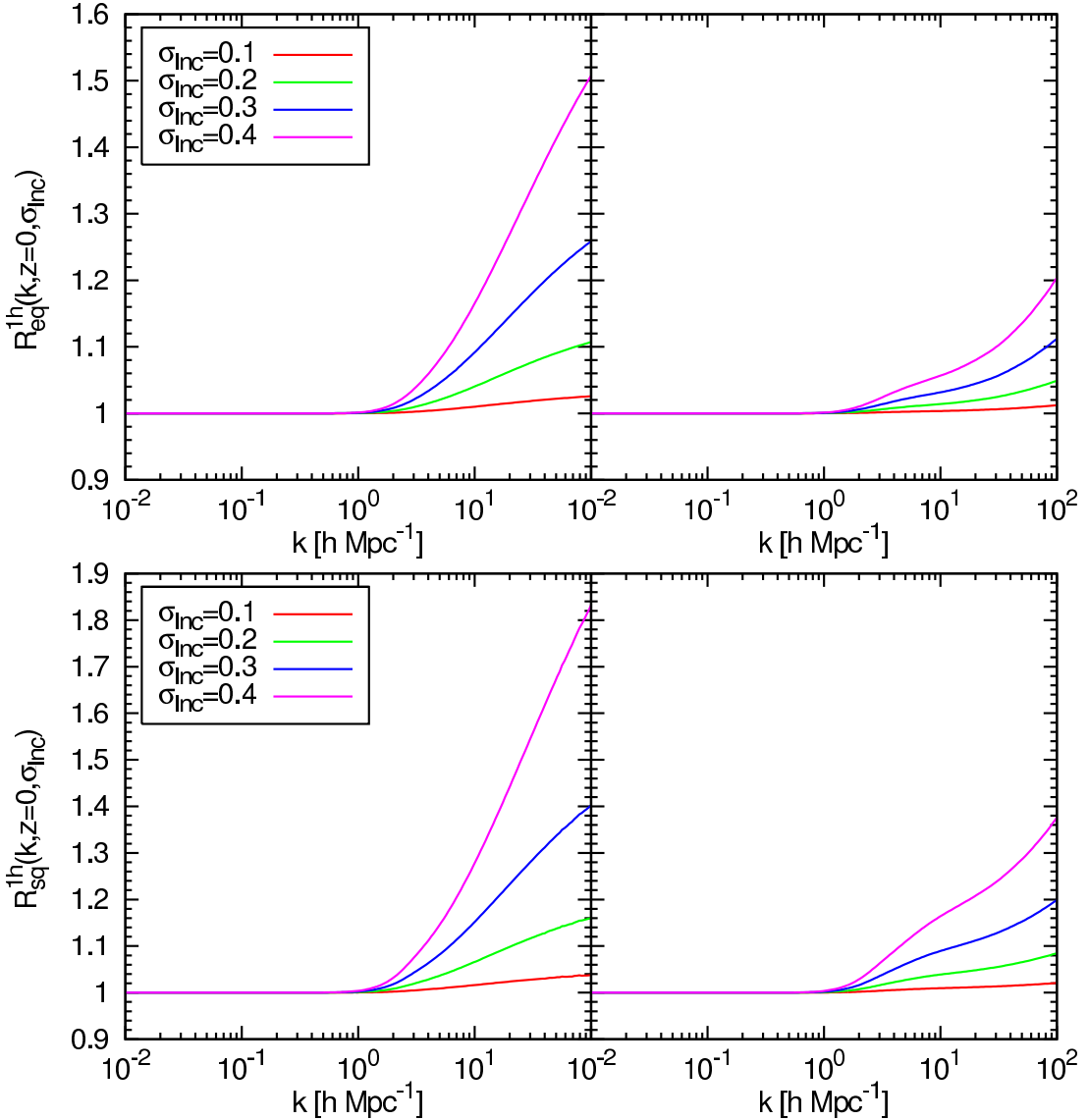
Figure 4.14: Ratio of the one-halo term of the equilateral bispectra including a concentration parameter distribution to the one-halo term with a deterministic concentration parameter as defined in Eq. (4.101) as a function of the Fourier mode k and at redshift $z = 0$ (upper panels). Additionally, we give the corresponding ratio for the one-halo terms of the trispectra in square configuration as a function of the wave-number k as defined in Eq. (4.103) (lower panels). All left-hand panels give the results for the dark matter spectra for reference. In the right-hand panels we plot the ratio of the galaxy bispectrum (upper right panel) and the cross-trispectrum (lower right panel). The four models of the concentration dispersion have different line colors as indicated in the figure. On large scales we see no deviations, whereas on small scales the ratio is larger than one.

Chapter 5

Weak Gravitational Lensing

Traditional probes of the large-scale structure like angular and redshift galaxy surveys basically measure the distribution of luminous matter in the Universe. However, as we already mentioned, the matter distribution of the Universe is dominated by non-luminous dark matter. A recent promising tool is weak gravitational lensing which is sensitive to the total mass distribution. The method makes use of the fact that inhomogeneities of the matter distribution induce multiple distortions of the shape of distant galaxies. Analyzing the statistics of this distortion pattern of galaxies is directly proportional to the dark matter power spectrum when we consider Gaussian fluctuations. This is a clear advantage over the analyses of galaxy surveys since it is then not necessary to consider the bias which involves the modeling of complex baryonic effects.

The deflection of light rays by mass concentrations is a prediction of general relativity. Already in 1919, Eddington performed empirical tests of this theory by observing the light of stars passing close to the Sun during a solar eclipse. He found that the light of the stars was slightly displaced and that the measured deflection could be explained by general relativity predictions[1]. Soon afterwards, it was suspected that in ideal source-lens configurations massive astronomical objects could lead to multiple images of high-redshift sources. However, only in 1979 the first double imaged quasar was observed (Walsh et al. 1979). Today the most prominent observed lensing features are *giant arcs* around the central region of massive galaxy clusters (discovered by Lynds & Petrosian 1986). They can be used to estimate the mass of the lensing galaxy cluster and the results can be compared to dynamical X-ray estimates. These strong effects are rare, however, less distorted images of background galaxies, so-called *arclets*, can be identified in many galaxy clusters. A perfectly alignment of source, lens and observer allows for a ring-like image around the lens, the so-called *Einstein ring* (e.g., Impey et al. 1998). All these effects occur in the regime of strong gravitational lensing.

Another method which uses the gravitational lensing effect is microlensing. It utilizes the fact that a moving object shows an enhanced magnification when it enters the line which connects a background source with our line-of-sight. This can be utilized for the search of non-luminous massive compact halo objects (MACHOs) in our Galaxy.

---

[1]In fact, a Newtonian consideration yields a deflection angle which is half as large as the general relativity prediction.

Intensive observations revealed that stellar-mass MACHOs cannot explain the amount of dark matter in our Galaxy (Alcock et al. 2000). Furthermore, the method can be used for the detection of extrasolar planets (e.g., Beaulieu et al. 2006). In summary, gravitational lensing applications provide us with a wealth of information of the matter distribution of the Universe at different length scales.

Although this chapter deals with the weak gravitational lensing effect, we first need to introduce the basic concepts of gravitational lensing which is done in Sect. 5.1. Subsequently, Sect. 5.2 provides a discussion of weak gravitational lensing induced by the large-scale structure of the Universe which is commonly referred to as cosmic shear.

5.1 Basic Concepts of Gravitational Lensing

Here we lay out the basic lensing formalism needed for the subsequent sections, most importantly the deflection angle of a mass distribution, the lens equation and magnification and distortion of source images caused by lensing.

5.1.1 The Deflection Angle of a Point-Mass Lens

The deflection angle describes the bending of a light ray in the presence of a gravitational field Φ induced by a mass distribution. In the limit of weak gravitational fields, where $|\Phi| \ll c^2$, one can use a slightly perturbed Minkowski space-time (Schneider et al. 1992)

$$\mathrm{d}s^2 = \left(1 + \frac{2\Phi}{c^2}\right) c^2 \mathrm{d}t^2 - \left(1 - \frac{2\Phi}{c^2}\right) \mathrm{d}l^2 \,, \tag{5.1}$$

where the three-dimensional spatial line element is defined by $\mathrm{d}l^2 \equiv \mathrm{d}x_i \mathrm{d}x^i = \mathrm{d}x^2 + \mathrm{d}y^2 + \mathrm{d}z^2$. As light rays travel on null geodesics, the line element fulfills the condition $\mathrm{d}s^2 = 0$. We find then from Eq. (5.1)

$$\mathrm{d}t = \frac{1}{c}\sqrt{\frac{1-x}{1+x}}\mathrm{d}l = \frac{1}{c}\left(1 - x\right)\mathrm{d}l + \mathcal{O}(x^2) \,, \tag{5.2}$$

where we took only linear terms in $x \equiv 2\Phi/c^2$ into account in the second step. The speed of light is changed due to the presence of the potential Φ according to

$$c' = \frac{\mathrm{d}l}{\mathrm{d}t} = \frac{c}{1-x} \,, \tag{5.3}$$

where c' is the speed of light in the presence of the potential. It is then common to introduce in analogy to classical optics the refraction index n as the ratio of the vacuum speed of light to the speed of light changed by a medium:

$$n \equiv \frac{c}{c'} = 1 - \frac{2\Phi}{c^2} \,. \tag{5.4}$$

As the potential fulfills $\Phi \leq 0$ (defining the potential such that it approaches zero at infinity), the refraction index is always larger than 1, i.e., $n \geq 1$. Hence, the velocity of light near a mass concentration is smaller than the vacuum speed of light, i.e., $c' < c$.

The analogy to classical optics is further used to apply Fermat's principle to derive an expression for the deflection angle. Fermat's principle states that light waves of a given frequency propagate along stationary-time paths with fixed end points. In other words, the integral along a light ray becomes stationary compared to all other hypothetical paths. Denoting the light path with $\boldsymbol{x}(l)$ we find

$$\delta \int_A^B n[\boldsymbol{x}(l)]\,\mathrm{d}l = 0\,, \tag{5.5}$$

where A and B denote the fixed start and end points and δ the variation of the light path. Parametrizing this curve with λ yields for Eq. (5.5)

$$\delta \int_A^B n[\boldsymbol{x}(\lambda)]|\dot{\boldsymbol{x}}|\,\mathrm{d}\lambda = 0\,, \tag{5.6}$$

where $\dot{\boldsymbol{x}} \equiv \mathrm{d}\boldsymbol{x}/\mathrm{d}\lambda$ is the tangent vector of the curve. We can set $\dot{\boldsymbol{x}} = \boldsymbol{e}$, where $\boldsymbol{e}$ is a unit vector because the parameter λ can be chosen arbitrarily. From the variation of Eq. (5.6), we get the Euler-Lagrange equations

$$\frac{\mathrm{d}}{\mathrm{d}\lambda}\frac{\partial L}{\partial \dot{\boldsymbol{x}}} - \frac{\partial L}{\partial \boldsymbol{x}} = 0\,, \tag{5.7}$$

where the Lagrangian is given by $L = n[\boldsymbol{x}(\lambda)]|\dot{\boldsymbol{x}}|$. Performing the derivatives, and rearranging the terms yields

$$n\dot{\boldsymbol{e}} = \boldsymbol{\nabla} n - \boldsymbol{e}(\boldsymbol{\nabla} n \cdot \boldsymbol{e}) \equiv \boldsymbol{\nabla}_\perp n(\boldsymbol{x})\,. \tag{5.8}$$

The term $\boldsymbol{e}(\boldsymbol{\nabla} n \cdot \boldsymbol{e})$ is the derivative along the light path. Thus, the whole expression is the derivative perpendicular to the light path which we have denoted by $\boldsymbol{\nabla}_\perp$. Finally, we have

$$\dot{\boldsymbol{e}} = \frac{\mathrm{d}^2\boldsymbol{x}}{\mathrm{d}\lambda^2} = \frac{1}{n}\boldsymbol{\nabla}_\perp n = \boldsymbol{\nabla}_\perp \ln n = \boldsymbol{\nabla}_\perp \ln\left(1 - \frac{2\Phi}{c^2}\right) \approx -\frac{2}{c^2}\boldsymbol{\nabla}_\perp \Phi\,, \tag{5.9}$$

where we inserted the index of refraction given by Eq. (5.4) in the fourth step and the expansion $\ln(1 + x) \approx x$ (valid for $x \ll 1$) in the last step. We can then calculate the total deflection angle of the light ray as the integral of $\dot{\boldsymbol{e}}$ along the light path because it describes the total change of the direction of the tangent vector $\boldsymbol{e}$:

$$\hat{\boldsymbol{\alpha}} = \frac{2}{c^2} \int_A^B \boldsymbol{\nabla}_\perp \Phi\,\mathrm{d}l\,. \tag{5.10}$$

As the potential and therefore the individual deflection angles are small, we integrate in first order along the unperturbed straight path instead of the true curved one. This is the so-called Born approximation according to scattering theory in quantum mechanics.
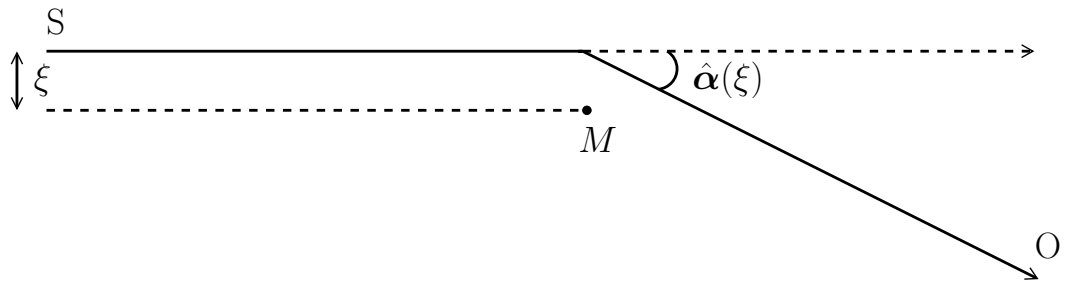
Figure 5.1: Shown is a point-mass lens system. The light ray coming from the source S with the impact parameter ξ is bent by the presence of the point mass M and arrives at the observer O. The total deflection angle of the light ray is $\hat{\alpha}$ which depends on the impact parameter.

5.1.2 Deflection Angle of a Mass Distribution

For a given potential, we are now able to calculate the deflection angle according to Eq. (5.10). The simplest case is a point-mass lens with the potential $\Phi(r) = -G_N M/r$ sketched in Fig. 5.1. Inserting this potential into Eq. (5.10), results in the deflection angle of a point-mass lens

$$\hat{\boldsymbol{\alpha}}(\boldsymbol{\xi}) = \frac{4G_N M}{c^2} \frac{\boldsymbol{\xi}}{\xi^2}, \qquad (5.11)$$

which exactly resembles the result one would obtain from general relativity. Note that here $\boldsymbol{\xi}$ is a two-dimensional vector in the plane perpendicular to the line-of-sight. Due to the linear mass dependence of $\hat{\boldsymbol{\alpha}}$, one can easily calculate the deflection angle of a distribution of point masses by superposition. Let us suppose we have a distribution of N point lenses on a plane with positions and masses $\boldsymbol{\xi}_i$ and M_i $(i = 1 \ldots N)$, respectively. Then superposing the deflection angles using Eq. (5.11) yields for the deflection angle of a light ray crossing the plane at $\boldsymbol{\xi}$

$$\hat{\boldsymbol{\alpha}}_{\text{tot}}(\boldsymbol{\xi}) = \sum_{i=1}^{N} \hat{\boldsymbol{\alpha}}(\boldsymbol{\xi} - \boldsymbol{\xi}_i) = \frac{4G_N}{c^2} \sum_{i=1}^{N} M_i \frac{\boldsymbol{\xi} - \boldsymbol{\xi}_i}{|\boldsymbol{\xi} - \boldsymbol{\xi}_i|^2}. \qquad (5.12)$$

We can generalize the concept of a deflection angle for a three-dimensional mass distribution of lenses. The distances between the source, lens and observer are typically much larger than the extent of the mass distribution of the lens. Therefore, one applies the approximation that the mass distribution can be projected onto a plane, the lens plane. This is the so-called *thin-screen* or *thin-lens approximation*. The distribution of matter is then fully described by the surface mass density

$$\Sigma(\boldsymbol{\xi}) = \int \mathrm{d}z \, \rho(\boldsymbol{\xi}, z), \qquad (5.13)$$

where ρ is the three-dimensional density, and it is assumed that the plane lies perpendicular to the line-of-sight. Note that in this expression the coordinate system is chosen

such that z denotes the coordinate which lies in direction of the line-of-sight. In the continuous limit, the deflection angle then becomes

$$\hat{\boldsymbol{\alpha}}(\boldsymbol{\xi}) = \frac{4G_N}{c^2} \int \mathrm{d}^2\xi' \, \Sigma(\boldsymbol{\xi}') \frac{\boldsymbol{\xi} - \boldsymbol{\xi}'}{|\boldsymbol{\xi} - \boldsymbol{\xi}'|^2} \,. \tag{5.14}$$

We obtain again the discrete result in Eq. (5.12) by inserting

$$\Sigma(\boldsymbol{\xi}) = \sum_{i=1}^{N} M_i \delta_\mathrm{D}(\boldsymbol{\xi} - \boldsymbol{\xi}_i) \tag{5.15}$$

into the continuous equation.

5.1.3 The Lens Equation

Foreground mass distributions deflect light rays from distant sources as shown in the previous section. Therefore, the true source position is different from the observed position of the source on the sky in the presence of gravitational lensing. However, using simple geometrical arguments, we can find a relation between the true and the observed position known as the lens equation as shown below.

A typical lens system is shown in Fig. 5.2, where $\boldsymbol{\eta}$ is the two-dimensional position of the source and $\boldsymbol{\xi}$ is the impact parameter of the light ray passing the lens plane. Due to the large distances between observer, lens and source one can approximate that the source and lens are lying in a two-dimensional plane, the source plane (Π_s) and the lens plane (Π_l), respectively. From the figure we infer that $\boldsymbol{\eta} = D_\mathrm{s}\boldsymbol{\beta}$ and $\boldsymbol{\xi} = D_\mathrm{l}\boldsymbol{\theta}$, where D_s is the distance from the observer to the source plane and D_l is the distance from the observer to the lens plane. Using the geometrical configuration shown in Fig. 5.2, we derive the *lens equation*

$$D_\mathrm{s}\boldsymbol{\theta} = D_\mathrm{s}\boldsymbol{\beta} + D_\mathrm{ls}\hat{\boldsymbol{\alpha}}(\boldsymbol{\xi}) \,, \tag{5.16}$$

where D_ls is the distance between lens and source plane. Defining the reduced deflection angle

$$\boldsymbol{\alpha}(\boldsymbol{\theta}) \equiv \frac{D_\mathrm{ls}}{D_\mathrm{s}} \hat{\boldsymbol{\alpha}}(D_\mathrm{l}\boldsymbol{\theta}) \,, \tag{5.17}$$

yields a simple relation between the image and the source plane

$$\boldsymbol{\beta} = \boldsymbol{\theta} - \boldsymbol{\alpha}(\boldsymbol{\theta}) \,. \tag{5.18}$$

The lens equation is also applicable on cosmological scales. Then the distances need to be calculated using the angular diameter distance relation in Eq. (1.33).

Using Eq. (5.14) for the deflection angle, the reduced deflection angle can be expressed by

$$\boldsymbol{\alpha}(\boldsymbol{\theta}) = \frac{1}{\pi} \int \mathrm{d}^2\theta' \, \kappa(\boldsymbol{\theta}') \frac{\boldsymbol{\theta} - \boldsymbol{\theta}'}{|\boldsymbol{\theta} - \boldsymbol{\theta}'|^2} \,, \tag{5.19}$$
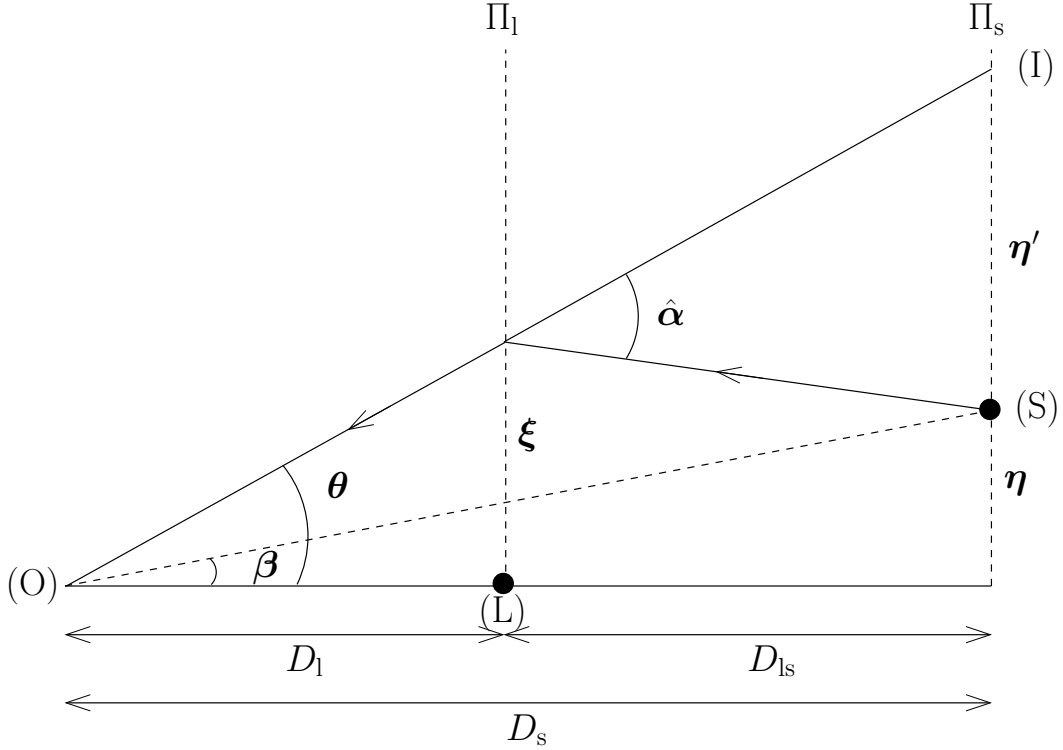
Figure 5.2: Sketch of a typical gravitational lens system. The light emitted by a source (S) is deflected by the gravitational field of the lens (L). An observer (O) therefore sees the object at the image position (I). Due to the large distances between observer, lens and source one can approximate that the source and lens is lying in a two-dimensional plane, the source plane (Π_s) and the lens plane (Π_l), respectively. The source has a separation of $\boldsymbol{\eta}$ from the line-of-sight. Afterwards the light ray passes the lens at a distance of $\boldsymbol{\xi}$. The path of the light ray is indicated by the arrows. The source is at an angle $\boldsymbol{\beta}$ from the line-of-sight and the light ray passes the source plane at an angle of $\boldsymbol{\theta}$.

where the *convergence* κ is a scaled dimensionless version of the surface mass density

$$\kappa(\boldsymbol{\theta}) \equiv \frac{\Sigma(D_l \boldsymbol{\theta})}{\Sigma_{\text{crit}}}\,, \tag{5.20}$$

and the *critical surface mass density* is given by

$$\Sigma_{\text{crit}} \equiv \frac{c^2}{4\pi G_N} \frac{D_s}{D_l D_{ls}}\,. \tag{5.21}$$

The scaled deflection angle can be written as the gradient of the *deflection potential*[2], i.e., $\boldsymbol{\alpha} = \nabla_\theta \psi$ with

$$\psi(\boldsymbol{\theta}) = \frac{1}{\pi} \int \mathrm{d}^2\theta'\, \kappa(\boldsymbol{\theta}') \ln |\boldsymbol{\theta} - \boldsymbol{\theta}'|\,. \tag{5.22}$$

_____

[2]Since the identity $\nabla_\theta \ln |\boldsymbol{\theta} - \boldsymbol{\theta}'| = (\boldsymbol{\theta} - \boldsymbol{\theta}')/|\boldsymbol{\theta} - \boldsymbol{\theta}'|^2$ holds.

Using the identity[3] $\Delta \ln |\boldsymbol{\theta}| = 2\pi\delta_{\mathrm{D}}(\boldsymbol{\theta})$, we get the two-dimensional Poisson equation

$$\Delta\psi = 2\kappa. \tag{5.23}$$

This equation is the analog to the (three-dimensional) Poisson equation in electrostatics, where the convergence κ is replaced by the charge density ρ.

5.1.4 Convergence and Shear

The lens equation is in general a nonlinear mapping of the true position of the source to its observed position. However, if the deflection angles involved are small we can perform a Taylor expansion of the lens equation

$$\beta_i(\boldsymbol{\theta}) = \beta_i(\mathbf{0}) + \left.\frac{\partial \beta_i}{\partial \theta_j}\right|_{\boldsymbol{\theta}=\mathbf{0}} \theta_j + \frac{1}{2}\left.\frac{\partial^2 \beta_i}{\partial \theta_j \partial \theta_k}\right|_{\boldsymbol{\theta}=\mathbf{0}} \theta_j\theta_k + \dots, \tag{5.24}$$

where summation over multiply occurring indices is assumed and β_i is the i-th component of the vector $\boldsymbol{\beta}$. We neglect higher-order terms in the following and consider only the first two terms of the expansion. However, the terms proportional to the second-order derivatives give rise to the so-called weak lensing *flexion* (Bacon et al. 2006). The distortion matrix which is the Jacobian of the mapping between source and lens coordinates is given by

$$A_{ij} \equiv \frac{\partial \beta_i}{\partial \theta_j} = \left(\delta_{ij} - \frac{\partial^2 \psi}{\partial \theta_i \partial \theta_j}\right) \equiv (\delta_{ij} - \psi_{ij}), \tag{5.25}$$

where we used the lens equation (5.18) in the second step and defined the compact notation for the derivative of the potential in the last step. Here δ_{ij} denotes the Kronecker delta. The trace-free part of this matrix is the so-called *shear matrix*

$$\Gamma_{ij} \equiv A_{ij} - \frac{\delta_{ij}}{2}\operatorname{tr} A = \begin{pmatrix} -\frac{1}{2}(\psi_{11} - \psi_{22}) & -\psi_{12} \\ -\psi_{12} & \frac{1}{2}(\psi_{11} - \psi_{22}) \end{pmatrix}. \tag{5.26}$$

This is a symmetric matrix that describes the distortion of background sources. For a compact notation we define $\boldsymbol{\gamma} = (\gamma_1, \gamma_2)$ which is a two-dimensional pseudo vector on the lens plane with the two components

$$\gamma_1(\boldsymbol{\theta}) \equiv \frac{1}{2}(\psi_{11} - \psi_{22}), \qquad \gamma_2(\boldsymbol{\theta}) \equiv \psi_{12}. \tag{5.27}$$

In terms of these components the shear matrix reads

$$\Gamma = \begin{pmatrix} -\gamma_1 & -\gamma_2 \\ -\gamma_2 & +\gamma_1 \end{pmatrix}. \tag{5.28}$$

---

[3]For $\boldsymbol{\theta} \neq \mathbf{0}$ the Dirac delta function and also the left-hand side of the identity vanishes. For $\boldsymbol{\theta} = \mathbf{0}$ there is a point of non-differentiability. However, integrating both sides over a unit 2-sphere and applying the divergence theorem for the left-hand side yields in both cases 2π, which proves the identity.

The total Jacobian is the sum the shear matrix in Eq. (5.28) and the remainder

$$\frac{\delta_{ij}}{2} \operatorname{tr} A = (1 - \kappa)\delta_{ij} \,, \tag{5.29}$$

where we used two-dimensional Poisson equation (5.23) to rewrite the remainder in terms of the convergence. Hence, the Jacobian is given by

$$A = \begin{pmatrix} 1 - \kappa & 0 \\ 0 & 1 - \kappa \end{pmatrix} + \begin{pmatrix} -\gamma_1 & -\gamma_2 \\ -\gamma_2 & +\gamma_1 \end{pmatrix} \,. \tag{5.30}$$

The first matrix is responsible for an isotropic magnification of the lensed image and depends only on the convergence field. The second matrix leads to distortions of the image in a preferred direction which depends on the two shear components.

As already mentioned, the shear is a pseudo vector or spin-2 field which has the following characteristic transformation behavior under rotations:

$$\Gamma' = R^{\mathrm{T}} \Gamma R \tag{5.31}$$

where the superscript "T" denotes the transposed of a matrix, and R is the two-dimensional rotation matrix given by

$$R = \begin{pmatrix} \cos\alpha & -\sin\alpha \\ \sin\alpha & \cos\alpha \end{pmatrix} \,. \tag{5.32}$$

We find then from Eq. (5.31) that after a rotation of $\alpha = \pi$ the spin-2 field is the same as the original one which is in contrast to a vector which transforms into itself after a full rotation of 2π. This behavior also reflects the fact that an ellipse is transformed into itself after a rotation of π. We can also write the two shear components as one complex quantity:

$$\gamma = \gamma_1 + \mathrm{i}\gamma_2 = |\gamma| \mathrm{e}^{2\mathrm{i}\varphi} \,, \tag{5.33}$$

where the factor 2 in the exponential accounts for the polar behavior of the shear.

5.1.5 Shear in a Rotated Coordinate System

In most measurements of the distortion of galaxy shapes it is best to define the shear in a coordinate-system-independent way. We determine in the following the shear with respect to the direction given by a vector $\boldsymbol{\theta}$ with polar angle ϕ. Using the setup sketched in Fig. 5.3 and the definition of the shear in complex notation in Eq. (5.33), we determine the *tangential-* and *cross*-component of the shear. Note that the shear has a relative orientation φ with respect to the Cartesian reference frame and α and β denote the angles of the rotated axes with respect to the Cartesian coordinate system onto which we want to project the shear. We find

$$\gamma_{\mathrm{t}} = \operatorname{Re}[|\gamma| \, \mathrm{e}^{2\mathrm{i}(\varphi+\alpha)}] = \operatorname{Re}[|\gamma| \, \mathrm{e}^{2\mathrm{i}\varphi} \, \mathrm{e}^{\mathrm{i}\pi} \, \mathrm{e}^{-2\mathrm{i}\phi}] = -\operatorname{Re}[\gamma \, \mathrm{e}^{-2\mathrm{i}\phi}] \,, \tag{5.34}$$

$$\gamma_{\times} = \operatorname{Re}[|\gamma| \, \mathrm{e}^{2\mathrm{i}(\varphi+\beta)}] = \operatorname{Re}[|\gamma| \, \mathrm{e}^{2\mathrm{i}\varphi} \, \mathrm{e}^{\mathrm{i}\pi/2} \, \mathrm{e}^{-2\mathrm{i}\phi}] = -\operatorname{Im}[\gamma \, \mathrm{e}^{-2\mathrm{i}\phi}] \,, \tag{5.35}$$
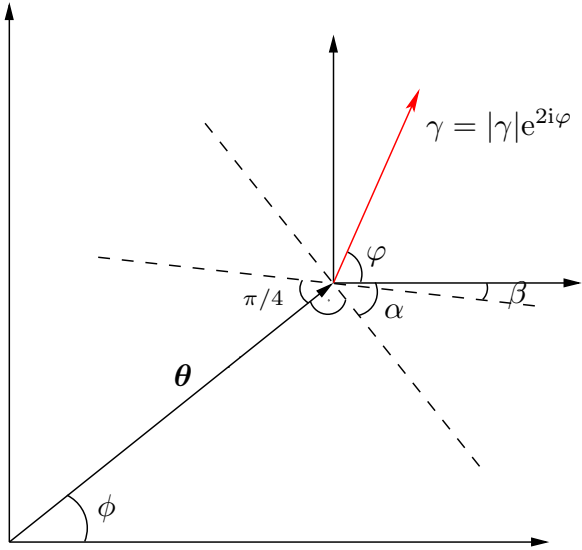
Figure 5.3: Illustration of the two shear components in a coordinate system defined by the vector $\boldsymbol{\theta}$ with polar angle ϕ with respect to a Cartesian reference coordinate system. We project the shear γ (indicated by the red arrow) onto the two dashed lines which enclose an angle of α and β with the abscissa of the Cartesian system. From the figure we find that the relations $\alpha + \phi = \pi/2$ and $\beta + \phi = \pi/4$ hold.

where we first rotate the complex shear vector onto the tangential (i.e., with an angle of $\varphi + \alpha$) and cross direction (i.e., with an angle of $\varphi + \beta$) as indicated by the two dashed lines in the figure and then project the shear by taking its real part. In the subsequent sections we define the shear two- and three-point correlation functions in terms of the defined tangential- and cross-component of the shear.

5.1.6 Kaiser-Squires Relation

The Kaiser-Squires relation provides the important link between the observed shear and the convergence κ which we present here in Fourier space. Transforming the convergence into Fourier space yields

$$\tilde{\kappa}(\boldsymbol{l}) = \int \mathrm{d}^2\theta \, \kappa(\boldsymbol{\theta}) \, \mathrm{e}^{\mathrm{i}\boldsymbol{l}\cdot\boldsymbol{\theta}} = \frac{1}{2} \int \mathrm{d}^2\theta \left[\frac{\partial^2\psi}{\partial\theta_1\partial\theta_1} + \frac{\partial^2\psi}{\partial\theta_2\partial\theta_2} \right] \mathrm{e}^{\mathrm{i}\boldsymbol{l}\cdot\boldsymbol{\theta}} = -\frac{1}{2}(l_1^2 + l_2^2)\tilde{\psi}(\boldsymbol{l}) \,, \quad (5.36)$$

where we employed the lensing Poisson equation (5.23) in the second step and computed the derivatives in the last step. Analogously, we find for the two components of the shear defined in Eq. (5.27)

$$\tilde{\gamma}_1(\boldsymbol{l}) = -\frac{1}{2}(l_1^2 - l_2^2)\tilde{\psi}(\boldsymbol{l}) = \frac{l_1^2 - l_2^2}{l^2}\tilde{\kappa}(\boldsymbol{l}) \,, \quad (5.37)$$

$$\tilde{\gamma}_2(\boldsymbol{l}) = -l_1 l_2 \tilde{\psi}(\boldsymbol{l}) = \frac{2l_1 l_2}{l^2}\tilde{\kappa}(\boldsymbol{l}) \,, \quad (5.38)$$

where $l^2 = l_1^2 + l_2^2$ is the modulus of the two-dimensional Fourier vector $\boldsymbol{l}$. By combining both components the shear is given by

$$\tilde{\gamma}(\boldsymbol{l}) = \tilde{\gamma}_1(\boldsymbol{l}) + \mathrm{i}\tilde{\gamma}_2(\boldsymbol{l}) = -\left[\frac{1}{2}(l_1^2 - l_2^2) + \mathrm{i}l_1 l_2\right]\tilde{\psi}(\boldsymbol{l}) = \left[\frac{(l_1^2 - l_2^2) + 2\mathrm{i}l_1 l_2}{l_1^2 + l_2^2}\right]\tilde{\kappa}(\boldsymbol{l})$$

$$\equiv \tilde{D}(\boldsymbol{l})\tilde{\kappa}(\boldsymbol{l}) \,, \quad (5.39)$$

where the function defined in the last step obeys $\tilde{D}(\boldsymbol{l})\tilde{D}^*(\boldsymbol{l}) = 1$ or equivalently $\tilde{D}^*(\boldsymbol{l}) = \tilde{D}^{-1}(\boldsymbol{l})$. Here a "*" denotes the complex conjugate of the corresponding term. Furthermore, we can express the relation in the following useful form:

$$\tilde{\gamma}(\boldsymbol{l}) = \tilde{D}(\boldsymbol{l})\tilde{\kappa}(\boldsymbol{l}) = \frac{(l_1 + \mathrm{i}l_2)^2}{l^2}\tilde{\kappa}(\boldsymbol{l}) = \mathrm{e}^{2\mathrm{i}\beta}\,\tilde{\kappa}(\boldsymbol{l})\,, \tag{5.40}$$

where we used the representation of the two-dimensional vector $\boldsymbol{l}$ as a complex number in the second step with the corresponding polar angle β.

5.2 Cosmic Shear

In this section we study the effect of small density perturbations on the propagation of light rays in a cosmological context, i.e., as they travel through a significant part of the Universe. The light rays are then multiply bend by the inhomogeneities of the large-scale structure, and thus the concept of scattering in a single lens plane as developed in the previous sections cannot simply be applied. Furthermore, we literally have to deal with cosmological scales in this problem making a description by general relativity mandatory.

To simplify the problem, we consider first the propagation of a thin light bundle neglecting the influence of inhomogeneities. The propagation of the light bundle is then described by the *geodesic deviation equation*. This is a second-order differential equation for the varying distance between two geodesics depending on the Riemann curvature tensor. A derivation of this equation can be found in most standard general relativity books, e.g., Weinberg (1972). In the review paper by Bartelmann & Schneider (2001), we find an application of this formalism to gravitational lensing. In this case, we study the evolution equation of the two-dimensional transverse separation vector $\boldsymbol{\xi}$ given by

$$\frac{\mathrm{d}^2\boldsymbol{\xi}}{\mathrm{d}\lambda^2} = \mathcal{T}\boldsymbol{\xi}\,, \tag{5.41}$$

where $\mathcal{T}$ is the *optical tidal matrix* which quantifies the influence of the space-time curvature on the propagation of light rays. Note that this equation is applicable for a general metric. The tidal matrix becomes especially simple if we consider the isotropic and homogeneous background Universe described by the Robertson-Walker metric (see Eq. 1.1). In this case the tidal matrix is proportional to the Ricci tensor. Computing the Ricci tensor for this metric and introducing the *comoving transverse separation vector* $\boldsymbol{x} = a^{-1}\boldsymbol{\xi}$, yields

$$\frac{\mathrm{d}^2\boldsymbol{x}}{\mathrm{d}w^2} + K\boldsymbol{x} = \boldsymbol{0}\,. \tag{5.42}$$

This is the familiar equation of a free harmonic oscillator. The solution is then a linear, trigonometric or hyperbolic function depending on the curvature K of the Universe. In order to solve the equation, we need to apply boundary conditions. Here we employ the

conditions that all light rays start at the coordinate origin at $w = 0$, and that the angle between the two light rays is given by $\boldsymbol{\theta}$ at $w = 0$, i.e.

$$\boldsymbol{x}|_{w=0} = \mathbf{0}\,, \qquad \frac{\mathrm{d}\boldsymbol{x}}{\mathrm{d}w}\bigg|_{w=0} = \boldsymbol{\theta}\,. \tag{5.43}$$

Applying the initial conditions, we find the solution

$$\boldsymbol{x} = f_K(w)\boldsymbol{\theta}\,. \tag{5.44}$$

Now we add small perturbations to the propagation of the light bundle produced by the inhomogeneities of the large-scale structure. Formally, the mass concentrations change the metric. In order to apply the results from Sect. 5.1.1, we have to make a few assumptions about the inhomogeneities: their gravitational potential needs to be small ($\Phi \ll c^2$), they need to be localized in the sense that the potential Φ changes on scales much smaller than the curvature K of the Universe and the velocity of the perturbations need to be much smaller than the speed of light. In this case we can neglect the cosmic expansion and are able to use the flat perturbed Minkowski metric. Locally, we found for the deflection of light rays (see Eq. 5.9)

$$\frac{\mathrm{d}^2\boldsymbol{x}}{\mathrm{d}w^2} = -\frac{2}{c^2}\nabla_\perp\Phi\,, \tag{5.45}$$

where we made a change of variables from λ to the comoving distance w. We consider now two light rays that arrive at the observer. The fiducial ray is situated at angular position $\boldsymbol{\theta} = \mathbf{0}$ and the deflected ray arrives at the observer at angular position of $\boldsymbol{\theta} \neq \mathbf{0}$. With this setup, we can use the difference of the local propagation equation combined with the equation for the background Universe yielding

$$\frac{\mathrm{d}^2\boldsymbol{x}}{\mathrm{d}w^2} + K\boldsymbol{x} = -\frac{2}{c^2}\left[\nabla_\perp\Phi(\boldsymbol{x}(\boldsymbol{\theta}, w)) - \nabla_\perp\Phi^{(0)}(w)\right]\,, \tag{5.46}$$

which is the sought-after propagation equation of light including inhomogeneities. The solution of the perturbed propagation equation is the sum of the homogeneous solution (5.44) and a particular solution to the inhomogeneous equation, which can be found by the method of Green's functions. The result is

$$\boldsymbol{x}(\boldsymbol{\theta}, w) = f_K(w)\boldsymbol{\theta} - \frac{2}{c^2}\int_0^w \mathrm{d}w'\, f_K(w - w')[\nabla_\perp\Phi(\boldsymbol{x}(\boldsymbol{\theta}, w')) - \nabla_\perp\Phi^{(0)}(w')]\,. \tag{5.47}$$

A simple cross-check of this solution is obtained by inserting it into the differential equation (5.46). This is an implicit nonlinear equation for the separation $\boldsymbol{x}(\boldsymbol{\theta}, w)$ because the solution depends on the perturbed photon path $\boldsymbol{x}(\boldsymbol{\theta}, w')$ in the Newtonian potential. More precisely, it is a Volterra integral equation of the second kind.

In the absence of lensing, the source is located at an angle of $\boldsymbol{\beta} = \boldsymbol{x}/f_K(w)$ which is just the definition of the comoving angular diameter distance[4]. Thus, we introduce in

---

[4]Note that in the absence of lensing source and lens coordinates are equal, i.e., $\boldsymbol{\beta} = \boldsymbol{\theta}$.

analogy to Eq. (5.25) the Jacobian

$$\mathcal{A}(\boldsymbol{\theta}, w) = \frac{\partial \boldsymbol{\beta}}{\partial \boldsymbol{\theta}} = \frac{\partial \boldsymbol{\beta}}{\partial \boldsymbol{x}} \frac{\partial \boldsymbol{x}}{\partial \boldsymbol{\theta}} = \frac{1}{f_K(w)} \frac{\partial \boldsymbol{x}}{\partial \boldsymbol{\theta}}, \tag{5.48}$$

which describes the linear mapping from lens to source coordinates. Applying this to the solution (5.47) yields[5]

$$
\begin{aligned}
\mathcal{A}_{ij}(\boldsymbol{\theta}, w) &= \delta_{ij} - \frac{2}{c^2} \int_0^w \mathrm{d}w' \frac{f_K(w-w')}{f_K(w)} \frac{\partial}{\partial \theta_j} \Phi_{,i}(\boldsymbol{x}(\boldsymbol{\theta}, w'), w') \\
&= \delta_{ij} - \frac{2}{c^2} \int_0^w \mathrm{d}w' \frac{f_K(w-w')f_K(w')}{f_K(w)} \Phi_{,ik}(\boldsymbol{x}(\boldsymbol{\theta}, w'), w') A_{kj}(\boldsymbol{\theta}, w'),
\end{aligned} \tag{5.49}
$$

where we used the chain rule in the second step, and the extra factor of $f_K(w')$ appears to rewrite the inner derivative in terms of the Jacobian using Eq. (5.48). In addition, we implicitly assumed summation over identical indices. We can solve this equation by expanding the gradient of the potential around the solution for an unperturbed ray. To first order, the Jacobian in the integrand becomes the identity matrix and the potential is evaluated at the unperturbed light path, i.e., $\boldsymbol{x}(\boldsymbol{\theta}, w') = f_K(w')\boldsymbol{\theta}$. The first order of the expansion is the so-called *Born approximation* in analogy to scattering theory. The next order involves terms that are proportional to Φ^2 giving rise to so-called *lens-lens coupling* terms (Cooray & Hu 2002) which are suppressed relative to the first-order solution by the smallness of the potential. By using the Born approximation, we find

$$\mathcal{A}_{ij}(\boldsymbol{\theta}, w) = \delta_{ij} - \frac{2}{c^2} \int_0^w \mathrm{d}w' \frac{f_K(w-w')f_K(w')}{f_K(w)} \Phi_{,ij}(f_K(w')\boldsymbol{\theta}, w'). \tag{5.50}$$

This result enables us to introduce the lensing potential for cosmic shear:

$$\Psi(\boldsymbol{\theta}, w) \equiv \frac{2}{c^2} \int_0^w \mathrm{d}w' \frac{f_K(w-w')}{f_K(w)f_K(w')} \Phi(f_K(w')\boldsymbol{\theta}, w'), \tag{5.51}$$

and write the solution in analogy to basic lensing as

$$\mathcal{A}_{ij}(\boldsymbol{\theta}, w) = \delta_{ij} - \Psi_{ij}(\boldsymbol{\theta}, w). \tag{5.52}$$

Due to the complete analogy of Eqs. (5.25) and (5.52), we can decompose this matrix as in Eq. (5.30), where the convergence and shear are now defined as

$$\kappa = \frac{1}{2}(\Psi_{11} + \Psi_{22}), \tag{5.53}$$

$$\gamma = \frac{1}{2}(\Psi_{11} - \Psi_{22}) + \mathrm{i}\Psi_{12}. \tag{5.54}$$

---

[5]We denote derivatives with respect to x_i with $\Phi_{,i} \equiv \frac{\partial \Phi}{\partial x_i}$. To distinguish between derivatives of the lensing potential with respect to θ, we use the definition of Eq. (5.25), i.e., with no commas.

Hence, we obtain the convergence by calculating the two-dimensional Laplacian of the potential Ψ. As it turns out, we can add the term Ψ_{33} to Eq. (5.53) which is the second-order derivative of the potential along the unperturbed light path. This is justified by the fact that the integral in Eq. (5.51) vanishes as can be seen by integration by parts. This enables us to use the three-dimensional Poisson equation in comoving coordinates (compare also with Eq. 2.18)

$$\triangle\Phi = \frac{3H_0^2\Omega_{\rm m}}{2a}\delta\,, \tag{5.55}$$

where δ is the linear density contrast and a denotes the scale factor. Finally we get

$$\kappa(\boldsymbol{\theta}, w) = \frac{3H_0^2\Omega_{\rm m}}{2c^2} \int_0^w {\rm d}w'\, \frac{f_K(w')f_K(w-w')}{f_K(w)}\frac{\delta[f_K(w')\boldsymbol{\theta}, w']}{a(w')}\,, \tag{5.56}$$

which is a relation between the convergence in terms of the three-dimensional density contrast projected along the line-of-sight.

Up to now we only considered a source at a fixed redshift or comoving distance w. However, in general the sources have a redshift distribution $p_{\rm s}(w)$. The total convergence is then the integral over the redshift distribution and the redshift-dependent convergence:

$$\kappa(\boldsymbol{\theta}) = \int_0^{w_{\rm H}} {\rm d}w\, p_{\rm s}(w)\kappa(\boldsymbol{\theta}, w)\,. \tag{5.57}$$

Changing the order of integration in Eqs. (5.56) and (5.57), we find

$$\kappa(\boldsymbol{\theta}) = \int_0^{w_{\rm H}} {\rm d}w\, f_K(w)G(w)\delta[f_K(w)\boldsymbol{\theta}, w]\,, \tag{5.58}$$

where the *weight function* or *lensing efficiency function* is given by

$$G(w) \equiv \frac{3}{2}\Omega_{\rm m} \left(\frac{H_0}{c}\right)^2 a^{-1}(w) \int_w^{w_{\rm H}} {\rm d}w'\, p_{\rm s}(w')\frac{f_K(w'-w)}{f_K(w')}\,. \tag{5.59}$$

The weight function is the angular diameter distance ratio $D_{\rm ls}/D_{\rm s}$ weighted over the source redshift distribution at a fixed lens redshift. Furthermore, it depends through the Poisson equation on the matter density parameter $\Omega_{\rm m}$.

Now, we want to find a relation between the shear- and the convergence power spectrum. This is of particular interest since cosmic shear observations are sensitive to the shear power spectrum whereas theoretical models predict the convergence power spectrum. The shear power spectrum is defined by

$$\langle\tilde{\gamma}(\boldsymbol{l})\tilde{\gamma}^*(\boldsymbol{l}')\rangle = (2\pi)^2\delta_{\rm D}(\boldsymbol{l}-\boldsymbol{l}')P_\gamma(\boldsymbol{l})\,, \tag{5.60}$$

and the convergence power spectrum is defined by

$$\langle\tilde{\kappa}(\boldsymbol{l})\tilde{\kappa}^*(\boldsymbol{l}')\rangle = (2\pi)^2\delta_{\rm D}(\boldsymbol{l}-\boldsymbol{l}')P_\kappa(\boldsymbol{l})\,. \tag{5.61}$$

Using the Kaiser-Squires relation in Eq. (5.39), we can relate the shear- and the convergence two-point correlators:

$$\langle\tilde{\gamma}(\boldsymbol{l})\tilde{\gamma}^*(\boldsymbol{l}')\rangle = \tilde{D}(\boldsymbol{l})\tilde{D}^{-1}(\boldsymbol{l})\langle\tilde{\kappa}(\boldsymbol{l})\tilde{\kappa}^*(\boldsymbol{l}')\rangle\,. \tag{5.62}$$

Thus, we find that both power spectra are equal, i.e., $P_\gamma(\boldsymbol{l}) = P_\kappa(\boldsymbol{l})$.

5.2.1 Limber's Equation

We showed in the previous three chapters how perturbation theory, the dark matter halo model and the halo model for galaxy clustering predict general three-dimensional spectra. However, cosmic shear measures a two-dimensional projection of the three-dimensional spectrum. To relate the measured projected two-point correlation function on the sky to the theoretically predicted three-dimensional correlation function, one uses Limber's approximation (Limber 1953). A generalization of the concept for the power spectrum is developed in Kaiser (1998). For cosmic shear we deal with general projections of the three-dimensional density contrast field to two-dimensions of the form (see e.g., Eq. 5.58)

$$g_i(\boldsymbol{\theta}) = \int_0^{w_{\mathrm{H}}} \mathrm{d}w \, q_i(w) \delta_i[f_K(w)\boldsymbol{\theta}, w] \,, \tag{5.63}$$

where $q_i(w)$ denotes the weight function of type i. The integral extends from $w = 0$ to the horizon at $w = w_{\mathrm{H}}$. The auto-correlation ($i = j$) and cross-correlation ($i \neq j$) functions of the projected fields are

$$P_{ij}(l) = \int_0^{w_{\mathrm{H}}} \mathrm{d}w \, \frac{q_i(w)q_j(w)}{f_K^2(w)} P_{IJ}\left(\frac{l}{f_K(w)}; w\right) \,. \tag{5.64}$$

In this thesis we differentiate between galaxies ($i = \mathrm{g}$) and dark matter ($i = \kappa$). Here the indices (I, J) are the corresponding three-dimensional counterparts of the projected fields (i, j). For example if $i = \kappa$ then $I = \delta$. This approximation is applicable if the weight functions are not considerably varying over the considered range (see Bartelmann & Schneider 2001; Simon 2007 for a comprehensive discussion).

We can generalize the Limber approximation to higher-order correlation functions (Bernardeau et al. 2002). Considering the projection of the n-th order spectrum yields

$$T_{i_1\dots i_n}(\boldsymbol{l}_1, \dots, \boldsymbol{l}_n) = \int_0^{w_{\mathrm{H}}} \mathrm{d}w \, \frac{\prod_{k=1}^n q_{i_k}(w)}{[f_K(w)]^{2(n-1)}} \, T_{I_1\dots I_n}(\boldsymbol{k}_1, \dots, \boldsymbol{k}_n; w) \,, \tag{5.65}$$

where $\boldsymbol{k}_i = \boldsymbol{l}_i/f_K(w)$. Again $(I_1, \dots, I_n)$ denote the three-dimensional counterparts of the projected fields $(i_1, \dots, i_n)$. In the following we give the explicit relations for the convergence power spectrum, bispectrum and trispectrum.

Convergence Spectra

We showed in Eq. (5.58) that for cosmic shear the convergence field is a weighted projection of the three-dimensional density contrast field where the weight function is given by

$$G(w) = \frac{3}{2}\Omega_{\mathrm{m}}\left(\frac{H_0}{c}\right)^2 a^{-1}(w) \int_w^{w_{\mathrm{H}}} \mathrm{d}w_{\mathrm{s}} \, p_{\mathrm{s}}(z) \frac{\mathrm{d}z}{\mathrm{d}w_{\mathrm{s}}} \frac{f_K(w_{\mathrm{s}} - w)}{f_K(w_{\mathrm{s}})} \,, \tag{5.66}$$

where we used that $p_{\mathrm{s}}(w)\mathrm{d}w = p_{\mathrm{s}}(z)\mathrm{d}z$. Here we consider a redshift distribution of source galaxies of the form

$$p_{\mathrm{s}}(z) = A\left(\frac{z}{z_0}\right)^\alpha \exp[-(z/z_0)^\beta] \,, \tag{5.67}$$

where α, β and z_0 are the parameters of the distribution function. This is a generalization of the distribution considered by Brainerd et al. (1996) who used $\alpha = 2$. From the requirement that the distribution is normalized, $\int_0^\infty \mathrm{d}z\, p_\mathrm{s}(z) = 1$, we find the normalization constant

$$A = \frac{\beta}{z_0\, \Gamma\left(\frac{1+\alpha}{\beta}\right)}\,, \tag{5.68}$$

where Γ denotes the Gamma function.

If the background sources all reside at a redshift of z_s then the weight function simplifies to

$$G(w) = \frac{3}{2}\Omega_\mathrm{m} \left(\frac{H_0}{c}\right)^2 a^{-1}(w)\frac{f_K(w_\mathrm{s} - w)}{f_K(w_\mathrm{s})}\,, \tag{5.69}$$

where $w_\mathrm{s} = w(z_\mathrm{s})$.

With the help of Limber's equation (5.64), one gets a simple expression for the power spectrum of the projected field. This so-called convergence power spectrum is given by

$$P_{\kappa\kappa}(l) = \int_0^{w_\mathrm{H}} \mathrm{d}w\, G^2(w) P_{\delta\delta}\left(\frac{l}{f_K(w)}; w\right)\,, \tag{5.70}$$

where $P_{\delta\delta}$ is the three-dimensional power spectrum.

Applying Limber's approximation in Eq. (5.65) for the dark matter bispectrum yields

$$B_{\kappa\kappa\kappa}(\boldsymbol{l}_1, \boldsymbol{l}_2, \boldsymbol{l}_3) = \int_0^{w_\mathrm{H}} \mathrm{d}w\, \frac{G^3(w)}{f_K(w)} B_{\delta\delta\delta}(\boldsymbol{k}_1, \boldsymbol{k}_2, \boldsymbol{k}_3; w)\,, \tag{5.71}$$

where $\boldsymbol{k}_i = \boldsymbol{l}_i/w$.

The projection of the dark matter trispectrum is given by (using Eq. 5.65)

$$T_{\kappa\kappa\kappa\kappa}(\boldsymbol{l}_1, \boldsymbol{l}_2, \boldsymbol{l}_3, \boldsymbol{l}_4) = \int_0^{w_\mathrm{H}} \mathrm{d}w\, \frac{G^4(w)}{f_K^2(w)} T_{\delta\delta\delta\delta}(\boldsymbol{k}_1, \boldsymbol{k}_2, \boldsymbol{k}_3, \boldsymbol{k}_4; w)\,, \tag{5.72}$$

where $\boldsymbol{k}_i = \boldsymbol{l}_i/w$.

5.2.2 Shear Two-Point Correlation Functions

We can define two shear two-point correlation functions:

$$\xi_+(\vartheta) = \langle \gamma(\boldsymbol{\theta}; \varphi)\gamma^*(\boldsymbol{\theta} + \boldsymbol{\vartheta}; \varphi)\rangle\,, \qquad \xi_-(\vartheta) = \langle \gamma(\boldsymbol{\theta}; \varphi)\gamma(\boldsymbol{\theta} + \boldsymbol{\vartheta}; \varphi)\rangle\,, \tag{5.73}$$

where the shear γ at an angle of φ with respect to a Cartesian frame is given by the sum of the tangential and the cross component:

$$\gamma(\boldsymbol{\theta}; \varphi) = \gamma_\mathrm{t}(\boldsymbol{\theta}; \varphi) + \mathrm{i}\gamma_\times(\boldsymbol{\theta}; \varphi) = -\mathrm{Re}(\gamma_\mathrm{c}\, \mathrm{e}^{-2\mathrm{i}\varphi}) - \mathrm{i}\,\mathrm{Im}(\gamma_\mathrm{c}\, \mathrm{e}^{-2\mathrm{i}\varphi}) = -\gamma_\mathrm{c}\, \mathrm{e}^{-2\mathrm{i}\varphi}\,. \tag{5.74}$$

The shear with respect to a Cartesian base is in the following denoted by $\gamma_\mathrm{c} \equiv \gamma_1 + \mathrm{i}\gamma_2$. Combining these relations we are able to calculate the correlation functions from the
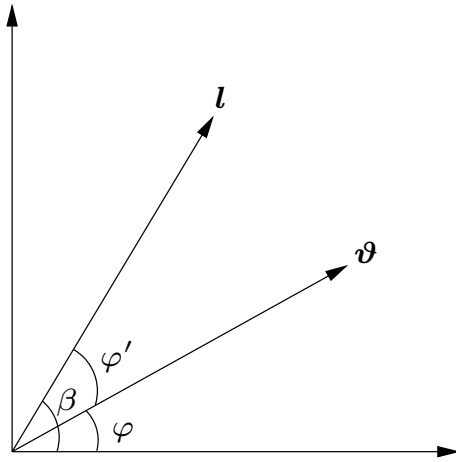
Figure 5.4: Angles of the Fourier vector $\boldsymbol{l}$ and correlation separation vector $\boldsymbol{\vartheta}$ with respect to a fixed coordinate system. Note that the angle between $\boldsymbol{\vartheta}$ and $\boldsymbol{l}$ is φ'.

convergence power spectrum. We first show the proof for ξ_-:

$$
\begin{aligned}
\xi_-(\vartheta) = \langle \gamma(\boldsymbol{\theta};\varphi)\gamma(\boldsymbol{\theta}+\boldsymbol{\vartheta};\varphi) \rangle &= \mathrm{e}^{-4\mathrm{i}\varphi} \langle \gamma_{\mathrm{c}}(\boldsymbol{\theta})\gamma_{\mathrm{c}}^*(\boldsymbol{\theta}+\boldsymbol{\vartheta}) \rangle \\
&= \mathrm{e}^{-4\mathrm{i}\varphi} \int \frac{\mathrm{d}^2 l}{(2\pi)^2} \int \frac{\mathrm{d}^2 l'}{(2\pi)^2} \, \mathrm{e}^{-\mathrm{i}\boldsymbol{\theta}\cdot\boldsymbol{l}} \, \mathrm{e}^{-\mathrm{i}(\boldsymbol{\theta}+\boldsymbol{\vartheta})\cdot\boldsymbol{l}'} \langle \tilde{\gamma}(\boldsymbol{l})\tilde{\gamma}(\boldsymbol{l}') \rangle \\
&= \int \frac{\mathrm{d}^2 l}{(2\pi)^2} \, P_{\kappa\kappa}(l) \, \mathrm{e}^{4\mathrm{i}(\beta-\varphi)} \, \mathrm{e}^{\mathrm{i}\boldsymbol{\vartheta}\cdot\boldsymbol{l}} \\
&= \int_0^\infty \frac{\mathrm{d}l}{(2\pi)^2} \, l P_{\kappa\kappa}(l) \int_0^{2\pi} \mathrm{d}\varphi' \, \mathrm{e}^{\mathrm{i}\vartheta l \cos\varphi'} [\cos(4\varphi') - \mathrm{i}\sin(4\varphi')] \\
&= \frac{1}{2\pi} \int_0^\infty \mathrm{d}l \, l P_{\kappa\kappa}(l) \, \mathrm{J}_4(l\vartheta) \,, \tag{5.75}
\end{aligned}
$$

where we employed Eq. (5.74) in the first step, transformed then the shear into Fourier space and expressed the two shears in terms of the convergence using the Kaiser-Squires relation in Eq. (5.40). In the last two steps we substitute the angles following the sketch in Fig. 5.4 and rewrite the angular integral in terms of the Bessel function. With this knowledge we can easily calculate the relation for the second correlation function:

$$
\begin{aligned}
\xi_+(\vartheta) = \langle \gamma(\boldsymbol{\theta};\varphi)\gamma^*(\boldsymbol{\theta}+\boldsymbol{\vartheta};\varphi) \rangle &= \langle \gamma_{\mathrm{c}}(\boldsymbol{\theta})\gamma_{\mathrm{c}}^*(\boldsymbol{\theta}+\boldsymbol{\vartheta}) \rangle \\
&= \int \frac{\mathrm{d}^2 l}{(2\pi)^2} \int \frac{\mathrm{d}^2 l'}{(2\pi)^2} \, \mathrm{e}^{-\mathrm{i}\boldsymbol{\theta}\cdot\boldsymbol{l}} \, \mathrm{e}^{\mathrm{i}(\boldsymbol{\theta}+\boldsymbol{\vartheta})\cdot\boldsymbol{l}'} \langle \tilde{\gamma}(\boldsymbol{l})\tilde{\gamma}^*(\boldsymbol{l}') \rangle \\
&= \int \frac{\mathrm{d}^2 l}{(2\pi)^2} \, P_{\kappa\kappa}(l) \, \mathrm{e}^{\mathrm{i}\boldsymbol{\vartheta}\cdot\boldsymbol{l}} = \frac{1}{2\pi} \int_0^\infty \mathrm{d}l \, l P_{\kappa\kappa}(l) \, \mathrm{J}_0(l\vartheta) \,.
\end{aligned}
$$
$$\tag{5.76}$$

The result is that both correlation functions are filtered versions of the convergence power spectrum (5.70), where the filter is given by the Bessel function of zeroth and fourth order, respectively.

Chapter 6

Galaxy-Galaxy and Galaxy-Galaxy-Galaxy Lensing

Galaxy-galaxy lensing describes the distortion pattern of the images of background galaxies induced by weak gravitational lensing of individual foreground galaxies. The galaxy lensing induces a mean tangential alignment of the shear distortions of background galaxies around foreground galaxies, which is the main observational signature. However, the weak lensing distortions around a single galaxy are very small compared to their intrinsic ellipticity. Therefore, we need to average over a large sample of foreground and background pairs to extract the tangential alignment of background galaxy images. Statistically galaxy-galaxy lensing determines then the cross-correlation of the tangential shear with the position of the foreground galaxy which is directly sensitive to the projected galaxy-dark matter cross-correlation function. Recently, this concept has been extended to third-order galaxy-shear correlations which is the so-called galaxy-galaxy-galaxy lensing effect.

We present here theoretical predictions of the galaxy lensing signal by combining the halo model for dark matter and for galaxy clustering. In particular, we use results from Sect. 4.3 where we derived the expressions for the three-dimensional cross-spectra. The chapter is organized as follows: We review the formalism of galaxy-galaxy lensing in Sect. 6.1 deriving the most important quantities. This provides us with the necessary background to define the galaxy-galaxy-galaxy lensing signal in Sect. 6.2. We give an overview of the most important observational and theoretical results at the beginning of each section for these young cosmological probes. Throughout this chapter we will adopt *Model B*, depicted in Table A.1, as the fiducial cosmological model.

6.1 Galaxy-Galaxy Lensing

Measurements of galaxy-galaxy lensing (GGL) can be used to determine the mass properties of the environment of galaxies. For small angular separations the signal is dominated by the galaxy halo, whereas for larger angular scales the measurements receive substantial contributions from the host group or cluster halo. These dependencies can give valuable constraints on the properties of dark matter halos of different masses, like their shape, the extent of the halo, the functional form of the halo density profile,

the concentration-mass relation etc. Another advantage is that the results are complementary to traditional probes that rely on luminous tracers of the mass distribution like measurements of the rotation curves of stars in spiral galaxies or the velocity dispersion in elliptical galaxies, which provide important evidence for dark matter halos around galaxies. However, with luminous tracers one can only probe the dark matter halo out to distances of roughly $100\,h^{-1}\,\mathrm{kpc}$. On the other hand, GGL is sensitive to the total mass and allows for measurements beyond $1\,h^{-1}\,\mathrm{Mpc}$. Furthermore, since GGL depends on the matter-galaxy cross-correlation function it can shed light on the scale-dependent galaxy bias. For example one can extract the galaxy bias by combining measurements of the cosmic shear and the GGL two-point correlation functions (Hoekstra et al. 2002).

The first attempt to measure the GGL signal failed due to the use of scans of photographic plates and the poor seeing (Tyson et al. 1984). We had to wait for more than 10 years until the breakthrough of the first detection of the GGL signal mostly due to the improvement of observational techniques (Brainerd et al. 1996). The advent of high-resolution telescopes and wide-field galaxy surveys greatly increased the number of useable foreground-background pairs thereby significantly reducing the statistical errors and improving the constraints on halo parameters. Current experiments can be divided into two main classes: shallow (low-redshift) and large-area surveys like the SDSS (Fischer et al. 2000; McKay et al. 2001) or relatively deep (higher-redshift) experiments like the RCS[1] (Hoekstra et al. 2002). At the moment, the tightest constraints on halo profiles are provided by results from the SDSS since this survey consists of a large field with exquisite redshift information of fore- and background galaxies in five different filters (e.g., Mandelbaum et al. 2006a,c,b). The main drawback is that the relatively bad seeing prevents cosmic shear analyses in the SDSS. Hence, the best galaxy bias constraints from GGL come from the RCS survey where one can combine cosmic shear and GGL measurements (Hoekstra et al. 2002).

6.1.1 Projected Power Spectrum

The three-dimensional number density contrast of galaxies at comoving position $\boldsymbol{x}$ and comoving distance w is defined as

$$\delta_{\mathrm{g}}(\boldsymbol{x}, w) \equiv \frac{n_{\mathrm{g}}(\boldsymbol{x}, w) - \bar{n}_{\mathrm{g}}(w)}{\bar{n}_{\mathrm{g}}(w)}\,, \tag{6.1}$$

where $\bar{n}_{\mathrm{g}}(w)$ is the mean number density of galaxies at distance w. Considering a population of foreground galaxies with spatial number density $n_{\mathrm{g}}(\boldsymbol{x}, w)$, the corresponding number density on the sky is then a projection

$$N(\boldsymbol{\theta}) = \int_0^{w_{\mathrm{H}}} \mathrm{d}w\, f_K^2(w)\nu(w)n_{\mathrm{g}}[f_K(w)\boldsymbol{\theta}, w]\,, \tag{6.2}$$

---

[1]Red-Sequence Cluster Survey.

where $\nu(w)$ is a selection function accounting for the fraction of objects that are included in the galaxy sample. Furthermore, we introduce the mean number density on the sky:

$$\bar{N} = \int_0^{w_{\mathrm{H}}} \mathrm{d}w \, f_K^2(w)\nu(w)\bar{n}_{\mathrm{g}}(w) \,. \tag{6.3}$$

These definitions lead to the redshift distribution of *foreground* galaxies (denoted by the subscript "f"), or more precisely, their distribution in comoving distance

$$p_{\mathrm{f}}(w) = \frac{f_K^2(w)\nu(w)\bar{n}_{\mathrm{g}}(w)}{\bar{N}} \,, \tag{6.4}$$

which is normalized by definition, such that $\int \mathrm{d}w \, p_{\mathrm{f}}(w) = 1$.

Employing Eq. (6.1), we get a relation between the two- and the three-dimensional number density contrast

$$N(\boldsymbol{\theta})/\bar{N} = 1 + \int_0^{w_{\mathrm{H}}} \mathrm{d}w \, p_{\mathrm{f}}(w)\delta_{\mathrm{g}}[f_K(w)\boldsymbol{\theta}, w] \,. \tag{6.5}$$

This allows us to define the *fractional density contrast* of the number density of foreground galaxies on the sky as

$$\kappa_{\mathrm{g}}(\boldsymbol{\theta}) \equiv \frac{N(\boldsymbol{\theta}) - \bar{N}}{\bar{N}} = \int_0^{w_{\mathrm{H}}} \mathrm{d}w \, p_{\mathrm{f}}(w)\delta_{\mathrm{g}}[f_K(w)\boldsymbol{\theta}, w] \,, \tag{6.6}$$

where we used Eq. (6.5) in the last step.

We can now build cross- and auto-power spectra of the convergence $\kappa(\boldsymbol{\theta})$ and the fractional density contrast $\kappa_{\mathrm{g}}(\boldsymbol{\theta})$ by using Limber's equation (5.64). The projected cross-power spectrum is defined by the two-point correlator

$$\langle \tilde{\kappa}(\boldsymbol{l})\tilde{\kappa}_{\mathrm{g}}(\boldsymbol{l}')\rangle = (2\pi)^2 \delta_{\mathrm{D}}(\boldsymbol{l} + \boldsymbol{l}')P_{\kappa\mathrm{g}}(l) \,. \tag{6.7}$$

The possible combinations are the dark matter auto-power spectrum

$$P_{\kappa\kappa}(l) = \int_0^{w_{\mathrm{H}}} \mathrm{d}w \, G^2(w)P_{\delta\delta}\left(\frac{l}{f_K(w)}; w\right) \,, \tag{6.8}$$

the galaxy auto-power spectrum

$$P_{\mathrm{gg}}(l) = \int_0^{w_{\mathrm{H}}} \mathrm{d}w \, \frac{p_{\mathrm{f}}^2(w)}{f_K^2(w)}P_{\mathrm{gg}}\left(\frac{l}{f_K(w)}; w\right) \,, \tag{6.9}$$

and the dark matter-galaxy cross-power spectrum

$$P_{\kappa\mathrm{g}}(l) = \int_0^{w_{\mathrm{H}}} \mathrm{d}w \, \frac{G(w)p_{\mathrm{f}}(w)}{f_K(w)}P_{\delta\mathrm{g}}\left(\frac{l}{f_K(w)}; w\right) \,. \tag{6.10}$$
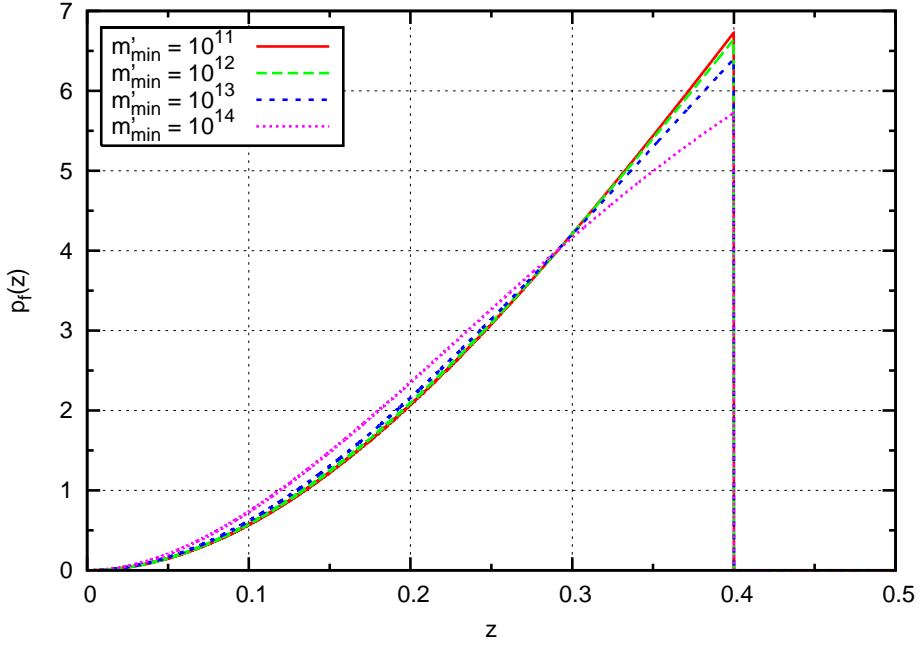
Figure 6.1: Redshift distribution of foreground galaxies shown for four different minimal HOD masses as indicated in the figure, where we use $m'_{\min} \equiv m_{\min}/(h^{-1}M_{\odot})$. We find that higher threshold masses lead to an enhancement of the probability for low redshifts and to a reduction for higher redshifts. Note that we employ a maximal redshift of $z_{\max,\mathrm{f}} = 0.4$ for the lenses. Moreover, we assume that all sources are located at a single redshift $z_{\mathrm{s}} = 1$.

Assuming that the distributions of foreground (lenses) and background galaxies (sources) are given by Dirac delta functions at redshift z_{l} ($p_{\mathrm{f}}(z) = \delta_{\mathrm{D}}(z - z_{\mathrm{l}})$) and at z_{s} ($p_{\mathrm{s}}(z) = \delta_{\mathrm{D}}(z - z_{\mathrm{s}})$), respectively, the projected cross-power spectrum (6.10) simplifies to

$$P_{\kappa\mathrm{g}}(l) = \frac{3}{2}\Omega_{\mathrm{m}}\left(\frac{H_0}{c}\right)^2 (1 + z_{\mathrm{l}})\frac{w(z_{\mathrm{s}}) - w(z_{\mathrm{l}})}{w(z_{\mathrm{l}})w(z_{\mathrm{s}})}P_{\delta\mathrm{g}}\left(\frac{l}{w(z_{\mathrm{l}})}; z_{\mathrm{l}}\right) , \qquad (6.11)$$

where we inserted the weight function (5.69) valid for a single source redshift. Note that we assumed in a flat Universe in the derivation of Eq. (6.11). Then the projected spectrum is directly proportional to the three-dimensional spectrum times geometrical factors that describe the distances of the lensing system. Note that we cannot derive an expression of the projected galaxy power spectrum (6.9) considering a Dirac delta distribution for the foreground redshift distribution because of the occurrence of the factor $p_{\mathrm{f}}^2(w)$. The cause of this problem is that Limber's approximation is not valid anymore for this product of weight functions (Schneider 1998).

Having laid out the concept of projected spectra, we want to adopt our halo model to predict their dependence on the Fourier mode l. First, we give the distribution of foreground galaxies (6.4) in terms of redshift using $p_{\mathrm{f}}(z)\mathrm{d}z = p_{\mathrm{f}}(w)\mathrm{d}w$. In this case we

find

$$p_{\mathrm{f}}(z) = \frac{c}{H(z)} \frac{w^2(z) \bar{n}_{\mathrm{g}}[w(z)]}{\bar{N}} \Theta(z_{\mathrm{max,f}} - z) \,, \tag{6.12}$$

where we assumed a flat Universe and the selection function $\nu(z) = \Theta(z_{\mathrm{max,f}} - z)$ for simplicity, and $\Theta(x)$ denotes the step function. Here $z_{\mathrm{max,f}}$ is the selected maximal redshift of a foreground galaxy sample. In addition, we could set a minimum redshift which is accessible in a potential experiment. The mean number density of galaxies $\bar{n}_{\mathrm{g}}$ is connected to the adopted form of the HOD by the completeness relation in Eq. (4.2). We depict the distribution in Fig. 6.1 for four different minimal masses m_{min} where we adopt the Kravtsov et al. (2004) parametrization of the HOD given in Eqs. (4.13) (central galaxies) and (4.14) (satellite galaxies). The corresponding angular number densities which define our galaxy samples are $\bar{N} \simeq 1.66\,\mathrm{arcmin}^{-2}$ for $m_{\mathrm{min}} = 10^{11} h^{-1}\,M_{\odot}$, $\bar{N} \simeq 0.19\,\mathrm{arcmin}^{-2}$ for $m_{\mathrm{min}} = 10^{12} h^{-1}\,M_{\odot}$, $\bar{N} \simeq 0.019\,\mathrm{arcmin}^{-2}$ for $m_{\mathrm{min}} = 10^{13} h^{-1}\,M_{\odot}$ and $\bar{N} \simeq 9.71 \times 10^{-4}\,\mathrm{arcmin}^{-2}$ for $m_{\mathrm{min}} = 10^{14} h^{-1}\,M_{\odot}$. Note that we truncate the foreground distribution at a maximal redshift of $z_{\mathrm{max,f}} = 0.4$. As one can see, the difference between the four curves is small. Since the distribution is normalized an enhancement (reduction) for small redshifts results in a reduction (enhancement) for large redshifts. We will employ this foreground redshift distribution for the following plots and assume that the background galaxies are located at a single redshift of $z_{\mathrm{s}} = 1$ (approximately twice as large as the maximal foreground redshift) unless otherwise stated[2].

We define for the three introduced projected power spectra their reduced (dimensionless) form as

$$\Delta_{\mathrm{XY}}(l) \equiv \frac{l^2}{2\pi} P_{\mathrm{XY}}(l) \,. \tag{6.13}$$

Here the two subscripts can take the values $(\mathrm{X,Y}) \in \{\kappa, \mathrm{g}\}$. The reduced spectra have a much weaker scale dependence than the spectra themselves. The three-dimensional spectra are calculated with our halo model implementation, in particular see Eqs. (3.103) and (3.106) for the dark matter, Eqs. (4.27) and (4.29) for the galaxy and Eqs. (4.36) and (4.37) for the cross-power spectrum. We depict them in Fig. 6.2 as a function of l for $m_{\mathrm{min}} = 10^{12}\,h^{-1}\,M_{\odot}$. Most notably, the galaxy and cross-spectrum can be approximately described by a single power law in l, whereas the convergence spectrum is first increasing and then decreasing for small scales. Hence, the form of the three-dimensional spectra is approximately maintained by the projections (compare with Fig. 4.3 and Fig. 4.6). On the other hand, at first sight it might be surprising that the (scale-dependent) difference between the galaxy, convergence and the cross-spectrum is very large (up to three to four orders of magnitude). To further analyze this difference, we define according to Eq. (4.53) the *projected bias factor* and the *projected correlation coefficient* by

$$\bar{b}(l) \equiv \sqrt{\frac{P_{\mathrm{gg}}(l)}{P_{\kappa\kappa}(l)}} \,, \qquad \bar{r}(l) = \frac{P_{\kappa\mathrm{g}}(l)}{\sqrt{P_{\kappa\kappa}(l) P_{\mathrm{gg}}(l)}} \,, \qquad \frac{\bar{b}(l)}{\bar{r}(l)} \equiv \frac{P_{\mathrm{gg}}(l)}{P_{\kappa\mathrm{g}}(l)} \,, \tag{6.14}$$

---

[2]This is similar to the redshift distribution used by Simon et al. (2008) in the analysis of the RCS field with maximal foreground redshift $z_{\mathrm{f}} = 0.4$ and mean background redshift of $\bar{z}_{\mathrm{s}} \approx 0.85$.
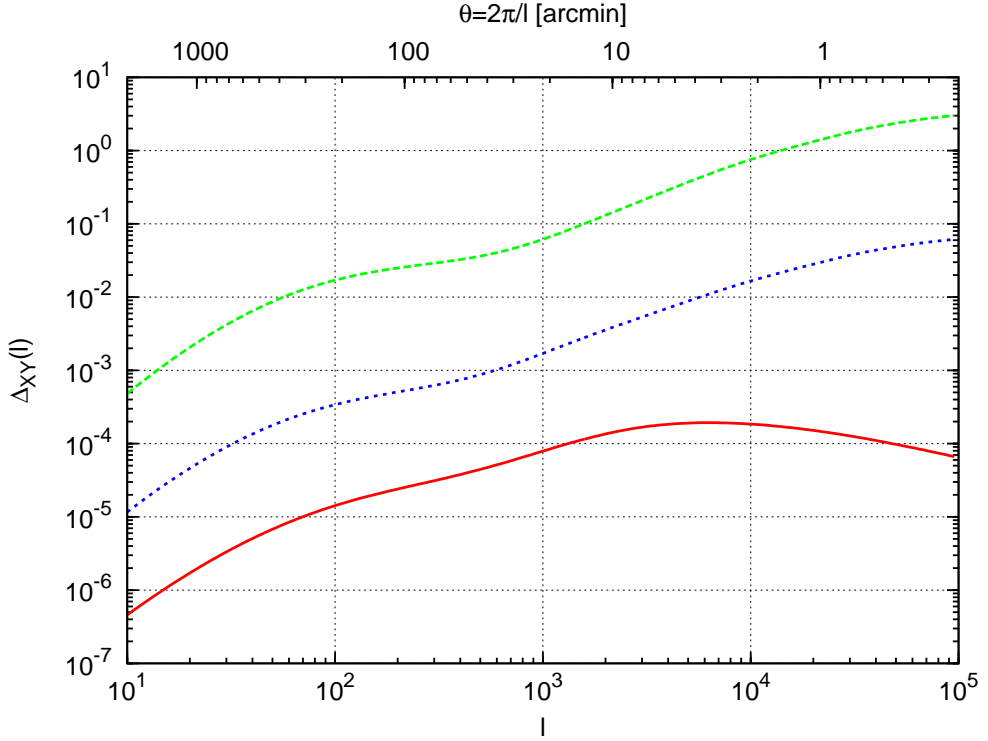
Figure 6.2: Reduced projected power spectra (6.13) versus Fourier mode l for $m_{\min} = 10^{12} \, h^{-1} \, M_\odot$. We show the convergence power spectrum (solid red line), the projected cross-power spectrum (dotted blue line) and the projected galaxy power spectrum (dashed green line). In addition, we depict on the upper abscissa the correspondence to the real-space Fourier conjugate of l defined as $\theta = 2\pi/l$ which is given in units of arcmin.

where the last relation quantifies the difference of the galaxy and cross-spectrum. Note that these quantities additionally depend on the redshift distribution of foreground and background galaxies. We show the results in Fig. 6.3 for the same l-range as before but for four different minimal masses as indicated in the figure. Now we can compare the left-hand panel which shows the projected bias factor with the left-hand panel of Fig. 4.6, where we plot the three-dimensional scale-dependent bias between galaxy and dark matter clustering. We find that the shape of the curves is similar. However, the amplitude is clearly enhanced for the projected spectra. This is mainly due to the different weight functions used in Limber's equation (compare the weightings in Eqs. 6.8 and 6.9). In addition, we note that $\bar{b}(l)$ does not converge to a constant on the largest depicted scales in contrast to the three-dimensional bias factor. Clearly, this is an effect of the redshift weighting of the projected spectra. On the right-hand panels of Fig. 6.3 and Fig. 4.6 we show the ratio $\bar{b}/\bar{r}$ of the projected and b/r of the three-dimensional correlation parameter, respectively. In this case the scale dependence is strongly reduced compared to the bias since the galaxy and the cross-spectrum have a similar shape especially on small scales. Furthermore, the form of the curves are slightly different
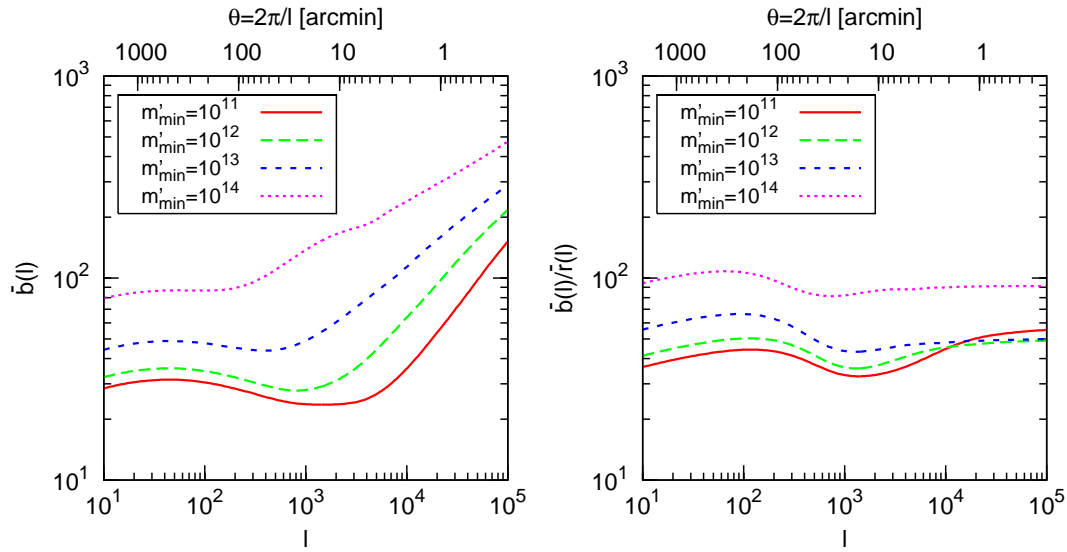
Figure 6.3: Projected bias factor (left panel) and ratio of the projected bias to the correlation coefficient (right panel) versus Fourier mode l (see definitions in Eq. 6.14) for four different minimal masses as indicated in the figure.

compared to their three-dimensional counterparts because of the redshift weighting of the projection.

We showed in Sect. 4.3.3 that for the three-dimensional spectra the amplitudes of the bias and correlation coefficient are enhanced for larger minimal masses $m_{\min}$. This is due to the fact that considering a larger minimal mass leads to a smaller number density of galaxies. Since the spectra are normalized by the mean number of galaxies a larger minimal mass results in an enhancement of the amplitudes. In Fig. 6.3 we see that this trend is preserved for the projected bias factor and correlation coefficient.

6.1.2 Mean Tangential Shear

Here we will define the real-space observable of galaxy-galaxy lensing. Galaxy-galaxy lensing is measured by cross-correlating the shear of background galaxies around foreground galaxy positions. We define the *mean tangential shear* signal around a foreground galaxy as

$$\langle \gamma_t(\vartheta) \rangle \equiv \langle \kappa_g(\boldsymbol{\theta}) \gamma(\boldsymbol{\theta} + \boldsymbol{\vartheta}; \varphi) \rangle , \qquad (6.15)$$

where φ is the polar angle of the connection vector $\boldsymbol{\vartheta}$. Again we can compute this cross-correlation with the techniques used in Eqs. (5.75) and (5.76) where we calculated

the shear correlation functions:

$$
\begin{aligned}
\langle \gamma_t(\vartheta) \rangle &= \langle \kappa_g(\boldsymbol{\theta}) \gamma_t(\boldsymbol{\theta} + \boldsymbol{\vartheta}; \varphi) \rangle + i \langle \kappa_g(\boldsymbol{\theta}) \gamma_\times(\boldsymbol{\theta} + \boldsymbol{\vartheta}; \varphi) \rangle \\
&= - e^{-2i\varphi} \langle \kappa_g(\boldsymbol{\theta}) \gamma_c(\boldsymbol{\theta} + \boldsymbol{\vartheta}) \rangle \\
&= - \int \frac{d^2 l}{(2\pi)^2} P_{\kappa g}(l) \, e^{i\boldsymbol{\vartheta}\cdot\boldsymbol{l}} \, e^{2i(\beta - \varphi)} \\
&= -\frac{1}{(2\pi)^2} \int_0^\infty dl \, l \int_0^{2\pi} d\phi' \, e^{i\vartheta l \cos\phi'} [\cos(2\phi') + i\sin(2\phi')] \\
&= \frac{1}{(2\pi)} \int_0^\infty dl \, l P_{\kappa g}(l) \, J_2(l\vartheta) \, .
\end{aligned}
\tag{6.16}
$$

In the second step we used the decomposition of Eq. (5.74). We set the correlator including $\gamma_\times$ to zero as it is a parity-violating term. Then we transform the fractional density and the shear into Fourier space, use the Kaiser-Squires relation (5.40) and insert Eq. (6.7) for the resulting two-point correlator. In the last step we evaluate the angular integral over the cosine-term which is equal to the negative second-order Bessel function, and the integral over the sinus-term is equal to zero. Thus, the mean tangential shear measures a filtered version of the projected cross-power spectrum of galaxies and dark matter, where the filter function is given by the second-order Bessel function of first kind.

The mean tangential shear measured on the circle of radius θ is related to the averaged convergence inside the circle and the azimuthally-averaged surface convergence at θ (Schneider et al. 2006)

$$
\langle \gamma_t(\theta) \rangle = \bar{\kappa}(< \theta) - \langle \kappa(\theta) \rangle = \frac{\bar{\Sigma}(< D_l \theta) - \langle \Sigma(D_l \theta) \rangle}{\Sigma_{\text{crit}}} \, ,
\tag{6.17}
$$

where we used in the last step that the convergence is a scaled version of the surface mass density (see Eq. 5.20). The averaged surface mass density inside the circle is given by

$$
\bar{\kappa}(< \theta) = \frac{2}{\theta^2} \int_0^\theta d\theta' \, \theta' \langle \kappa(\theta') \rangle \, .
\tag{6.18}
$$

Note that this relation is also valid for non-azimuthally symmetric density profiles. From the sketch of a general lens system in Fig. 5.2, we find that the distance transverse to the line-of-sight of the lensing galaxy is given by the physical distance $R \equiv \xi = D_l \theta$, and inserting this into (6.17) yields

$$
\Sigma_{\text{crit}} \langle \gamma_t(R/D_l) \rangle = \bar{\Sigma}(< R) - \langle \Sigma(R) \rangle \equiv \Delta\Sigma(R) \, ,
\tag{6.19}
$$

where we defined the *excess surface mass density* $\Delta\Sigma$ in the last step which is the observable in GGL experiments. We can easily evaluate the left-hand side of Eq. (6.19) by inserting into the mean tangential shear (6.16) the expression for the projected
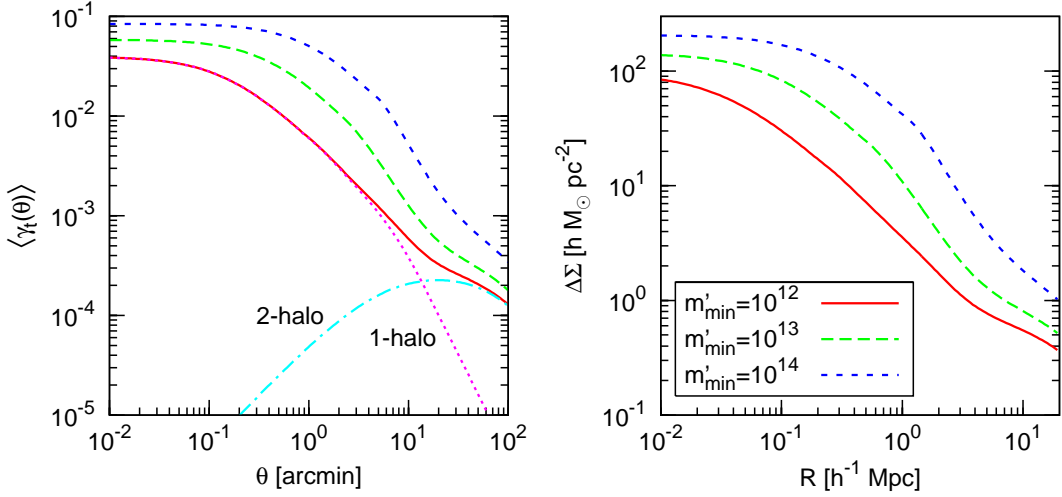
Figure 6.4: Mean tangential shear as a function of θ in arcmin (left panel) and the projected surface mass density as a function of the distance from the halo center (right panel). We show the results for three different minimal masses as indicated in the figure with $m'_{min} = m_{min}/(h^{-1} M_\odot)$. Here we assume that the lenses and the sources are located at a single redshift $\bar{z}_f = 0.29$ and $z_s = 1$, respectively. Moreover, we show for $m_{min} = 10^{12} h^{-1} M_\odot$ the contributions of the one-halo (dotted magenta line) and two-halo terms (dot-dashed light blue line).

cross-spectrum for a single foreground (located at z_l) and background galaxy (located at z_s) as given in Eq. (6.11). In this case we find

$$\Sigma_{crit}\langle\gamma_t\,[R/D_l]\rangle = \frac{\bar{\rho}c}{H_0}\pi \int \frac{\mathrm{d}k}{k}\left(\frac{H_0}{ck}\right)\frac{k^3 P_{\delta g}(k; z_l)}{2\pi^2}\,\mathrm{J}_2(kR)\,. \tag{6.20}$$

Here we used the fact that the inverse critical surface mass density can be expressed in terms of comoving distances which is valid for a flat Universe:

$$\Sigma_{crit}^{-1} = \frac{4\pi G_N}{c^2}\frac{D_l D_{ls}}{D_s} = \frac{3}{2}\left(\frac{H_0}{c}\right)^2\frac{\Omega_m}{\bar{\rho}}(1+z_l)\frac{w(z_l)[w(z_s) - w(z_l)]}{w(z_s)}\,. \tag{6.21}$$

Furthermore, we wrote the integrand in (6.20) in dimensionless terms such that the dimensions of the whole expression are specified by $\bar{\rho}c/H_0 \approx 832\,\Omega_m h\,M_\odot\,\mathrm{pc}^{-2}$.

All this is valid if we have perfect spectroscopic and photometric redshift information for the foreground and background galaxies, respectively. If at least spectroscopic redshifts for the foreground galaxies are available (which is the case for the SDSS- and RCS analyses) we have to average the mean tangential shear over the source redshift distribution:

$$\langle\gamma_t(R/D_l)\rangle = \int \mathrm{d}z_s\, p_s(z_s)\frac{\bar{\Sigma}(< R) - \langle\Sigma(R)\rangle}{\Sigma_{crit}}\,. \tag{6.22}$$
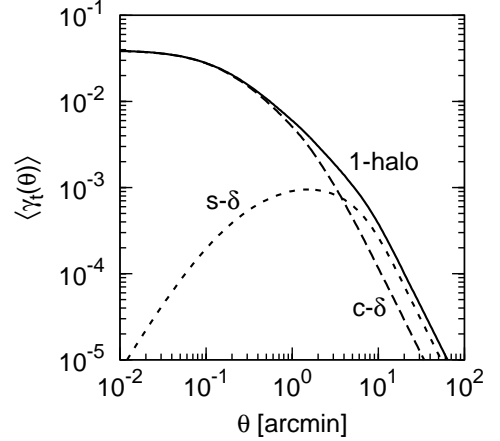
Figure 6.5: Contributions of the central-matter (c-δ) and satellite-matter (s-δ) correlations to the one-halo term of the mean tangential shear as a function of θ. Note that the one-halo term is the same as in the left-hand panel of Fig. 6.4.

In Fig. 6.4 we plot the GGL signal for three different minimal masses where we depict the mean tangential shear as a function of the angular position on the sky (left panel) and the projected surface mass density as a function of the separation from the halo center (right panel). Note that we assume that all lenses and sources are located at $\bar{z}_\mathrm{f} = 0.29$ and $z_\mathrm{s} = 1$, respectively. We choose the single foreground redshift as the mean redshift of the foreground galaxy distribution shown in Fig. 6.1, i.e., $\bar{z}_\mathrm{f} = \int_0^\infty \mathrm{d}z\, z\, p_\mathrm{f}(z)$. Taking the mean redshift value is a good approximation for the projected cross-spectrum including the full distribution. Moreover, this enables us to employ Eq. (6.11) which simplifies the calculation. We show the one- and two-halo contributions to the mean tangential shear for $m_\mathrm{min} = 10^{12}\, h^{-1}\, M_\odot$. The two-halo term only becomes important for large transverse distances from the halo center ($R > 1\, h^{-1}\, \mathrm{Mpc}$) and thus is excluded in some analyses (e.g., Guzik & Seljak 2002). Note that the excess surface mass density in the right-hand panel shows the same functional form as the mean tangential shear because both quantities directly probe the three-dimensional cross-spectrum. Furthermore, note that the mean tangential shear becomes more steep at approximately $\theta = 5\,\mathrm{arcmin}$ which is clearly visible for $m_\mathrm{min} = 10^{14}\, h^{-1}\, M_\odot$. At these scales the angular radius resolves the scale radius of the halo profile (Hu & Jain 2004).

In Fig. 6.5 we show the contributions from central-mass and satellite-mass correlations on the one-halo term of the mean tangential shear. The former dominate the signal on small scales, whereas the latter give the dominant contribution for scales larger than $\theta \approx 4\,\mathrm{arcmin}$. At these scales we see a change in the slope of the one-halo term.

6.2 Galaxy-Galaxy-Galaxy Lensing

With current and planned large-area surveys it is possible to reliably measure higher-order correlation functions. This inspired Schneider & Lombardi (2003) to define the natural components of the third-order cosmic shear correlation functions which probe the dark matter bispectrum (Schneider et al. 2005). However, the higher-order shear correlation functions are hard to measure because the shear is a polar which depends

on 2 independent components. These developed techniques can also be applied to generalize the concept of GGL which probes the two-point cross-correlation function to third-order correlations between galaxies and dark matter which are characterized by the corresponding three-point cross-correlation functions. These quantities are defined in Schneider & Watts (2005) where also practical estimators of the cross-correlation functions are developed. Moreover, they derive the connections to their Fourier-space counterparts and define higher-order aperture mass correlators which are useful since they can separate systematic B-modes and parity-violating modes from the cosmological E-mode signal. The physical interpretation of the newly developed galaxy-galaxy-galaxy lensing (GGGL) signal was analyzed in Watts & Schneider (2005). In the language of the halo model of galaxy clustering as introduced in Chapter 4, higher-order cross-spectra probe also higher-order moments of the HOD and additionally show a stronger dependence on the radial distribution of galaxies $\tilde{u}_{\mathrm{g}}$. This is in contrast to GGL which is only sensitive to the first moment of the HOD. We emphasize again that the moments of the HOD are the key quantities to understand the dark matter-galaxy bias and thus constrain theoretical models of galaxy formation. Furthermore, the analysis of the GGGL signal can help us to learn more about the distribution of galaxies in their host halos which could finally lead to a parametrization of the galaxy density profile. Apart from the halo model interpretation, it was pointed out that galaxy-galaxy-shear correlations[3] are a measure for the shear pattern around pairs of foreground galaxies. Thus, their determination is a promising tool for studying the environment of gravitationally bound systems which contain a small number of galaxies like galaxy groups (Watts & Schneider 2005; Johnston 2006).

Only very recently, the first detection of GGGL was reported in Simon et al. (2008) using data from the RCS fields (Gladders & Yee 2005) and utilizing the detailed photometric redshift information of the background galaxies. They determined the galaxy-galaxy-shear and the shear-shear-galaxy correlation functions from the data and computed from these the corresponding aperture mass statistics to separate the cosmological from the systematic signal. The obtained results were compared to halo model predictions which revealed that at least the galaxy-galaxy-shear correlations are of cosmological origin. Future wide-field surveys which are substantially larger than the RCS fields should yield significantly improved results making GGGL a promising future cosmological tool. Furthermore, we can use the well-known methods of GGL, for example dividing the sample in early- and late-type galaxies, studying low- and high-density environments etc., which provide us with a wealth of cosmological information. A related work is presented in Johnston (2006) who determines the galaxy-galaxy-mass three-point correlation functions from a large N-body simulation (populated with galaxies using the HOD formalism) and estimates mass and shear maps. The author points out that already current SDSS weak-lensing data should be sufficient to determine the three-point

---

[3]These build only one part of the GGGL signal. In addition, one could measure shear-shear-galaxy correlations. However, the physical interpretation of these correlations yet has to be determined. Nevertheless, we will include them in our subsequent halo model analysis.
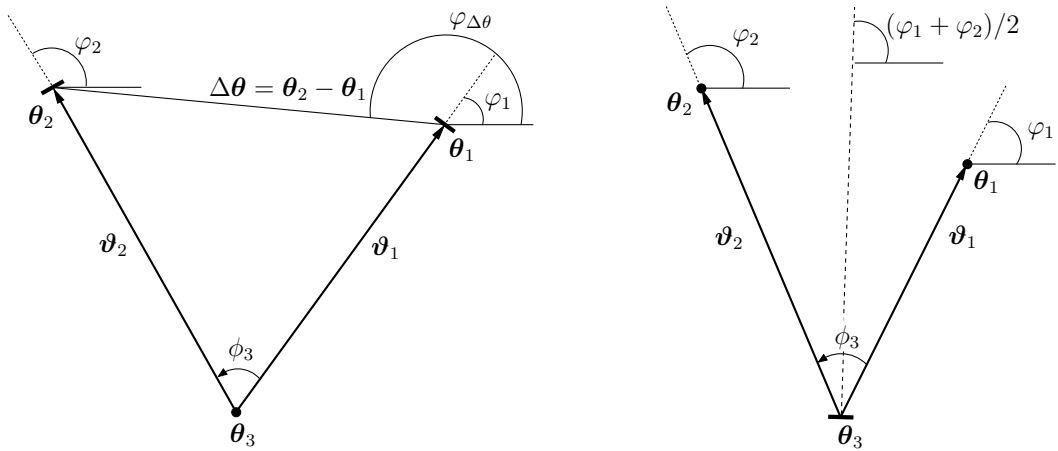
Figure 6.6: Sketch of the geometry of the GGGL correlation functions. We show the shear-shear-galaxy correlations $G_\pm(\vartheta_1, \vartheta_2, \phi_3)$ in the left panel (see Eqs. 6.23 and 6.24) and the galaxy-galaxy-shear correlation $\mathcal{G}(\vartheta_1, \vartheta_2, \phi_3)$ in the right panel (see Eq. 6.30). Each filled circle corresponds to a foreground galaxy and each stick indicates the tangential shear at the corresponding position. Note that the sign of the angle $\phi_3 = \varphi_2 - \varphi_1$ is important. The figure is adapted from Schneider & Watts (2005).

cross-correlation function. Future theoretical work for this new cosmological tool is mandatory which includes extended studies with N-body simulations (ideally including baryons) and detailed predictions of the analytic halo model which might give more physical insights. A major part of this thesis is to provide an analytical treatment for the GGGL signal showing all needed assumptions and parameters. Even though Simon et al. showed halo model predictions for the GGGL aperture statistics, a detailed presentation of the model is missing.

We define in the following the two observables of GGGL, namely the galaxy-galaxy-matter and the matter-matter-galaxy correlation functions. Both quantities depend on the corresponding projected cross-bispectra which we predict with our halo model implementation. These results enable us to compute the aperture mass correlators which are of key importance for future experiments. Our findings can be used as a guidance for the results of future experiments to test if their signal is of cosmological origin. A major goal is to constrain different theoretical HOD models by comparison with observational data which enables us to empirically test different physical models of galaxy formation.

6.2.1 Correlation Functions

Schneider & Watts (2005) extended the concept of two-point cross-correlations between galaxies and shear as measured by GGL to third-order galaxy-shear correlations. They showed that one can define three third-order correlators. The first two describe the

cross-correlation of the shear of two background galaxies at positions $\boldsymbol{\theta}_1$ and $\boldsymbol{\theta}_2$, with a foreground galaxy at position $\boldsymbol{\theta}_3$:

$$G_+(\boldsymbol{\vartheta}_1, \boldsymbol{\vartheta}_2) = G_+(\vartheta_1, \vartheta_2, \phi_3) = \langle \gamma(\boldsymbol{\theta}_1; \varphi_1) \gamma^*(\boldsymbol{\theta}_2; \varphi_2) \kappa_{\mathrm{g}}(\boldsymbol{\theta}_3) \rangle \,, \tag{6.23}$$

$$G_-(\boldsymbol{\vartheta}_1, \boldsymbol{\vartheta}_2) = G_-(\vartheta_1, \vartheta_2, \phi_3) = \langle \gamma(\boldsymbol{\theta}_1; \varphi_1) \gamma(\boldsymbol{\theta}_2; \varphi_2) \kappa_{\mathrm{g}}(\boldsymbol{\theta}_3) \rangle \,, \tag{6.24}$$

where the separation vectors between the two background galaxies and the foreground galaxy are denoted by $\boldsymbol{\vartheta}_i = \boldsymbol{\theta}_i - \boldsymbol{\theta}_3$ with $i = \{1, 2\}$, and φ_i denotes the corresponding polar angle. For a sketch of the vectors and angles we refer to the left-hand panel of Fig. 6.6. Note that we parametrized the scale dependence of the correlation functions by the modulus of the two connection vectors, ϑ_1 and ϑ_2, and the angle ϕ_3 between them[4] which is valid for homogeneous and isotropic correlations. However, for the construction of practical estimators it is better to use the slightly modified correlators which are defined by

$$\tilde{G}_+(\vartheta_1, \vartheta_2, \phi_3) \equiv \frac{1}{\bar{N}} \langle \gamma(\boldsymbol{\theta}_1; \varphi_1) \gamma^*(\boldsymbol{\theta}_2; \varphi_2) N(\boldsymbol{\theta}_3) \rangle$$
$$= G_+(\vartheta_1, \vartheta_2, \phi_3) + \langle \gamma(\boldsymbol{\theta}_1; \varphi_1) \gamma^*(\boldsymbol{\theta}_2; \varphi_2) \rangle \,, \tag{6.25}$$

$$\tilde{G}_-(\vartheta_1, \vartheta_2, \phi_3) \equiv \frac{1}{\bar{N}} \langle \gamma(\boldsymbol{\theta}_1; \varphi_1) \gamma(\boldsymbol{\theta}_2; \varphi_2) N(\boldsymbol{\theta}_3) \rangle$$
$$= G_-(\vartheta_1, \vartheta_2, \phi_3) + \langle \gamma(\boldsymbol{\theta}_1; \varphi_1) \gamma(\boldsymbol{\theta}_2; \varphi_2) \rangle \,, \tag{6.26}$$

where we used $N(\boldsymbol{\theta}_i)/\bar{N} = 1 + \kappa_{\mathrm{g}}(\boldsymbol{\theta}_i)$ in the second step of both equations to express the modified correlators in terms of the original definitions of the correlation functions. We see that the modified correlators depend also on the second-order shear correlation functions. First, however, we need to calculate the correlation of the shear at two different angles. We note that

$$\gamma(\boldsymbol{\theta}; \varphi_1) = \gamma(\boldsymbol{\theta}; \varphi_2) \, \mathrm{e}^{2\mathrm{i}(\varphi_2 - \varphi_1)} \,, \tag{6.27}$$

which can be seen by inserting (5.74) for $\gamma(\boldsymbol{\theta}; \varphi_2)$. Then we can rewrite the shear two-point correlator in (6.25) by rotating the two shear terms onto the separation vector of the background galaxies (i.e., rotation by $\varphi_{\Delta\theta}$, see Fig. 6.6):

$$\langle \gamma(\boldsymbol{\theta}_1; \varphi_1) \gamma^*(\boldsymbol{\theta}_2; \varphi_2) \rangle = \mathrm{e}^{2\mathrm{i}(\varphi_{\Delta\theta} - \varphi_1)} \, \mathrm{e}^{2\mathrm{i}(\varphi_2 - \varphi_{\Delta\theta})} \langle \gamma(\boldsymbol{\theta}_1; \varphi_{\Delta\theta}) \gamma^*(\boldsymbol{\theta}_2; \varphi_{\Delta\theta}) \rangle$$
$$= \langle \gamma(\boldsymbol{\theta}_1; \varphi_{\Delta\theta}) \gamma^*(\boldsymbol{\theta}_2; \varphi_{\Delta\theta}) \rangle \, \mathrm{e}^{2\mathrm{i}\phi_3} = \xi_+(\Delta\theta) \, \mathrm{e}^{2\mathrm{i}\phi_3} \,, \tag{6.28}$$

where $\Delta\boldsymbol{\theta} = \boldsymbol{\vartheta}_2 - \boldsymbol{\vartheta}_1$ is the separation vector of the two background galaxies and $\varphi_{\Delta\theta}$ is the corresponding polar angle. In addition, we see from Fig. 6.6 that $\phi_3 = \varphi_2 - \varphi_1$ and in the last step we used the definition of the shear two-point correlation function given

---

[4]Another possible way is to parametrize the correlation function by the length of the three triangle sides.

in Eq. (5.73). Similarly, we can derive the other two-point shear correlator in (6.26):

$$
\begin{aligned}
\langle \gamma(\boldsymbol{\theta}_1; \varphi_1)\gamma(\boldsymbol{\theta}_2; \varphi_2)\rangle &= \xi_-(\Delta\theta)\, \mathrm{e}^{4\mathrm{i}\varphi_\Delta}\, \mathrm{e}^{-2\mathrm{i}(\varphi_1+\varphi_2)} \\
&= \xi_-(\Delta\theta)\frac{\left[\vartheta_2\, \mathrm{e}^{\mathrm{i}\phi_3/2} - \vartheta_1\, \mathrm{e}^{-\mathrm{i}\phi_3/2}\right]^4}{(\Delta\theta)^4}\,,
\end{aligned}
\tag{6.29}
$$

where we used the fact that we can represent two-dimensional vectors by complex numbers such that $\boldsymbol{\vartheta}_i \to |\boldsymbol{\vartheta}_i|\,\mathrm{e}^{\mathrm{i}\varphi_i}$ (for $i = 1, 2$) and $\Delta\boldsymbol{\theta} \to |\Delta\boldsymbol{\theta}|\,\mathrm{e}^{\mathrm{i}\varphi_\Delta\theta}$ in the last step. In particular, we can then show that $\vartheta_i\,\mathrm{e}^{\mathrm{i}\phi_3/2} = \mathrm{e}^{\mathrm{i}/2(\varphi_1+\varphi_2)}\,\vartheta_i\,\mathrm{e}^{\mathrm{i}\varphi_i}$ which proofs the relation.

The third correlation function, besides Eqs. (6.23) and (6.24), quantifies the shear around pairs of galaxies:

$$
\mathcal{G}(\boldsymbol{\vartheta}_1, \boldsymbol{\vartheta}_2) = \mathcal{G}(\vartheta_1, \vartheta_2, \phi_3) = \left\langle \kappa_{\mathrm{g}}(\boldsymbol{\theta}_1)\kappa_{\mathrm{g}}(\boldsymbol{\theta}_2)\gamma\left(\boldsymbol{\theta}_3; \frac{\varphi_1+\varphi_2}{2}\right)\right\rangle.
\tag{6.30}
$$

Note that the shear in Eq. (6.30) is projected onto the line which bisects the angle ϕ_3 because we cannot project the shear onto both separation vectors $\boldsymbol{\vartheta}_1$ and $\boldsymbol{\vartheta}_2$. Again, we define the modified correlator by

$$
\tilde{\mathcal{G}}(\boldsymbol{\vartheta}_1, \boldsymbol{\vartheta}_2) = \tilde{\mathcal{G}}(\vartheta_1, \vartheta_2, \phi_3) = \frac{1}{\bar{N}^2}\left\langle N(\boldsymbol{\theta}_1)N(\boldsymbol{\theta}_2)\gamma\left(\boldsymbol{\theta}_3; \frac{\varphi_1+\varphi_2}{2}\right)\right\rangle,
\tag{6.31}
$$

which is related to the original correlator by

$$
\tilde{\mathcal{G}}(\vartheta_1, \vartheta_2, \phi_3) = \mathcal{G}(\vartheta_1, \vartheta_2, \phi_3) + \langle \kappa_{\mathrm{g}}(\boldsymbol{\theta}_1)\gamma\left(\boldsymbol{\theta}_3; \varphi_{12}/2\right)\rangle + \langle \kappa_{\mathrm{g}}(\boldsymbol{\theta}_2)\gamma\left(\boldsymbol{\theta}_3; \varphi_{12}/2\right)\rangle.
\tag{6.32}
$$

Here we defined $\varphi_{12} \equiv \varphi_1 + \varphi_2$. Now we project the shear onto the vectors $\boldsymbol{\vartheta}_1$ and $\boldsymbol{\vartheta}_2$ which connect each of the two foreground galaxies with the background galaxy. This results in $\gamma(\boldsymbol{\theta}_3; \varphi_{12}/2) = \gamma(\boldsymbol{\theta}_3; \varphi_i)\,\mathrm{e}^{2\mathrm{i}(\varphi_i-\varphi_{12}/2)} = \gamma(\boldsymbol{\theta}_3; \varphi_i)\,\mathrm{e}^{\pm\mathrm{i}\phi_3}$ with a minus sign in the exponential for $i = 1$ and plus sign for $i = 2$. Finally, the modified three-point correlator is

$$
\tilde{\mathcal{G}}(\vartheta_1, \vartheta_2, \phi_3) = \mathcal{G}(\vartheta_1, \vartheta_2, \phi_3) + \langle\gamma_{\mathrm{t}}(\vartheta_1)\rangle\,\mathrm{e}^{-\mathrm{i}\phi_3} + \langle\gamma_{\mathrm{t}}(\vartheta_2)\rangle\,\mathrm{e}^{\mathrm{i}\phi_3}\,,
\tag{6.33}
$$

where we used the definition of the mean tangential shear (6.15). Again the modified correlation function depends on two-point correlation functions which are in this case GGL signals. Hence, for a purely Gaussian density field the modified correlation function measures the mean tangential shear around each foreground galaxy times phase factors.

6.2.2 Projected Cross-Bispectra

Similar to the two-point shear correlation functions, we can write the GGGL correlation functions as a weighted integral over the corresponding projected bispectra. For a detailed derivation of these relations we refer to Schneider & Watts (2005). We analyze here the behavior of the two cross-bispectra which are probed by GGGL surveys and
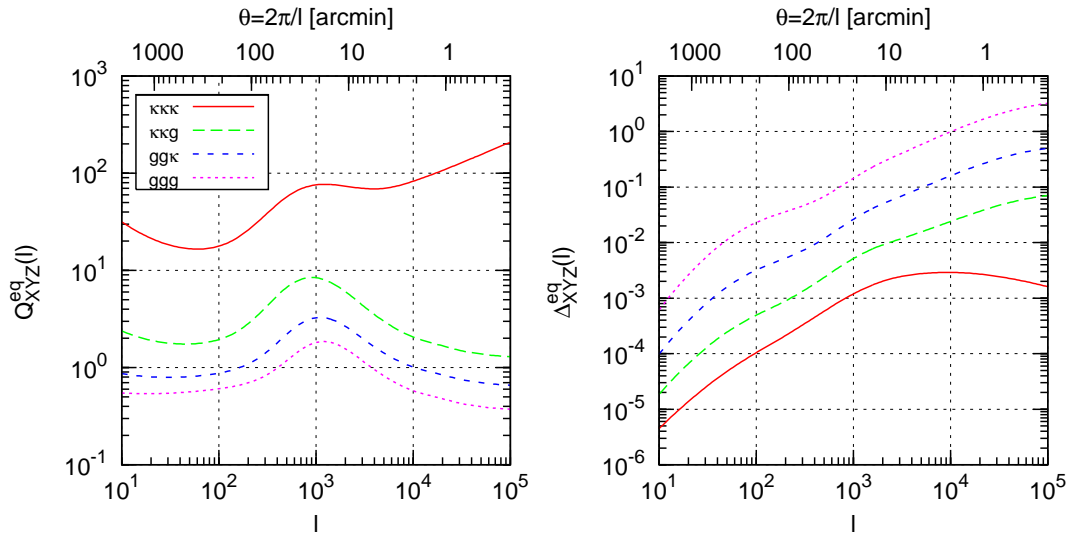
Figure 6.7: Reduced projected bispectra as a function of Fourier mode l for an equilateral configuration (see text for details). We show the four possible auto- and cross-bispectra which are the galaxy bispectrum (dotted magenta line), the dark matter bispectrum (solid red line) and the two cross-bispectra, namely $Q_{\kappa\kappa g}$ (long dashed green line) and $Q_{gg\kappa}$ (short dashed blue line). We use a minimal mass $m_{\min} = 10^{12}\, h^{-1}\, M_{\odot}$ for the HOD. A higher (lower) threshold mass results in a reduction (enhancement) of the scale-dependence of the spectra including galaxies and the maximum is shifted to lower (higher) l. The left- and right-hand panels show two different definitions of the dimensionless bispectrum (see text for details).

compare the results with the two auto-bispectra probed in galaxy and in cosmic shear surveys. We show predictions for all of these spectra with our halo model implementation.

The four projected auto- and cross-bispectra are defined by the following connected three-point correlators:

$$\langle\tilde{\kappa}(\boldsymbol{l}_1)\tilde{\kappa}(\boldsymbol{l}_2)\tilde{\kappa}(\boldsymbol{l}_3)\rangle_{\rm c} = (2\pi)^2\delta_{\rm D}(\boldsymbol{l}_{123})B_{\kappa\kappa\kappa}(\boldsymbol{l}_1,\boldsymbol{l}_2,\boldsymbol{l}_3)\,, \tag{6.34}$$

$$\langle\tilde{\kappa}(\boldsymbol{l}_1)\tilde{\kappa}(\boldsymbol{l}_2)\tilde{\kappa}_{\rm g}(\boldsymbol{l}_3)\rangle_{\rm c} = (2\pi)^2\delta_{\rm D}(\boldsymbol{l}_{123})B_{\kappa\kappa{\rm g}}(\boldsymbol{l}_1,\boldsymbol{l}_2;\boldsymbol{l}_3)\,, \tag{6.35}$$

$$\langle\tilde{\kappa}_{\rm g}(\boldsymbol{l}_1)\tilde{\kappa}_{\rm g}(\boldsymbol{l}_2)\tilde{\kappa}(\boldsymbol{l}_3)\rangle_{\rm c} = (2\pi)^2\delta_{\rm D}(\boldsymbol{l}_{123})B_{{\rm gg}\kappa}(\boldsymbol{l}_1,\boldsymbol{l}_2;\boldsymbol{l}_3)\,, \tag{6.36}$$

$$\langle\tilde{\kappa}_{\rm g}(\boldsymbol{l}_1)\tilde{\kappa}_{\rm g}(\boldsymbol{l}_2)\tilde{\kappa}_{\rm g}(\boldsymbol{l}_3)\rangle_{\rm c} = (2\pi)^2\delta_{\rm D}(\boldsymbol{l}_{123})B_{{\rm ggg}}(\boldsymbol{l}_1,\boldsymbol{l}_2,\boldsymbol{l}_3)\,, \tag{6.37}$$

with $\boldsymbol{l}_{123} \equiv \boldsymbol{l}_1 + \boldsymbol{l}_2 + \boldsymbol{l}_3$. Applying Limber's approximation (5.65) to the two three-dimensional cross-spectra in Eqs. (6.35) and (6.36) yields the corresponding projected cross-spectra:

$$B_{\kappa\kappa{\rm g}}(\boldsymbol{l}_1,\boldsymbol{l}_2;\boldsymbol{l}_3) = \int_0^{w_{\rm H}} {\rm d}w\,\frac{G^2(w)p_{\rm f}(w)}{w^2}B_{\delta\delta{\rm g}}\left(\frac{\boldsymbol{l}_1}{w},\frac{\boldsymbol{l}_2}{w};\frac{\boldsymbol{l}_3}{w};w\right)\,, \tag{6.38}$$

$$B_{{\rm gg}\kappa}(\boldsymbol{l}_1,\boldsymbol{l}_2;\boldsymbol{l}_3) = \int_0^{w_{\rm H}} {\rm d}w\,\frac{G(w)p_{\rm f}^2(w)}{w^3}B_{{\rm gg}\delta}\left(\frac{\boldsymbol{l}_1}{w},\frac{\boldsymbol{l}_2}{w};\frac{\boldsymbol{l}_3}{w};w\right)\,, \tag{6.39}$$

and the projected galaxy bispectrum

$$B_{{\rm ggg}}(\boldsymbol{l}_1,\boldsymbol{l}_2;\boldsymbol{l}_3) = \int_0^{w_{\rm H}} {\rm d}w\,\frac{p_{\rm f}^3(w)}{w^4}B_{{\rm ggg}}\left(\frac{\boldsymbol{l}_1}{w},\frac{\boldsymbol{l}_2}{w};\frac{\boldsymbol{l}_3}{w};w\right)\,. \tag{6.40}$$

Note that the expression for the convergence bispectrum is given in the previous chapter in Eq. (5.71). If all foreground galaxies are located at a single redshift $z_{\rm l}$ and background galaxies at $z_{\rm s}$ the first projected bispectrum (6.38) simplifies to

$$B_{\kappa\kappa{\rm g}}(\boldsymbol{l}_1,\boldsymbol{l}_2;\boldsymbol{l}_3) = \frac{9}{4}\Omega_{\rm m}^2\left(\frac{H_0}{c}\right)^4(1+z_{\rm l})^2\frac{(w_{\rm s}-w_{\rm l})^2}{w_{\rm s}^2 w_{\rm l}^2}B_{\delta\delta{\rm g}}\left(\frac{\boldsymbol{l}_1}{w_{\rm l}},\frac{\boldsymbol{l}_2}{w_{\rm l}};\frac{\boldsymbol{l}_3}{w_{\rm l}};z_{\rm l}\right)\,, \tag{6.41}$$

where $w_{\rm l} = w(z_{\rm l})$ and $w_{\rm s} = w(z_{\rm s})$. Note that we cannot derive such an expression for the galaxy and the galaxy-galaxy-mass bispectrum since Limber's approximation is not valid in this case.

We define the two reduced projected cross-bispectra according to the three-dimensional reduced bispectra introduced in Eqs. (4.72) and (4.73):

$$Q_{{\rm gg}\kappa}(\boldsymbol{l}_1,\boldsymbol{l}_2;\boldsymbol{l}_3) \equiv \frac{B_{{\rm gg}\kappa}(\boldsymbol{l}_1,\boldsymbol{l}_2;\boldsymbol{l}_3)}{P_{\kappa{\rm g}}(l_1)P_{\kappa{\rm g}}(l_2) + P_{{\rm gg}}(l_1)P_{\kappa{\rm g}}(l_3) + P_{{\rm gg}}(l_2)P_{\kappa{\rm g}}(l_3)}\,, \tag{6.42}$$

$$Q_{\kappa\kappa{\rm g}}(\boldsymbol{l}_1,\boldsymbol{l}_2;\boldsymbol{l}_3) \equiv \frac{B_{\kappa\kappa{\rm g}}(\boldsymbol{l}_1,\boldsymbol{l}_2;\boldsymbol{l}_3)}{P_{\kappa{\rm g}}(l_1)P_{\kappa{\rm g}}(l_2) + P_{\kappa\kappa}(l_1)P_{\kappa{\rm g}}(l_3) + P_{\kappa\kappa}(l_2)P_{\kappa{\rm g}}(l_3)}\,. \tag{6.43}$$

Accordingly, we define the two reduced projected auto-bispectra following Eq. (4.71). Note that we parametrize in the following the reduced bispectra by the length of the three sides, l_1, l_2 and l_3 that build a closed triangle in Fourier space.

In Fig. 6.7 we depict the four reduced bispectra as a function of Fourier mode l for an equilateral configuration defined such that $Q_{\text{XYZ}}^{\text{eq}}(l) \equiv Q_{\text{XYZ}}(l, l, l)$ where $(\text{X,Y,Z}) \in \{\kappa, \text{g}\}$ (left panel). Furthermore, we show another definition of the dimensionless bispectrum given by $\Delta_{\text{XYZ}}^{\text{eq}}(l) \equiv (l^2/2\pi)\sqrt{B_{\text{XYZ}}(l, l, l)}$ (right panel). As already seen for the projected power spectra, the difference between the projected bispectra is much larger than their non-projected three-dimensional counterparts that are depicted in Fig. 4.7. This can be easily explained by the different weight functions used in the projections. The shape of the three-dimensional bispectra is roughly conserved by the projections. In particular, we find that the reduced convergence bispectrum is increasing for small scales, whereas the bispectra including galaxy correlations are decreasing for small scales. For the three-dimensional spectra we pointed out that the different behavior on small scales stems from the dependence of the bispectra on the density profile. More specifically, the bispectra including galaxy correlations are on small scales dominated by central galaxy correlations which are only weighted by two density profiles.

Projected Bispectrum Bias

To clarify this issue, we define analogous to the three-dimensional bispectrum bias factors (see Eqs. 4.77, 4.78 and 4.79), the *projected bispectrum bias factors*:

$$\bar{b}_3 = \left(\frac{B_{\text{ggg}}}{B_{\kappa\kappa\kappa}}\right)^{1/3}, \qquad \bar{R}_2 \equiv \frac{\bar{b}_3}{\bar{r}_2} = \frac{B_{\text{ggg}}}{B_{\text{gg}\kappa}}, \qquad \bar{R}_1 \equiv \frac{\bar{b}_3}{\sqrt{\bar{r}_1}} = \sqrt{\frac{B_{\text{ggg}}}{B_{\kappa\kappa\text{g}}}}, \qquad (6.44)$$

$$\bar{r}_1 = \frac{B_{\kappa\kappa\text{g}}}{B_{\kappa\kappa\kappa}}\left(\frac{B_{\kappa\kappa\kappa}}{B_{\text{ggg}}}\right)^{1/3}, \qquad \bar{r}_2 = \frac{B_{\text{gg}\kappa}}{B_{\kappa\kappa\kappa}}\left(\frac{B_{\kappa\kappa\kappa}}{B_{\text{ggg}}}\right)^{2/3}, \qquad (6.45)$$

where the functions depend on the triangle sides l_1, l_2 and l_3. We illustrate $\bar{b}_3^{\text{eq}}(l) \equiv \bar{b}_3(l, l, l)$ in Fig. 6.8 for equilateral configurations as a function of l for three different minimal masses (left panel). Furthermore, we depict $\bar{R}_1^{\text{eq}}(l) \equiv \bar{R}_1(l, l, l)$ (left panel) and $\bar{R}_2^{\text{eq}}(l) \equiv \bar{R}_2(l, l, l)$ (right panel) in Fig. 6.9. We see that for small l the functions do not converge to a constant value in contrast to the three-dimensional functions (compare with Fig. 4.8 and Fig. 4.10) and are rather decreasing. On small scales $\bar{b}_3^{\text{eq}}$ becomes highly scale-dependent, whereas $\bar{R}_1^{\text{eq}}$ and $\bar{R}_2^{\text{eq}}$ approximately converge to a constant. In addition, all curves have a bump feature at $l \approx 60$ which is not seen for the three-dimensional spectra. To analyze the origin of the bump feature, we employed an approximation of the galaxy and convergence bispectra which is composed of the one-halo terms and the large-scale limit of the three-halo terms (e.g., the projected tree-level bispectrum for the convergence bispectrum). We find that the bump is still persistent for this approximation of $\bar{b}_3$ which means that it cannot be explained by our lack of modeling halo exclusion (which affects the two- and three-halo terms). In the right-hand panel of Fig. 6.8 we study the dependence of the bump feature by varying specific input parameters of the halo model keeping the minimal mass $m_{\min} = 10^{13} h^{-1} M_\odot$ fixed. Enhancing (reducing) Ω_{m} and σ_8 results in a reduced (enhanced) amplitude of the bias with a stronger effect for variations of Ω_{m}. The position of the bump is approximately
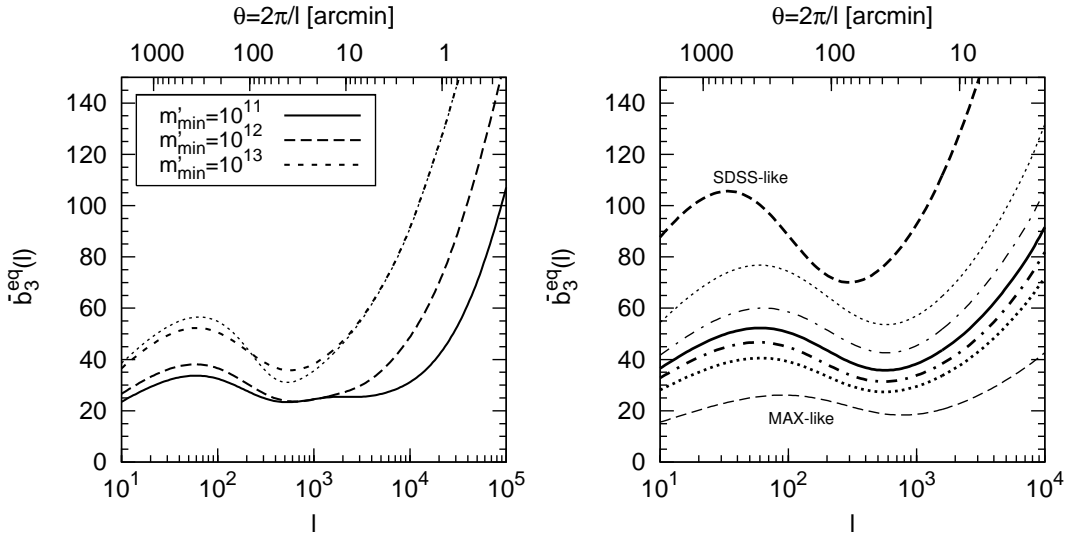
Figure 6.8: Equilateral configuration of the projected bias factor $\bar{b}_3^{\mathrm{eq}}$ (see Eq. 6.44) as a function of l for three different minimal masses (left panel). The dotted magenta line gives the result for $m_{\mathrm{min}} = 10^{13}\,h^{-1}\,M_\odot$ when approximating the bispectra by a sum of their one-halo contribution and the large-scale limit of the three-halo terms. We showed the corresponding three-dimensional bispectrum bias factor in Fig. 4.10. In the right-hand panel we study the dependence of the bump feature at small l by varying specific input parameters of the halo model keeping $m_{\mathrm{min}} = 10^{13}\,h^{-1}\,M_\odot$ fixed. We analyze the dependence on the redshift distribution of fore- and background galaxies depicting the results for an SDSS-like survey with $z_{\mathrm{max,f}} = 0.2$ and $z_{\mathrm{s}} = 0.4$ (thick long-dashed line) and for a future deep survey (MAX) with $z_{\mathrm{max,f}} = 0.6$ and $z_{\mathrm{s}} = 1.5$ (thin long-dashed line). Additionally, we show the influence on the cosmological parameters Ω_{m} and σ_8, namely $\Omega_{\mathrm{m}} = 0.2$ (thin dotted line) and $\Omega_{\mathrm{m}} = 0.4$ (thick dotted line), and $\sigma_8 = 0.8$ (thin dot-dashed line) and $\sigma_8 = 1$ (thick dot-dashed line).
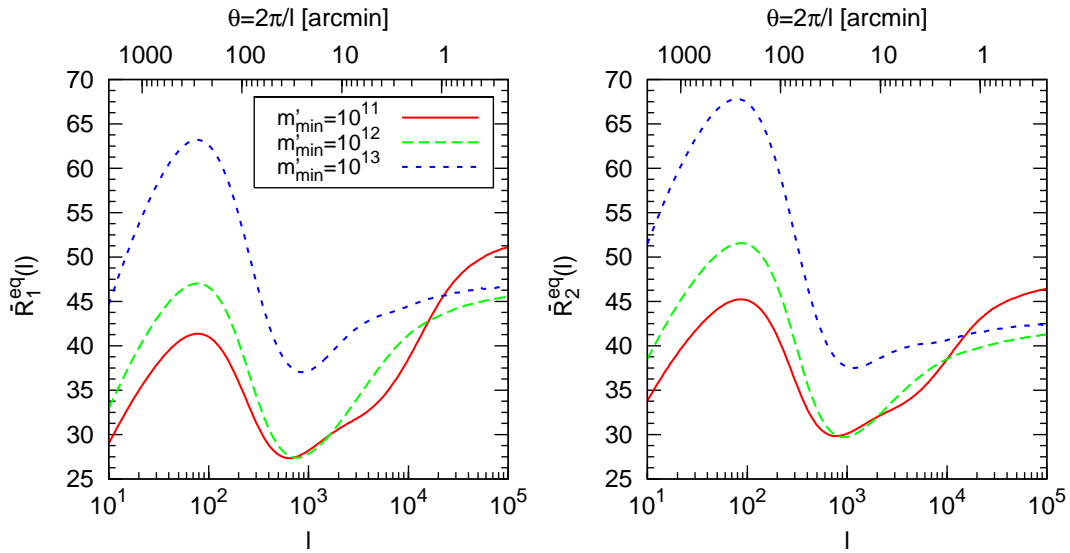
Figure 6.9: Square root of the ratio of the projected galaxy to the convergence-convergence-galaxy bispectrum (left panel), and ratio of the projected galaxy to the galaxy-galaxy-convergence bispectrum (right panel) (see Eq. 6.44). In particular we depict the ratios in equilateral configuration as a function of l for three different minimal masses as indicated in the figure.

invariant under these variations. However, changing the redshift distribution of sources and lenses (here we study an SDSS-like survey and a potential future deep survey which we termed MAX-like) results in a change of the amplitude and slope of the curves and an off-set of the position of the bump. For a larger lens and source redshift the bump feature is strongly reduced and shifted to larger values of l, whereas for smaller redshifts it is strongly enhanced. Hence, we conclude that the bump mainly depends on the adopted redshift distributions. The difference between the three-dimensional and the projected bias is then due to the redshift-dependent weight factors in Limber's approximation.

In Fig. 6.10 we give the results for the two projected correlation coefficients $\bar{r}_1^{\rm eq}$ and $\bar{r}_2^{\rm eq}$ as a function of l. On large scales both quantities converge to a constant value, whereas they are increasing on small scales. In addition, the amplitude of $\bar{r}_1^{\rm eq}$ is larger than $\bar{r}_2^{\rm eq}$ on small scales which is the behavior we already found for their three-dimensional counterparts (see Fig. 4.9). However, on large scales the projected coefficients do not converge to 1 due to the redshift weighting of the projections.

Configuration Dependence

The configuration dependence of the reduced projected bispectra is shown in Fig. 6.11 as a function of the three sides of the triangle l_1, l_2 and l_3. We keep l_2 fixed to a value indicated in each panel, whereas l_1 and l_3 vary from 50 to 2×10^5. We show four
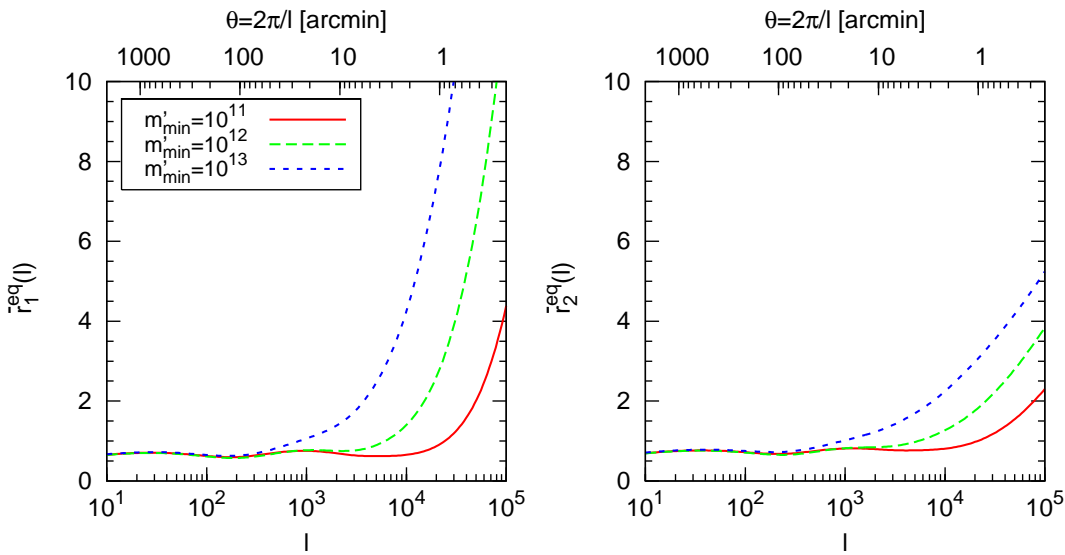
Figure 6.10: Projected correlation coefficients $\bar{r}_1^{\mathrm{eq}}$ (left panel) and $\bar{r}_2^{\mathrm{eq}}$ (right panel) as defined in Eq. (6.45). In particular, we depict the coefficients in equilateral configuration as a function of l for three different minimal masses as indicated in the figure.

columns which illustrate the results for $Q_{\mathrm{ggg}}(l_1, l_2, l_3)$, $Q_{\mathrm{gg}\kappa}(l_1, l_2; l_3)$, $Q_{\kappa\kappa\mathrm{g}}(l_1, l_2; l_3)$ and $Q_{\kappa\kappa\kappa}(l_1, l_2, l_3)$ going from left to right. Each column consists of three panels where we fixed $l_2 = 10$, $l_2 = 10^3$ and $l_2 = 10^5$ going from bottom to top. Note that we chose these combination of parameters to study the amount of asymmetry when we interchange l_1 and l_3 in the two cross-spectra. Moreover, we show contour lines for the amplitudes $10^2, 10^4, 10^6, 10^8, 10^{10}, 10^{12}$ and 10^{14} in each panel. First of all we notice that the reduced bispectra cover a large range of scales. We see that the amplitude of Q is enhanced if we go from the left panels to the right panels which is best visible for large l_1 and l_3. If we compare the bottom to the top panels of each row the yellow region that corresponds to small values of Q is extended and shifted to larger l. Moreover, in the two middle columns we can study the asymmetry inherent in the cross-spectra. The asymmetry amounts to a factor of 2 for large l_1 and l_3 (and $l_2 = 10^3, 10^5$) and is reduced for small l. In all the plots (also for the cross-spectra) we have to keep in mind that the plots for different l_2 carry not completely independent information because of the symmetry properties of the functions.

In Fig. (6.12) we compare the results of the configuration dependence of the convergence bispectrum obtained with tree-level perturbation theory (left panel) and the full halo model (right panel). We find that the halo model result is in accordance with perturbation theory on large scales, whereas the perturbative result underestimates the result of the halo model on small scales as expected.
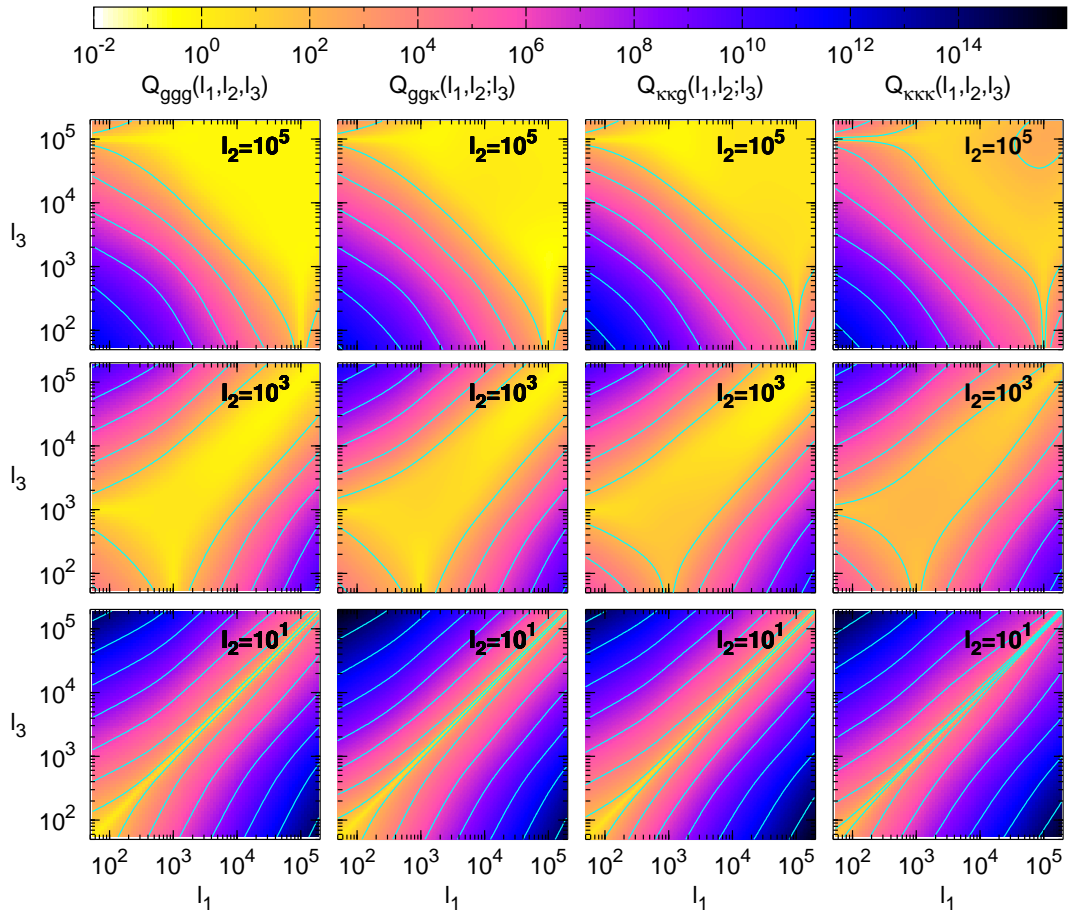
Figure 6.11: Configuration dependence of the reduced bispectra shown as a contour plot. We vary l_1 and l_3 by keeping l_2 fixed as indicated in each panel. The different rows show the four different bispectra. Note that the two-cross spectra are not symmetric under interchanging l_1 and l_3. We refer to the text for detailed explanations.
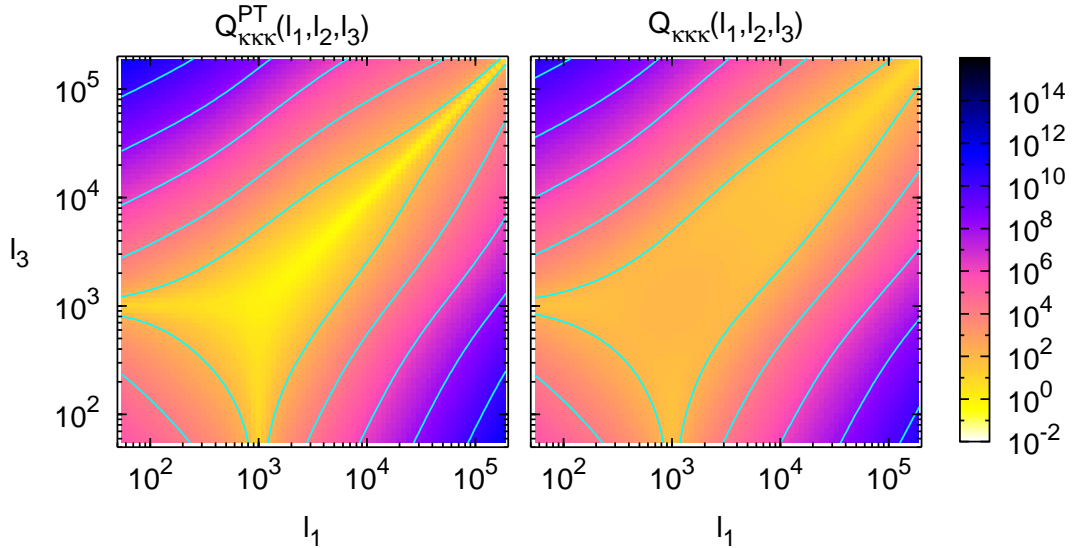
Figure 6.12: Configuration dependence of the reduced convergence bispectrum shown as a contour plot. We vary l_1 and l_3 and set $l_2 = 10^3$. The left-hand panel depicts the convergence bispectrum using only tree-level perturbation theory and the right-hand panel shows the full halo model result of the bispectrum.

6.2.3 Aperture Statistics

The aperture mass is defined as the filtered surface mass density κ inside an aperture of radius θ (Schneider 1996):

$$M_{\mathrm{ap}}(\theta) = \int \mathrm{d}^2\vartheta \, U_\theta(\vartheta)\kappa(\boldsymbol{\vartheta}) = \int \mathrm{d}^2\vartheta \, Q_\theta(\vartheta)\gamma_{\mathrm{t}}(\boldsymbol{\vartheta})\,. \tag{6.46}$$

In the second step we see that the aperture mass can also be expressed in terms of the tangential shear which is measured with respect to the direction $\boldsymbol{\vartheta}$. Note that we need to assume that U_θ is a compensated filter function which means that

$$\int \mathrm{d}^2\vartheta \, U_\theta(\vartheta) = 2\pi \int_0^\infty \mathrm{d}\vartheta \, \vartheta \, U_\theta(\vartheta) = 0\,. \tag{6.47}$$

The second filter function Q_θ can be obtained from U_θ by

$$Q_\theta(\vartheta) = \left[\frac{2}{\vartheta^2} \int_0^\vartheta \mathrm{d}\vartheta' \, \vartheta' U_\theta(\vartheta')\right] - U_\theta(\vartheta)\,. \tag{6.48}$$

Furthermore, we define the *aperture number counts* of galaxies as (Schneider 1998)

$$\mathcal{N}(\theta) = \int \mathrm{d}^2\vartheta \, U_\theta(\vartheta)\kappa_{\mathrm{g}}(\boldsymbol{\vartheta}) = \frac{1}{\bar{N}} \int \mathrm{d}^2\vartheta \, U_\theta(\vartheta)N(\boldsymbol{\vartheta})\,, \tag{6.49}$$

where we used the fact that U_θ is a compensated filter function in the second step. There are several reason to prefer the aperture statistics over the correlation functions. First of all, the aperture statistics allow for a separation of the cosmological signal (E-mode) and systematic effects (B-modes). In addition, they provide very localized measurements of the corresponding spectra. This is in contrast to the shear correlation functions which weight the corresponding spectra with a broad filter function (see e.g., the expression for ξ_+ in Eq. 5.76). The third-order aperture correlators contain essentially all information of the bispectra due to this property (Schneider et al. 2005).

We employ here the filter function introduced in Crittenden et al. (2002) by writing $U_\theta(\vartheta) = \theta^{-2} u(\vartheta/\theta)$. The dimensionless function is then given by

$$u(x) = \frac{1}{2\pi} \left(1 - \frac{x^2}{2} \right) e^{-x^2/2} \ . \tag{6.50}$$

This particular form of the filter function has the advantage of having a simple analytic Fourier transform:

$$\tilde{u}(l) = \int \mathrm{d}^2 x \, u(|\boldsymbol{x}|) \, e^{\mathrm{i}\boldsymbol{l} \cdot \boldsymbol{x}} = \frac{l^2}{2} \, e^{-l^2/2} \ . \tag{6.51}$$

On the other hand, the filter function has no finite support. However, in practice the exponential factor makes the filter function very small for $x \gtrsim 3$ resulting in an effective finite support.

We can now build three-point correlators of the aperture mass (6.46) and aperture number counts (6.49). First we consider the correlator

$$
\begin{aligned}
\langle M_{\mathrm{ap}}(\theta_1) M_{\mathrm{ap}}(\theta_2) \mathcal{N}(\theta_3) \rangle &\equiv \langle M_{\mathrm{ap}} M_{\mathrm{ap}} \mathcal{N} \rangle (\theta_1, \theta_2; \theta_3) \\
&= \int \mathrm{d}^2\vartheta_1 \, U_{\theta_1}(\vartheta_1) \int \mathrm{d}^2\vartheta_2 \, U_{\theta_2}(\vartheta_2) \int \mathrm{d}^2\vartheta_3 \, U_{\theta_3}(\vartheta_3) \\
&\quad \times \langle \kappa(\boldsymbol{\vartheta}_1) \kappa(\boldsymbol{\vartheta}_2) \kappa_{\mathrm{g}}(\boldsymbol{\vartheta}_3) \rangle \\
&= \left[\prod_{i=1}^{3} \int \mathrm{d}^2\vartheta_i \, U_{\theta_i}(\vartheta_i) \, e^{-\mathrm{i}\boldsymbol{l}_i \cdot \boldsymbol{\vartheta}_i} \right] \int \frac{\mathrm{d}^2 l_1}{(2\pi)^2} \int \frac{\mathrm{d}^2 l_2}{(2\pi)^2} \int \frac{\mathrm{d}^2 l_3}{(2\pi)^2} \\
&\quad \times \langle \tilde{\kappa}(\boldsymbol{l}_1) \tilde{\kappa}(\boldsymbol{l}_2) \tilde{\kappa}_{\mathrm{g}}(\boldsymbol{l}_3) \rangle \\
&= \int \frac{\mathrm{d}^2 l_1}{(2\pi)^2} \int \frac{\mathrm{d}^2 l_2}{(2\pi)^2} \, \tilde{u}(l_1\theta_1) \tilde{u}(l_2\theta_2) \tilde{u}(|\boldsymbol{l}_1 + \boldsymbol{l}_2|\theta_3) \\
&\quad \times B_{\kappa\kappa\mathrm{g}}(\boldsymbol{l}_1, \boldsymbol{l}_2; -\boldsymbol{l}_1 - \boldsymbol{l}_2) \, , \tag{6.52}
\end{aligned}
$$

where we replaced the κ_i by their Fourier transforms, and in the last step we used the fact that

$$\int \mathrm{d}^2\vartheta \, U_\theta(\vartheta) \, e^{-\mathrm{i}\boldsymbol{l} \cdot \boldsymbol{\vartheta}} = \theta^{-2} \int \mathrm{d}^2\vartheta \, u(\vartheta/\theta) \, e^{-\mathrm{i}\boldsymbol{l} \cdot \boldsymbol{\vartheta}} = \int \mathrm{d}^2 x \, u(x) \, e^{-\mathrm{i}\theta\boldsymbol{l} \cdot \boldsymbol{x}} = \tilde{u}(l\theta) \, . \tag{6.53}$$

Additionally, we inserted the definition of the cross-bispectrum (6.35) which allows us to carry out the $\boldsymbol{l}_3$-integration. The expression (6.52) can be further simplified using

polar coordinates for the $\boldsymbol{l}_1$- and $\boldsymbol{l}_2$-integrations. In this case one angular integral is trivial yielding 2π and we are left with

$$
\langle M_{\mathrm{ap}} M_{\mathrm{ap}} \mathcal{N} \rangle (\theta_1, \theta_2; \theta_3) = \frac{1}{(2\pi)^3} \int_0^\infty \mathrm{d}l_1\, l_1 \int_0^\infty \mathrm{d}l_2\, l_2 \int_0^{2\pi} \mathrm{d}\varphi
$$
$$
\times\, \tilde{u}(l_1 \theta_1) \tilde{u}(l_2 \theta_2) \tilde{u}(|\boldsymbol{l}_1 + \boldsymbol{l}_2| \theta_3) B_{\kappa\kappa g}(\boldsymbol{l}_1, \boldsymbol{l}_2; -\boldsymbol{l}_1 - \boldsymbol{l}_2)\,, \quad (6.54)
$$

where φ is the angle between the vectors $\boldsymbol{l}_1$ and $\boldsymbol{l}_2$.

In complete analogy, we can express the other possible correlations in terms of the corresponding bispectra

$$
\langle \mathcal{N} \mathcal{N} M_{\mathrm{ap}} \rangle (\theta_1, \theta_2; \theta_3) = \int \frac{\mathrm{d}^2 l_1}{(2\pi)^2} \int \frac{\mathrm{d}^2 l_2}{(2\pi)^2}\, \tilde{u}(l_1 \theta_1) \tilde{u}(l_2 \theta_2) \tilde{u}(|\boldsymbol{l}_1 + \boldsymbol{l}_2| \theta_3)
$$
$$
\times\, B_{ggκ}(\boldsymbol{l}_1, \boldsymbol{l}_2; -\boldsymbol{l}_1 - \boldsymbol{l}_2)\,, \quad (6.55)
$$
$$
\langle M_{\mathrm{ap}} M_{\mathrm{ap}} M_{\mathrm{ap}} \rangle (\theta_1, \theta_2, \theta_3) = \int \frac{\mathrm{d}^2 l_1}{(2\pi)^2} \int \frac{\mathrm{d}^2 l_2}{(2\pi)^2}\, \tilde{u}(l_1 \theta_1) \tilde{u}(l_2 \theta_2) \tilde{u}(|\boldsymbol{l}_1 + \boldsymbol{l}_2| \theta_3)
$$
$$
\times\, B_{\kappa\kappa\kappa}(\boldsymbol{l}_1, \boldsymbol{l}_2, -\boldsymbol{l}_1 - \boldsymbol{l}_2)\,, \quad (6.56)
$$
$$
\langle \mathcal{N} \mathcal{N} \mathcal{N} \rangle (\theta_1, \theta_2, \theta_3) = \int \frac{\mathrm{d}^2 l_1}{(2\pi)^2} \int \frac{\mathrm{d}^2 l_2}{(2\pi)^2}\, \tilde{u}(l_1 \theta_1) \tilde{u}(l_2 \theta_2) \tilde{u}(|\boldsymbol{l}_1 + \boldsymbol{l}_2| \theta_3)
$$
$$
\times\, B_{ggg}(\boldsymbol{l}_1, \boldsymbol{l}_2, -\boldsymbol{l}_1 - \boldsymbol{l}_2)\,. \quad (6.57)
$$

The presented aperture mass three-point correlators can also be calculated from the corresponding three-point correlation functions introduced above (see Schneider & Watts 2005)

We employ the following approximations for the three-dimensional bispectra

$$
B^{ggg}(k_1, k_2, k_3; z) \approx B_{1\text{-h}}^{ggg}(k_1, k_2, k_3; z) + [b_1^{\mathrm{L}}(z)]^3 B_{\mathrm{pt}}(k_1, k_2, k_3; z)\,, \quad (6.58)
$$
$$
B^{gg\delta}(k_1, k_2; k_3; z) \approx B_{1\text{-h}}^{gg\delta}(k_1, k_2; k_3; z) + [b_1^{\mathrm{L}}(z)]^2 B_{\mathrm{pt}}(k_1, k_2, k_3; z)\,, \quad (6.59)
$$
$$
B^{\delta\delta g}(k_1, k_2; k_3; z) \approx B_{1\text{-h}}^{\delta\delta g}(k_1, k_2; k_3; z) + b_1^{\mathrm{L}}(z) B_{\mathrm{pt}}(k_1, k_2, k_3; z)\,, \quad (6.60)
$$
$$
B^{\delta\delta\delta}(k_1, k_2, k_3; z) \approx B_{1\text{-h}}^{\delta\delta\delta}(k_1, k_2, k_3; z) + B_{\mathrm{pt}}(k_1, k_2, k_3; z)\,, \quad (6.61)
$$

where $b_1^{\mathrm{L}}(z)$ is the first-order large-scale bias factor as given in Eq. (4.48) and B_{pt} is the lowest-order bispectrum in perturbation theory (see Eq. 2.123). Inserting these relations in the corresponding Limber equation (5.65) yields the projected bispectra. In total, we need to perform a 6-dimensional integration for the one-halo terms of the aperture statistics (i.e., with respect to the halo mass m, concentration c, redshift z, l_1, l_2 and φ)[5] and 4-dimensional integration for the perturbation theory terms of the aperture statistics (i.e., with respect to the redshift z, l_1, l_2 and φ). For the calculation of the aperture statistics we use adaptive multi-dimensional Monte Carlo integration routines

---

[5]For the bispectra including galaxy correlations the concentration distribution has only a small effect on the one-halo terms (see Sect. 4.6) and thus we need only a 5-dimensional integration.

which are much faster to perform than adaptive Gaussian quadrature routines. However, we checked that both integration methods give the same results. The approximations are much faster to numerically calculate than the full halo model. This is due to the fact that the two- and three-halo terms of the three-dimensional bispectrum are composed of products of integrals, whereas the one-halo term is only composed of a single mass integral. The approximation is especially suited in time-consuming computation, e.g., the determination of the information content of the aperture statistics.

In Fig. 6.13 we show the two cross-aperture statistics, i.e., $\langle \mathcal{N}\mathcal{N}M_{\rm ap}\rangle(\theta, \theta; \theta)$ (upper panel) and $\langle M_{\rm ap}M_{\rm ap}\mathcal{N}\rangle(\theta, \theta; \theta)$ (lower panel) as a function of the aperture radius assuming that the three radii are equal, i.e., $\theta_1 = \theta_2 = \theta_3 \equiv \theta$. For each panel we show the individual contributions of the one-, two- and three-halo terms, and the sum of all terms (Full halo model). In addition, we employ the corresponding approximations for the three-dimensional bispectra, (6.59) and (6.60), which are composed of a sum of the one-halo term and the result of the large-scale limit of the three-halo term. The ratio of the approximation to the full halo model is shown in the lower part of each panel. We find that for the angular range covered the deviation peaks at approximately 30 per cent for $\theta \approx 10\,\mathrm{arcmin}$. The peak is at slightly larger angular radii for $\langle M_{\rm ap}M_{\rm ap}\mathcal{N}\rangle(\theta, \theta; \theta)$. This is not surprising since at these scales the two-halo term gives a significant contribution to the total function. Note that up to $\theta \approx 2\,\mathrm{arcmin}$ the difference in using the approximation or the full halo model is only 10 per cent. Both panels show that for a broad range of scales one can apply the approximation if one wants to get a rough estimate of the aperture statistics. Moreover, the assumption that one can use tree-level perturbation theory for calculating the correlations of halo centers, as is done for the full halo model, is almost certainly wrong (Smith et al. 2007; Takada & Jain 2008). For example the clustering of two distinct non-overlapping halos which have a small separation is not well described by the linear power spectrum. In this case one should take higher-order terms in the perturbative expansion into account.

In Fig. 6.14 we depict for comparison the two auto-aperture statistics, namely $\langle M_{\rm ap}M_{\rm ap}M_{\rm ap}\rangle$ (upper panel) and $\langle \mathcal{N}\mathcal{N}\mathcal{N}\rangle$ (lower panel) as a function of the aperture radius θ. We basically recover the results for the ratio of the full halo model to the approximation as in Fig. 6.13. We note that the shape of the dark matter aperture statistics is different from the other three functions which include galaxy correlations. Most notably, for small aperture radii the dark matter aperture statistics is a slowly decreasing function of θ. In addition, we find that the two-halo term gives still an important effect on large scales making the approximation to the full halo model less accurate.

We note that we can divide the behavior of the aperture statistics involving galaxies into four regimes: for $0 \lesssim \theta/\mathrm{arcmin} \lesssim 4$ the one-halo term is dominant. In Fig. 6.15 we study this regime for the galaxy-galaxy-mass aperture statistics in detail splitting the one-halo term into contributions from central-satellite-mass and satellite-satellite-mass correlations. We see that the former dominates the one-halo term for $0 < \theta/\mathrm{arcmin} \lesssim 0.3$, whereas the latter takes over for $0.3 \lesssim \theta/\mathrm{arcmin} \lesssim 4$. The change manifests itself in a small turnover of the slope at approximately $0.3\,\mathrm{arcmin}$. At intermediate scales,
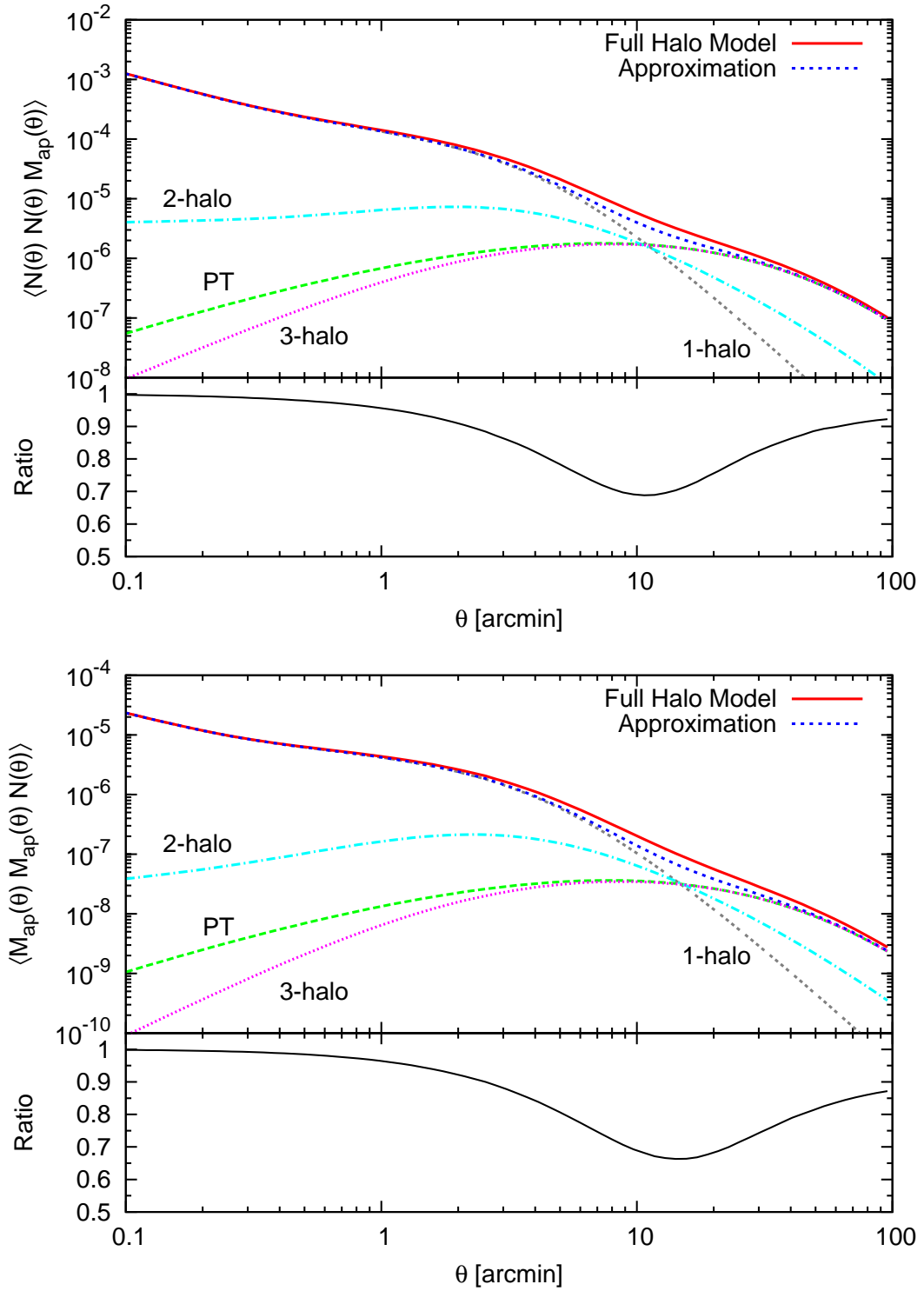
Figure 6.13: Comparison of the aperture statistics $\langle \mathcal{N}\mathcal{N}M_{\mathrm{ap}}\rangle(\theta,\theta;\theta)$ (upper panel) and $\langle M_{\mathrm{ap}}M_{\mathrm{ap}}\mathcal{N}\rangle(\theta,\theta;\theta)$ (lower panel) computed with the approximation and with the full halo model as a function of the aperture radius θ. We assumed for both panels a minimal mass of $m_{\mathrm{min}} = 10^{11}\,h^{-1}\,M_{\odot}$. We depict the individual contributions of the one-, two- and three-halo terms, and of the bispectrum in lowest-order perturbation theory (PT). In the lower part of each panel we give the ratio of the approximation to the full halo model.
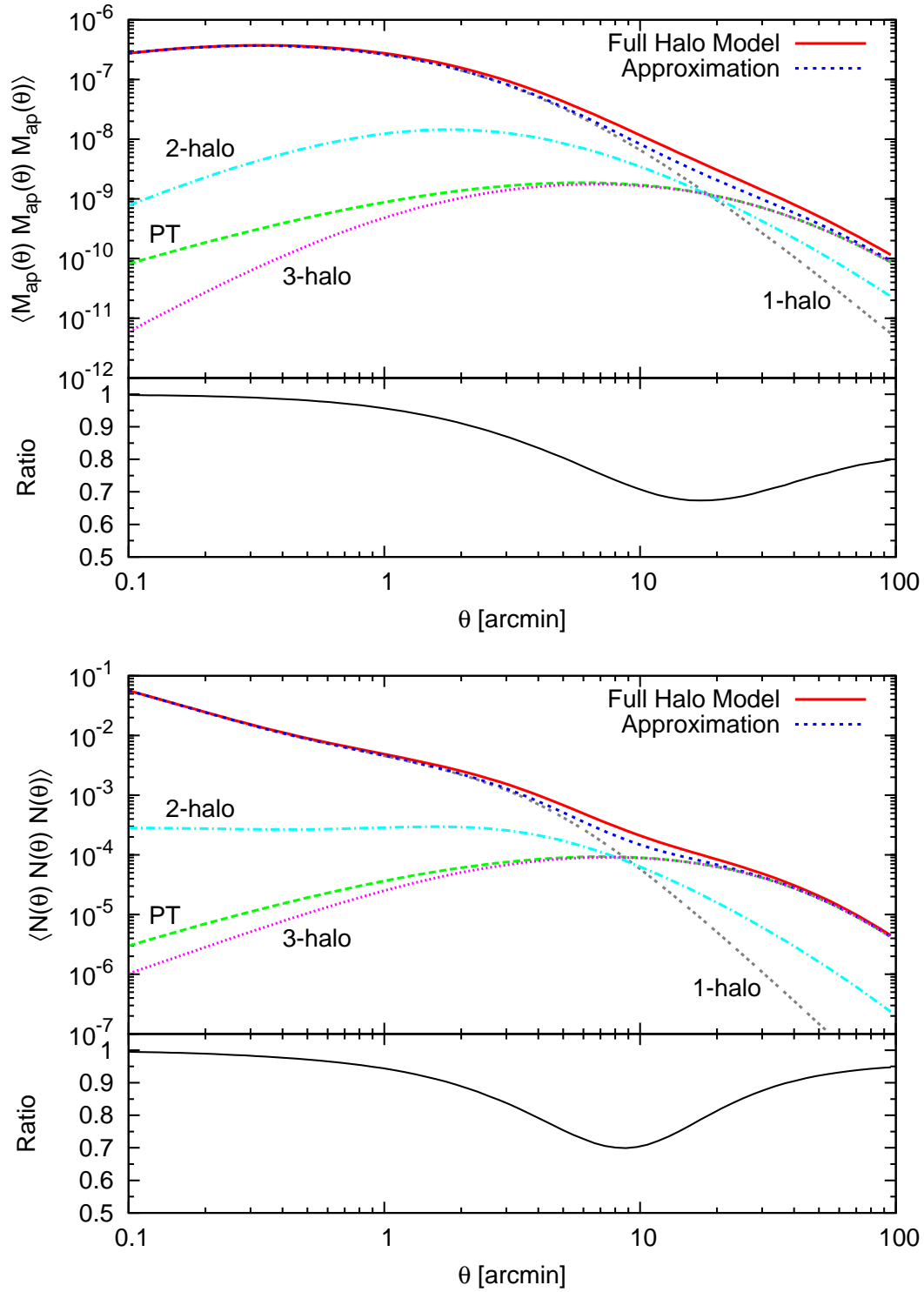
Figure 6.14: Aperture statistics $\langle M_{\mathrm{ap}} M_{\mathrm{ap}} M_{\mathrm{ap}} \rangle(\theta, \theta, \theta)$ (upper panel) and $\langle \mathcal{N}\mathcal{N}\mathcal{N} \rangle(\theta, \theta, \theta)$ (lower panel) as a function of the aperture radius θ. We included a concentration distribution for the calculation of the dark matter bispectrum with $\sigma_{\ln c} = 0.3$, and we assumed a minimal mass of $m_{\min} = 10^{11}\, h^{-1}\, M_\odot$. For details on the different lines and the ratios see caption of Fig. 6.13.
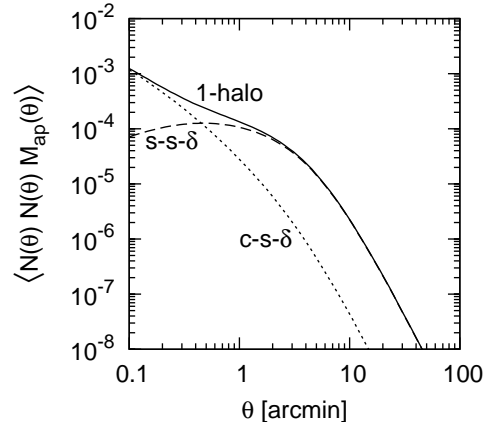
Figure 6.15: Contributions of the central-satellite-matter (c-s-δ) and satellite-satellite-matter (s-s-δ) correlations to the one-halo term of the galaxy-galaxy-mass aperture statistics as a function of aperture radius θ. Note that the one-halo term is the same as in the upper panel of Fig. 6.13.

$4 \lesssim \theta/\mathrm{arcmin} \lesssim 30$, the amplitudes of one-, two- and three-halo terms are comparable. Note that we see in this regime a small dip of the aperture statistics which is an effect of our missing modeling of halo exclusion. Finally, for large aperture radii ($\theta \gtrsim 30\,\mathrm{arcmin}$) the results are well described by the perturbation theory bispectrum (times corresponding factors of the large-scale bias parameter).

For a higher minimal mass $m_{\min}$ of the HOD, we also find a higher signal of the aperture statistics including galaxies (not shown). This is due to the fact that more galaxies are contained in more massive halos.

In the following we analyze the dependence of the galaxy-galaxy-mass and mass-mass galaxy aperture statistics which are probed by GGGL on specific assumptions made in the halo model. In particular, we study the behavior on variations of the first moment of satellite galaxies, a change of foreground and background redshifts, a modification of the radial galaxy distribution from the dark matter density profile and the inclusion of the color dependence of the HOD.

Variations in the first-order moment of satellite galaxies

In Fig. 6.16 we study the dependence of the cross-aperture statistics on the mean number of satellite galaxies populating a halo of mass m. The mean number can be described by a simple power law in halo mass with two parameters that determine the amplitude (fixed by A_s) and the slope (fixed by β) of the power law (for details see Eq. 4.14). Note that our fiducial choice of the parameters in the previous plots was $A_\mathrm{s} = 30$ and $\beta = 1$. We only allow for the variation of one parameter keeping the other fixed to its fiducial value. First of all, we find that $\langle \mathcal{N}\mathcal{N}M_\mathrm{ap} \rangle$ has a stronger dependence on variations of the HOD compared to $\langle M_\mathrm{ap}M_\mathrm{ap}\mathcal{N} \rangle$. This is due to the fact that the former has a stronger dependence on the HOD than the latter. For example the one-halo term of the galaxy-galaxy-mass bispectrum depends on the second-order moment of the HOD, whereas the mass-mass-galaxy bispectrum depends only on the first-order moment of the HOD. For large aperture radii all models approximately converge to the fiducial model since in this regime the three-halo term is dominant which shows only a small dependence on the HOD. An exception of this general trend is the $\beta = 1.2$
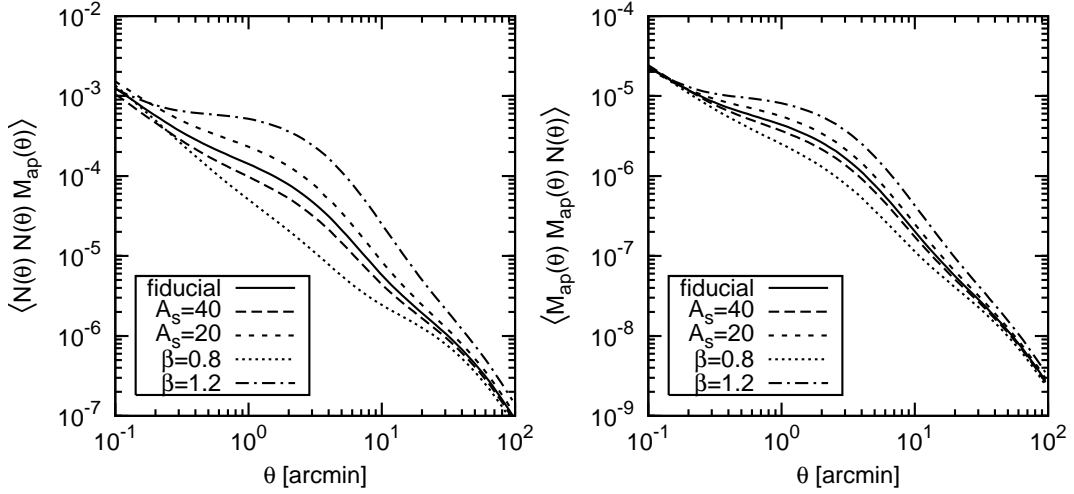
Figure 6.16: Dependence of the third-order aperture statistics on the two HOD parameters A_s and β that define the form of the first moment of satellite galaxies (see Eq. 4.14). We depict the fiducial model with $A_s = 30$ and $\beta = 1$. The curves show variations of either A_s and β keeping the other parameter fixed to the fiducial model. We show the effect on the galaxy-galaxy-mass (left panel) and the mass-mass-galaxy correlators (right panel) as a function of θ.

model. A higher value of β yields a stronger weighting of massive halo. In this case the one-halo term gives an important contributions to the aperture statistics up to larger radii (compared to a lower value of β) overcoming the strong reduction caused by the exponential decrease of the halo mass function. Thus, the transition of the one-halo term to the two- and three-halo terms occurs on larger scales. Also on the smallest depicted scales the curves approximately converge to the fiducial model since the one-halo terms are dominated by central galaxy correlations and thus show a weaker dependence on the mean number of satellites. Moreover, we see that a variation in A_s results in an off-set of the amplitude keeping the shape of the curve approximately fixed, whereas a variation in β changes the shape of the curve. A higher (smaller) value of β results in an enhancement (reduction) of the amplitude of the corresponding curves and additionally to a flatter (steeper) curve for the small-scale regime ($\theta \lesssim 3$ arcmin). In contrast to this behavior, we observe an enhancement (reduction) for a smaller (larger) value of the parameter A_s. A higher β gives more weight to more massive halos and thus the signal is enhanced. On the other hand, a higher A_s reduces the amplitude of the mean number of satellite galaxies and thus results in a reduction of the signal.

At $\theta \approx 2$ arcmin the difference between the amplitude of the $\beta = 0.8$ and $\beta = 1.2$ models is approximately two orders of magnitude for the galaxy-galaxy-mass aperture statistics (left panel). Hence, future observations of the GGGL signal should be able to distinguish between these two cases setting tight constraints on the shape of the first-order moment of the satellite HOD.

Influence of the redshift distributions

So far, we employed the redshift distribution of foreground galaxies as plotted in Fig. 6.1 and assumed a single source redshift. Here we want to explore the dependence of the aperture statistics on the redshift distribution analyzing three cases: an RCS-like survey with lenses in the redshift range $0 \leq z_l \leq 0.4$ and sources at a single redshift $z_s = 1$ which is our fiducial model, an SDSS-like survey with $0 \leq z_l \leq 0.2$ and $z_s = 0.4$, and a (hypothetical) future deep survey with $0 \leq z_l \leq 0.6$ and $z_s = 1.5$.

In Fig. 6.17 we give the results for the SDSS-like survey in the two left-hand panels and for the deep survey in the two right-hand panels. The upper panels depict the galaxy-galaxy-mass and the lower panels the mass-mass-galaxy aperture statistics. In each panel we show the contributions from the one-, two- and three-halo terms. The results should be compared to the relevant plots of the fiducial model depicted in Fig. 6.13. For $\langle \mathcal{N}\mathcal{N}M_{\mathrm{ap}} \rangle$ we get the surprising result that the signal is enhanced for the low-redshift survey and reduced for the high-redshift survey compared to the fiducial RCS-like survey. This is in contrast to $\langle M_{\mathrm{ap}}M_{\mathrm{ap}}\mathcal{N} \rangle$ where the signal is enhanced (reduced) for the high (low) redshift survey.

The origin of this behavior is that there are two competing effects if one lowers the redshifts: the smaller path-length reduces the lensing efficiency, whereas a given angle corresponds to a smaller length scale at the lens redshift which results in an enhancement of the signal. It depends on the redshift dependence of the bispectra and the redshift dependence of the weights in Limber's equation which of the two effects is stronger. This particular effect was mentioned in Jain et al. (2003). They studied, with a simple power-law toy model for the galaxy-matter cross-power spectrum, the effect on the angular quasar-galaxy cross-correlation function.

Radial distribution of galaxies

Up to now, we assumed for simplicity that the radial distribution of galaxies (galaxy density profile) follows exactly the dark matter density profile. However, results from simulations resolving subhalos and observations of galaxy groups and clusters find that the radial profile of the distribution of subhalos or galaxies is shallower than the dark matter density profile. For example Nagai & Kravtsov (2005), who performed NFW fits to 8 simulated clusters at redshift $z = 0$, find that the radial distribution of galaxies is described by a concentration parameter of $c_{\mathrm{gal}} \approx 2 - 3$, whereas the corresponding dark matter halos have $c_{\mathrm{dm}} \approx 10$. The difference between the two concentrations is explained by tidal stripping effects of the subhalos in the dense environment of cluster cores. Ongoing observational and theoretical work is needed to constrain the redshift and mass dependence on the concentration parameter for the radial distribution of galaxies. Hence, we consider only a variation of the amplitude of the NFW concentration parameter, which is given by the concentration-mass relation of the Bullock et al. (2001) parametrization given in Eq. (3.62). More specifically, we assume a concentration
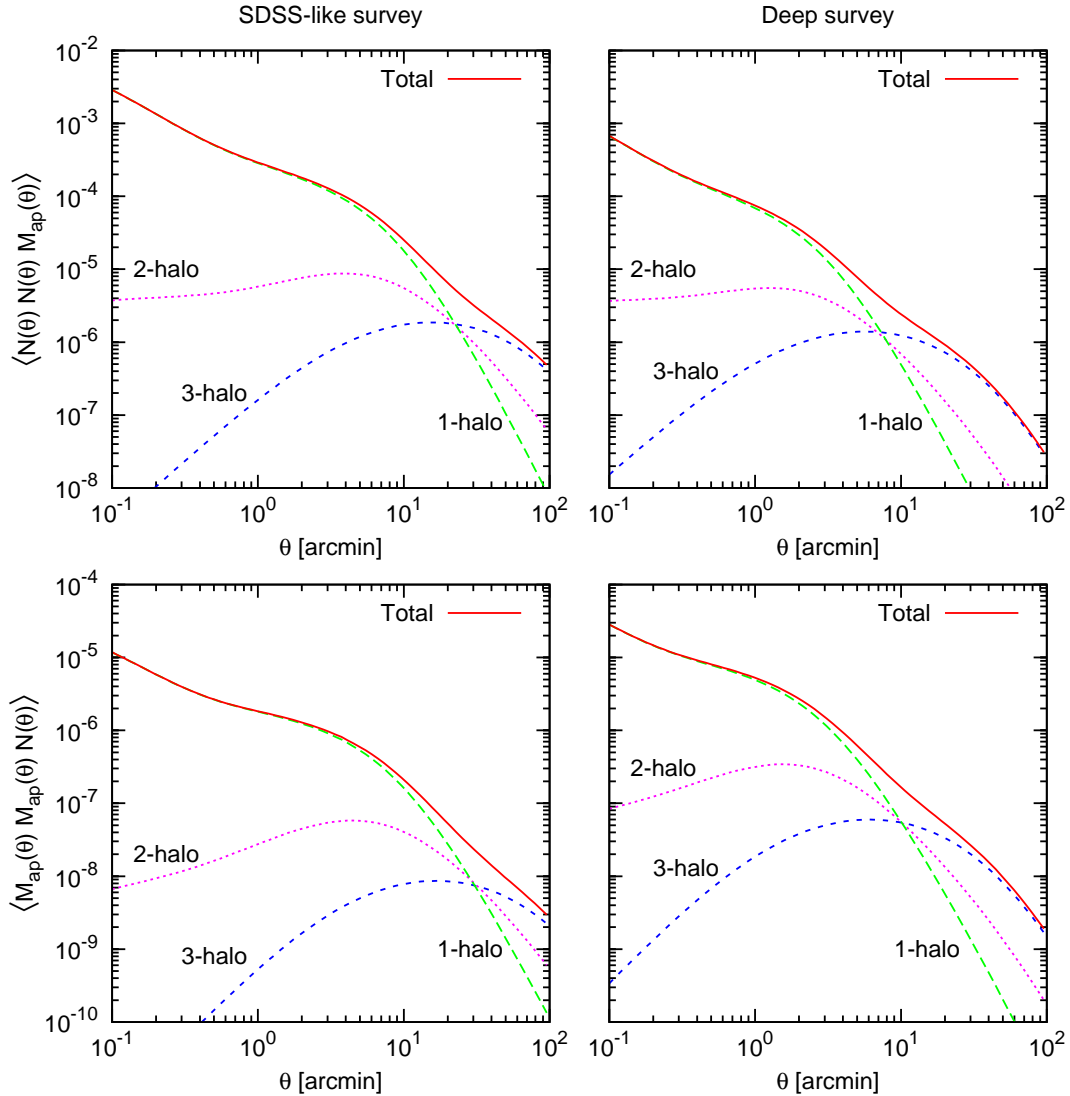
Figure 6.17: Influence of the redshift distribution of foreground and background galaxies on the galaxy-galaxy-mass (upper panels) and the mass-mass-galaxy aperture statistics (lower panels) as a function of the aperture radius θ. The left-hand panels present the results for the foreground redshift range of $0 \leq z_l \leq 0.2$ and a single background redshift at $z_s = 0.4$ (*SDSS-like survey*), whereas the right-hand panels use $0 \leq z_l \leq 0.6$ and $z_s = 1.5$ (*Deep survey*). We show the contributions of the three halo terms to the total aperture statistics.
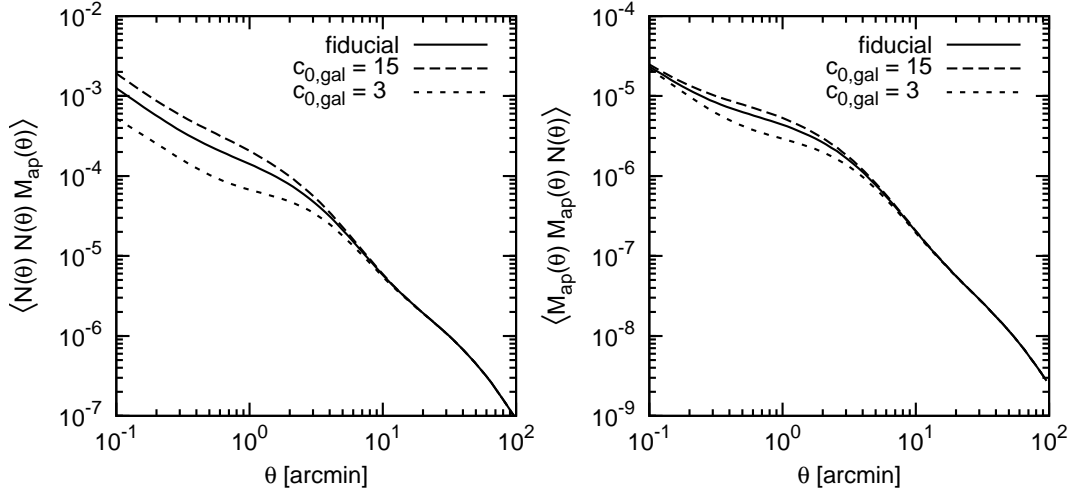
Figure 6.18: Variation of the radial galaxy distribution $\tilde{u}_{\rm g}$ parametrized by the concentration-mass relation from Bullock et al. (2001) which is a power law with two free parameters (see Eq. 6.62). We only show variations of the power-law amplitude $c_{0,{\rm gal}}$. We depict the fiducial model for comparison which assumes that galaxy and dark matter profiles are equal ($\tilde{u}_{\rm g} = \tilde{u}_{\rm dm}$) with $c_{0,{\rm gal}} = c_0 = 9$. In addition, we give the results for less concentrated profiles with $c_{0,{\rm gal}} = 3$ (short-dashed line) and more concentrated profiles with $c_{0,{\rm gal}} = 15$ (long-dashed line).

parameter relation of

$$c_{\rm gal}(m, z) = \frac{c_{0,{\rm gal}}}{1 + z} \left[\frac{m}{m_*(z = 0)} \right]^{-\alpha_{\rm gal}}, \qquad (6.62)$$

with the parameters $c_{0,{\rm gal}}$ and $\alpha_{\rm gal}$, and m_* is the nonlinear mass scale as defined in Eq. (3.31). We consider only variations in the amplitude $c_{0,{\rm gal}}$ keeping the power-law index fixed to the dark matter relation ($\alpha_{\rm gal} = \alpha$). The results are shown in Fig. 6.18 for the galaxy-galaxy-mass (left panel) and the mass-mass-galaxy (right panel) correlations as a function of θ. We consider a small ($c_{0,{\rm gal}} = 3$) and a large ($c_{0,{\rm gal}} = 15$) concentration parameter. For both aperture statistics we find that the signal is enhanced (reduced) for more (less) concentrated profiles. This is due to the fact that taking a more concentrated galaxy distribution, more galaxies are closer to the cluster center where the halo density is higher. For large scales all curves in the corresponding panel converge to the fiducial model since the density profile is 1 in this regime, i.e., $\tilde{u}(k \to 0, m) = 1$. Another feature that is worth mentioning is that the curves converge also on the smallest depicted scales for the mass-mass-galaxy signal in contrast to the galaxy-galaxy-mass signal. On these scales central galaxy correlations dominate the signal as shown for example in Fig. 6.15 for $\langle \mathcal{N}\mathcal{N}M_{\rm ap} \rangle$. Hence, the special case of $\langle M_{\rm ap}M_{\rm ap}\mathcal{N} \rangle$ is on the smallest scales independent of the radial distribution of galaxies since it is dominated by central-mass-mass correlations.
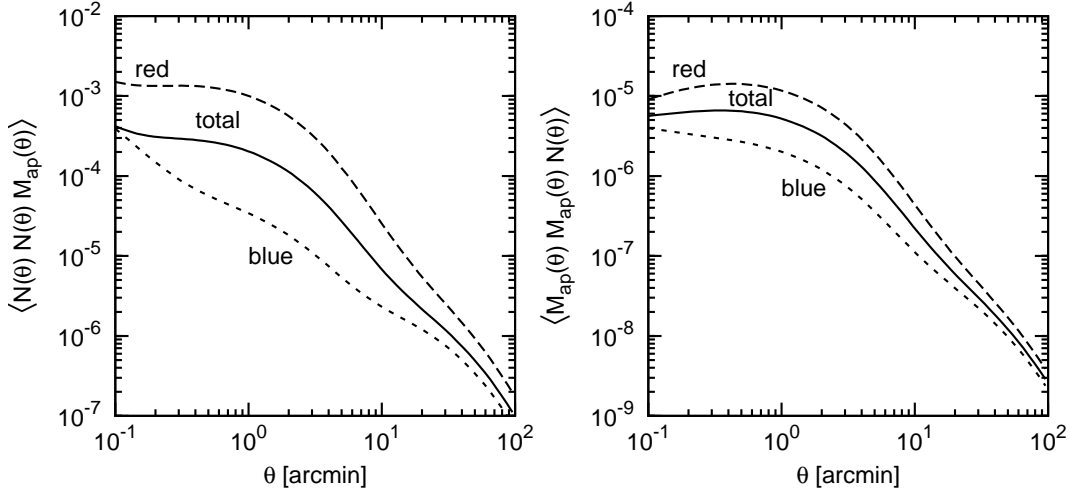
Figure 6.19: Dependence of the cross-aperture statistics on galaxy color. We give results for red galaxies (long-dashed line), blue galaxies (short-dashed line) and the sum of the HOD of both components (solid line).

Color dependence of the signal

We already discussed in Sect. 4.1.1 that different simulations and observations show that the form of the HOD is different for different galaxy colors. In the following we analyze the color dependence of the GGGL signal employing the parametrization of Sheth & Diaferio (2001) which divides the total HOD in individual contributions from red and blue galaxies (see Eq. 4.19). The halo mass dependence of this HOD was shown in Fig. 4.2. We found that in small-mass halos the mean number of blue galaxies is dominant. Furthermore, the mean number of blue galaxies is constant up to $4 \times 10^{12} \, h^{-1} \, M_\odot$. For higher masses it is a power law with spectral index $\alpha_{\rm b} = 0.8$. Red galaxies, on the other hand, have a steeper power law in halo mass ($\alpha_{\rm r} = 0.9$) and their mean number becomes dominant for masses larger than $2 \times 10^{12} \, h^{-1} \, M_\odot$. Hence, the mean number of galaxies in group- and cluster-sized halos are predominantly red galaxies as is also observationally established.

To calculate the second-order moment of the HOD, we use the ansatz of Eq. (4.10) as developed in Scoccimarro et al. (2001). This means that here we make an exception from using the Kravtsov et al. ansatz for the HOD which distinguishes between contributions from central and satellite galaxies. We do this mainly for simplicity since otherwise we have to model four HOD components, namely red and blue central and satellite galaxies.

The results are depicted in Fig. 6.19 for $\langle \mathcal{N} \mathcal{N} M_{\rm ap} \rangle$ (left panel) and for $\langle M_{\rm ap} M_{\rm ap} \mathcal{N} \rangle$ (right panel). First of all, we find that the signal of red galaxies is larger than for blue galaxies which is due to the fact that red galaxies are more strongly clustered as they preferentially reside in galaxy groups and clusters. This is also observationally measured, see e.g., the study of the galaxy two-point correlation function of red and blue galaxies
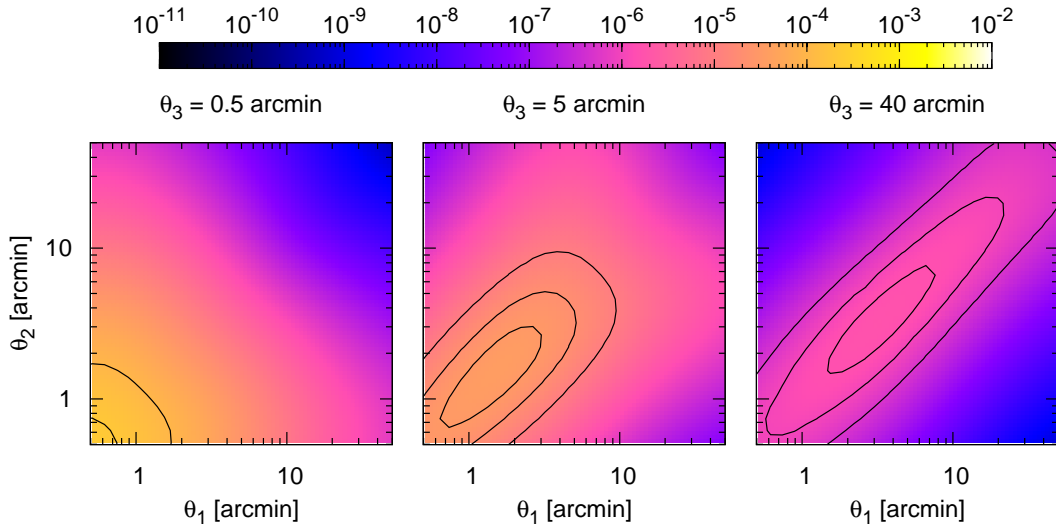
Figure 6.20: Contour plot of the configuration dependence of $\langle \mathcal{NN}M_{\mathrm{ap}}\rangle(\theta_1, \theta_2; \theta_3)$ as a function of θ_1 and θ_2 keeping θ_3 fixed to a value given above each panel. Note that the function is symmetric under exchanging θ_1 and θ_2. We employ the approximation (6.59) for the calculation of the galaxy-galaxy-mass bispectrum.

in the SDSS survey by Zehavi et al. (2005). In addition, we find that the variation of the curves is larger in the left-hand panel. As mentioned above, this is an effect of the stronger dependence of the galaxy-galaxy-mass signal on the moments of the HOD (it depends on the variance of the HOD, whereas the mass-mass-galaxy signal depends on the mean of the HOD). Furthermore, we note that the slope of the curves is steeper for blue galaxies and flatter for red galaxies on small scales compared to the sum of both HOD components. The signal for red galaxies is even decreasing for scales smaller than 1 arcmin in the right-hand panel. Moreover, we note that on large scales the curves in both panels approximately converge to a common curve. The strong variation of the curves are encouraging for getting constraints on HOD of different galaxy colors using fits to current and future observations.

Configuration dependence

The defined third-order aperture statistics in Eqs. (6.52), (6.55), (6.56) and (6.57) depend on three aperture radii. So far, we restricted our analysis of the aperture statistics to the "diagonal" case where $\theta_1 = \theta_2 = \theta_3$. However, the general case provides valuable and independent information on HOD models.

We study the configuration dependence of the two cross-aperture statistics in Fig. 6.20 for $\langle \mathcal{NN}M_{\mathrm{ap}}\rangle$ and in Fig. 6.21 for $\langle M_{\mathrm{ap}}M_{\mathrm{ap}}\mathcal{N}\rangle$. For each figure, we vary θ_1 and θ_2 keeping the value of θ_3 fixed to a specific value as indicated above each panel. We consider three values for θ_3 which roughly correspond to the regime of the one-halo term, the intermediate regime and the regime of the three-halo term (compare with
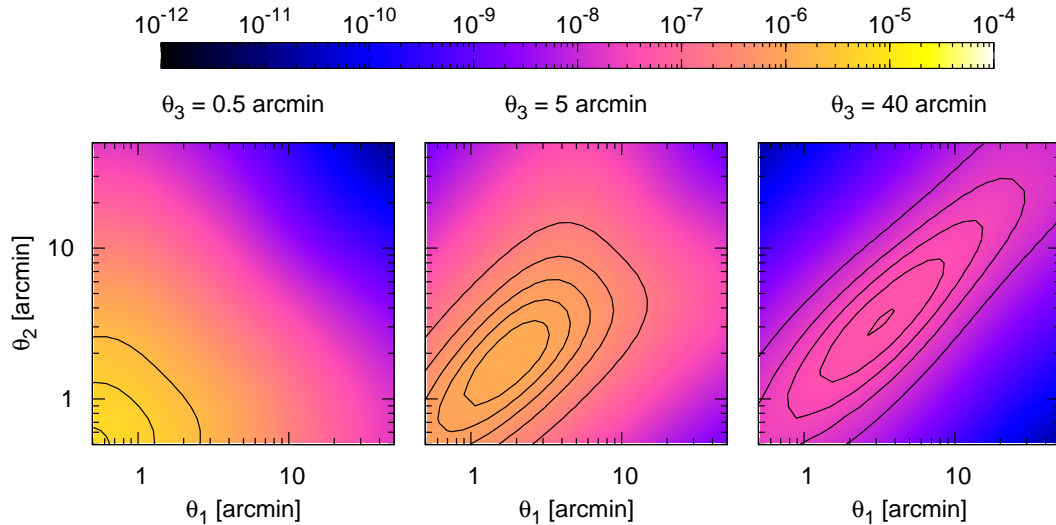
Figure 6.21: Contour plot of the configuration dependence of $\langle M_{\mathrm{ap}} M_{\mathrm{ap}} \mathcal{N} \rangle (\theta_1, \theta_2; \theta_3)$ as a function of θ_1 and θ_2 keeping θ_3 fixed to a value given above each panel. We employ the approximation (6.60) for the calculation of the mass-mass-galaxy bispectrum.

Fig. 6.13), namely $\theta_3 = 0.5$, $\theta_3 = 5$ and $\theta_3 = 40$ (depicted from left to right in both figures). To calculate the configuration dependence of the aperture statistics, we employ the approximations of the corresponding three-dimensional bispectra since we showed above that they maximally deviate by 30 per cent from the full halo model. We use a logarithmic color-coding of the amplitude since we cover a large range of scales in each figure. Hence, the difference between the full halo model and the approximation is too small to be visible in these plots. Note that the contours of both figures are symmetric with respect to θ_1 and θ_2 which reflect the symmetry properties of the two aperture statistics. We find for the galaxy-galaxy-mass and the mass-mass-galaxy function that enhancing θ_3 also moves the maximum of the aperture statistics to larger angular scales. In addition, we note that the signal of $\langle \mathcal{N} \mathcal{N} M_{\mathrm{ap}} \rangle$ is larger than $\langle M_{\mathrm{ap}} M_{\mathrm{ap}} \mathcal{N} \rangle$ as we found already in the diagonal case. We could now also study the dependence on HOD parameters for the general aperture statistics which could be done when measurements of the configuration dependence are available.

6.3 Projected Cross-Trispectrum

For the covariance of the GGL power spectrum estimator we need the projected dark matter-galaxy cross-trispectrum which is discussed in the next chapter. In particular we give in Eq. (7.73) an analytic expression of the covariance. Moreover, for the covariance of the convergence power spectrum we need the projected convergence trispectrum (see Eq. 7.61 below).
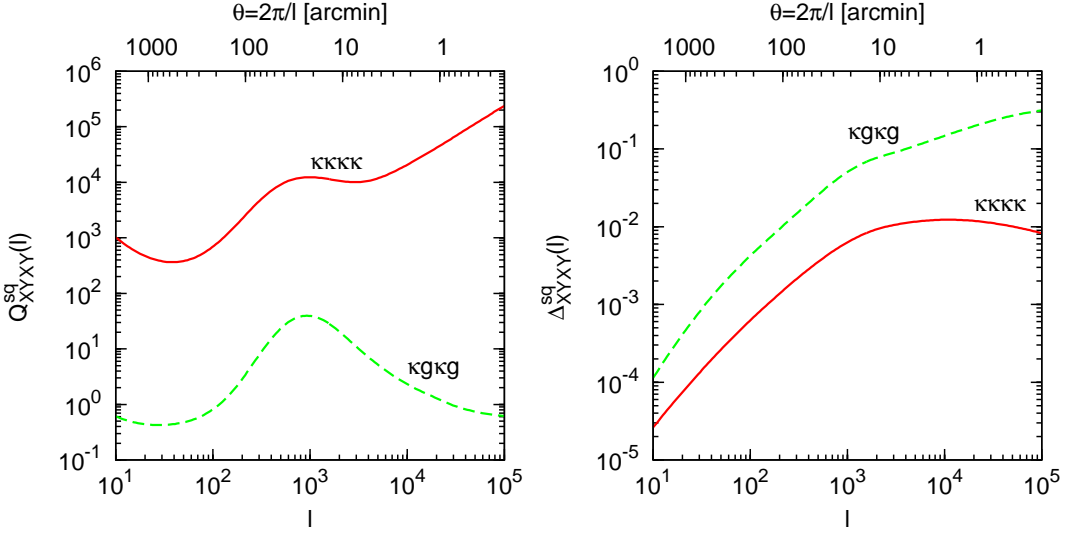
Figure 6.22: Reduced projected trispectra as a function of Fourier mode l for a square configuration (see text for details). We show the dark matter trispectrum (solid red line) and the cross-trispectrum (dashed green line). We use a minimal mass $m_{\min} = 10^{12} \, h^{-1} \, M_\odot$ for the HOD. On the left panel a higher (lower) threshold mass results in a reduction (enhancement) of the scale-dependence of the spectra including galaxies and the maximum is shifted to lower (higher) l.

The projected cross-trispectrum is defined by the four-point correlator

$$\langle \kappa(\boldsymbol{l}_1)\kappa_{\mathrm{g}}(\boldsymbol{l}_2)\kappa(\boldsymbol{l}_3)\kappa_{\mathrm{g}}(\boldsymbol{l}_4)\rangle_{\mathrm{c}} = (2\pi)^2 \delta_{\mathrm{D}}(\boldsymbol{l}_{1234}) T_{\kappa\mathrm{g}\kappa\mathrm{g}}(\boldsymbol{l}_1, \boldsymbol{l}_2, \boldsymbol{l}_3, \boldsymbol{l}_4) \tag{6.63}$$

with $\boldsymbol{l}_{1234} \equiv \boldsymbol{l}_1 + \boldsymbol{l}_2 + \boldsymbol{l}_3 + \boldsymbol{l}_4$. The projection of the three-dimensional cross-trispectrum $T_{\delta\mathrm{g}\delta\mathrm{g}}$ is obtained using Limber's approximation (5.65) which in this case is given by

$$T_{\kappa\mathrm{g}\kappa\mathrm{g}}(\boldsymbol{l}_1, \boldsymbol{l}_2, \boldsymbol{l}_3, \boldsymbol{l}_4) = \int_0^{w_{\mathrm{H}}} \mathrm{d}w \, \frac{G^2(w) p_{\mathrm{f}}^2(w)}{f_K^4(w)} T_{\delta\mathrm{g}\delta\mathrm{g}}(\boldsymbol{k}_1, \boldsymbol{k}_2, \boldsymbol{k}_3, \boldsymbol{k}_4; w) , \tag{6.64}$$

where $\boldsymbol{k}_i = \boldsymbol{l}_i/w$. An analogous expression was already defined for the convergence trispectrum in Eq. (5.71).

In accordance with the definition of the reduced three-dimensional cross-trispectrum, as given in Eqs. (4.95), (4.96) and (4.97), we define the projected cross-trispectrum $Q_{\kappa\mathrm{g}\kappa\mathrm{g}}$ by replacing the three-dimensional spectra in the equations by their projected counterparts. We do the same to define the convergence trispectrum $Q_{\kappa\kappa\kappa\kappa}$ following its three-dimensional counterpart in Eq. (4.99). Moreover, we define another dimensionless form of the trispectrum by $\Delta_{\mathrm{XYXY}}^{\mathrm{sq}}(l) \equiv l^2/(2\pi)[T_{\mathrm{XYXY}}(l, l, l, l)]^{1/3}$ where $(\mathrm{X,Y}) \in \{\kappa, \mathrm{g}\}$. Note that we assumed here the square configuration of the trispectrum.

We illustrate the two reduced trispectra as a function of l in Fig. 6.22, where we assumed a minimal mass of $m_{\min} = 10^{12} \, h^{-1} M_\odot$. In the left panel we depict $Q_{\mathrm{XYXY}}^{\mathrm{sq}}$ and in the right panel $\Delta_{\mathrm{XYXY}}^{\mathrm{sq}}$. Basically we get the same qualitative behavior as obtained

for the projected power spectra and bispectra. The difference between the two projected spectra is enhanced compared to the unprojected spectra. The right-hand panel shows that the cross-trispectrum is larger than the matter trispectrum, whereas this trend is reversed for the reduced trispectra depicted in the left-hand panel. The origin of this different behavior is that the galaxy power spectra in the denominator of the reduced cross-trispectrum are much larger than the convergence power spectra in the denominator of the reduced trispectrum (see Fig. 6.2).

6.4 Summary and Conclusions

In this chapter, we studied many aspects of GGL and GGGL using theoretical models of the nonlinear clustering of the continuous dark matter field and the discrete galaxy distribution. We showed that the observational signal of GGL probes the projected galaxy-mass cross-power spectrum and the signal of GGGL probes the projected mass-mass-galaxy and galaxy-galaxy-mass bispectra. Hence, for the predictions, we employed a combination of the dark matter halo model and the halo model for galaxy clustering as developed in Chapter 3 and Chapter 4.

First, we studied the *l*-dependence of the projected galaxy, galaxy-convergence cross and convergence power spectrum. To better illustrate the difference between the spectra, we introduced in analogy to the three-dimensional spectra a projected bias factor and correlation coefficient. We found that the difference between the spectra is enhanced compared to their three-dimensional counterparts which we explained by the different weight functions used in the projections (Limber's equations). Furthermore, on large scales the projected bias factor is a slowly decreasing function of *l* and thus does not converge to a constant.

Then we investigated real-space observables of GGL, namely the mean tangential shear and the excess surface mass density which are linearly related. We showed predictions for single foreground and background redshifts. In accordance to previous studies, we found that the two-halo term is only important for scales larger than $1\,h^{-1}\,\mathrm{Mpc}$. Most current experiments use only small to intermediate scales and thus one needs only a reliable model for the one-halo term. We showed that the one-halo term itself receives contributions from central galaxy-mass correlations which are dominant on the smallest scales and satellite galaxy-mass correlations which take over on larger scales. We did not introduce an additional parameter in our halo model for the fraction of galaxies which are part of group- and cluster-sized halos as is done for example in Guzik & Seljak (2002).

The main new results of this chapter are related to the modeling of the recently proposed GGGL signal which was already measured in the RCS field. We presented in detail the observables which are the galaxy-galaxy-shear and the shear-shear-galaxy three-point correlation functions. These are filtered versions of the corresponding projected cross-bispectra (shown in Schneider & Watts 2005). Hence, we studied in detail the properties of the projected bispectra. Again, we found that the difference between

the projected spectra is larger than the difference between their three-dimensional counterparts. We explained this fact by the different weight functions used in the projections. To further analyze the scale-dependence of the spectra, we introduced a projected third-order bias factor and two correlation coefficients which should fully encode the difference between dark matter and galaxy clustering. Since the bispectra depend on three different wave-vectors which build up a triangle in Fourier space, we investigated the configuration dependence of the two cross-bispectra in comparison to the galaxy and convergence bispectra.

We motivated that it is better to study third-order aperture statistics than the correlation functions since they allow for a clean separation of the cosmological signal (E-modes) and systematic effects (B-modes). This is the reason why we concentrated on analyzing the dependence of the galaxy-galaxy-mass and mass-mass-galaxy aperture statistics on specific assumptions made in the halo model. In particular, we studied the behavior on variations of the first moment of satellite galaxies, a change of foreground and background redshifts, a modification of the radial galaxy distribution from the dark matter density profile and the inclusion of the color dependence of the HOD. In general, we found that the variation of the considered parameters have a stronger effect on the galaxy-galaxy-mass than on the mass-mass-galaxy aperture statistics. This is due to the fact that the former depends on the second-order moment of the HOD, whereas the latter depends only on the first-order moment of the HOD. In addition, the galaxy-galaxy-mass statistics has also a stronger dependence on the radial distribution of galaxies. These distinct features of the two cross-aperture statistics can be used in future GGGL experiments to constrain the different galaxy formation models which is one of the key goals of modern cosmology. Our results could be used as input fitting functions to the data. Moreover, we computed the configuration dependence of the two cross-aperture statistics which provides more information than the diagonal term where the three aperture radii are equal. However, up to now observations of the GGGL signal have not utilized the full configuration dependence in their analyses.

We developed approximations of the three-dimensional bispectra which are composed of the one-halo terms which are dominant on small scales and the bispectrum in lowest-order perturbation theory which is dominant on large scales. To test this approach, we compared the approximations to the corresponding full halo model which includes the one-, two- and three-halo terms. In all cases, we showed that the deviation is maximally 30 per cent around 10 arcmin. This is because at intermediate scales the two-halo term gives a significant contribution to the signal. Up to $\theta \approx 2$ arcmin the deviation is smaller than 10 per cent. The approximations can be applied to computationally costly numerical calculations like the determination of the information content of the cross-aperture statistics which involves computing the covariance of a given bispectrum estimator.

Finally, we studied the scale dependence of the projected mass-galaxy-mass-galaxy trispectrum which determines the non-Gaussian part of the GGL covariance. This will be examined in detail in Chapter 7.

Chapter 7

Covariance of Galaxy-Galaxy Lensing Power Spectrum Estimator

Galaxy and weak lensing surveys measure correlation functions of galaxies and cosmic shear, respectively. The limited number of galaxies and their unknown intrinsic ellipticity induce statistical errors that hamper the determination of cosmological parameters, namely the so-called shot noise and shape noise. Moreover, the fact that cosmological experiments only use a finite patch of the sky to estimate statistical quantities like the power spectrum leads to an additional error source, the so-called *cosmic variance* or *sample variance* term. Both error sources enter in the covariance of the power spectrum estimator which is essential to calculate the likelihood function. These errors are inevitable also for the planned and ongoing large area surveys. But with increasing the number of galaxies or enlarging the survey area these errors will become smaller. Due to this effect the main emphasis for weak lensing studies is recently the quantification of systematic errors, for example the determination of intrinsic alignments of galaxies (Heymans & Heavens 2003; Hirata & Seljak 2004). However, we will not consider this complication here and focus on defining correlation function estimators. We show that the covariance of these estimators receives three different contributions, namely shape and shot noise and cosmic variance errors. The direct observables of the experiments are the real-space correlation functions whereas theoretical models are most easily expressed in terms of the corresponding spectra. Hence, we first construct real-space estimators which we then transform into Fourier space.

A simple way to determine the cosmic-variance dominated covariance from theoretical models is to assume that the corresponding (dark matter, galaxy, shear, etc.) field is Gaussian (e.g., Schneider et al. 2002 for cosmic shear). In this case the covariance of the power spectrum becomes diagonal and the amplitude is proportional to the power spectrum squared. However, galaxy and weak lensing experiments also use small scales to enhance their signal where this approximation will inevitably break down. It is thus important to determine the influence of non-Gaussianity on small scales.

The first theoretical study of the effect of the non-Gaussian density field on the error determination of cosmological parameters was done by Scoccimarro et al. (1999). They find an enhancement in the diagonal of the dark matter power spectrum covariance in combination with significant cross-correlations between small- and large-scale band

powers which is given by the dark matter trispectrum. To model the nonlinear regime, they applied the hierarchical ansatz for higher-order correlation functions (see Appendix B.4) which they also compared to the covariance as obtained from an ensemble of 20 numerical simulations. The comparison showed that the hierarchical ansatz does not accurately reproduce the configuration dependence of the trispectrum as determined in simulations. Furthermore, they generalized this concept to the covariance of the convergence power spectrum which tends to reduce the importance of non-Gaussian clustering due to projection effects. Following the main ideas of this work Eisenstein & Zaldarriaga (2001) use the hierarchical ansatz for higher-order moments to determine the covariance of the angular two-point correlation function of galaxies for the APM (Automated Plate Measuring) galaxy survey.

A significant improvement in the modeling of higher-order spectra is given in Cooray & Hu (2001) who applied the halo model of dark matter clustering to study the nonlinear regime. Their results are tested against results from simulations by Meiksin & White (1999) for the dark matter power spectrum covariance and the results from ray-tracing simulations given in White & Hu (2000) for the convergence power spectrum covariance. Both comparisons showed in general a good agreement which motivated subsequent semi-analytic studies to also adopt the halo model. Recently, Takada & Bridle (2007) provide estimates of the joint constraints of cluster counts and lensing power spectrum tomography modeling the full cross-covariance using the halo model. Moreover, Takada & Jain (2008) determine the covariance of the convergence power spectrum including the *beat-coupling effect* which was previously only studied in three-dimensional simulations (Rimes & Hamilton 2006). Beat-coupling is an effect due to the finite survey area (it induces a nonlinear coupling of products of closely spaced Fourier modes to a large-scale mode between them) which can enhance the amount of non-Gaussian errors. By using ray-tracing simulations Semboloni et al. (2007) determined the covariance of the two-point shear correlation functions and provided a fitting formula which reproduces the simulation results at 20 per cent accuracy for diagonal elements and becomes less accurate for off-diagonal elements. To achieve the goal of precise parameter forecasts, ongoing work on the determination of the covariance from simulations and theoretical models is mandatory.

In this chapter we combine the dark matter and galaxy halo model as developed in Chapter 3 and Chapter 4 to estimate the covariance for the projected galaxy-dark matter cross-power spectrum. The result can then be used to determine the errors of cosmological parameters estimated in galaxy-galaxy lensing surveys. The chapter is structured as follows: we derive unbiased estimators for the convergence power spectrum, galaxy power spectrum and cross-power spectrum in Sect. 7.1 and obtain their corresponding statistical noise contributions. To determine the non-Gaussian contribution of the covariance for the convergence and cross-power spectrum estimator, we define in Sect. 7.2 simplified estimators without shot- and shape-noise contributions.

7.1 **Estimator of the Power Spectrum**

We introduce the estimator of the convergence power spectrum in Sect. 7.1.1 and the estimator of the angular power spectrum of galaxies in Sect. 7.1.2, and show that their statistical noise is given by shape and shot noise, respectively. Combining the results from both sections, we construct an unbiased estimator for the projected cross-power spectrum in Sect. 7.1.3 and calculate the covariance matrix of this estimator. Note that we will distinguish from the start between background and foreground galaxies although it is only needed for the cross-power spectrum. Moreover, we employ throughout this section the Gaussian approximation for the sample variance of the covariance matrix and discuss the influence of a non-Gaussian part in the next section.

7.1.1 **Convergence Power Spectrum**

In this section we follow Joachimi et al. (2008) for the construction of the convergence power spectrum estimator. Let us consider a hypothetical survey where the measured data consists of N_{b} background galaxies at positions $\boldsymbol{\theta}_i$ contained in a field of area A with measured complex ellipticities

$$\epsilon(\boldsymbol{\theta}_i) = \epsilon_1(\boldsymbol{\theta}_i) + \mathrm{i}\epsilon_2(\boldsymbol{\theta}_i) \equiv \epsilon_{1,i} + \mathrm{i}\epsilon_{2,i}\,, \tag{7.1}$$

where we introduced the short notation $\epsilon_{\alpha,i} \equiv \epsilon_\alpha(\boldsymbol{\theta}_i)$ in the second step with $\alpha = 1, 2$ denoting the two ellipticity components. From the weak lensing limit we know that the galaxy ellipticity is the sum of shear and intrinsic ellipticity:

$$\epsilon_\alpha(\boldsymbol{\theta}_i) = \gamma_\alpha(\boldsymbol{\theta}_i) + \epsilon_\alpha^{\mathrm{s}}(\boldsymbol{\theta}_i)\,. \tag{7.2}$$

The ensemble average is

$$\langle \epsilon_\alpha(\boldsymbol{\theta}_i) \rangle = \langle \gamma_\alpha(\boldsymbol{\theta}_i) \rangle\,, \tag{7.3}$$

where the ensemble average of the second term in Eq. (7.2) vanishes because we assume that galaxies have a random intrinsic orientation. As we seek an estimator for the power spectrum, we need to transform Eq. (7.2) into Fourier space. Note that we need to apply the discrete Fourier transform because of the limited sample of ellipticity measurements:

$$\tilde{\epsilon}_\alpha(\boldsymbol{l}) = \sum_{i=1}^{N_{\mathrm{b}}} \epsilon_\alpha(\boldsymbol{\theta}_i)\mathrm{e}^{\mathrm{i}\boldsymbol{l}\cdot\boldsymbol{\theta}_i}\,, \tag{7.4}$$

where a tilde denotes the Fourier transformed quantity. Inserting Eq. (7.2), we find

$$\tilde{\epsilon}_\alpha(\boldsymbol{l}) = \int \mathrm{d}^2\theta\,\mathrm{e}^{\mathrm{i}\boldsymbol{l}\cdot\boldsymbol{\theta}}n(\boldsymbol{\theta})\gamma_\alpha(\boldsymbol{\theta}) + \sum_{i=1}^{N_{\mathrm{b}}} \epsilon_{\alpha,i}^{\mathrm{s}}\mathrm{e}^{\mathrm{i}\boldsymbol{l}\cdot\boldsymbol{\theta}_i}\,, \tag{7.5}$$

where the number density of background galaxies is

$$n(\boldsymbol{\theta}) = \sum_{i=1}^{N_{\mathrm{b}}} \delta_{\mathrm{D}}(\boldsymbol{\theta} - \boldsymbol{\theta}_i)\,. \tag{7.6}$$

Fourier transforming the shear field yields

$$\tilde{\epsilon}_\alpha(\boldsymbol{l}) = \int \frac{\mathrm{d}^2 l'}{(2\pi)^2} \, \tilde{\gamma}_\alpha(\boldsymbol{l}')\tilde{n}(\boldsymbol{l} - \boldsymbol{l}') + \sum_{i=1}^{N_\mathrm{b}} \epsilon_{\alpha,i}^\mathrm{s} \mathrm{e}^{\mathrm{i}\boldsymbol{l}\cdot\boldsymbol{\theta}_i} \,, \tag{7.7}$$

with

$$\tilde{n}(\boldsymbol{l}) = \int \mathrm{d}^2\theta \, n(\boldsymbol{\theta}) \mathrm{e}^{\mathrm{i}\boldsymbol{l}\cdot\boldsymbol{\theta}} = \sum_{i=1}^{N_\mathrm{b}} \mathrm{e}^{\mathrm{i}\boldsymbol{l}\cdot\boldsymbol{\theta}_i} \,, \tag{7.8}$$

where the definition of $n(\boldsymbol{\theta})$ (Eq. 7.6) is inserted in the second step. The ensemble average of the estimator in Eq. (7.7) splits into an average over the intrinsic ellipticities and an average over the galaxy positions. We assume for simplicity that the background galaxies are randomly distributed in space[1]. In this case, the ensemble average E[] of the number density is obtained by an average over all N_b galaxy positions $\boldsymbol{\theta}_j$:

$$\mathrm{E}[n(\boldsymbol{\theta})] \equiv \left[\prod_{j=1}^{N_\mathrm{b}} \int \mathrm{d}^2\theta_j \right] p(\boldsymbol{\theta}_1, \ldots, \boldsymbol{\theta}_{N_\mathrm{b}}) \, n(\boldsymbol{\theta})$$

$$= \prod_{j=1}^{N_\mathrm{b}} \left[\frac{1}{A} \int \mathrm{d}^2\theta_j \right] \sum_{i=1}^{N_\mathrm{b}} \delta_\mathrm{D}(\boldsymbol{\theta} - \boldsymbol{\theta}_i) = \frac{N_\mathrm{b}}{A} = \bar{n} \,, \tag{7.9}$$

where we used in the second step that the joint PDF resolves into a product of individual PDFs, each giving $p(\boldsymbol{\theta}_j) = 1/A$ for uncorrelated galaxies. In the last step, we defined the mean number density of background galaxies in the field $\bar{n}$. Furthermore, we assumed a simple field geometry, namely a connected field where all relevant angles are smaller than the extent of the field, i.e., $|\boldsymbol{\theta}|^2 \ll A$. For this approximation we find $\tilde{n}(\boldsymbol{l}) = (2\pi)^2 \delta_\mathrm{D}(\boldsymbol{l}) \, \bar{n}$ using Eq. (7.8). The final result for the estimator of galaxy ellipticities in Fourier space is

$$\tilde{\epsilon}_\alpha(\boldsymbol{l}) = \bar{n}\tilde{\gamma}_\alpha(\boldsymbol{l}) + \sum_{i=1}^{N_\mathrm{b}} \epsilon_{\alpha,i}^\mathrm{s} \mathrm{e}^{\mathrm{i}\boldsymbol{l}\cdot\boldsymbol{\theta}_i} \,. \tag{7.10}$$

For the discussion of the covariance matrix we need the intrinsic ellipticity dispersion

$$\langle \epsilon_i^\mathrm{s} \epsilon_j^{\mathrm{s}*} \rangle = \delta_{ij}\sigma_\epsilon^2 \,, \qquad \langle \epsilon_i^\mathrm{s} \epsilon_j^\mathrm{s} \rangle = 0 \,. \tag{7.11}$$

The first relation states that intrinsic ellipticities at different positions are uncorrelated. The second relation vanishes due to the assumed isotropy of the Universe, as a non-vanishing result would yield a net orientation of galaxies. Using the individual components of the ellipticities, we deduce from the two relations above

$$\langle \epsilon_{\alpha,i}^\mathrm{s} \epsilon_{\beta,j}^\mathrm{s} \rangle = \delta_{ij}\delta_{\alpha\beta}\frac{\sigma_\epsilon^2}{2} \,. \tag{7.12}$$

---

[1]This ceases to be valid for the foreground galaxies which are correlated.

The Kaiser-Squires relation provides the connection between the cosmic shear and the convergence field (also see the discussion in Sect. 5.1.6). In Fourier space it is given by

$$\tilde{\gamma}(\boldsymbol{l}) = e^{2i\beta}\tilde{\kappa}(\boldsymbol{l}) , \qquad (7.13)$$

where β is the polar angle of the Fourier mode vector $\boldsymbol{l}$. To include B-modes we write the convergence as a complex quantity, i.e., $\tilde{\kappa}(\boldsymbol{l}) = \tilde{\kappa}_{\mathrm{E}}(\boldsymbol{l}) + i\tilde{\kappa}_{\mathrm{B}}(\boldsymbol{l})$, where $\tilde{\kappa}_{\mathrm{E}}$ is the curl-free E-mode and $\tilde{\kappa}_{\mathrm{B}}$ is the divergence-free B-mode. We obtain

$$\tilde{\kappa}_{\mathrm{E}}(\boldsymbol{l}) = \tilde{\gamma}_1(\boldsymbol{l})\cos(2\beta) + \tilde{\gamma}_2(\boldsymbol{l})\sin(2\beta) , \qquad (7.14)$$

$$\tilde{\kappa}_{\mathrm{B}}(\boldsymbol{l}) = -\tilde{\gamma}_1(\boldsymbol{l})\sin(2\beta) + \tilde{\gamma}_2(\boldsymbol{l})\cos(2\beta) , \qquad (7.15)$$

and define their correlation functions

$$\langle\tilde{\kappa}_{\mathrm{E}}(\boldsymbol{l})\tilde{\kappa}_{\mathrm{E}}^*(\boldsymbol{l}')\rangle = (2\pi)^2\delta_{\mathrm{D}}(\boldsymbol{l}-\boldsymbol{l}')P_{\mathrm{E}}(l) , \qquad (7.16)$$

$$\langle\tilde{\kappa}_{\mathrm{B}}(\boldsymbol{l})\tilde{\kappa}_{\mathrm{B}}^*(\boldsymbol{l}')\rangle = (2\pi)^2\delta_{\mathrm{D}}(\boldsymbol{l}-\boldsymbol{l}')P_{\mathrm{B}}(l) , \qquad (7.17)$$

$$\langle\tilde{\kappa}_{\mathrm{E}}(\boldsymbol{l})\tilde{\kappa}_{\mathrm{B}}^*(\boldsymbol{l}')\rangle = (2\pi)^2\delta_{\mathrm{D}}(\boldsymbol{l}-\boldsymbol{l}')P_{\mathrm{EB}}(l) . \qquad (7.18)$$

The cross-power spectrum P_{EB} vanishes when assuming parity invariance of the Universe. With the tools developed, we construct the estimators for the E-mode and B-mode power spectra. They are given by

$$\hat{P}_{\mathrm{E}}(\bar{l}) = \left[\frac{1}{\bar{n}^2 A A_{\mathrm{r}}(\bar{l})}\int_{A_{\mathrm{r}}(\bar{l})}\mathrm{d}^2l\,|\hat{\kappa}_{\mathrm{E}}(\boldsymbol{l})|^2\right] - \frac{\sigma_\epsilon^2}{2\bar{n}} , \qquad (7.19)$$

$$\hat{P}_{\mathrm{B}}(\bar{l}) = \left[\frac{1}{\bar{n}^2 A A_{\mathrm{r}}(\bar{l})}\int_{A_{\mathrm{r}}(\bar{l})}\mathrm{d}^2l\,|\hat{\kappa}_{\mathrm{B}}(\boldsymbol{l})|^2\right] - \frac{\sigma_\epsilon^2}{2\bar{n}} , \qquad (7.20)$$

where we introduced the estimators

$$\hat{\kappa}_{\mathrm{E}}(\boldsymbol{l}) = \tilde{\epsilon}_1(\boldsymbol{l})\cos(2\beta) + \tilde{\epsilon}_2(\boldsymbol{l})\sin(2\beta) , \qquad (7.21)$$

$$\hat{\kappa}_{\mathrm{B}}(\boldsymbol{l}) = -\tilde{\epsilon}_1(\boldsymbol{l})\sin(2\beta) + \tilde{\epsilon}_2(\boldsymbol{l})\cos(2\beta) . \qquad (7.22)$$

One easily verifies that the ensemble average of both estimators is given by $\langle\hat{\kappa}_{\mathrm{E(B)}}(\boldsymbol{l})\rangle = \bar{n}\tilde{\kappa}_{\mathrm{E(B)}}(\boldsymbol{l})$ by inserting the ellipticity estimators defined in Eq. (7.10) and the fact that the ensemble average of intrinsic ellipticities is equal to zero. The estimators of the power spectra are constructed by averaging over annuli with mean radius $\bar{l}$ and area $A_{\mathrm{r}}(\bar{l}) = 2\pi\bar{l}\Delta l$, where Δl denotes the bin-width. These are unbiased estimators as we show explicitly for the E-mode power spectrum. After rewriting the estimator in Eq. (7.21) as

$$\hat{\kappa}_{\mathrm{E}}(\boldsymbol{l}) = \bar{n}\tilde{\kappa}_{\mathrm{E}}(\boldsymbol{l}) + \left(\sum_{i=1}^{N_{\mathrm{b}}}\epsilon_{1,i}^{\mathrm{s}}e^{i\boldsymbol{l}\cdot\boldsymbol{\theta}_i}\right)\cos(2\beta) + \left(\sum_{j=1}^{N_{\mathrm{b}}}\epsilon_{2,j}^{\mathrm{s}}e^{i\boldsymbol{l}\cdot\boldsymbol{\theta}_j}\right)\sin(2\beta) , \qquad (7.23)$$

we get for the correlator of the integrand in Eq. (7.19)

$$\langle|\hat{\kappa}_{\mathrm{E}}(\boldsymbol{l})|^2\rangle = \bar{n}^2\langle\tilde{\kappa}_{\mathrm{E}}(\boldsymbol{l})\tilde{\kappa}_{\mathrm{E}}^*(\boldsymbol{l})\rangle + N_{\mathrm{b}}\frac{\sigma_\epsilon^2}{2} , \qquad (7.24)$$

where we used the properties of the intrinsic ellipticity correlator given in Eq. (7.12). Finally, we find

$$
\begin{aligned}
\langle \hat{P}_{\mathrm{E}}(\bar{l}) \rangle &= \frac{1}{A A_{\mathrm{r}}(\bar{l})} \int_{A_{\mathrm{r}}(\bar{l})} \mathrm{d}^2 l \, \langle \tilde{\kappa}_{\mathrm{E}}(\boldsymbol{l}) \tilde{\kappa}_{\mathrm{E}}(-\boldsymbol{l}) \rangle \\
&= \frac{(2\pi)^2}{A A_{\mathrm{r}}(\bar{l})} \int_{A_{\mathrm{r}}(\bar{l})} \mathrm{d}^2 l \, \delta_{\mathrm{D}}(\mathbf{0}) P_{\mathrm{E}}(l) = P_{\mathrm{E}}(\bar{l}) ,
\end{aligned}
\tag{7.25}
$$

which proves that the estimator is unbiased for small bin sizes. Additionally, the correspondence of the Dirac delta distribution function for a finite field size A was used for the derivation, namely $\delta_{\mathrm{D}}(\mathbf{0}) = A/(2\pi)^2$.

In order to find an expression for the covariance of the cross-power spectrum we also need the two-point correlator for E- and B-mode spectra at different scales (see Eq. 7.42 below). By using the estimator of $\hat{\kappa}_{\mathrm{E}}$ in Eq. (7.23) we find for the E-mode

$$
\begin{aligned}
\langle \hat{\kappa}_{\mathrm{E}}(\boldsymbol{l}) \hat{\kappa}_{\mathrm{E}}^*(\boldsymbol{l}') \rangle &= \bar{n}^2 \langle \tilde{\kappa}_{\mathrm{E}}(\boldsymbol{l}) \tilde{\kappa}_{\mathrm{E}}^*(\boldsymbol{l}') \rangle + \frac{\sigma_\epsilon^2}{2} \left(\sum_{i=1}^{N_{\mathrm{b}}} \mathrm{e}^{\mathrm{i}(\boldsymbol{l}-\boldsymbol{l}') \cdot \boldsymbol{\theta}_i} \right) \\
&= (2\pi)^2 \delta_{\mathrm{D}}(\boldsymbol{l} - \boldsymbol{l}') \bar{n}^2 \left[P_{\mathrm{E}}(l) + \frac{\sigma_\epsilon^2}{2\bar{n}} \right] .
\end{aligned}
\tag{7.26}
$$

In complete analogy we find the B-mode two-point correlator. Thus, the final result is

$$
\langle \hat{\kappa}_{\mathrm{X}}(\boldsymbol{l}) \hat{\kappa}_{\mathrm{X}}^*(\boldsymbol{l}') \rangle = (2\pi)^2 \delta_{\mathrm{D}}(\boldsymbol{l} - \boldsymbol{l}') \bar{n}^2 \left[P_{\mathrm{X}}(l) + \frac{\sigma_\epsilon^2}{2\bar{n}} \right] ,
\tag{7.27}
$$

for $\mathrm{X} = \{\mathrm{E}, \mathrm{B}\}$. The last term in squared brackets originates from the intrinsic ellipticity dispersion and is mnemonically called *shape noise*.

7.1.2 Galaxy Power Spectrum

The estimator for the foreground galaxies in real space is simply

$$
\hat{N}(\boldsymbol{\theta}) = \sum_{i=1}^{N_{\mathrm{f}}} \delta_{\mathrm{D}}(\boldsymbol{\theta} - \boldsymbol{\theta}_i) ,
\tag{7.28}
$$

where $\boldsymbol{\theta}_i$ is the i-th *foreground* galaxy position and N_{f} is the number of *foreground* galaxies. Accordingly, the fractional density contrast estimator is

$$
\hat{\kappa}_{\mathrm{g}}(\boldsymbol{\theta}) = \frac{\hat{N}(\boldsymbol{\theta}) - \bar{N}}{\bar{N}} .
\tag{7.29}
$$

Here caution is advisable to distinguish between the number density of background galaxies denoted by $\bar{n}$ and the number density of foreground galaxies denoted by $\bar{N}$. Transforming this relation into Fourier space yields

$$
\hat{\kappa}_{\mathrm{g}}(\boldsymbol{l}) = \int \mathrm{d}^2\theta \, \mathrm{e}^{\mathrm{i}\boldsymbol{l}\cdot\boldsymbol{\theta}} \, \hat{\kappa}_{\mathrm{g}}(\boldsymbol{\theta}) = \frac{\tilde{N}(\boldsymbol{l})}{\bar{N}} - (2\pi)^2 \delta_{\mathrm{D}}(\boldsymbol{l}) = \frac{1}{\bar{N}} \sum_{i=1}^{N_{\mathrm{f}}} \mathrm{e}^{\mathrm{i}\boldsymbol{l}\cdot\boldsymbol{\theta}_i} - (2\pi)^2 \delta_{\mathrm{D}}(\boldsymbol{l}) ,
\tag{7.30}
$$

where $\tilde{N}(\boldsymbol{l})$ is the Fourier space counterpart of $\hat{N}(\boldsymbol{\theta})$. The two-point correlator is then

$$
\langle \hat{\kappa}_{\mathrm{g}}(\boldsymbol{l}) \hat{\kappa}_{\mathrm{g}}^*(\boldsymbol{l}') \rangle = \frac{1}{\bar{N}^2} \left[\sum_{i=1}^{N_{\mathrm{f}}} \langle \mathrm{e}^{\mathrm{i}(\boldsymbol{l}-\boldsymbol{l}')\cdot\boldsymbol{\theta}_i} \rangle + \sum_{i \neq j}^{N_{\mathrm{f}}} \langle \mathrm{e}^{\mathrm{i}\boldsymbol{l}\cdot\boldsymbol{\theta}_i} \mathrm{e}^{-\mathrm{i}\boldsymbol{l}'\cdot\boldsymbol{\theta}_j} \rangle \right] - \frac{(2\pi)^2}{\bar{N}} \delta_{\mathrm{D}}(\boldsymbol{l}) \sum_{i=1}^{N_{\mathrm{f}}} \langle \mathrm{e}^{-\mathrm{i}\boldsymbol{l}'\cdot\boldsymbol{\theta}_i} \rangle
$$

$$
- \frac{(2\pi)^2}{\bar{N}} \delta_{\mathrm{D}}(\boldsymbol{l}') \sum_{i=1}^{N_{\mathrm{f}}} \langle \mathrm{e}^{\mathrm{i}\boldsymbol{l}\cdot\boldsymbol{\theta}_i} \rangle + (2\pi)^4 \delta_{\mathrm{D}}(\boldsymbol{l}) \delta_{\mathrm{D}}(\boldsymbol{l}') \,, \tag{7.31}
$$

where we split the double sum into parts where $i = j$ and where $i \neq j$ in the first step. For the derivation of the correlator we use the identities:

$$
\langle \mathrm{e}^{\mathrm{i}\boldsymbol{l}\cdot\boldsymbol{\theta}_i} \rangle = \left(\prod_{j=1}^{N_{\mathrm{f}}} \int \frac{\mathrm{d}^2\theta_j}{A} \right) \mathrm{e}^{\mathrm{i}\boldsymbol{l}\cdot\boldsymbol{\theta}_i} = \frac{(2\pi)^2}{A} \delta_{\mathrm{D}}(\boldsymbol{l}) \,, \tag{7.32}
$$

$$
\langle \mathrm{e}^{\mathrm{i}\boldsymbol{l}\cdot\boldsymbol{\theta}_i} \mathrm{e}^{-\mathrm{i}\boldsymbol{l}'\cdot\boldsymbol{\theta}_j} \rangle = \int \frac{\mathrm{d}^2\theta_i}{A} \int \frac{\mathrm{d}^2\theta_j}{A} [1 + w(\boldsymbol{\theta}_i, \boldsymbol{\theta}_j)] \mathrm{e}^{\mathrm{i}\boldsymbol{l}\cdot\boldsymbol{\theta}_i} \mathrm{e}^{-\mathrm{i}\boldsymbol{l}'\cdot\boldsymbol{\theta}_j}
$$

$$
= \int \frac{\mathrm{d}^2\theta_i}{A} \mathrm{e}^{\mathrm{i}\boldsymbol{l}\cdot\boldsymbol{\theta}_i} \int \frac{\mathrm{d}^2\theta_j}{A} \mathrm{e}^{-\mathrm{i}\boldsymbol{l}'\cdot\boldsymbol{\theta}_j} + \int \frac{\mathrm{d}^2\theta_i}{A} \mathrm{e}^{\mathrm{i}(\boldsymbol{l}-\boldsymbol{l}')\cdot\boldsymbol{\theta}_i} \int \frac{\mathrm{d}^2r}{A} w(r) \mathrm{e}^{-\mathrm{i}\boldsymbol{l}'\cdot\boldsymbol{r}}
$$

$$
= \frac{(2\pi)^4}{A^2} \delta_{\mathrm{D}}(\boldsymbol{l}) \delta_{\mathrm{D}}(\boldsymbol{l}') + \frac{(2\pi)^2}{A^2} \delta_{\mathrm{D}}(\boldsymbol{l}-\boldsymbol{l}') P_{\mathrm{gg}}(l) \,, \tag{7.33}
$$

where $w(\boldsymbol{\theta}_i, \boldsymbol{\theta}_j)$ denotes the angular galaxy two-point correlation function which is related to the angular galaxy power spectrum by

$$
P_{\mathrm{gg}}(l) = \int \mathrm{d}^2r \, w(r) \mathrm{e}^{-\mathrm{i}\boldsymbol{l}\cdot\boldsymbol{r}} \,. \tag{7.34}
$$

We assumed in this expression that the correlation function is homogeneous and isotropic such that it only depends on $r = |\boldsymbol{\theta}_j - \boldsymbol{\theta}_i|$. In the second step of Eq. (7.33) we performed a change of variables to $\boldsymbol{r} = \boldsymbol{\theta}_j - \boldsymbol{\theta}_i$. The correlator (7.31) finally becomes in the limit of a large number of foreground galaxies ($N_{\mathrm{f}} \gg 1$)

$$
\langle \hat{\kappa}_{\mathrm{g}}(\boldsymbol{l}) \hat{\kappa}_{\mathrm{g}}^*(\boldsymbol{l}') \rangle = (2\pi)^2 \delta_{\mathrm{D}}(\boldsymbol{l}-\boldsymbol{l}') \left[P_{\mathrm{gg}}(l) + \frac{1}{\bar{N}} \right] \,. \tag{7.35}
$$

The second term is the so-called *shot noise* which is a result of the finite number of galaxies in the field. We can now define analogously to the E-mode convergence power spectrum estimator given in Eq. (7.19) an estimator of the angular power spectrum of galaxies by

$$
\hat{P}_{\mathrm{gg}}(\bar{l}) = \left[\frac{1}{A A_{\mathrm{r}}(\bar{l})} \int_{A_{\mathrm{r}}(\bar{l})} \mathrm{d}^2l \, |\hat{\kappa}_{\mathrm{g}}(\boldsymbol{l})|^2 \right] - \frac{1}{\bar{N}} \,. \tag{7.36}
$$

and we can show that the estimator is unbiased, i.e. $\langle \hat{P}_{\mathrm{gg}}(\bar{l}) \rangle = P_{\mathrm{gg}}(\bar{l})$, by applying Eq. (7.35) for the two-point correlator. This is a simple form of the galaxy power spectrum estimator since a more realistic approach requires to include finite-field effects (such as the survey window function), selection effects and weights (e.g., Feldman et al. 1994).

7.1.3 Galaxy-Galaxy Lensing Power Spectrum

In analogy to the definition of the three convergence power spectra in Eqs. (7.16), (7.17) and (7.18), one defines the E- and B-mode cross-power spectrum between the convergence and the fractional density contrast which we defined in Eq. (6.6) as

$$\langle \tilde{\kappa}_{\mathrm{E}}(\boldsymbol{l})\tilde{\kappa}_{\mathrm{g}}^*(\boldsymbol{l}')\rangle = (2\pi)^2 \delta_{\mathrm{D}}(\boldsymbol{l}-\boldsymbol{l}')P_{\kappa\mathrm{g}}^{\mathrm{E}}(\boldsymbol{l})\,, \tag{7.37}$$

$$\langle \tilde{\kappa}_{\mathrm{B}}(\boldsymbol{l})\tilde{\kappa}_{\mathrm{g}}^*(\boldsymbol{l}')\rangle = (2\pi)^2 \delta_{\mathrm{D}}(\boldsymbol{l}-\boldsymbol{l}')P_{\kappa\mathrm{g}}^{\mathrm{B}}(\boldsymbol{l})\,. \tag{7.38}$$

The second correlator defines a parity violating mode. Therefore, measurements of $P_{\kappa\mathrm{g}}^{\mathrm{B}}$ allow us to check for systematic effects in the data. Inspired by the previous two sections, we introduce the two cross-power spectrum estimators

$$\hat{P}_{\kappa\mathrm{g}}^{\mathrm{E}}(\bar{l}) = \frac{1}{\bar{n}AA_{\mathrm{r}}(\bar{l})}\int_{A_{\mathrm{r}}(\bar{l})} \mathrm{d}^2l\,\hat{\kappa}_{\mathrm{E}}(\boldsymbol{l})\hat{\kappa}_{\mathrm{g}}^*(\boldsymbol{l})\,, \tag{7.39}$$

$$\hat{P}_{\kappa\mathrm{g}}^{\mathrm{B}}(\bar{l}) = \frac{1}{\bar{n}AA_{\mathrm{r}}(\bar{l})}\int_{A_{\mathrm{r}}(\bar{l})} \mathrm{d}^2l\,\hat{\kappa}_{\mathrm{B}}(\boldsymbol{l})\hat{\kappa}_{\mathrm{g}}^*(\boldsymbol{l})\,. \tag{7.40}$$

In analogy to the convergence power spectrum estimator in Eq. (7.25) we can show that both estimators are unbiased.

The final goal is to calculate the covariance matrix of the cross-power spectrum which is defined by

$$\mathcal{C}\left[\hat{P}_{\kappa\mathrm{g}}^{\mathrm{E(B)}}(\bar{l}_i); \hat{P}_{\kappa\mathrm{g}}^{\mathrm{E(B)}}(\bar{l}_j)\right] \equiv \langle \hat{P}_{\kappa\mathrm{g}}^{\mathrm{E(B)}}(\bar{l}_i)\hat{P}_{\kappa\mathrm{g}}^{\mathrm{E(B)}}(\bar{l}_j)\rangle - P_{\kappa\mathrm{g}}^{\mathrm{E(B)}}(\bar{l}_i)P_{\kappa\mathrm{g}}^{\mathrm{E(B)}}(\bar{l}_j)\,. \tag{7.41}$$

Focussing first on the correlator, we find from the definitions of the estimators

$$\langle \hat{P}_{\kappa\mathrm{g}}^{\mathrm{E(B)}}(\bar{l}_i)\hat{P}_{\kappa\mathrm{g}}^{\mathrm{E(B)}}(\bar{l}_j)\rangle$$

$$= \int_{A_{\mathrm{r}}(\bar{l}_i)} \frac{\mathrm{d}^2l}{\bar{n}AA_{\mathrm{r}}(\bar{l}_i)} \int_{A_{\mathrm{r}}(\bar{l}_j)} \frac{\mathrm{d}^2l'}{\bar{n}AA_{\mathrm{r}}(\bar{l}_j)} \langle \hat{\kappa}_{\mathrm{E(B)}}(\boldsymbol{l})\hat{\kappa}_{\mathrm{g}}(-\boldsymbol{l})\hat{\kappa}_{\mathrm{E(B)}}(\boldsymbol{l}')\hat{\kappa}_{\mathrm{g}}(-\boldsymbol{l}')\rangle$$

$$= \int_{A_{\mathrm{r}}(\bar{l}_i)} \frac{\mathrm{d}^2l}{\bar{n}AA_{\mathrm{r}}(\bar{l}_i)} \int_{A_{\mathrm{r}}(\bar{l}_j)} \frac{\mathrm{d}^2l'}{\bar{n}AA_{\mathrm{r}}(\bar{l}_j)} \left[\langle \hat{\kappa}_{\mathrm{E(B)}}(\boldsymbol{l})\hat{\kappa}_{\mathrm{g}}(-\boldsymbol{l})\rangle\langle \hat{\kappa}_{\mathrm{E(B)}}(\boldsymbol{l}')\hat{\kappa}_{\mathrm{g}}(-\boldsymbol{l}')\rangle \right.$$

$$\left. + \langle \hat{\kappa}_{\mathrm{E(B)}}(\boldsymbol{l})\hat{\kappa}_{\mathrm{E(B)}}(\boldsymbol{l}')\rangle\langle \hat{\kappa}_{\mathrm{g}}(-\boldsymbol{l})\hat{\kappa}_{\mathrm{g}}(-\boldsymbol{l}')\rangle + \langle \hat{\kappa}_{\mathrm{E(B)}}(\boldsymbol{l})\hat{\kappa}_{\mathrm{g}}(-\boldsymbol{l}')\rangle\langle \hat{\kappa}_{\mathrm{E(B)}}(\boldsymbol{l}')\hat{\kappa}_{\mathrm{g}}(-\boldsymbol{l})\rangle \right]\,, \tag{7.42}$$

where we assumed Gaussian fields and used the Wick theorem (see Eq. 2.111) to express the four-point correlator as products of two-point correlators. The first term in square brackets cancels the second term on the right-hand side in the covariance matrix (7.41). The correlators of the second term are given by the results of the previous sections, see Eqs. (7.26) and (7.35), respectively:

$$\langle \hat{\kappa}_{\mathrm{E(B)}}(\boldsymbol{l})\hat{\kappa}_{\mathrm{E(B)}}(\boldsymbol{l}')\rangle\langle \hat{\kappa}_{\mathrm{g}}(-\boldsymbol{l})\hat{\kappa}_{\mathrm{g}}(-\boldsymbol{l}')\rangle = (2\pi)^2\delta_{\mathrm{D}}(\boldsymbol{l}+\boldsymbol{l}')\bar{n}^2\left[P_{\mathrm{E(B)}}(l)+\frac{\sigma_\epsilon^2}{2\bar{n}}\right]$$

$$\times (2\pi)^2\delta_{\mathrm{D}}(\boldsymbol{l}+\boldsymbol{l}')\left[P_{\mathrm{gg}}(l)+\frac{1}{\bar{N}}\right] \tag{7.43}$$

The last term is proportional to the product of the two cross-power spectra. For example

$$\langle \hat{\kappa}_{\mathrm{E(B)}}(\boldsymbol{l})\hat{\kappa}_{\mathrm{g}}(-\boldsymbol{l}')\rangle = \langle \mathrm{E}_\epsilon[\hat{\kappa}_{\mathrm{E(B)}}(\boldsymbol{l})]\,\mathrm{E}[\hat{\kappa}_{\mathrm{g}}(-\boldsymbol{l}')]\rangle = \langle \tilde{\kappa}_{\mathrm{E}}(\boldsymbol{l})\tilde{\kappa}_{\mathrm{g}}(-\boldsymbol{l}')\rangle$$
$$= (2\pi)^2 \delta_{\mathrm{D}}(\boldsymbol{l}-\boldsymbol{l}')P_{\kappa\mathrm{g}}^{\mathrm{E(B)}}(l)\,, \tag{7.44}$$

where we splitted the total ensemble average in an expectation over realization of the density contrast fields (angle brackets), an expectation over the intrinsic ellipticities (denoted by $\mathrm{E}_\epsilon[\ ]$) and an expectation over the ensemble of point processes (denoted by $\mathrm{E}[\ ]$). Note that we assumed in the first step that the shape noise of background and the shot noise of foreground galaxies are uncorrelated. The final result is

$$\mathcal{C}\left[\hat{P}_{\kappa\mathrm{g}}^{\mathrm{E(B)}}(\bar{l}_i); \hat{P}_{\kappa\mathrm{g}}^{\mathrm{E(B)}}(\bar{l}_j)\right] = \frac{(2\pi)^2}{AA_{\mathrm{r}}(\bar{l}_i)}\delta_{\bar{l}_i\bar{l}_j}[\bar{P}_{\mathrm{E(B)}}(\bar{l}_i)\bar{P}_{\mathrm{gg}}(\bar{l}_i) + P_{\kappa\mathrm{g}}^{\mathrm{E(B)}}(\bar{l}_i)P_{\kappa\mathrm{g}}^{\mathrm{E(B)}}(\bar{l}_i)]\,, \tag{7.45}$$

where we defined the power spectra including the statistical noise as

$$\bar{P}_{\mathrm{E(B)}}(\bar{l}_i) \equiv P_{\mathrm{E(B)}}(\bar{l}_i) + \frac{\sigma_\epsilon^2}{2\bar{n}}\,, \tag{7.46}$$

$$\bar{P}_{\mathrm{gg}}(\bar{l}_i) \equiv P_{\mathrm{gg}}(\bar{l}_i) + \frac{1}{\bar{N}}\,. \tag{7.47}$$

7.2 Covariance of the Power Spectrum Estimator

In this section we want to compare the covariance of the convergence power spectrum with the covariance of the galaxy-galaxy lensing power spectrum. We first show the results for the dark matter power spectrum covariance and then we consider the covariance of the projected power spectrum, which can be treated analogously.

7.2.1 Dark Matter Power Spectrum Covariance

Let us assume a given survey of a connected volume V and that Fourier space is divided into a number of bins k_i of a corresponding bin width Δk_i. In the following we assume that we have a constant shell width Δk. Using this setup, we define an unbiased estimator of the dark matter power spectrum as (Scoccimarro et al. 1999)

$$\hat{P}(k_i) = \frac{1}{V}\int_{k_i} \frac{\mathrm{d}^3k}{V_{\mathrm{s}}(k_i)}\,\delta(\boldsymbol{k})\delta(-\boldsymbol{k})\,, \tag{7.48}$$

where we estimate the power spectrum by averaging over all wave-vectors $\boldsymbol{k}$ within a thin shell of width Δk with radius k_i. Here $V_{\mathrm{s}}(k_i)$ ("s" stands for shell) is the volume of the i-th shell in Fourier space which can be easily computed from

$$V_{\mathrm{s}}(k) = \int_k \mathrm{d}^3q = 4\pi\int_{k-\Delta k/2}^{k+\Delta k/2} \mathrm{d}q\, q^2 = 4\pi k^2\Delta k\left(1 + \frac{\Delta k^2}{12k^2}\right) \approx 4\pi k^2\Delta k\,, \tag{7.49}$$

where we can neglect the second term in brackets for small bin widths Δk as assumed in the last step. The covariance matrix of the power spectrum estimator in Eq. (7.48) is defined as

$$
\mathcal{C}\left[\hat{P}_i; \hat{P}_j\right] \equiv \mathcal{C}_{ij} = \left\langle \left(\hat{P}_i - \langle \hat{P}_i \rangle\right) \left(\hat{P}_j - \langle \hat{P}_j \rangle\right) \right\rangle = \langle \hat{P}_i \hat{P}_j \rangle - \langle \hat{P}_i \rangle \langle \hat{P}_j \rangle \,, \tag{7.50}
$$

where we used the compact notation $\hat{P}_i \equiv \hat{P}(k_i)$. Combining Eqs. (7.48) and (7.50), the covariance matrix of the power spectrum estimator can be computed (Scoccimarro et al. 1999, Cooray & Hu 2001):

$$
\begin{aligned}
\mathcal{C}_{ij} &= \frac{1}{V^2} \int_{k_i} \frac{\mathrm{d}^3 k_1}{V_{\mathrm{s}}(k_i)} \int_{k_j} \frac{\mathrm{d}^3 k_2}{V_{\mathrm{s}}(k_j)} \Big[\langle \delta(\boldsymbol{k}_1)\delta(-\boldsymbol{k}_1)\delta(\boldsymbol{k}_2)\delta(-\boldsymbol{k}_2) \rangle \\
&\quad - \langle \delta(\boldsymbol{k}_1)\delta(-\boldsymbol{k}_1) \rangle \langle \delta(\boldsymbol{k}_2)\delta(-\boldsymbol{k}_2) \rangle \Big] \\
&= \frac{1}{V^2} \int_{k_i} \frac{\mathrm{d}^3 k_1}{V_{\mathrm{s}}(k_i)} \int_{k_j} \frac{\mathrm{d}^3 k_2}{V_{\mathrm{s}}(k_j)} \Big[\langle \delta(\boldsymbol{k}_1)\delta(-\boldsymbol{k}_1)\delta(\boldsymbol{k}_2)\delta(-\boldsymbol{k}_2) \rangle_{\mathrm{c}} \\
&\quad + \langle \delta(\boldsymbol{k}_1)\delta(\boldsymbol{k}_2) \rangle \langle \delta(-\boldsymbol{k}_1)\delta(-\boldsymbol{k}_2) \rangle + \langle \delta(\boldsymbol{k}_1)\delta(-\boldsymbol{k}_2) \rangle \langle \delta(-\boldsymbol{k}_1)\delta(\boldsymbol{k}_2) \rangle \Big] \\
&= \frac{(2\pi)^3}{V^2} \int_{k_i} \frac{\mathrm{d}^3 k_1}{V_{\mathrm{s}}(k_i)} \int_{k_j} \frac{\mathrm{d}^3 k_2}{V_{\mathrm{s}}(k_j)} \Big\{ \delta_{\mathrm{D}}(\boldsymbol{0}) T(\boldsymbol{k}_1, -\boldsymbol{k}_1, \boldsymbol{k}_2, -\boldsymbol{k}_2) \\
&\quad + (2\pi)^3 P^2(k_1)[\delta_{\mathrm{D}}(\boldsymbol{k}_1 + \boldsymbol{k}_2)\delta_{\mathrm{D}}(-\boldsymbol{k}_1 - \boldsymbol{k}_2) + \delta_{\mathrm{D}}(\boldsymbol{k}_1 - \boldsymbol{k}_2)\delta_{\mathrm{D}}(-\boldsymbol{k}_1 + \boldsymbol{k}_2)] \Big\} \\
&= \left[\frac{(2\pi)^6}{V^2} \int_{k_i} \frac{\mathrm{d}^3 k_1}{V_{\mathrm{s}}(k_i) V_{\mathrm{s}}(k_j)} 2 P^2(k_1) \delta_{\mathrm{D}}(\boldsymbol{0}) \delta_{k_i k_j} \right] + \frac{1}{V} \bar{T}(k_i, k_j) \\
&= \frac{1}{V} \left[\frac{(2\pi)^3}{V_{\mathrm{s}}(k_i)} 2 P^2(k_i) \delta_{k_i k_j} + \bar{T}(k_i, k_j) \right] \,, \tag{7.51}
\end{aligned}
$$

where we expanded the four-point correlator in terms of two-point correlators and the connected fourth-order moment (denoted by the subscript "c") in the second step and defined the bin-averaged dark matter trispectrum in the fourth step as

$$
\bar{T}(k_i, k_j) = \int_{k_i} \frac{\mathrm{d}^3 k_1}{V_{\mathrm{s}}(k_i)} \int_{k_j} \frac{\mathrm{d}^3 k_2}{V_{\mathrm{s}}(k_j)} T(\boldsymbol{k}_1, -\boldsymbol{k}_1, \boldsymbol{k}_2, -\boldsymbol{k}_2) \,. \tag{7.52}
$$

In the last step we assumed that the power spectrum is approximately constant over the shell integral valid for small bin sizes. In addition, we used the discrete form of the Dirac function, $\delta_{\mathrm{D}}(\boldsymbol{0}) = V/(2\pi)^3$, in the last step. Furthermore, $\delta_{k_i k_j}$ denotes the Kronecker delta. Hence, we found that the covariance of the power spectrum estimator is given by

$$
\mathcal{C}\left[\hat{P}(k_i); \hat{P}(k_j)\right] \equiv \mathcal{C}_{ij} = \frac{1}{V} \left[\frac{(2\pi)^3}{V_{\mathrm{s}}(k_i)} 2 P^2(k_i) \delta_{k_i k_j} + \bar{T}(k_i, k_j) \right] \equiv \mathcal{C}_{ij}^{\mathrm{G}} + \mathcal{C}_{ij}^{\mathrm{NG}} \,, \tag{7.53}
$$

which is composed of two statistically different terms: a *Gaussian part* $\mathcal{C}^{\mathrm{G}}$ which is proportional to the power spectrum squared and only contributes to diagonal elements

of the covariance, and a *non-Gaussian part* $\mathcal{C}^{\mathrm{NG}}$ which depends on the trispectrum and contributes to diagonal and off-diagonal elements. The off-diagonal elements correspond to correlations between different band powers which is a unique signature of the non-Gaussian density field. As the covariance is inversely proportional to the survey volume, one survey strategy to reduce statistical errors is to cover a large volume in the observations. In addition, the Gaussian term depends on the adopted binning scheme such that enhancing the bin size results in a smaller Gaussian part. On the other hand, the non-Gaussian part is independent of the binning since the shell volume cancels with the integration in Eq. (7.52). Moreover, the covariance depends only on a specific configuration of the trispectrum, namely the *parallelogram configuration* where the trispectrum depends only on two wave-vectors that can have an arbitrary relative orientation.

We can parametrize the trispectrum by $T(\boldsymbol{k}_1, -\boldsymbol{k}_1, \boldsymbol{k}_2, -\boldsymbol{k}_2) \equiv T(k_1, k_2, x)$, valid for homogeneous and isotropic spectra, where $x \equiv \cos(\theta) = \boldsymbol{k}_1 \cdot \boldsymbol{k}_2 / k_1 k_2$ is the cosine of the angle between the two vectors $\boldsymbol{k}_1$ and $\boldsymbol{k}_2$. Introducing spherical coordinates in Eq. (7.52) leads to

$$\bar{T}(k_i, k_j) = \frac{1}{2} \frac{1}{(k_i k_j \Delta k)^2} \int_{k_i - \frac{\Delta k}{2}}^{k_i + \frac{\Delta k}{2}} \mathrm{d}k_1 \, k_1^2 \int_{k_j - \frac{\Delta k}{2}}^{k_j + \frac{\Delta k}{2}} \mathrm{d}k_2 \, k_2^2 \int_{-1}^{1} \mathrm{d}x \, T(k_1, k_2, x) \,, \qquad (7.54)$$

where we selected the coordinate system such that one angular integration becomes trivial.

Studying the dark matter power spectrum covariance is the basis for the statistical error estimates of cosmological probes which analyze the three-dimensional matter distribution in the Universe, like galaxy redshift surveys. However, one needs a model for the galaxy-dark matter bias factor. In the following we consider the covariance of projected power spectra.

7.2.2 Convergence Power Spectrum Covariance

The power spectrum and trispectrum for the convergence field κ in the flat-sky approximation are defined analogously to the three-dimensional case as

$$\langle \kappa(\boldsymbol{l}_1) \kappa(\boldsymbol{l}_2) \rangle = (2\pi)^2 \delta_{\mathrm{D}}(\boldsymbol{l}_{12}) P_{\kappa\kappa}(l) \,, \qquad (7.55)$$

$$\langle \kappa(\boldsymbol{l}_1) \kappa(\boldsymbol{l}_2) \kappa(\boldsymbol{l}_3) \kappa(\boldsymbol{l}_4) \rangle_{\mathrm{c}} = (2\pi)^2 \delta_{\mathrm{D}}(\boldsymbol{l}_{1234}) T_\kappa(\boldsymbol{l}_1, \boldsymbol{l}_2, \boldsymbol{l}_3, \boldsymbol{l}_4) \,, \qquad (7.56)$$

where $\boldsymbol{l}_{12} \equiv \boldsymbol{l}_1 + \boldsymbol{l}_2$ and $\boldsymbol{l}_{1234} \equiv \boldsymbol{l}_1 + \boldsymbol{l}_2 + \boldsymbol{l}_3 + \boldsymbol{l}_4$. In the following we neglect B-modes and consider only the E-mode power spectrum which is here denoted by $P_{\kappa\kappa}$ in contrast to the original definition in Eq. (7.16). Additionally, we study in this section the sample-variance dominated part of the covariance without any shape noise contribution which simplifies the calculation of the non-Gaussian part of the covariance. The shape-noise contribution of the Gaussian part, which we studied in Sect. 7.1.1, can be included in the final result.

Table 7.1: Initial cosmological parameters used by the Virgo N-body simulation (Jenkins et al. 1998). The simulation employs the BBKS transfer function (Bardeen et al. 1986) for the linear power spectrum. We use this particular simulation as we compare the halo model covariance results with results from convergence maps obtained with ray-tracing through the Virgo simulation in Pielorz et al. (2009).

Simulation	Ω_{m}	Ω_Λ	h	Ω_{b}	σ_8	n_{s}	Γ	z_{s}	$T(k)$
Virgo	0.3	0.7	0.7	0.0	0.9	1.0	0.21	1 (2)	BBKS

We construct the following estimator for the projected power spectrum

$$\hat{P}_{\kappa\kappa}(l_i) = \frac{1}{A} \int_{l_i} \frac{\mathrm{d}^2 l}{A_{\mathrm{r}}(l_i)} \kappa(\boldsymbol{l})\kappa(-\boldsymbol{l}) \,, \tag{7.57}$$

with the area of the survey $A = 4\pi f_{\mathrm{sky}}$, where f_{sky} is the fractional sky coverage. The area of the two-dimensional shell of the bin l_i is given by

$$A_{\mathrm{r}}(l_i) = \int_{l_i} \mathrm{d}^2 l = 2\pi \int_{l_i - \Delta l_i/2}^{l_i + \Delta l_i/2} l \, \mathrm{d}l = 2\pi l_i \Delta l_i \tag{7.58}$$

or

$$A_{\mathrm{r}}(l_i) = \int_{l_i} \mathrm{d}^2 l = 2\pi \int_{l_i}^{l_i + \Delta l_i} l \, \mathrm{d}l = 2\pi l_i \Delta l_i + \pi (\Delta l_i)^2 \,, \tag{7.59}$$

depending on the binning scheme. The width of the bin l_i is given by Δl_i. The ensemble average of the estimator is

$$\begin{aligned}\langle \hat{P}_{\kappa\kappa}(l_i) \rangle &= \frac{1}{A} \int_{l_i} \frac{\mathrm{d}^2 l}{A_{\mathrm{r}}(l_i)} \langle \kappa(\boldsymbol{l})\kappa(-\boldsymbol{l}) \rangle \\ &= \frac{1}{A} \int_{l_i} \frac{\mathrm{d}^2 l}{A_{\mathrm{r}}(l_i)} (2\pi)^2 \delta_{\mathrm{D}}(\mathbf{0}) P_{\kappa\kappa}(l) = P_{\kappa\kappa}(l) \,,\end{aligned} \tag{7.60}$$

where we assumed that $P_{\kappa\kappa}$ is only slowly varying over the bin width and used the discrete limit of the two-dimensional Dirac delta function $\delta_{\mathrm{D}}(\mathbf{0}) = A/(2\pi)^2$ in the third step. This proofs that we have defined an unbiased estimator.

The covariance of the convergence power spectrum estimator in Eq. (7.57) is

$$\mathcal{C}[\hat{P}_{\kappa\kappa}(l_i); \hat{P}_{\kappa\kappa}(l_j)] \equiv \mathcal{C}_{ij}^{\kappa\kappa} = \frac{1}{A} \left[\frac{(2\pi)^2}{A_{\mathrm{r}}(l_i)} 2 P_{\kappa\kappa}^2(l_i) \delta_{l_i l_j} + \bar{T}_\kappa(l_i, l_j) \right] \,, \tag{7.61}$$

with the bin-averaged projected trispectrum

$$\bar{T}_\kappa(l_i, l_j) = \int_{l_i} \frac{\mathrm{d}^2 l_1}{A_{\mathrm{r}}(l_i)} \int_{l_j} \frac{\mathrm{d}^2 l_2}{A_{\mathrm{r}}(l_j)} T_\kappa(\boldsymbol{l}_1, -\boldsymbol{l}_1, \boldsymbol{l}_2, -\boldsymbol{l}_2) \,. \tag{7.62}$$

We see that the covariance of the convergence power spectrum again decomposes into *Gaussian part* and a *non-Gaussian part*.

Using the assumed homogeneity and isotropy of the Universe, we can parametrize the convergence trispectrum with the modulus of the two wave-vectors and the angle φ between them which is given by $\cos\varphi = \boldsymbol{l}_1 \cdot \boldsymbol{l}_2 / l_1 l_2$. We can then define $T_\kappa(l_1, l_2, \cos\varphi) \equiv T_\kappa(\boldsymbol{l}_1, -\boldsymbol{l}_1, \boldsymbol{l}_2, -\boldsymbol{l}_2)$. We are free to choose the coordinate system such that one angular integration is trivial for the bin-averaged trispectrum, leading to

$$\bar{T}_\kappa(l_i, l_j) = 2\pi \int_{l_i - \Delta l/2}^{l_i + \Delta l/2} \frac{\mathrm{d}l_1}{A_\mathrm{r}(l_i)} \, l_1 \int_{l_j - \Delta l/2}^{l_j + \Delta l/2} \frac{\mathrm{d}l_2}{A_\mathrm{r}(l_j)} \, l_2 \int_0^{2\pi} \mathrm{d}\varphi \, T_\kappa(l_1, l_2, \cos\varphi) \,. \quad (7.63)$$

The integration can be approximated by a simple one-dimensional integral over the angle φ if the trispectrum is only slowly varying over the chosen bin size:

$$\bar{T}_\kappa(l_i, l_j) \simeq \frac{1}{2\pi} \int_0^{2\pi} \mathrm{d}\varphi \, T_\kappa(l_i, l_j, \cos\varphi) \,. \quad (7.64)$$

Parallelogram Configuration of the Halo Model Trispectrum

To determine the covariance matrix in Eq. (7.61) for a fiducial survey, we need a model for the dark matter trispectrum. We employ here the dark matter halo model as developed in Chapter 3 where we showed that the trispectrum depends on four halo terms which are dominant on different scales. However, we need only the special case of the parallelogram configuration of the trispectrum, where $\boldsymbol{k}_2 = -\boldsymbol{k}_1$ and $\boldsymbol{k}_4 = -\boldsymbol{k}_3$. In this case the equations for the trispectrum simplify considerably. The one-halo term in Eq. (3.133) changes to

$$T_\mathrm{1-h}^\mathrm{pc} = \int \mathrm{d}m \, n(m) \left(\frac{m}{\bar{\rho}}\right)^4 \tilde{u}^2(k_1, m) \tilde{u}^2(k_3, m) \,. \quad (7.65)$$

Note that the angle-independent one-halo term is simply equal to its bin-averaged counterpart without having to perform an integration at all. The two-halo term is composed of two different contributions defined in Eqs. (3.142) and (3.143). For the parallelogram configuration we find

$$\begin{aligned} T_\mathrm{2-h}^\mathrm{pc} = {}& 2 P_\mathrm{pt}(k_1) I_{13}(k_1, k_3, k_3) I_{11}(k_1) + 2 P_\mathrm{pt}(k_3) I_{13}(k_1, k_1, k_3) I_{11}(k_3) \,, \\ & + \left[P_\mathrm{pt}(|\boldsymbol{k}_1 + \boldsymbol{k}_3|) + P_\mathrm{pt}(|\boldsymbol{k}_1 - \boldsymbol{k}_3|) \right] [I_{12}(k_1, k_3)]^2 \,. \end{aligned} \quad (7.66)$$

Accordingly the three-halo term in Eq. (3.145) is

$$T_\mathrm{3-h}^\mathrm{pc} = 2 I_{11}(k_1) I_{11}(k_3) I_{12}(k_1, k_3) [B_\mathrm{pt}(\boldsymbol{k}_1, \boldsymbol{k}_3, -\boldsymbol{k}_1 - \boldsymbol{k}_3) + B_\mathrm{pt}(\boldsymbol{k}_1, -\boldsymbol{k}_3, -\boldsymbol{k}_1 + \boldsymbol{k}_3)] \,, \quad (7.67)$$

Finally, the four-halo in Eq. (3.137) simplifies to

$$T_\mathrm{4-h}^\mathrm{pc} = [I_{11}(k_1)]^2 [I_{11}(k_3)]^2 T_\mathrm{pt}(\boldsymbol{k}_1, -\boldsymbol{k}_1, \boldsymbol{k}_3, -\boldsymbol{k}_3) \,. \quad (7.68)$$

Results for the covariance

We define the *correlation coefficients* of a given covariance matrix by

$$r_{ij}^{\mathrm{XY}} \equiv \frac{\mathcal{C}_{ij}^{\mathrm{XY}}}{\sqrt{\mathcal{C}_{ii}^{\mathrm{XY}} \mathcal{C}_{jj}^{\mathrm{XY}}}}\,, \qquad (7.69)$$

where we consider two kinds of correlation coefficients, namely $\mathrm{X} = \kappa$ and $\mathrm{Y} \in \{\kappa, \mathrm{g}\}$. These coefficients are a measure for the relative strength of off-diagonal elements compared to diagonal elements and are normalized such that $r_{ii}^{\mathrm{XY}} = 1$. In the case of the convergence power spectrum covariance the r_{ij}-elements describe the correlation strength between band powers at different lengths.

In addition to the "full" covariance matrix in Eq. (7.61) calculated with the halo model approach which includes all four halo terms of the trispectrum, we employ an approximation for the non-Gaussian part of the covariance matrix following Takada & Jain (2008). In the approximation they use for the trispectrum only those terms that are dominant in the large-scale and small-scale regime. The four-halo term gives the dominant contribution to the trispectrum on large scales. On the largest scale the consistency relation of the first-order halo bias ensures that $I_{11}(k) \rightarrow 1$ in Eq. (3.138) and thus the four-halo term converges to the trispectrum in tree-level perturbation theory given in Eqs. (2.130) and (2.131):

$$T_{4\text{-h}}^{\delta\delta\delta\delta}(\boldsymbol{k}_1, \boldsymbol{k}_2, \boldsymbol{k}_3, \boldsymbol{k}_4; z) \rightarrow T_{\mathrm{pt}}(\boldsymbol{k}_1, \boldsymbol{k}_2, \boldsymbol{k}_3, \boldsymbol{k}_4; z) = D^6(z) T_{\mathrm{pt}}(\boldsymbol{k}_1, \boldsymbol{k}_2, \boldsymbol{k}_3, \boldsymbol{k}_4; 0)\,, \quad (7.70)$$

where the redshift-dependence is governed by the growth factor (given in Eq. 2.48) to the power of 6 since $T_{\mathrm{pt}} \propto (P_{\mathrm{pt}})^3 \propto D^6(z)$. The small-scale regime is dominated by the one-halo term of the trispectrum. Thus, the approximation for the non-Gaussian part of the covariance is given by

$$\bar{T}_{\kappa}(l_i, l_j) \approx T_{\kappa\kappa\kappa\kappa}^{1\text{-h}}(l_i, l_j) + \frac{1}{2\pi} \int_0^{2\pi} \mathrm{d}\varphi\, T_{\mathrm{pt}}^{\kappa}(l_i, l_j, \cos\varphi)\,, \qquad (7.71)$$

where T_{pt}^{κ} denotes the projected tree-level trispectrum in parallelogram configuration which is computed from inserting Eq. (7.70) into the Limber's approximation given in Eq. (5.65).

We consider in the following a fiducial survey with intrinsic ellipticity dispersion of $\sigma_{\epsilon} = 0.22$ and mean number density of background sources of $\bar{n} = 3.55 \times 10^8\,\mathrm{sr}^{-1}$ which corresponds to $\bar{n} \simeq 30\,\mathrm{arcmin}^{-2}$. With this setup, we can determine the amount of shape noise in the covariance of the convergence power spectrum in Eq. (7.61) by replacing the convergence power spectrum with the relation (7.46).

In Fig. 7.1 we show the results of the correlation coefficients for the convergence power spectrum covariance for 40 logarithmically-spaced bins in the range $50 \leq l \leq 6000$ which roughly corresponds to $3.6 \lesssim \theta/\mathrm{arcmin} \lesssim 430$ in real space where we used $\theta = 2\pi/l$. For this binning scheme we have checked that the approximation (7.64) for the bin-averaged
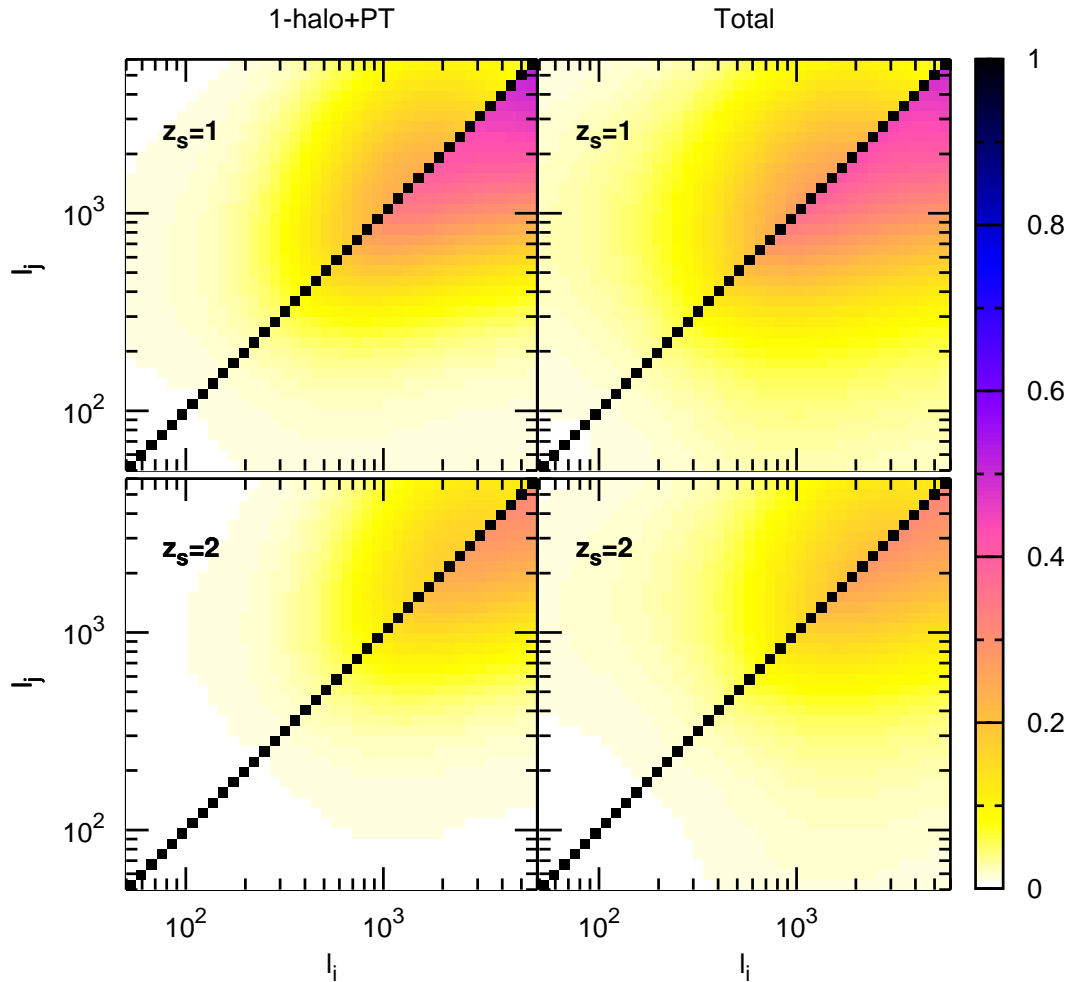
Figure 7.1: Correlation coefficients $r_{ij}^{\kappa\kappa}$ (see Eq. 7.69) of the covariance matrix of the convergence power spectrum estimator for 40 logarithmically-spaced bins in l in the range $50 \leq l \leq 6000$. In the left panels we show the approximation of the covariance as given in Eq. (7.71) whereas the right panels show the covariance including all four halo terms (here denoted by "Total"). The cosmological model is adapted from the Virgo simulation as given in Table 7.1. In the upper (lower) triangle of each plot we depict the results with (without) shape noise of the power spectrum. In addition, we show the correlation coefficients for a source redshift of $z_s = 1$ and $z_s = 2$ as marked in the panels.

trispectrum works well ($< 1\%$ deviation from the exact relation 7.63) and thus we will employ this approximation in the following. We included a stochastic concentration parameter in the one-halo term of the trispectrum with a dispersion of $\sigma_{\ln c} = 0.3$ which enters in the log-normal distribution in Eq. (3.63). For $l_i \lesssim 500$ the off-diagonal elements are well below $r_{ij} = 0.4$. Going to smaller scales, we note that the correlation coefficients increase until $r_{ij} \simeq 0.6$ on the smallest scales depicted which corresponds to a strong correlation of the corresponding Fourier modes. This is due to the fact that in the small-scale regime lensing is more affected by the nonlinear clustering.

In each plot we show the correlation coefficients with shape noise in the upper triangle and without shape noise in the lower triangle. The inclusion of shape noise reduces the effect of cross-correlations between different band powers. This is due to the fact that it enters only in the power spectrum which only contributes to the diagonal part of the covariance matrix. Hence, an enhancement of the diagonal part leads to a reduction of the correlation coefficient as it is normalized by the diagonal part. We see that at $l \simeq 10^3$ shot noise becomes important which suppresses the importance of including the non-Gaussian part in the covariance. Furthermore, we show the correlation coefficients for a single source redshift at $z_{\rm s} = 1$ and $z_{\rm s} = 2$. Clearly, r_{ij} is reduced if we increase the source redshift.

In the left panels we show the covariance approximation in Eq. (7.71) and in the right panels the full covariance matrix. The approximation reproduces the results of the full halo model trispectrum quite well. The only significant deviations occur on intermediate scales where the two-halo term is important. We thus expect that one can safely use the approximation for the covariance to determine the errors of cosmological parameters. In addition, using the approximation results in significantly reduced computation times. This is crucial if one needs to compute the covariance many times, for example if one wants to explore the dependence of the covariance matrix on cosmological parameters.

7.2.3 Galaxy-Galaxy Lensing Power Spectrum Covariance

We neglect for the derivation of the non-Gaussian part the shot and shape noise contribution as given in Eqs. (7.46) and (7.47) and define the following estimator for the two-dimensional cross-power spectrum

$$\hat{P}_{\kappa g}(l_i) = \frac{1}{A} \int_{l_i} \frac{\mathrm{d}^2 l}{A_{\rm r}(l_i)} \, \kappa(\boldsymbol{l}) \kappa_g(-\boldsymbol{l}) \,, \tag{7.72}$$

which is a generalization of the estimator of the convergence power spectrum in Eq. (7.57) and thus we can show accordingly that this is an unbiased estimator. Using this estimator, we can perform an analogous calculation to the full dark matter power spectrum covariance matrix presented in Sect. 7.2.1. Then the covariance matrix of the cross-power spectrum estimator is given by

$$\mathcal{C}_{ij}^{\kappa g} = \frac{1}{A} \left\{ \frac{(2\pi)^2}{A_{\rm r}(l_i)} \left[P_{\kappa\kappa}(l_i) P_{\rm gg}(l_i) + P_{\kappa g}^2(l_i) \right] \delta_{l_i l_j} + \bar{T}_{\kappa g \kappa g}(l_i, l_j) \right\} \,, \tag{7.73}$$

where we introduced the bin-averaged convergence cross-trispectrum

$$\bar{T}_{\kappa g \kappa g}(l_i, l_j) = \int_{l_i} \frac{\mathrm{d}^2 l_1}{A_{\mathrm{r}}(l_i)} \int_{l_j} \frac{\mathrm{d}^2 l_2}{A_{\mathrm{r}}(l_j)} \, T_{\kappa g \kappa g}(\boldsymbol{l}_1, -\boldsymbol{l}_1, \boldsymbol{l}_2, -\boldsymbol{l}_2) \,. \tag{7.74}$$

We infer from the definition of the cross-trispectrum in Eq. (6.63) that the bin-averaged cross-trispectrum and the full covariance are symmetric under permutations of l_i and l_j. The result of the covariance can be compared to the result obtained in Eq. (7.42) where we used the Gaussian approximation for the four-point correlator and included shape and shot noise. We see that the auto- and cross-power spectra contribute only to the diagonal of the covariance matrix whereas the bin-averaged cross-trispectrum contributes to diagonal and non-diagonal elements. When we consider shot and shape noise, we have to replace the auto-power spectra in Eq. (7.73) by

$$P_{\kappa\kappa}(l_i) \to \bar{P}_{\kappa\kappa}(l_i) = P_{\kappa\kappa}(l_i) + \frac{\sigma_\epsilon^2}{2\bar{n}} \,, \qquad P_{\mathrm{gg}}(l_i) \to \bar{P}_{\mathrm{gg}}(l_i) = P_{\mathrm{gg}}(l_i) + \frac{1}{\bar{N}} \,, \tag{7.75}$$

as was shown in Sect. 7.1.3. The large-scale limit of the four-halo term of the cross-trispectrum in Eq.(4.91) is

$$T_{4\text{-h}}^{\delta g \delta g}(\boldsymbol{k}_1, \boldsymbol{k}_2, \boldsymbol{k}_3, \boldsymbol{k}_4; z) \to \mathcal{T}_{\mathrm{pt}}(\boldsymbol{k}_1, \boldsymbol{k}_2, \boldsymbol{k}_3, \boldsymbol{k}_4; z) = \left[b_1^{\mathrm{L}}(z)\right]^2 D^6(z) T_{\mathrm{pt}}(\boldsymbol{k}_1, \boldsymbol{k}_2, \boldsymbol{k}_3, \boldsymbol{k}_4; 0) \,, \tag{7.76}$$

where b_1^{L} is the first-order large-scale bias parameter given in Eq. (4.48) and the growth factor dependence originates from the tree-level trispectrum which is proportional to the linear power spectrum cubed. In accordance with the approximation of the covariance of the convergence power spectrum in Eq. (7.71) we employ an approximation for the galaxy-galaxy-lensing covariance matrix in Eq. (7.73):

$$\bar{T}_{\kappa g \kappa g}(l_i, l_j) \approx T_{\kappa g \kappa g}^{1\text{-h}}(l_i, l_j) + \frac{1}{2\pi} \int_0^{2\pi} \mathrm{d}\varphi \, \mathcal{T}_{\mathrm{pt}}^{\kappa g \kappa g}(l_i, l_j, \cos\varphi) \,, \tag{7.77}$$

where $\mathcal{T}_{\mathrm{pt}}^{\kappa g \kappa g}$ is the projected form of the trispectrum defined in Eq. (7.76).

In Fig. 7.2 we plot the correlation coefficients for the galaxy-galaxy lensing covariance matrix for 40 logarithmically distributed bins in the range $50 \le l \le 6000$. We assume that all the source galaxies are located at a single redshift of $z_{\mathrm{s}} = 1$. In contrast to the convergence covariance we neglect the influence of a stochastic concentration parameter as it provides only a small contribution (see discussion in Sect. 4.6 and in particular Fig. 4.14). All left-hand panels display the approximation (7.77) whereas all right-hand panels show the full model (7.73). Each row corresponds to a specific minimal mass, i.e., $m_{\mathrm{min}} = 10^{11} h^{-1} M_\odot$, $m_{\mathrm{min}} = 10^{12} h^{-1} M_\odot$ and $m_{\mathrm{min}} = 10^{13} h^{-1} M_\odot$ from top to bottom. In the upper triangle of each individual plot we included shot and shape noise whereas the lower triangle is without noise contributions. For the lens galaxies, we limit the population to the range $0 \le z_{\mathrm{l}} \le 0.4$ (this means that we cut off the redshift integration of the projection at z_{l}). Note that our choice of the maximal lens redshift is approximately half as large as the source redshift. The total lens population then has an angular
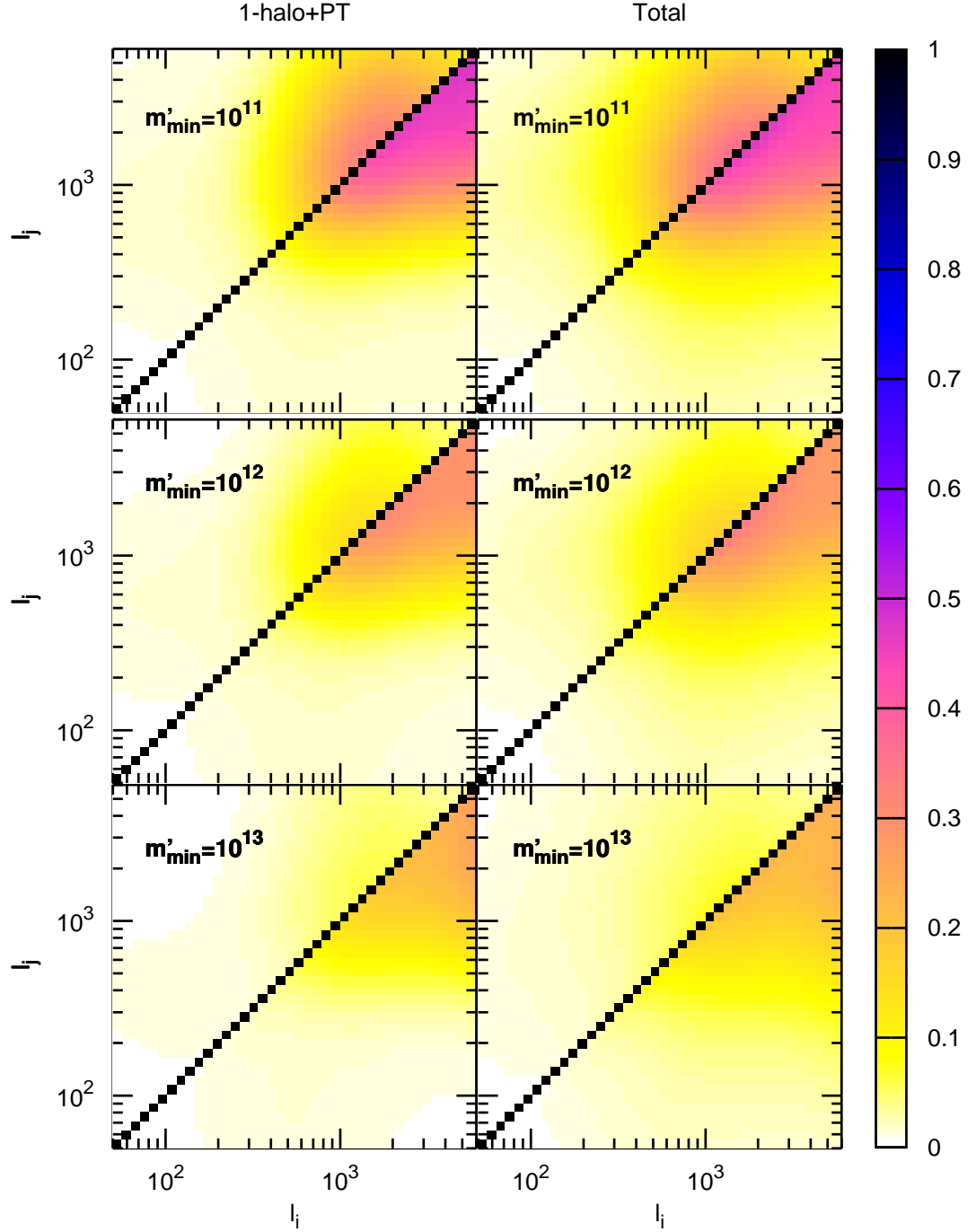
Figure 7.2: Correlation coefficients $r_{ij}^{\kappa g}$ (see Eq. 7.69) of the galaxy-galaxy lensing power spectrum covariance as defined in Eq. (7.73) for 40 logarithmically-spaced bins in l. We show the results for the approximation of the covariance given in Eq. (7.77) (left panels) and the result for the full covariance (right panels). In addition, we depict the plots for three different minimal masses for the HOD: $m_{\min} = 10^{11} h^{-1} M_{\odot}$, $m_{\min} = 10^{12} h^{-1} M_{\odot}$ and $m_{\min} = 10^{13} h^{-1} M_{\odot}$ as indicated in the plots, where we use dimensionless parameters defined by $m'_{\min} = m_{\min}/(h^{-1} M_{\odot})$. In each panel we include shot and shape noise in the upper triangle and no noise in the lower triangle.

number density of $\bar{N} \simeq 1.66\,\mathrm{arcmin}^{-2}$ for $m_{\min} = 10^{11} h^{-1}\,M_\odot$, $\bar{N} \simeq 0.19\,\mathrm{arcmin}^{-2}$ for $m_{\min} = 10^{12} h^{-1}\,M_\odot$ and $\bar{N} \simeq 0.019\,\mathrm{arcmin}^{-2}$ for $m_{\min} = 10^{13} h^{-1}\,M_\odot$. As the shot noise terms enter only in the diagonal of the covariance, the correlation coefficients are reduced in the upper triangles compared to the lower triangles.

We note that the approximation in the left panels reproduces the result of the full covariance in the right panels on small and large scales well. Comparisons of the obtained results to the covariance of the convergence power spectrum plotted in Fig. 7.1 reveal that the approximation is in both cases quite accurate. Increasing the minimal mass leads to a reduction of cross-correlations of the covariance. This seems surprising at first sight since the amplitude of the power spectra and the cross-trispectrum are larger for a larger minimal mass (see e.g., the projected third-order bias depicted in Fig. 6.8). However, the Gaussian part of the covariance enters only in diagonal elements of $\mathcal{C}^{\kappa\mathrm{g}}$ and is on the considered scales larger than the non-Gaussian part. Since $r_{ij}^{\kappa\mathrm{g}}$ is normalized by the diagonal elements of the covariance its entries are reduced when enhancing $m_{\min}$.

To illustrate the composition of the covariance, we depict in Fig. 7.3 the contributions of the trispectrum halo terms to the correlation coefficients with the same binning scheme as above. We find that the two-halo term gives rise to large off-diagonal correlations at intermediate scales which are not accounted for in the approximation. The maximal contributions of the three- and four-halo terms to the correlation coefficients are on small scales roughly a factor of 10 smaller than the one- and two-halo terms. Furthermore, the three-halo term shows a strong enhancement of the correlation coefficients near the diagonal which is not present in the other halo terms.

7.2.4 Ratio of the non-Gaussian to the Gaussian Contribution of the Covariance

Here, we analyze the amount of the non-Gaussian compared to the Gaussian contribution of the covariances studied in the previous sections. Since the Gaussian part only gives a contribution to diagonal elements, we determine the ratio only for diagonal entries of the covariance. We derived in Sect. 7.2.3 the following expression for the covariance of the cross-power spectrum estimator

$$\mathcal{C}_{ij}^{\kappa\mathrm{g}} = \frac{1}{A} \left\{ \frac{(2\pi)^2}{A_\mathrm{r}(l_i)} \left[P_{\kappa\kappa}(l_i) P_{\mathrm{gg}}(l_i) + P_{\kappa\mathrm{g}}^2(l_i) \right] \delta_{l_i l_j} + \bar{T}_{\kappa\mathrm{g}\kappa\mathrm{g}}(l_i, l_j) \right\} \equiv \mathcal{C}_{ij}^{\kappa\mathrm{g(G)}} + \mathcal{C}_{ij}^{\kappa\mathrm{g(NG)}} \,,$$

$$(7.78)$$

where we defined the Gaussian and non-Gaussian contribution to the covariance in the second step. Using this partition of the covariance, we define the non-Gaussian to Gaussian ratio as

$$\mathcal{R}_{\kappa\mathrm{g}}(l) \equiv \frac{\mathcal{C}_{ij}^{\kappa\mathrm{g(NG)}}}{\mathcal{C}_{ij}^{\kappa\mathrm{g(G)}}} = \frac{\bar{T}_{\kappa\mathrm{g}\kappa\mathrm{g}}(l, l)}{2\pi \left[P_{\kappa\kappa}(l) P_{\mathrm{gg}}(l) + P_{\kappa\mathrm{g}}^2(l) \right]} \Delta l \cdot l \,, \qquad (7.79)$$
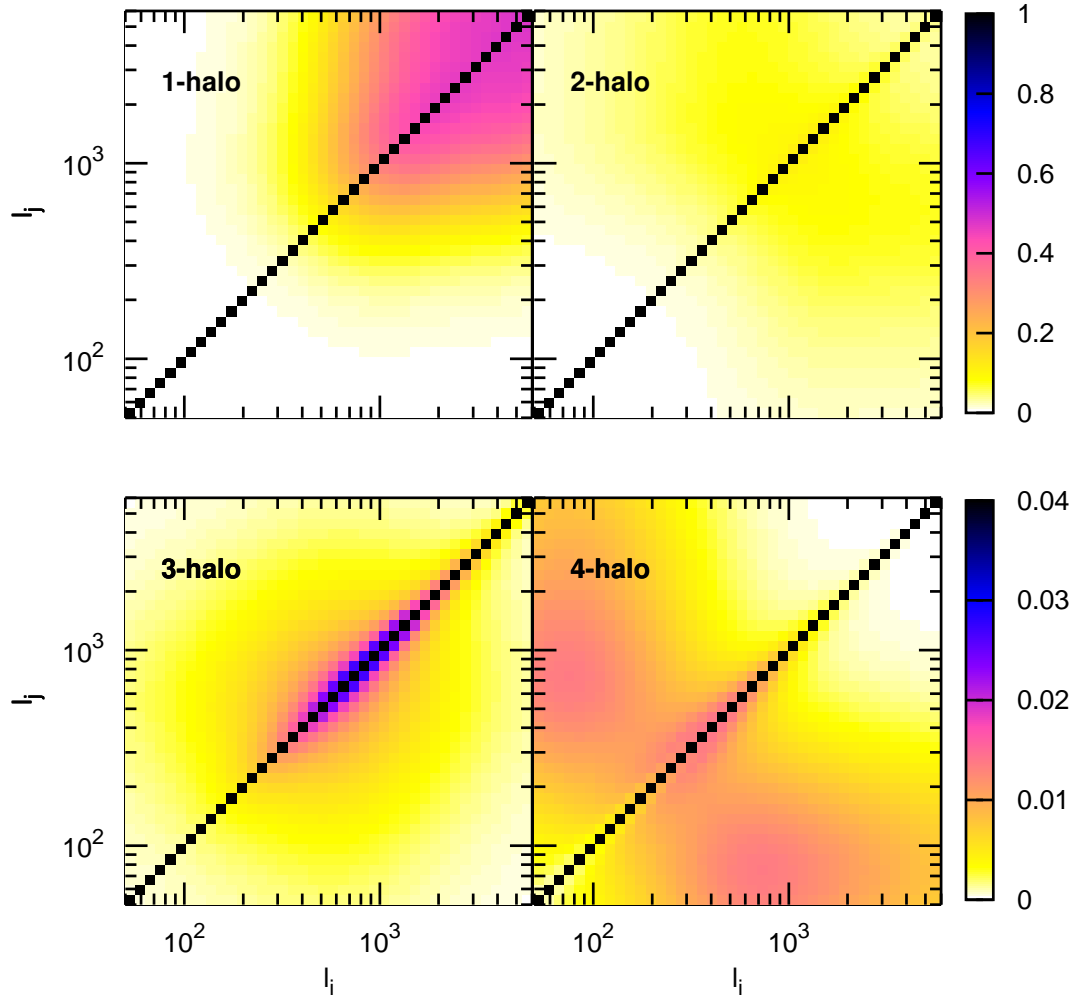
Figure 7.3: Contributions of the individual terms of the halo model trispectrum to the correlation coefficients of the galaxy-galaxy lensing power spectrum estimator for the same l-binning as in Fig. 7.2 neglecting shot and shape noise. For all plots we use the minimal mass $m_{\min} = 10^{11} h^{-1} M_\odot$. Note that the three- and four-halo term contributions are much smaller (approximately a factor of 10) than the one- and two-halo terms. Thus, we use for the two lower panels a smaller interval in the color-coded r_{ij} value.
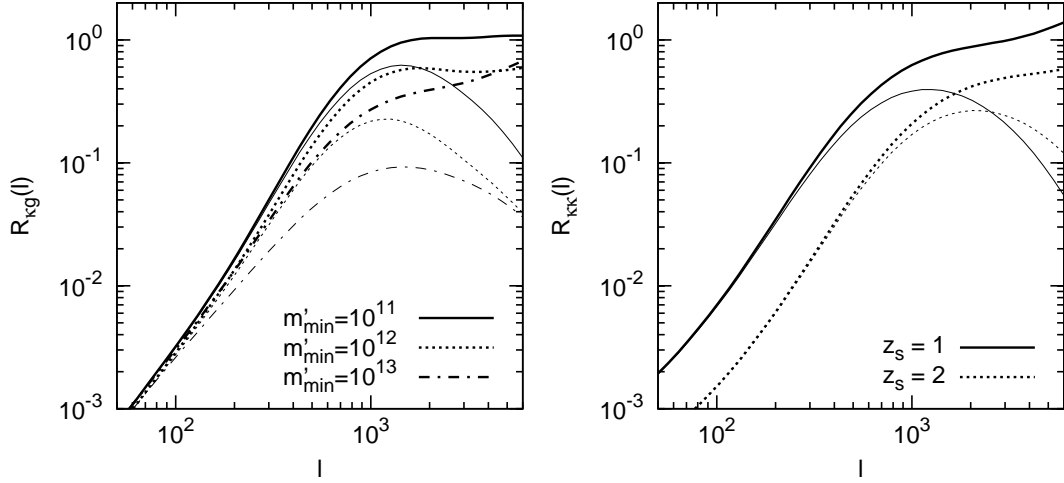
Figure 7.4: Ratio of the non-Gaussian to the Gaussian part of the diagonal covariance elements as a function of l. Thick lines give the results without shot and shape noise, whereas the thin lines with the same linestyle as the corresponding thick lines give the results including shot and shape noise. We show the ratio of the projected cross-power spectrum covariance for three different minimal masses (left panel). For reference, we give the ratio of the convergence power spectrum covariance considering two different source redshifts (right panel).

which depends on the employed binning scheme but is independent on the survey area. Additionally, we derived in Sect. 7.2.2 the covariance for an unbiased convergence power spectrum estimator as

$$\mathcal{C}_{ij}^{\kappa\kappa} = \frac{1}{A} \left[\frac{(2\pi)^2}{A_{\rm r}(l_i)} 2P_{\kappa\kappa}^2(l_i)\delta_{l_i l_j} + \bar{T}_\kappa(l_i, l_j) \right] \equiv \mathcal{C}_{ij}^{\kappa\kappa({\rm G})} + \mathcal{C}_{ij}^{\kappa\kappa({\rm NG})}, \qquad (7.80)$$

and we define the corresponding non-Gaussian to Gaussian ratio as

$$\mathcal{R}_{\kappa\kappa}(l) \equiv \frac{\mathcal{C}_{ij}^{\kappa\kappa({\rm NG})}}{\mathcal{C}_{ij}^{\kappa\kappa({\rm G})}} = \frac{\bar{T}_{\kappa\kappa\kappa\kappa}(l, l)}{4\pi P_{\kappa\kappa}^2(l)} \Delta l \cdot l . \qquad (7.81)$$

In Fig. 7.4 we give the results for the ratios defined in Eqs. (7.79) and (7.81) as a function of the bin l. We consider the same logarithmic binning scheme as in the previous sections. The left panel depicts the ratio for the covariance of the cross-power spectrum for three different minimal masses. A higher (lower) minimal mass leads to a reduction (enhancement) of the ratio. As expected, we find that the ratios are increasing with l which means that the non-Gaussian part gives the largest contribution on small scales. For $m_{\rm min} = 10^{11} \, h^{-1} \, M_\odot$ and $m_{\rm min} = 10^{12} \, h^{-1} \, M_\odot$ the ratios reach a plateau for large l. If we include the shot and shape noise contributions to the Gaussian part of the covariance the ratios reach a maximum at $l \approx 10^3$ and then begin to decrease. Thus, the inclusion of shot and shape noise reduces the importance of non-Gaussian errors on small scales.

The right panel shows the ratio for the covariance of the convergence power spectrum estimator considering two different source redshifts, i.e., $z_s = 1$ and $z_s = 2$. We find that a larger source redshift reduces the amount of non-Gaussian contributions. Note that we already observed a similar behavior for the correlation matrix (see Fig. 7.1). The amplitude of both the convergence power spectrum and trispectrum is enhanced for a larger source redshift since the projections extend over a larger redshift range. However, the inverse squared convergence power spectrum enters in the non-Gaussian to Gaussian ratio which results in a reduction of the ratio for larger z_s.

In addition, we give results for the ratios considering the shape noise contribution to the Gaussian part. Similar to the results of the cross-covariance, we find in this case that the ratios reach a maximum at $l \approx 10^3$ and $l \approx 2 \times 10^3$ for $z_s = 1$ and $z_s = 2$, respectively, and are decreasing for smaller scales. In summary we find that the importance of non-Gaussian errors crucially depends on the considered survey sample (number density or redshift distribution). Furthermore, we find that the non-Gaussian part is of the same size as the Gaussian contribution on the smallest depicted scales. We refrain from giving absolute values for the ratios since all of the obtained results depend on the adopted binning scheme. Future weak lensing and galaxy surveys will yield reduced amounts of shot and shape noise and thus the modeling of the non-Gaussian part of the covariance will be more important as we showed in Fig. 7.4.

7.2.5 Covariance of the Bispectrum

The covariance of the convergence bispectrum can be calculated with the techniques that we already used for the power spectrum (Sefusatti et al. 2006). First we need an estimator for the bispectrum from which we can calculate the covariance using

$$\mathcal{C}_{ij}^{\mathrm{B}} = \langle \hat{B}_i \hat{B}_j \rangle - B_i B_j \,, \tag{7.82}$$

where the indices $i = (i_1, i_2, i_3)$ and $j = (j_1, j_2, j_3)$ label complete triangles with sub-components i_1, i_2 and i_3 which label the three sides of the corresponding triangle. To make a rough estimate which terms are involved in the calculation, we can make a simple qualitative analysis for the first term, i.e., we perform an expansion into connected moments of the six-point correlator as in Eq. (2.88):

$$\begin{aligned}
\langle \kappa\kappa\kappa\kappa\kappa\kappa \rangle &= \langle \kappa\kappa \rangle \langle \kappa\kappa \rangle \langle \kappa\kappa \rangle + \langle \kappa\kappa\kappa \rangle_{\mathrm{c}} \langle \kappa\kappa\kappa \rangle_{\mathrm{c}} \\
&\quad + \langle \kappa\kappa\kappa\kappa \rangle_{\mathrm{c}} \langle \kappa\kappa \rangle + \langle \kappa\kappa\kappa\kappa\kappa\kappa \rangle_{\mathrm{c}} \,.
\end{aligned} \tag{7.83}$$

Hence, the calculation of the covariance matrix of the bispectrum involves the knowledge of the two-point, three-point, four-point and six-point spectrum. As a first approximation, one can use the one-halo term in each of the n-point functions as this is the dominant term in the nonlinear regime. In the Gaussian approximation only the first term is contributing.

7.3 Summary and Conclusions

In this chapter we have studied the effect of non-Gaussian errors on the measurements of weak lensing and for the first time for galaxy-galaxy lensing power spectra. The non-Gaussian errors emerge from the nonlinear gravitational clustering of dark matter and galaxies. To estimate the importance of this effect, we employed the halo model as developed in Chapters 3 and 4.

We started this chapter with a review of the construction of an unbiased estimator for the convergence power spectrum and for the projected galaxy power spectrum. We combined the results of both cases to develop an unbiased estimator of the projected matter-galaxy cross-power spectrum and calculated its covariance. For the calculation we assumed that the four-point correlator resolves into products of two-point correlators which is valid for Gaussian random fields. The resulting covariance is composed of several different contributions: a shape-noise term which arises from the intrinsic ellipticity dispersion of foreground galaxies and a shot-noise term due to the limited number of galaxies in the field. These two terms are dominant on small scales. On the other hand, the error budget on large scales is dominated by the cosmic variance term which is composed of a product of the convergence and the galaxy power spectrum plus the cross-power spectrum squared. Additionally, there are two mixed terms which are products of both contributions. We emphasized that all these terms contribute only to diagonal elements of the covariance.

Next we took the neglected connected fourth-order moment or trispectrum for the covariance of the convergence and the convergence-galaxy cross-power spectrum estimator into account following an approach introduced by Scoccimarro et al. (1999). This led to a new term in each covariance which depends on the corresponding bin-averaged trispectrum in parallelogram configuration. The non-Gaussian terms contribute in contrast to the Gaussian terms to both diagonal and non-diagonal elements. We tested that for small bin width the non-Gaussian part can be computed as a simple one-dimensional angular average of the projected trispectrum.

For the theoretical predictions we considered a fiducial survey with a single source redshift $z_{\rm s} = 1$, intrinsic ellipticity dispersion of $\sigma_\epsilon = 0.22$ and a mean number density of background galaxies of $\bar{n} \simeq 30\,{\rm arcmin}$, where the last two components determine the amount of shape noise. To present the results, we considered the correlation coefficients r_{ij} which are independent of the survey area. Additionally, we employed a reference cosmology adapted to the Virgo simulation since they are used for a comparison of results from ray-tracing simulations and the dark matter halo model (Pielorz et al. 2009). The results were shown for 40 logarithmically-spaced bins in the range of $50 \leq l \leq 6000$ which are roughly the scales accessible to current experiments. Going to smaller scales, the influence of baryonic effects becomes important which are theoretically not well understood. We showed that the covariance of the convergence power spectrum on large scales ($l \lesssim 500$) has small off-diagonal elements and thus modeling the covariance with the Gaussian part is sufficient in this regime. However, the cross-correlations significantly increase on smaller scales up to $r_{ij} \simeq 0.6$ on the smallest considered scales which reflects

the fact that on small scales lensing is more affected by nonlinear clustering. Hence, in this regime it is mandatory to take the non-Gaussian part into account. The inclusion of shot noise significantly reduced the strength of cross-correlations for scales smaller than $l \simeq 10^3$.

To optimize the time for the calculation of the halo model trispectrum, we developed an approximation which is composed of the one-halo term of the trispectrum and the trispectrum in lowest-order perturbation theory. The former term is dominant on small scales, whereas the latter is dominant on large scales. We emphasized that it is convenient to adopt the approximation when the full halo model calculation of the covariance becomes computationally too costly. Comparison of the approximation to the full halo model calculation showed a good agreement in the considered range of scales. Naturally, for intermediate scales where the two- and three-halo term are important the approximation is less accurate. Furthermore, we analyzed the dependence of the covariance on the source redshift. A larger source redshift $z_s = 2$ resulted in a reduction of the cross-correlations.

In addition to the fiducial survey and background cosmology we needed to specify the lens redshift distribution for the covariance of the cross-power spectrum. We chose an RCS-like survey with foreground galaxies in the range $0 \le z_l \le 0.4$. Moreover, we considered three different minimal masses $m_{\min} = 10^{11} \, h^{-1} \, M_\odot$, $m_{\min} = 10^{12} \, h^{-1} \, M_\odot$ and $m_{\min} = 10^{13} \, h^{-1} \, M_\odot$ which define three different foreground galaxy samples of decreasing number density and showed that the correlation coefficients are reduced for larger minimal masses. In analogy to the convergence covariance, we developed an approximation of the non-Gaussian part. Subsequent comparisons revealed good agreement of the covariance calculated with the full halo model and the approximation for all three minimal masses.

Summary and Outlook

In this thesis we focused on the modeling of higher-order spectra of cosmological random fields, in particular galaxy and dark matter density fields, and on the interpretation of the results in terms of cosmological parameters. We applied these results to the study of two distinct projects related to galaxy-galaxy lensing (GGL) as a particular example of a powerful cosmological probe and to the analysis of higher-order galaxy-mass correlations. The GGL effect measures the distortion pattern of the images of background galaxies induced by weak gravitational lensing by individual foreground galaxies. Its main observational signature is the mean tangential alignment of the shear distortions of background galaxies around individual foreground galaxies. This signature can be used to study the bias between dark matter and galaxy clustering and to constrain the properties of dark matter halos.

In our first project, we have analyzed the recently proposed and measured method of galaxy-galaxy-galaxy lensing (GGGL) which is sensitive to the shear pattern around pairs of foreground galaxies and is thus a promising tool to constrain the properties of the environment of galaxy groups. We developed detailed theoretical predictions of the observational GGGL signal.

To study the predictive power of current and future GGL surveys, we dedicated our second project to the determination of statistical errors in matter-galaxy cross-power spectrum measurements. These results can be used to additionally constrain the errors of the GGL signal since it is a filtered version of the cross-power spectrum. We put the main focus on developing an analytical model which is applicable to the whole range of scales probed by observations.

For both projects an in-depth knowledge of the physics of nonlinear gravitational clustering is mandatory. We have devoted a significant part of this thesis, more precisely Chapters 2–4, gathering information from the literature to build a reliable theoretical model of gravitational clustering. The first important step toward the modeling of the nonlinear regime is addressed in Chapter 2. There we gave a comprehensive review on cosmological perturbation theory which provides an ansatz to solve the coupled dark matter fluid equations as long as the dark matter density contrast and the peculiar velocity field are small (following Bernardeau et al. 2002). Transforming the fluid equations into Fourier space revealed that in the linear regime different Fourier modes evolve independently of each other, whereas the nonlinear clustering induces a coupling of different Fourier modes. We showed that for an Einstein-de Sitter background Universe one can separate the time dependence of the equations and find a general solution in the single-flow approximation which is valid on large to intermediate scales. On small scales, however, the perturbative approach inevitably breaks down. In addition, we introduced

in Chapter 2 a statistical description of the Universe in terms of moments of random fields which are the so-called correlation functions in real space and spectra in Fourier space. The n-point correlation functions are the central observables to determine the statistical information of the Universe.

Studies of the small-scale regime either involve detailed numerical simulations, semi-analytic models or analytic models. In Chapter 3, we adopted an analytic model, the so-called halo model, which combines the results of cosmological perturbation theory on large scales with the well-known properties of dark matter halos on small scales. The properties of these halos are obtained from theoretical models and results from simulations. The main result of this chapter is that we can express general n-point correlation functions of the dark matter field in terms of the abundance of halos, the halo density profile and the clustering of halos.

To complete our theoretical description of the cosmological fields probed by GGL, we introduced in Chapter 4 the halo model for galaxy clustering. The model is an extension of the dark matter halo model with two additional ingredients, namely the halo occupation distribution (HOD) and the radial distribution of galaxies in their host halo. We adopted the approach that central and satellite galaxies give different statistical contributions to the HOD, following Kravtsov et al. (2004). In order to investigate the reliability of our halo model implementation, we calculated several three-dimensional spectra and compared our results to the literature when possible. We showed that the halo model predicts the observed scale dependence of the galaxy power spectrum, which approximately follows a single power law in wave-number k. On the other hand, we stressed that the dark matter power spectrum cannot be described by a single power law over the whole range of scales. This behavior is reflected in the scale dependence of the matter-galaxy bias. We illustrated that the bias converges to a constant on large scales and is strongly scale-dependent on small scales.

Most importantly for our two projects, we developed in Chapter 4 expressions for various galaxy-matter cross-spectra which can be obtained by a combination of the dark matter and galaxy halo models. In particular, we obtained explicit relations for the cross-power spectrum and for the first time for the two cross-bispectra $B^{\mathrm{gg}\delta}$ and $B^{\delta\delta\mathrm{g}}$, and the cross-trispectrum $T^{\delta\mathrm{g}\delta\mathrm{g}}$. The matter-galaxy cross-power spectrum has a similar scale dependence compared to the galaxy power spectrum. We explained these results in terms of the halo model since on small scales both spectra have the same dependence on the halo density profile. Subsequently, we studied the scale dependence of the four bispectra, namely the galaxy and dark matter auto-bispectra B^{ggg} and $B^{\delta\delta\delta}$, and the two cross-bispectra. In agreement with previous studies (e.g., Scoccimarro et al. 2001) we found that, on small scales, the reduced bispectra which include galaxy correlations decrease with the wave-number k, whereas the reduced dark matter bispectrum increases. We interpreted the difference of the bispectra in terms of the halo model, showing that on small scales the one-halo terms of the galaxy spectra are dominated by correlations with central galaxies. These correlations are weighted by two density profiles, in contrast to the dark matter bispectrum which is always weighted by three density profiles. This property of the halo model explains the

difference between galaxy and dark matter clustering on small scales. Comparing the scale dependence of the reduced dark matter trispectrum $T^{\delta\delta\delta\delta}$ to the matter-galaxy cross-spectrum $T^{\delta g \delta g}$, yielded the same qualitative behavior as observed for the reduced bispectra.

Since numerical simulations indicate a significant scatter in the concentration-mass relation of the halo density profile, we analyzed the impact of a stochastic concentration parameter on the various spectra. In general, the inclusion of a stochastic concentration led to an enhancement of the spectra on small scales compared to a deterministic concentration-mass relation. The enhancement is less pronounced for galaxy spectra and galaxy-matter cross-spectra as compared to dark matter spectra. The effect is most important for higher-order spectra which have a stronger dependence on the density profile. Thus, in subsequent analysis we only included the scatter for the dark matter trispectrum calculation.

In Chapter 5, we introduced the basic quantities needed to describe gravitational lensing. Subsequently, we presented cosmic shear as a powerful cosmological probe, e.g., it is one of the most promising tools to investigate the nature of dark energy. The shear spectra are obtained by projections (using Limber's approximation) of the corresponding three-dimensional dark matter spectra for which we adopted the halo model predictions as developed in Chapter 3. This chapter mainly serves as a reference for comparisons to the results obtained for GGL and GGGL in Chapter 6.

One of the main new results of this thesis is the modeling of the GGGL signal in terms of the aperture statistics, which are filtered versions of the two projected cross-bispectra $B_{\kappa\kappa g}$ and $B_{gg\kappa}$. We analyzed the dependence of the signal on various halo model input parameters such as the power-law quantifying the mean number of satellite galaxies contained in a halo of mass m, the radial distribution of galaxies in their host halo and the dependence on galaxy color. We discovered that, for small aperture radii, the galaxy-galaxy-mass correlations depend more strongly on the parameters than the mass-mass-galaxy correlations. This is due to the fact that the one-halo term of the former is weighted by the second-order moment of the HOD, whereas the latter is weighted by the first-order moment of the HOD. We stressed that fitting measurements of the GGGL signal with our halo model results can put tight constraints on physical models of galaxy formation. Moreover, we developed approximations for calculating the three-dimensional halo model bispectra which allow for a rapid exploration of the large parameter space of the halo model. The approximations deviate on small and large scales by less than 10 per cent from the full halo model, and they are less accurate on intermediate scales, where the deviation is up to 30 per cent.

Our second project, discussed in detail in Chapter 7, focused on the theoretical predictions of the statistical errors of GGL power spectrum measurements. The errors are determined by the covariance of the GGL power spectrum and also depend on the observed galaxy sample. We showed that the covariance of an unbiased cross-power spectrum estimator splits into a Gaussian part, which is proportional to the auto- and cross-power spectra, and a non-Gaussian part, which depends on the connected fourth-order moment. We modeled for the first time the non-Gaussian part and showed that it

introduces an enhancement of the diagonal elements of the total covariance. Additionally, it introduces significant non-diagonal elements on small scales, corresponding to cross-correlations of different Fourier mode bins. The amount of cross-correlations depends on the galaxy sample used, for example considering a survey with a larger angular number density results in an enhancement of cross-correlations. In addition, we developed an approximation for the time-consuming calculations of the cross-trispectrum which describes with good accuracy the large- and small-scale regimes of the covariance. The results can be used to perform likelihood analyses of GGL measurements which quantify how well future experiments can constrain cosmological parameters.

Outlook

Most of the ingredients of the halo model are directly obtained from numerical simulations. However, combining these ingredients to build general n-point spectra is a highly non-trivial task. The results of the halo model and simulations are roughly in agreement for two-point function predictions, i.e., for the power spectra and correlation functions (e.g., Pielorz et al. 2009). On the other hand, there are only few studies that compare the results from simulations and the halo model for the bispectra and trispectra. This is due to the fact that the simulations need to test the complete configuration dependence of the bispectra and trispectra. The bispectra and trispectra depend, considering homogeneous and isotropic random fields, on the three sides of the triangle and the four sides of the quadrilateral, respectively. Furthermore, these analyses require high-resolution and large-volume simulations since small box sizes have a deficit of massive halos which give the main contributions to higher-order spectra (Scoccimarro et al. 2001). Besides these difficulties, we need to test our main results for the covariance of the cross-power spectrum and for the GGGL aperture statistics against suited numerical simulations which are populated with galaxies following a semi-analytic model.

The next generation of galaxy and weak lensing surveys such as the RCS2[2] (ongoing; Yee et al. 2007), the SDSS-II (data already released in Abazajian et al. 2008), and the SDSS-III[3], especially the BOSS[4] project (taking data from 2008-2014; see Weinberg et al. 2007), will yield significantly improved measurements of the GGL and GGGL signals. In particular, we expect an enhancement of the observed number of galaxies and an optimization of the reconstruction of galaxy shapes. These improvements will lead to a reduction of shape and shot noise which currently dominate the error budget on small scales. Hence, to accurately estimate the amount of cross-correlations in the statistical errors of cross-power spectrum measurements (which are important on small scales), one should employ our approach for the non-Gaussian part of the sample-variance dominated covariance. The results of the full covariance, including the Gaussian and non-Gaussian parts, can be applied to make realistic forecasts of the ability of future

---

[2]`http://www.rcs2.org/`.
[3]`http://www.sdss3.org/`.
[4]Baryon Oscillation Spectroscopic Survey.

GGL surveys to constrain cosmological parameters. For example, studies of the cosmic shear power spectrum show that the inclusion of the non-Gaussian part results in a degradation of cosmological parameters constraints in comparison to employing the Gaussian approximation (Scoccimarro et al. 1999; Takada & Jain 2008). Due to the crucial role of the covariance in the estimation of parameter constraints, we plan to construct a fitting formula which significantly reduces the computation time of the covariance and is easy to employ. We can find a fitting function for the cross-power spectrum covariance using the same techniques that we already employed for the fitting function of the covariance of the convergence power spectrum (Pielorz et al. 2009). In addition, we would like to test the accuracy of our developed approximation of the non-Gaussian part of the covariance, which is composed of the one-halo term of the trispectrum and the trispectrum in lowest-order perturbation theory (times the squared large-scale bias parameter). Similar to the fitting formula, the approximation allows for a fast computation of the covariance, and it needs to be also tested against the results from numerical simulations. Another approach is to obtain the covariance directly from a number of realizations of ray-tracing simulations. However, this is very time consuming since one needs more than 1000 realizations to estimate the covariance to better than 10 per cent accuracy (Takahashi et al. 2009). To obtain the cosmological parameter dependence of the covariance with this approach is computationally even more demanding.

Since the next generation of galaxy and weak lensing surveys will measure the GGGL correlation functions to unprecedented accuracy, one can fit halo model parameters to the data using our developed halo model implementation. This will put important constraints on the halo occupation distribution and on the radial distribution of galaxies that are complementary to the results obtained from other cosmological probes like galaxy surveys.

A challenging future project is to extend the halo-model based approach for the determination of the information content of the power spectrum to higher-order spectra (e.g., Kilbinger & Schneider 2005 for a study of cosmic shear). As a particular example, we would like to study the covariance of the third-order aperture statistics of the GGGL signal using their full configuration dependence. This requires the modeling of connected correlators up to 6-order, which should be feasible using the halo-model based approach.

New results from simulations on the properties of dark matter halos, the HOD and the radial distribution of galaxies can be used to improve our theoretical model of dark matter and galaxy clustering. In addition, substantial progress has been recently made in the theoretical modeling of nonlinear gravitational clustering via cosmological perturbation theory (e.g., Crocce & Scoccimarro 2006; Smith et al. 2007; McDonald 2007). Up to now, this mainly has been used for the modeling of baryonic acoustic oscillations, but could be adapted and applied to gravitational lensing.

Measurements of GGGL correlation functions just have started since the cosmological origin of the signal has only recently been verified (Simon et al. 2008). We hope that our work can contribute to the theoretical modeling of future observational results.

Appendix A

General Background Information

We give in this appendix the general background information on our thesis project, namely our adopted sign convention of the Einstein equation in Sect. A.1, the astronomical units used in this thesis in Sect. A.2, and in Sect. A.3 the fiducial cosmological models used throughout this thesis.

A.1 Sign Convention in General Relativity

There is no accepted general sign convention for general relativity. The dynamic equations (i.e., the Friedmann equations) are invariant under these different conventions. Although one needs to be careful not to mix different conventions which can lead to "hard to spot" errors in the calculations. In general, one finds in the literature several sign conventions. For the sake of clarity, we will give a review of the essential quantities used in general relativity and point out the conventions that are used for our approach. We will follow here Peacock (1999).

The Minkowski metric of special relativity is

$$\eta^{\mu\nu} = \begin{pmatrix} 1 & 0 & 0 & 0 \\ 0 & -1 & 0 & 0 \\ 0 & 0 & -1 & 0 \\ 0 & 0 & 0 & -1 \end{pmatrix} . \tag{A.1}$$

One is free to introduce a global minus sign and choose instead $\eta^{\mu\nu} = \mathrm{diag}(-1, 1, 1, 1)$. This choice influences the global sign of the Robertson-Walker metric which then is given by

$$\mathrm{d}s^2 = c^2 \mathrm{d}t^2 - a^2(t) \left[\mathrm{d}w^2 + f_K^2(w) \mathrm{d}\Omega^2 \right] . \tag{A.2}$$

The Christoffel symbols that are needed for the calculation of the Einstein tensor are defined as

$$\Gamma^\mu_{\alpha\beta} = \frac{g^{\mu\nu}}{2} \left(g_{\alpha\nu,\beta} + g_{\beta\nu,\alpha} - g_{\alpha\beta,\nu} \right) , \tag{A.3}$$

which are symmetric in their two lower indices. Here and in the following we will denote covariant derivatives with

$$g_{\alpha\nu,\beta} \equiv \frac{\partial g_{\alpha\nu}}{\partial x^\beta} . \tag{A.4}$$

The Riemann tensor describes the curvature of a given manifold and is defined as

$$R^{\mu}_{\ \alpha\beta\gamma} = \Gamma^{\mu}_{\alpha\gamma,\beta} - \Gamma^{\mu}_{\alpha\beta,\gamma} + \Gamma^{\mu}_{\sigma\beta}\Gamma^{\sigma}_{\alpha\gamma} - \Gamma^{\mu}_{\sigma\gamma}\Gamma^{\sigma}_{\alpha\beta}\,, \tag{A.5}$$

where it is possible to change the global sign (e.g., Weinberg 1972). It has the following symmetries

$$R_{abcd} = -R_{bacd}\,, \qquad R_{abcd} = -R_{abdc}\,, \qquad R_{abcd} = R_{cdab}\,, \tag{A.6}$$

meaning that it is antisymmetric in the first and last two lower indices. Using the first relation, we find that the contraction

$$R^{a}_{\ acd} = g^{ab}R_{bacd} = -g^{ab}R_{abcd} = -R^{a}_{\ acd} = 0 \tag{A.7}$$

vanishes. The Ricci tensor is thus defined as a different contraction

$$R_{\mu\nu} = -R^{\alpha}_{\ \mu\alpha\nu} = R^{\alpha}_{\ \mu\nu\alpha}\,, \tag{A.8}$$

where we note that two different definitions of the contraction lead to different signs. The Ricci scalar is the contraction of both indices of the Ricci tensor:

$$R = g^{\mu\nu}R_{\mu\nu}\,. \tag{A.9}$$

Using these conventions, leads to the Einstein equation

$$G_{\mu\nu} = -\frac{8\pi G_N}{c^4}T_{\mu\nu}\,, \tag{A.10}$$

where the Einstein tensor is

$$G_{\mu\nu} = R_{\mu\nu} - \frac{1}{2}Rg_{\mu\nu} + \Lambda g_{\mu\nu}\,, \tag{A.11}$$

and the energy-momentum tensor of a perfect fluid

$$T^{\mu\nu} = (\rho + p/c^2)u^{\mu}u^{\nu} - p\eta^{\mu\nu}\,. \tag{A.12}$$

A.2 Important Astrophysical Constants

We give in the following a list of the astrophysical constants used in this work:

- Solar mass $\qquad M_{\odot} = 1.9889 \times 10^{30}\,\mathrm{kg}$

- Parsec $\qquad 1\mathrm{pc} = 3.085677581 \times 10^{16}\,\mathrm{m} = 3.262\,\mathrm{ly}$

- Newtons constant $\qquad G_N = 6.673 \times 10^{-11}\,\mathrm{m^3\,kg^{-1}\,s^{-2}}$

- Critical density today $\qquad \rho_{\mathrm{crit}} = \frac{3H_0^2}{8\pi G_N} \approx 2.775 \times 10^{11}\,h^2\,M_{\odot}\,\mathrm{Mpc}^{-3}$

A.3 Fiducial Cosmological Model

In this work we applied two fiducial cosmological models, and we present the adopted parameters in Table A.1. We used *Model A* in Chapter 3 and Chapter 4, where we presented the results of the various three-dimensional spectra. We applied *Model B* in the two chapters, which give the main new results of this thesis, namely Chapter 6 where we discuss galaxy-galaxy lensing and higher-order galaxy-mass correlations, and Chapter 7 which gives results for the covariance of the projected cross-power spectrum.

Table A.1: Cosmological parameters of our two adopted fiducial models.

	Model A	Model B
Cosmological parameters		
Ω_{m}	0.28	0.3
Ω_{Λ}	0.72	0.7
Ω_{b}	0.046	-
Γ	-	0.21
σ_8	0.8	0.9
n_{s}	0.96	1
Halo model parameters		
$\Delta_{\mathrm{vir}}(0)$	200	334
$\delta_{\mathrm{c}}(0)$	1.686	1.686
p	0.3	0.3
q	0.707	0.707
α	0.13	0.13
c_0	11	9
HOD model parameters		
A_{s}	20	30
β	1	1
$\sigma_{\ln m}$	0.2	0.1
Source redshift distribution		
z_0	-	1
β	-	-

The table is divided in cosmological parameters that characterize the homogeneous and isotropic background Universe (given in Chapter 1), dark matter halo model parameters (given in Chapter 3), galaxy HOD parameters (given in Chapter 4) and source redshift distribution parameters (given in Chapter 5). The cosmological parameters of *Model A* are adopted following the latest WMAP 5-year release (Komatsu et al. 2009), whereas

we use the parameters of *Model B* since the same model is adopted for the first results of the galaxy-galaxy-galaxy lensing signal (Simon et al. 2008) and of many numerical N-body simulations (here we use the cosmology of the Virgo simulation).

For the cosmological parameters we consider the matter density parameter Ω_m and the density parameter of a cosmological constant Ω_Λ, which determine the Hubble expansion via the Friedmann equation (1.25). Furthermore, we give the baryon density parameter Ω_b or the shape parameter Γ depending on the adopted transfer function (Eisenstein & Hu 1998 or Bardeen et al. 1986). The linear dark matter power spectrum (2.161) is specified by the amplitude σ_8 and the spectral index of the primordial power spectrum n_s (see Eq. 2.163).

The first depicted halo model parameters are related to the spherical collapse model, namely the linear density contrast at the time of collapse δ_c and the density ratio of a virialized halo Δ_vir (see Eqs. 3.18 and 3.21). For the halo mass function we applied the parametrization of Sheth & Tormen (1999) with the parameters p and q (see Eq. 3.36). Finally, we give the parameters of the power law of the concentration-mass relation with the amplitude c_0 and the slope α following Bullock et al. (2001) (see Eq. 3.62). Our fiducial halo occupation distribution model follows the Kravtsov et al. (2004) approach, which assumes that central and satellite galaxies give two statistically different contributions to the mean number of galaxies. The mean number of central galaxies follows a smooth-out step function with scatter $\sigma_{\ln m}$ (see Eq. 4.13) and mean number of satellite galaxies is described by a power law with amplitude A_s and slope β (see Eq. 4.14).

To get the cosmic shear and galaxy-galaxy lensing spectra, we have to perform projections of the corresponding three-dimensional spectra. For the projections we need to give a redshift distribution of the sources (see Eq. 5.67). We consider for simplicity that all sources are located at a single redshift $z_\mathrm{s} \equiv z_0$ in both fiducial models.

Appendix B

Perturbation Theory and Halo Model

B.1 Perturbative Solution to the Spherical Collapse Model

This discussion follows mainly the work in Fosalba & Gaztanaga (1998). We already discussed the equation of motion of a spherical mass distribution in Sect. 3.1. It is given by

$$\frac{\mathrm{d}^2 r}{\mathrm{d}t^2} = -\frac{G_N M(r)}{r^2} = -\frac{4\pi}{3} G_N \rho r \,, \tag{B.1}$$

where we adopt that the mass is confined to a spherical region in the second step. We can define a spherical density perturbation δ according to

$$(1 + \delta) = \left(\frac{r(a)}{r_0}\right)^{-3} = \left(\frac{r}{ar_0}\right)^{-3} \,. \tag{B.2}$$

Rewriting the equation of motion in terms of δ with the use of both Friedmann equations (Eqs. 1.25 and 1.13), yields the differential equation

$$\ddot{\delta} + 2H\dot{\delta} - \frac{4}{3}\frac{\dot{\delta}^2}{1 + \delta} = \frac{3}{2}\Omega_\mathrm{m}(a)H^2\delta(1 + \delta) \,. \tag{B.3}$$

For the numerical solution of the equation it is useful to introduce the new variable $\eta = \ln a$. For an EdS universe we obtain then

$$\delta'' + \frac{1}{2}\delta' - \frac{3}{2}\delta = \frac{4}{3}\frac{(\delta')^2}{1 + \delta} + \frac{3}{2}\delta^2 \,, \tag{B.4}$$

where $\delta' \equiv \mathrm{d}\delta/\mathrm{d}\eta$. For $\delta_\mathrm{lin} \ll 1$ we can make the following power series ansatz

$$\delta(\delta_\mathrm{lin}) = \sum_{n=1}^{\infty} \frac{a_n}{n!}(\delta_\mathrm{lin})^n \,. \tag{B.5}$$

Note that for an EdS universe we have $\delta_\mathrm{lin} = a = \mathrm{e}^\eta$ and the initial condition $a_1 = 1$. We find for the next three coefficients

$$a_2 = \frac{34}{21}, \quad a_3 = \frac{682}{189}, \quad a_4 = \frac{446440}{43659} \,. \tag{B.6}$$

Note that the power-series ansatz is only valid for $\delta_\mathrm{lin} \ll 1$, i.e., in the quasilinear regime. But it is also possible to find a solution for all scales.

B.2 Helmholtz's Theorem

Helmholtz's theorem states that any differentiable vector field $\boldsymbol{v}(\boldsymbol{r})$ can be decomposed into a curl-free part $\boldsymbol{v}_\parallel$ and a divergence-free part $\boldsymbol{v}_\perp$ such that $\boldsymbol{v}(\boldsymbol{r}) = \boldsymbol{v}_\parallel(\boldsymbol{r}) + \boldsymbol{v}_\perp(\boldsymbol{r})$. A curl-free field can be represented by the scalar potential ϕ with $\boldsymbol{v}_\parallel = -\nabla\phi$ and a divergence-free field by the vector potential $\boldsymbol{A}$ with $\boldsymbol{v}_\perp = \nabla \times \boldsymbol{A}$. Hence, the decomposition of a general vector field is

$$\boldsymbol{v} = -\nabla\phi + \nabla \times \boldsymbol{A}\,. \tag{B.7}$$

This decomposition is used heavily in physics. For example, the decomposition of the electric field into contributions from electrostatics described by a scalar potential and the divergence-free magnetic field.

   The proof of this theorem is made by construction. We define the fields θ and $\boldsymbol{w}$ as the divergence and the curl of the known field $\boldsymbol{v}$, respectively:

$$\nabla \cdot \boldsymbol{v} \equiv \theta\,, \tag{B.8}$$

$$\nabla \times \boldsymbol{v} \equiv \boldsymbol{w}\,. \tag{B.9}$$

The two potentials can be calculated from this new fields using the relations

$$\phi(\boldsymbol{r}) = \frac{1}{4\pi} \int \frac{\theta(\boldsymbol{r}')}{|\boldsymbol{r} - \boldsymbol{r}'|}\, \mathrm{d}^3 r'\,, \qquad \boldsymbol{A}(\boldsymbol{r}) = \frac{1}{4\pi} \int \frac{\boldsymbol{w}(\boldsymbol{r}')}{|\boldsymbol{r} - \boldsymbol{r}'|}\, \mathrm{d}^3 r'\,. \tag{B.10}$$

Using the identity

$$\nabla^2 \left(\frac{1}{|\boldsymbol{r} - \boldsymbol{r}'|} \right) = -4\pi \delta_\mathrm{D}(\boldsymbol{r} - \boldsymbol{r}')\,, \tag{B.11}$$

we easily verify Eq. (B.8). To prove the second relation (B.9), we need the following calculus identity

$$\nabla \times \boldsymbol{v} = \nabla \times (\nabla \times \boldsymbol{A}) = -\nabla(\nabla \cdot \boldsymbol{A}) + \nabla^2 \boldsymbol{A}\,. \tag{B.12}$$

The first term is equal to zero which can be shown by integration by parts. The second term can be treated analogously to the first proof and we finally get $\nabla \times \boldsymbol{v}(\boldsymbol{r}) = \boldsymbol{w}(\boldsymbol{r})$. For a complete discussion of Helmholtz's theorem we refer to Arfken & Weber (2001). In particular, this decomposition is helpful for the evolution equations of structure formation.

B.3 Divergent Terms of the Tree-Level Trispectrum

The problematic terms in the trispectrum (see Eq. 2.130) are

$$\begin{aligned} T_\mathrm{pt} \propto\; & P_1 P_3 P_{12} F_2(\boldsymbol{k}_1, -\boldsymbol{k}_{12}) F_2(\boldsymbol{k}_3, \boldsymbol{k}_{12}) + P_1 P_4 P_{12} F_2(\boldsymbol{k}_1, -\boldsymbol{k}_{12}) F_2(\boldsymbol{k}_4, \boldsymbol{k}_{12}) \\ & + P_2 P_3 P_{12} F_2(\boldsymbol{k}_2, -\boldsymbol{k}_{12}) F_2(\boldsymbol{k}_3, \boldsymbol{k}_{12}) + P_2 P_4 P_{12} F_2(\boldsymbol{k}_2, -\boldsymbol{k}_{12}) F_2(\boldsymbol{k}_4, \boldsymbol{k}_{12})\,, \end{aligned} \tag{B.13}$$

where $P_i \equiv P_{\mathrm{pt}}(k_i)$, $P_{ij} \equiv P_{\mathrm{pt}}(|\boldsymbol{k}_i + \boldsymbol{k}_j|)$ and $\boldsymbol{k}_{ij} \equiv \boldsymbol{k}_i + \boldsymbol{k}_j$. In the case of a parallelogram configuration one gets

$$
\begin{aligned}
T_{\mathrm{pt}} \propto\ & P_1 P_3 P_\epsilon F_2(\boldsymbol{k}_1, -\boldsymbol{\epsilon}) F_2(\boldsymbol{k}_3, \boldsymbol{\epsilon}) + P_1 P_3 P_\epsilon F_2(\boldsymbol{k}_1, -\boldsymbol{\epsilon}) F_2(-\boldsymbol{k}_3, \boldsymbol{\epsilon}) \\
& + P_1 P_3 P_\epsilon F_2(-\boldsymbol{k}_1, -\boldsymbol{\epsilon}) F_2(\boldsymbol{k}_3, \boldsymbol{\epsilon}) + P_1 P_3 P_\epsilon F_2(-\boldsymbol{k}_1, -\boldsymbol{\epsilon}) F_2(-\boldsymbol{k}_3, \boldsymbol{\epsilon}) ,
\end{aligned}
\tag{B.14}
$$

with the limit $\epsilon \to 0$. All divergent terms cancel and the remaining ones are equal to zero. This is easy to show when one assigns a variable to each of the three terms of F_2 (see Eq. 2.75). For example

$$
F_2(\boldsymbol{k}_1, -\boldsymbol{\epsilon}) = \frac{5}{7} - \frac{1}{2} \frac{\boldsymbol{k}_1 \cdot \boldsymbol{\epsilon}}{k_1 \epsilon} \left(\frac{k_1}{\epsilon} + \frac{\epsilon}{k_1} \right) + \frac{2}{7} \frac{(\boldsymbol{k}_1 \cdot \boldsymbol{\epsilon})^2}{k_1^2 \epsilon^2} \equiv A - B + C ,
\tag{B.15}
$$

$$
F_2(\boldsymbol{k}_3, \boldsymbol{\epsilon}) = \frac{5}{7} + \frac{1}{2} \frac{\boldsymbol{k}_3 \cdot \boldsymbol{\epsilon}}{k_3 \epsilon} \left(\frac{k_3}{\epsilon} + \frac{\epsilon}{k_3} \right) + \frac{2}{7} \frac{(\boldsymbol{k}_3 \cdot \boldsymbol{\epsilon})^2}{k_3^2 \epsilon^2} \equiv A + D + E ,
\tag{B.16}
$$

and similar for the other terms. The second term of both equations (denoted by the variables B and D) is divergent as ϵ goes to zero. But these terms cancel with each other:

$$
\begin{aligned}
T_{\mathrm{pt}} \propto\ & (A - B + C)(A + D + E) + (A - B + C)(A - D + E) \\
& + (A + B + C)(A + D + E) + (A + B + C)(A - D + E) \\
= \ & 4A^2 + 4AE + 4CA + 4CE .
\end{aligned}
\tag{B.17}
$$

The remaining terms vanish because they are multiplied with $P_0 = 0$.

B.4 Hierarchical Model of Higher-Order Correlation Functions

In the *hierarchical model* the connected N-point correlation function ξ_N resolves into a number of products of two-point correlation functions (e.g., Peebles 1980; Fry 1984):

$$
\xi_N \equiv \langle \delta(\boldsymbol{x}_1) \cdots \delta(\boldsymbol{x}_N) \rangle_{\mathrm{c}} = \sum_{a=1}^{T(N)} Q_{N,a} \sum_{\mathrm{labelings}} \prod_{\mathrm{edges}}^{N-1} \xi_{ij} = Q_N \sum_{a=1}^{T(N)} \sum_{\mathrm{labelings}} \prod_{\mathrm{edges}}^{N-1} \xi_{ij} ,
\tag{B.18}
$$

where each different contribution is weighted by the constant factors $Q_{N,a}$. The product runs over all $N-1$ connections or edges that link the N positions, where each connection stands for a two-point correlation function $\xi_{ij} \equiv \xi(\boldsymbol{x}_i, \boldsymbol{x}_j)$ (see also Fig. 2.1). These links thus form in the language of quantum field theory a tree-like structure. The first sum runs over the number of trees with different topologies, where $T(2) = 1$, $T(3) = 1$, $T(4) = 2$, ... The second sum runs for each tree over the number of possible relabelings. In the second step, we assumed that each topologically different tree has the same constant Q. In this model the reduced three-point correlation function is given by

$$
\langle \delta(\boldsymbol{x}_1) \delta(\boldsymbol{x}_2) \delta(\boldsymbol{x}_3) \rangle_{\mathrm{c}} = Q[\xi_{12}\xi_{23} + \xi_{12}\xi_{13} + \xi_{13}\xi_{23}] .
\tag{B.19}
$$

This model was successfully applied to early angular galaxy surveys which led to the conjecture that the model also applies to higher-order correlation functions (Groth & Peebles 1977; Fry & Peebles 1978). However, newer observational results show that the hierarchical model does not hold meaning that Q becomes configuration dependent. Nevertheless, the configuration dependence of Q is much smaller than the dependence of the correlation functions and spectra. This is the basis for the definition of the reduced correlation functions and spectra (e.g., Eq. 4.71).

We consider now the four-point cross-correlation function which is defined by $\eta_{\delta g \delta g} = \langle \delta(\boldsymbol{x}_1)\delta_g(\boldsymbol{x}_2)\delta(\boldsymbol{x}_3)\delta_g(\boldsymbol{x}_4)\rangle_c$ in detail, where we place two galaxies at the positions $\boldsymbol{x}_2$ and $\boldsymbol{x}_4$ and probe the dark matter field at the positions $\boldsymbol{x}_1$ and $\boldsymbol{x}_3$. We show all different diagrams that contribute to the four-point function. In addition, we transform each product of two-point correlation functions into Fourier space. Hence, in the end we have a representation of the cross-trispectrum in the hierarchical model. The cross-trispectrum consists of two different contributions which we call "snake" (joining 4 points by an unbroken line) and "star" (joining three points to a common fourth one) diagrams. We show the contribution of each term in the following first in real space and then give its Fourier transform:

$$\equiv \xi_{12}^{g\delta}\xi_{23}^{g\delta}\xi_{34}^{g\delta} \to P_1^{g\delta}P_{12}^{g\delta}P_4^{g\delta} \qquad \equiv \xi_{12}^{g\delta}\xi_{23}^{g\delta}\xi_{14}^{g\delta} \to P_{14}^{g\delta}P_3^{g\delta}P_4^{g\delta}$$

$$\equiv \xi_{12}^{g\delta}\xi_{14}^{g\delta}\xi_{34}^{g\delta} \to P_2^{g\delta}P_{12}^{g\delta}P_3^{g\delta} \qquad \equiv \xi_{14}^{g\delta}\xi_{34}^{g\delta}\xi_{23}^{g\delta} \to P_1^{g\delta}P_{14}^{g\delta}P_2^{g\delta}$$

$$\equiv \xi_{14}^{g\delta}\xi_{24}^{gg}\xi_{23}^{g\delta} \to P_1^{g\delta}P_{14}^{gg}P_3^{g\delta} \qquad \equiv \xi_{14}^{g\delta}\xi_{13}^{\delta\delta}\xi_{23}^{g\delta} \to P_4^{g\delta}P_{14}^{\delta\delta}P_2^{g\delta}$$

$$\equiv \xi_{12}^{g\delta}\xi_{24}^{gg}\xi_{34}^{g\delta} \to P_1^{g\delta}P_{12}^{gg}P_3^{g\delta} \qquad \equiv \xi_{12}^{g\delta}\xi_{13}^{\delta\delta}\xi_{34}^{g\delta} \to P_2^{g\delta}P_{12}^{\delta\delta}P_4^{g\delta}$$

$$\equiv \xi_{12}^{g\delta}\xi_{24}^{gg}\xi_{13}^{\delta\delta} \to P_{13}^{g\delta}P_4^{gg}P_3^{\delta\delta} \qquad \equiv \xi_{13}^{\delta\delta}\xi_{24}^{gg}\xi_{23}^{g\delta} \to P_1^{\delta\delta}P_4^{gg}P_{13}^{g\delta}$$

$\boldsymbol{x}_1 \quad \boldsymbol{x}_2$

$\boldsymbol{x}_4 \quad \boldsymbol{x}_3$
$\equiv \xi_{13}^{\delta\delta}\xi_{24}^{\mathrm{gg}}\xi_{34}^{\mathrm{g}\delta} \to P_1^{\delta\delta}P_2^{\mathrm{gg}}P_{13}^{\mathrm{g}\delta}$

$\boldsymbol{x}_1 \quad \boldsymbol{x}_2$

$\boldsymbol{x}_4 \quad \boldsymbol{x}_3$
$\equiv \xi_{13}^{\delta\delta}\xi_{14}^{\mathrm{g}\delta}\xi_{24}^{\mathrm{gg}} \to P_3^{\delta\delta}P_{13}^{\mathrm{g}\delta}P_2^{\mathrm{gg}}$

$\boldsymbol{x}_1 \quad \boldsymbol{x}_2$

$\boldsymbol{x}_4 \quad \boldsymbol{x}_3$
$\equiv \xi_{12}^{\mathrm{g}\delta}\xi_{14}^{\mathrm{g}\delta}\xi_{13}^{\delta\delta} \to P_2^{\mathrm{g}\delta}P_4^{\mathrm{g}\delta}P_3^{\delta\delta}$

$\boldsymbol{x}_1 \quad \boldsymbol{x}_2$

$\boldsymbol{x}_4 \quad \boldsymbol{x}_3$
$\equiv \xi_{12}^{\mathrm{g}\delta}\xi_{24}^{\mathrm{gg}}\xi_{23}^{\mathrm{g}\delta} \to P_1^{\mathrm{g}\delta}P_4^{\mathrm{gg}}P_3^{\mathrm{g}\delta}$

$\boldsymbol{x}_1 \quad \boldsymbol{x}_2$

$\boldsymbol{x}_4 \quad \boldsymbol{x}_3$
$\equiv \xi_{13}^{\delta\delta}\xi_{23}^{\mathrm{g}\delta}\xi_{34}^{\mathrm{g}\delta} \to P_1^{\delta\delta}P_2^{\mathrm{g}\delta}P_4^{\mathrm{g}\delta}$

$\boldsymbol{x}_1 \quad \boldsymbol{x}_2$

$\boldsymbol{x}_4 \quad \boldsymbol{x}_3$
$\equiv \xi_{14}^{\mathrm{g}\delta}\xi_{24}^{\mathrm{gg}}\xi_{34}^{\mathrm{g}\delta} \to P_1^{\mathrm{g}\delta}P_2^{\mathrm{gg}}P_3^{\mathrm{g}\delta}$
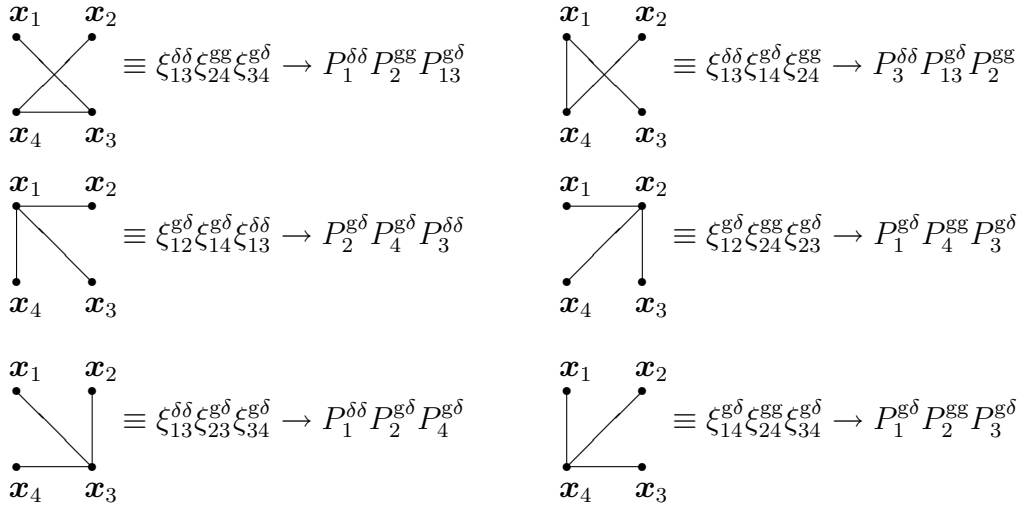
We used the compact notation $\xi_{ij}^{AB} \equiv \langle \delta_A(\boldsymbol{x}_i)\delta_B(\boldsymbol{x}_j)\rangle$, $P_i^{AB} \equiv P^{AB}(k_i)$ and $P_{ij}^{AB} \equiv P^{AB}(|\boldsymbol{k}_i + \boldsymbol{k}_j|)$, where $A, B \in \{\mathrm{g}, \delta\}$. In the parallelogram configuration four snake terms vanish and the rest of the terms can be partially combined to yield Eqs. (4.96) and (4.97).

B.5 Smoothing of Gaussian Random Fields

The dark matter density field needs to be smoothed with a filter function W_R of a given size R when one wants to compare with results obtained from observations and simulations which are limited to a specific resolution. The smoothing of the density field in real space is a convolution

$$\delta_R(\boldsymbol{x}) = \int \mathrm{d}^3 y\, W_R(|\boldsymbol{y} - \boldsymbol{x}|)\delta(\boldsymbol{y})\,. \tag{B.20}$$

Transforming this relation into Fourier space and using the convolution theorem yields

$$\delta_R(\boldsymbol{k}) = W_R(\boldsymbol{k})\delta(\boldsymbol{k})\,. \tag{B.21}$$

The smoothed density field is still a Gaussian random field because the integral can be seen as a sum of Gaussian random variables. For the filter one usually takes a Gaussian or spherically-symmetric top-hat function. Here we will use the top-hat function which is given by

$$W_R(x) = \begin{cases} 3/(4\pi R^3) & \text{for } x \le R\,, \\ 0 & \text{for } x > R\,. \end{cases} \tag{B.22}$$

Note that the top-hat function is defined such that it is normalized to unity. The Fourier transform of the top-hat function is

$$W_R(k) = \frac{3}{(kR)^3}[\sin(kR) - kR\cos(kR)]\,. \tag{B.23}$$

Then the filtered power spectrum is

$$P_R(k) = P(k)W_R^2(k) \, . \tag{B.24}$$

The result of this procedure is a Gaussian random field with variance

$$\sigma_R^2(m) = \int \frac{\mathrm{d}k}{k} \frac{k^3 P(k, z=0)}{2\pi^2} |W_R(k)|^2 \, . \tag{B.25}$$

B.6 Implementation of the Halo Mass Function

For programming it is useful to rewrite the definition of the mass function in Eq. (3.33) as

$$\frac{\mathrm{d}n}{\mathrm{d}\ln m} = \frac{\bar{\rho}}{m} \nu f(\nu) \frac{\mathrm{d}\ln\sigma^{-1}}{\mathrm{d}\ln m} \, . \tag{B.26}$$

The next step is to calculate

$$\frac{\mathrm{d}\ln\sigma^{-1}}{\mathrm{d}\ln m} = -\frac{m}{2\sigma^2} \int \frac{\mathrm{d}k}{k} \Delta(k, z=0) \frac{\mathrm{d}}{\mathrm{d}m} |W(kR)|^2 \, . \tag{B.27}$$

Finally, we rewrite the mass derivative as:

$$\frac{\mathrm{d}}{\mathrm{d}m} |W(kR)|^2 = \frac{\mathrm{d}(kR)}{\mathrm{d}m} \frac{\mathrm{d}}{\mathrm{d}(kR)} |W(kR)|^2 = \frac{\mathrm{d}(kR)}{\mathrm{d}m} 2W(kR) \frac{\mathrm{d}W}{\mathrm{d}(kR)} \, ,$$

and perform the derivative of the weight function

$$\frac{\mathrm{d}W}{\mathrm{d}x} = 3\frac{\sin x}{x^2} - 9\frac{\sin x - x\cos x}{x^4} \qquad \text{and} \qquad \frac{\mathrm{d}R}{\mathrm{d}m} = \frac{1}{R^2 4\pi\bar{\rho}} \, .$$

B.7 Central Galaxy Contribution

In this section we will investigate the impact of a central galaxy population on the small-scale clustering of galaxies following the derivation in Cooray & Sheth (2002) and Smith et al. (2006). First, we derive the behavior for a general HOD and then adopt the Kravtsov et al. (2004) parametrization described in Sect. 4.1.1.

Let us consider that we have a halo of mass m containing N galaxies. In addition, we assume that one galaxy is always placed in the center of the halo and the other (satellite) galaxies are placed around the center. Using this setup, we first consider the effect on the correlation of two points in a single halo. In this halo we have $(N-1)$ central-satellite correlations and $(N-1)(N-2)/2$ satellite-satellite correlations. Pairs that include the central galaxy are weighted by the density profile, whereas satellite pairs are weighted by the squared density profile. This is due to the fact that the probability of finding a satellite galaxy at distance $\boldsymbol{r}$ from the center follows the density profile of galaxies. We define for the following discussion the weight factor

$$W^{\mathrm{nc}}(k_1, k_2, m) \equiv \langle N(N-1)(m)\rangle \tilde{u}_{\mathrm{g}}(k_1, m)\tilde{u}_{\mathrm{g}}(k_2, m) \, . \tag{B.28}$$

Setting in this expression $k_1 = k_2 \equiv k$ we get the weight factor for the one-halo term of the galaxy power spectrum (see Eq. 4.26). Including a central galaxy this weight factor is replaced by

$$
\begin{aligned}
W_{12}^{\mathrm{g}}(m) &= 2! \sum_{N>1} P(N|m) \left[\frac{(N-1)}{2}(\tilde{u}_1 + \tilde{u}_2) + \frac{1}{2}(N-1)(N-2)\tilde{u}_1\tilde{u}_2 \right] \\
&= \sum_{N>1} P(N|m) \left[N(N-1)\tilde{u}_1\tilde{u}_2 + (N-1)(\tilde{u}_1 + \tilde{u}_2 - 2\tilde{u}_1\tilde{u}_2) \right] \\
&= \langle N(N-1)(m)\rangle \tilde{u}_1\tilde{u}_2 + [\langle N(m)\rangle - 1 + P(0|m)][\tilde{u}_1 + \tilde{u}_2 - 2\tilde{u}_1\tilde{u}_2], \quad \text{(B.29)}
\end{aligned}
$$

where we employed the short-hand notation $\tilde{u}_i \equiv \tilde{u}_{\mathrm{g}}(k_i, m)$ and $W_{12}^{\mathrm{g}}(m) \equiv W^{\mathrm{g}}(k_1, k_2, m)$. Note that the sum starts from $N > 1$ because we consider correlations of pairs and thus there must be at least two galaxies in the halo. The factor of 2! is introduced because the term $\tilde{u}_{\mathrm{g}}\tilde{u}_{\mathrm{g}}$ is normalized by the total number of pairs including double counting. Furthermore, we have to symmetrize the central-satellite correlations in order to ensure that the weight function is symmetric in the two wave-numbers, i.e., $W^{\mathrm{g}}(k_1, k_2, m) = W^{\mathrm{g}}(k_2, k_1, m)$ which results here in a factor of $1/2$. In the last step we used the definition of the first- and second-order moments of the HOD given in Eqs. (4.6) and (4.7), and the relation

$$
\begin{aligned}
\sum_{N>1}^{\infty}(N-1)P(N|m) &= \sum_{N=1}^{\infty} NP(N|m) - P(1|m) - \sum_{N=0}^{\infty} P(N|m) + P(0|m) + P(1|m) \\
&= \langle N(m)\rangle - 1 + P(0|m), \quad \text{(B.30)}
\end{aligned}
$$

where we used the normalization of the HOD, $\sum_{N=0}^{\infty} P(N|m) = 1$, and the definition of the first moment in the second step. Here $P(0|m)$ is the probability of finding no galaxies in a halo of mass m. Applying the HOD parametrization of Kravtsov et al. (2004) which separates the contributions from central and satellite galaxies we showed that the first- and second-order moments are given by

$$
\langle N(m)\rangle = \bar{N}_{\mathrm{sat}} + \bar{N}_{\mathrm{cen}}, \quad \text{(B.31)}
$$

$$
\langle N(N-1)(m)\rangle = \bar{N}_{\mathrm{sat}}^2 + 2\bar{N}_{\mathrm{cen}}\bar{N}_{\mathrm{sat}}. \quad \text{(B.32)}
$$

In addition to these moments, we need a model for the probability of $P(0|m)$. When the number of galaxies in a halo is large we can set $P(0|m) = 0$. On the other hand, if the number of galaxies in the halo is very small, the HOD is dominated by the central galaxy. The central galaxy population in a halo follows a Bernoulli distribution because there is either one central or none:

$$
P_{\mathrm{cen}}(1|m) = 1 - P_{\mathrm{cen}}(0|m) = \bar{N}_{\mathrm{cen}} \equiv \sum_{N=1}^{\infty} NP_{\mathrm{cen}}(N|m), \quad \text{(B.33)}
$$

where in the last two steps we used the fact that we have only one central galaxy per halo implying that $P_{\mathrm{cen}}(2|m) = P_{\mathrm{cen}}(3|m) = \ldots = 0$. In the following we set for

simplicity $\bar{N}_{\mathrm{cen}} = \Theta(m - m_{\mathrm{min}})$. In this case we find

$$W_{12}^{\mathrm{g}}(m) = \bar{N}_{\mathrm{sat}}^2 \tilde{u}_{\mathrm{g}}(k_1, m) \tilde{u}_{\mathrm{g}}(k_2, m) + \bar{N}_{\mathrm{sat}}[\tilde{u}_{\mathrm{g}}(k_1, m) + \tilde{u}_{\mathrm{g}}(k_2, m)], \qquad (B.34)$$

When we want to apply this weighting to the one-halo term of the power spectrum we need to set $k_1 = k_2 \equiv k$.

Next we consider the weight factor of triplets of galaxies in a single halo which is needed for the one-halo term of the galaxy bispectrum (see Eq. 4.55):

$$W^{\mathrm{nc}}(k_1, k_2, k_3, m) \equiv \langle N(N-1)(N-2)(m) \rangle \tilde{u}_{\mathrm{g}}(k_1, m) \tilde{u}_{\mathrm{g}}(k_2, m) \tilde{u}_{\mathrm{g}}(k_3, m). \qquad (B.35)$$

With the same setup as above we have $(N-1)(N-2)/2$ central-satellite-satellite correlations and $(N-1)(N-2)(N-3)/6$ satellite-satellite-satellite-correlations giving

$$\begin{aligned}
W_{123}^{\mathrm{g}}(m) = 3! \sum_{N>2} P(N|m) &\left\{ \frac{1}{6}(N-1)(N-2)(\tilde{u}_1\tilde{u}_2 + \tilde{u}_1\tilde{u}_3 + \tilde{u}_2\tilde{u}_3) \right. \\
&\left. + \frac{1}{6}(N-1)(N-2)(N-3)\tilde{u}_1\tilde{u}_2\tilde{u}_3 \right\} \\
= \sum_{N>2} P(N|m) &\left\{ \left[N(N-1)(N-2) - 3N(N-1) + 6(N-1)\right]\tilde{u}_1\tilde{u}_2\tilde{u}_3 \right. \\
&\left. + \left[N(N-1) - 2(N-1)\right](\tilde{u}_1\tilde{u}_2 + \tilde{u}_1\tilde{u}_3 + \tilde{u}_2\tilde{u}_3) \right\} \\
= \langle N(N-1)&(N-2)(m) \rangle \tilde{u}_1\tilde{u}_2\tilde{u}_3 \\
&+ 6\left[\frac{1}{2}\langle N(N-1)(m) \rangle - \langle N(m) \rangle + 1 - P(0|m)\right] \\
&\times \left[\frac{1}{3}(\tilde{u}_1\tilde{u}_2 + \tilde{u}_1\tilde{u}_3 + \tilde{u}_2\tilde{u}_3) - \tilde{u}_1\tilde{u}_2\tilde{u}_3\right], \qquad (B.36)
\end{aligned}$$

where $W_{123}^{\mathrm{g}}(m) = W^{\mathrm{g}}(k_1, k_2, k_3, m)$. The factor of 3! accounts for the fact that the profiles are normalized by the total number of triplets including repetition. The sum is for $N > 2$ because there must be at least 3 galaxies in the halo to calculate the three-point correlation function. Again, we have to symmetrize the central-satellite-satellite correlations in order to ensure that the weight function is symmetric in its three wave-numbers which results here in a factor of $1/3$. Employing Eq. (4.17) for the third-order moment results in

$$\begin{aligned}
W_{123}^{\mathrm{g}}(m) = \bar{N}_{\mathrm{sat}}^3 \prod_{i=1}^{3} \tilde{u}_{\mathrm{g}}(k_i, m) &+ \bar{N}_{\mathrm{sat}}^2 \left[\tilde{u}_{\mathrm{g}}(k_1, m)\tilde{u}_{\mathrm{g}}(k_2, m) + \tilde{u}_{\mathrm{g}}(k_1, m)\tilde{u}_{\mathrm{g}}(k_3, m) \right. \\
&\left. + \tilde{u}_{\mathrm{g}}(k_2, m)\tilde{u}_{\mathrm{g}}(k_3, m)\right], \qquad (B.37)
\end{aligned}$$

where we assumed for simplicity that $\bar{N}_{\mathrm{cen}} = \Theta(m - m_{\mathrm{min}})$.

Bibliography

Abazajian, K., Adelman-McCarthy, J. K., Agüeros, M. A., et al. 2008, arXiv:0812.0649

Adler, R. J. 1981, The Geometry of Random Fields (Wiley, Chichester)

Ahmad, Q. R. et al. 2001, Phys. Rev. Lett., 87, 071301

Albrecht, A., Bernstein, G., Cahn, R., et al. 2006, arXiv:astro-ph/0609591

Alcock, C., Allsman, R. A., Alves, D. R., et al. 2000, ApJ, 542, 281

Aldering, G., Akerlof, C. W., Amanullah, R., et al. 2002, in Society of Photo-Optical Instrumentation Engineers (SPIE) Conference Series, Vol. 4835, Society of Photo-Optical Instrumentation Engineers (SPIE) Conference Series, ed. A. M. Dressler, 146–157

Amsler, C. et al. 2008, Phys. Lett., B667, 1

Arfken, G. B. & Weber, H. J. 2001, Mathematical Methods for Physicists, Vol. Fifth (Academic Press, San Diego)

Bacon, D. J., Goldberg, D. M., Rowe, B. T. P., & Taylor, A. N. 2006, MNRAS, 365, 414

Bardeen, J. M., Bond, J. R., Kaiser, N., & Szalay, A. S. 1986, ApJ, 304, 15

Barkana, R. & Loeb, A. 2007, Reports on Progress in Physics, 70, 627

Bartelmann, M. & Schneider, P. 2001, Phys. Rep., 340, 291

Beaulieu, J.-P., Bennett, D. P., Fouqué, P., et al. 2006, Nature, 439, 437

Berlind, A. A. & Weinberg, D. H. 2002, ApJ, 575, 587

Bernardeau, F., Colombi, S., Gaztañaga, E., & Scoccimarro, R. 2002, Phys. Rep., 367, 1

Bond, J. R., Cole, S., Efstathiou, G., & Kaiser, N. 1991, ApJ, 379, 440

Brainerd, T. G., Blandford, R. D., & Smail, I. 1996, ApJ, 466, 623

Bullock, J. S., Kolatt, T. S., Sigad, Y., et al. 2001, MNRAS, 321, 559

Burles, S. & Tytler, D. 1998, ApJ, 499, 699

Carroll, S. M., Press, W. H., & Turner, E. L. 1992, ARA&A, 30, 499

Cole, S., Percival, W. J., Peacock, J. A., et al. 2005, MNRAS, 362, 505

Colless, M., Dalton, G., Maddox, S., et al. 2001, MNRAS, 328, 1039

Cooray, A. & Hu, W. 2001, ApJ, 554, 56

Cooray, A. & Hu, W. 2002, ApJ, 574, 19

Cooray, A. & Sheth, R. 2002, Phys. Rep., 372, 1

Copeland, E. J. 2007, in American Institute of Physics Conference Series, Vol. 957, Particles, Strings, and Cosmology-PASCOS 2007, ed. A. Rajantie, C. Contaldi, P. Dauncey, & H. Stoica, 21–29

Crittenden, R. G., Natarajan, P., Pen, U.-L., & Theuns, T. 2002, ApJ, 568, 20

Crocce, M. & Scoccimarro, R. 2006, Phys. Rev. D, 73, 063519

Cyburt, R. H., Fields, B. D., Olive, K. A., & Skillman, E. 2005, Astroparticle Physics, 23, 313

Dodelson, S. 2003, Modern cosmology (Academic Press)

Eisenstein, D. J. & Hu, W. 1998, ApJ, 496, 605

Eisenstein, D. J. & Hu, W. 1999, ApJ, 511, 5

Eisenstein, D. J. & Zaldarriaga, M. 2001, ApJ, 546, 2

Eisenstein, D. J., Zehavi, I., Hogg, D. W., et al. 2005, ApJ, 633, 560

Feldman, H. A., Kaiser, N., & Peacock, J. A. 1994, ApJ, 426, 23

Fischer, P., McKay, T. A., Sheldon, E., et al. 2000, AJ, 120, 1198

Fosalba, P. & Gaztanaga, E. 1998, MNRAS, 301, 503

Freedman, W. L., Madore, B. F., Gibson, B. K., et al. 2001, ApJ, 553, 47

Frieman, J. A., Turner, M. S., & Huterer, D. 2008, ARA&A, 46, 385

Fry, J. N. 1984, ApJ, 279, 499

Fry, J. N. & Gaztanaga, E. 1993, ApJ, 413, 447

Fry, J. N. & Peebles, P. J. E. 1978, ApJ, 221, 19

Fu, L., Semboloni, E., Hoekstra, H., et al. 2008, A&A, 479, 9

Fukuda, Y. et al. 1998, Phys. Rev. Lett., 81, 1562

Gao, L., Navarro, J. F., Cole, S., et al. 2008, MNRAS, 387, 536

Gladders, M. D. & Yee, H. K. C. 2005, ApJS, 157, 1

Groth, E. J. & Peebles, P. J. E. 1977, ApJ, 217, 385

Guth, A. H. 1981, Phys. Rev. D, 23, 347

Guzik, J. & Seljak, U. 2002, MNRAS, 335, 311

Hawkins, E., Maddox, S., Cole, S., et al. 2003, MNRAS, 346, 78

Heath, D. J. 1977, MNRAS, 179, 351

Henry, J. P. 2000, ApJ, 534, 565

Hernquist, L. 1990, ApJ, 356, 359

Heymans, C. & Heavens, A. 2003, MNRAS, 339, 711

Hirata, C. M. & Seljak, U. 2004, Phys. Rev. D, 70, 063526

Hoekstra, H., van Waerbeke, L., Gladders, M. D., Mellier, Y., & Yee, H. K. C. 2002, ApJ, 577, 604

Hu, W. & Jain, B. 2004, Phys. Rev. D, 70, 043009

Impey, C. D., Falco, E. E., Kochanek, C. S., et al. 1998, ApJ, 509, 551

Jain, B. & Bertschinger, E. 1994, ApJ, 431, 495

Jain, B., Scranton, R., & Sheth, R. K. 2003, MNRAS, 345, 62

Jenkins, A., Frenk, C. S., Pearce, F. R., et al. 1998, ApJ, 499, 20

Jenkins, A., Frenk, C. S., White, S. D. M., et al. 2001, MNRAS, 321, 372

Jeong, D. & Komatsu, E. 2006, ApJ, 651, 619

Jing, Y. P. 2000, ApJ, 535, 30

Joachimi, B., Schneider, P., & Eifler, T. 2008, A&A, 477, 43

Johnston, D. E. 2006, MNRAS, 367, 1222

Kaiser, N. 1998, ApJ, 498, 26

Kauffmann, G., Colberg, J. M., Diaferio, A., & White, S. D. M. 1999, MNRAS, 303, 188

Kilbinger, M. & Schneider, P. 2005, A&A, 442, 69

Komatsu, E., Dunkley, J., Nolta, M. R., et al. 2009, ApJS, 180, 330

Kravtsov, A. V., Berlind, A. A., Wechsler, R. H., et al. 2004, ApJ, 609, 35

Lacey, C. & Cole, S. 1993, MNRAS, 262, 627

Landau, L. D. & Lifshitz, E. M. 1959, Fluid mechanics (Pergamon Press, Oxford)

LaRoque, S. J., Bonamente, M., Carlstrom, J. E., et al. 2006, ApJ, 652, 917

Lewis, A., Challinor, A., & Lasenby, A. 2000, Astrophys. J., 538, 473

Limber, D. N. 1953, ApJ, 117, 134

Lynds, R. & Petrosian, V. 1986, in Bulletin of the American Astronomical Society, Vol. 18, Bulletin of the American Astronomical Society, 1014

Ma, C.-P. & Fry, J. N. 2000, ApJ, 543, 503

Mandelbaum, R., Hirata, C. M., Broderick, T., Seljak, U., & Brinkmann, J. 2006a, MNRAS, 370, 1008

Mandelbaum, R., Seljak, U., Cool, R. J., et al. 2006b, MNRAS, 372, 758

Mandelbaum, R., Seljak, U., Kauffmann, G., Hirata, C. M., & Brinkmann, J. 2006c, MNRAS, 368, 715

Matarrese, S., Verde, L., & Heavens, A. F. 1997, MNRAS, 290, 651

Mather, J. C., Fixsen, D. J., Shafer, R. A., Mosier, C., & Wilkinson, D. T. 1999, ApJ, 512, 511

McClelland, J. & Silk, J. 1977, ApJ, 217, 331

McDonald, P. 2007, Phys. Rev. D, 75, 043514

McKay, T. A., Sheldon, E. S., Racusin, J., et al. 2001, arXiv:astro-ph/0108013

Meiksin, A. & White, M. 1999, MNRAS, 308, 1179

Mo, H. J., Jing, Y. P., & White, S. D. M. 1997, MNRAS, 284, 189

Mo, H. J. & White, S. D. M. 1996, MNRAS, 282, 347

Moore, B., Quinn, T., Governato, F., Stadel, J., & Lake, G. 1999, MNRAS, 310, 1147

Nagai, D. & Kravtsov, A. V. 2004, in IAU Colloq. 195: Outskirts of Galaxy Clusters: Intense Life in the Suburbs, ed. A. Diaferio, 296–298

Nagai, D. & Kravtsov, A. V. 2005, ApJ, 618, 557

Navarro, J. F., Frenk, C. S., & White, S. D. M. 1996, ApJ, 462, 563

Neto, A. F., Gao, L., Bett, P., et al. 2007, MNRAS, 381, 1450

Neyman, J. & Scott, E. L. 1952, ApJ, 116, 144

Peacock, J. A. 1999, Cosmological Physics (Cambridge University Press)

Peacock, J. A. & Dodds, S. J. 1996, MNRAS, 280, L19

Peebles, P. J. E. 1974, A&A, 32, 197

Peebles, P. J. E. 1980, The large-scale structure of the universe (Princeton University
    Press)

Penzias, A. A. & Wilson, R. W. 1965, ApJ, 142, 419

Perlmutter, S., Aldering, G., Goldhaber, G., et al. 1999, ApJ, 517, 565

Pielorz, J., Rödiger, J., & Schneider, P. 2009, in prep.

Press, W. H. & Schechter, P. 1974, ApJ, 187, 425

Riess, A. G., Filippenko, A. V., Challis, P., et al. 1998, AJ, 116, 1009

Rimes, C. D. & Hamilton, A. J. S. 2006, MNRAS, 371, 1205

Sahlén, M., Viana, P. T. P., Liddle, A. R., et al. 2008, arXiv:0802.4462

Scherrer, R. J. & Bertschinger, E. 1991, ApJ, 381, 349

Schneider, P. 1996, MNRAS, 283, 837

Schneider, P. 1998, ApJ, 498, 43

Schneider, P., Ehlers, J., & Falco, E. E. 1992, Gravitational Lenses (Springer-Verlag,
    Berlin)

Schneider, P., Kilbinger, M., & Lombardi, M. 2005, A&A, 431, 9

Schneider, P., Kochanek, C. S., & Wambsganss, J. 2006, Gravitational Lensing: Strong,
    Weak and Micro (Saas-Fee Advanced Courses, Volume 33, Springer-Verlag, Berlin)

Schneider, P. & Lombardi, M. 2003, A&A, 397, 809

Schneider, P., van Waerbeke, L., Kilbinger, M., & Mellier, Y. 2002, A&A, 396, 1

Schneider, P. & Watts, P. 2005, A&A, 432, 783

Scoccimarro, R., Colombi, S., Fry, J. N., et al. 1998, ApJ, 496, 586

Scoccimarro, R. & Couchman, H. M. P. 2001, MNRAS, 325, 1312

Scoccimarro, R. & Frieman, J. 1996, ApJS, 105, 37

Scoccimarro, R. & Frieman, J. A. 1999, ApJ, 520, 35

Scoccimarro, R., Sheth, R. K., Hui, L., & Jain, B. 2001, ApJ, 546, 20

Scoccimarro, R., Zaldarriaga, M., & Hui, L. 1999, ApJ, 527, 1

Sefusatti, E., Crocce, M., Pueblas, S., & Scoccimarro, R. 2006, Phys. Rev. D, 74, 023522

Seljak, U. 2000, MNRAS, 318, 203

Seljak, U. & Zaldarriaga, M. 1996, ApJ, 469, 437

Semboloni, E., van Waerbeke, L., Heymans, C., et al. 2007, MNRAS, 375, L6

Sheth, R. K. & Diaferio, A. 2001, MNRAS, 322, 901

Sheth, R. K., Mo, H. J., & Tormen, G. 2001, MNRAS, 323, 1

Sheth, R. K. & Tormen, G. 1999, MNRAS, 308, 119

Simon, P. 2007, A&A, 473, 711

Simon, P., Watts, P., Schneider, P., et al. 2008, A&A, 479, 655

Smith, R. E., Peacock, J. A., Jenkins, A., et al. 2003, MNRAS, 341, 1311

Smith, R. E., Scoccimarro, R., & Sheth, R. K. 2007, Phys. Rev. D, 75, 063512

Smith, R. E. & Watts, P. I. R. 2005, MNRAS, 360, 203

Smith, R. E., Watts, P. I. R., & Sheth, R. K. 2006, MNRAS, 365, 214

Spergel, D. N., Verde, L., Peiris, H. V., et al. 2003, ApJS, 148, 175

Sugiyama, N. 1995, ApJS, 100, 281

Takada, M. & Bridle, S. 2007, New Journal of Physics, 9, 446

Takada, M. & Jain, B. 2003, MNRAS, 340, 580

Takada, M. & Jain, B. 2008, arXiv:0810.4170

Takahashi, R., Yoshida, N., Takada, M., et al. 2009, arXiv:0902.0371

Tinker, J., Kravtsov, A. V., Klypin, A., et al. 2008, ApJ, 688, 709

Tinker, J. L., Weinberg, D. H., Zheng, Z., & Zehavi, I. 2005, ApJ, 631, 41

Tyson, J. A., Valdes, F., Jarvis, J. F., & Mills, Jr., A. P. 1984, ApJ, 281, L59

Walsh, D., Carswell, R. F., & Weymann, R. J. 1979, Nature, 279, 381

Watts, P. & Schneider, P. 2005, in IAU Symposium, Vol. 225, Gravitational Lensing Impact on Cosmology, ed. Y. Mellier & G. Meylan, 243–248

Weinberg, D. H., Beers, T., Blanton, M., et al. 2007, in Bulletin of the American Astronomical Society, Vol. 38, Bulletin of the American Astronomical Society, 963

Weinberg, S. 1972, Gravitation and Cosmology: Principles and Applications of the General Theory of Relativity (Wiley, New York)

White, M. & Hu, W. 2000, ApJ, 537, 1

White, S. D. M. & Rees, M. J. 1978, MNRAS, 183, 341

Yang, X., Mo, H. J., Jing, Y. P., & van den Bosch, F. C. 2005, MNRAS, 358, 217

Yee, H. K. C., Gladders, M. D., Gilbank, D. G., et al. 2007, in Astronomical Society of the Pacific Conference Series, Vol. 379, Cosmic Frontiers, ed. N. Metcalfe & T. Shanks, 103

Zehavi, I., Weinberg, D. H., Zheng, Z., et al. 2004, ApJ, 608, 16

Zehavi, I., Zheng, Z., Weinberg, D. H., et al. 2005, ApJ, 630, 1

Zentner, A. R. 2007, International Journal of Modern Physics D, 16, 763

Zheng, Z., Berlind, A. A., Weinberg, D. H., et al. 2005, ApJ, 633, 791

Zheng, Z., Coil, A. L., & Zehavi, I. 2007, ApJ, 667, 760

Acknowledgments

A PhD thesis is an extended project that lasts for approximately three years and as such is influenced by several people I would like to thank in the following. In particular, during my time at the Argelander-Institut für Astronomie (AIfA) of the university of Bonn, I gained a lot from the help and discussions with other people. First of all, I am deeply indebted to my supervisor Peter Schneider who provided the necessary guidance and always helped me when needed. Especially in the last part of my project his profound proof-reading significantly improved my thesis manuscript and pointed me to a scientific writing style. In addition, I thank him for accepting me to work in his research group as I did my Diploma at the university of Dortmund in the field of theoretical high-energy particle physics.

I am deeply grateful for the fruitful and ongoing collaboration with Jasmin Pielorz on the dark matter halo model and covariance modeling of the convergence power spectrum estimator. Moreover, I had many inspiring theoretical discussions on the halo model of galaxy clustering with Leonardo Castañeda, Ismael Tereno and Emilio Pastor Mira. I appreciate stimulating discussions I had with Martin Kilbinger on higher-order correlation functions and HEPT leading me the way in the first part of my thesis. Furthermore, I thank Patrick Simon for sharing his results of the galaxy-galaxy-galaxy lensing analysis in the RCS field. Finally, a special thanks to Benjamin Joachimi for sharing his knowledge on cosmic shear estimators which was important to construct an unbiased galaxy-galaxy lensing estimator in Fourier space.

I enjoyed a lot the inspiring and warm working atmosphere at the AIfA institute. Many thanks to my former office-mate Patrick Hudelot who is now working for the Terapix project in Paris and my current office-mates Jasmin Pielorz and Xinzhong Er for several scientific and non-scientific discussions. Moreover, I am thankful to Philip Bett, Alex Böhnert, Leonardo Castañeda, Jacqueline Chen, Helen Eckmiller, Tim Eifler, Xinzhong Er, Thomas Erben, Jan Hartlap, Philippe Heraudeau, Stefan Hilbert, Karianne Holhjem, Holger Israel, Benjamin Joachimi, Julian Krause, Andreas Küpper, Rupal Mittal, Oxana Nenestyan, Emilio Pastor Mira, Jennifer Piel, Jasmin Pielorz, Nina Roth, Mischa Schirmer, Elisabetta Semboloni, Sherry Suyu, Ismael Tereno, Filomena Volino, Daniela Wuttke and Achim Zien.

The quality of this thesis improved by the tedious work of proof-reading by several people, most notably Jasmin Pielorz, Ismael Tereno and Benjamin Joachimi.

Even though I spend a significant part of my time in Bonn at work, there were also activities that improved my work-life balance. A special thanks goes to all participants of our weekly soccer seminar organized by Emilio Pastor Mira which was a lot of fun despite some (minor) injuries (*Sport ist Mord*). Moreover, I enjoyed the beautiful

landscape of the Eifel during hiking trips with Andreas Schulz.

And not to forget the irreplaceable and fast help in administrative issues provided by Kathy Schrüfer, Christina Stein-Schmitz and Elisabeth Danne. Even theoreticians need to rely more and more on numerical calculations performed on computers. Occurring computer and printer problems were smoothly solved by our administrators Oliver-Mark Cordes, Ole Marggraf, Günther Lay and Uwe Naß.

I especially acknowledge Cristiano Porciani for accepting to be the co-referee of my thesis and the other members of the thesis committee.

Last but not least, I thank my parents for their continuous support and encouragement during my studies in Dortmund and in Bonn, and Katharina for her love and patience during the whole phase of my thesis project.